Platinum Pincer Complexes: In Pursuit of Switchable Materials

Bryant, Mathew

Award date:
2016

Awarding institution:
University of Bath

Platinum Pincer Complexes: In Pursuit of Switchable Materials

---

Mathew James Bryant

A thesis submitted for the degree of Doctor of Philosophy

Department of Chemistry

University of Bath

September 2015

Dedicated to Elina

Abbreviation	Definition
°	Degrees (angle)
°C	Degrees Celsius
[$P_{14,666}$][TPTP]	Trihexyl(tetradecyl)phosphonium tris(pentafluoroethyl)trifluorophosphate
μ	Magnetic moment
A	Amperes
Å	Ångströms
A.U	Absorbance units
bpy	2,2-bipyridine
C	Side centred cell
C^N^C	Pincer ligand based on 2,6-diphenyl-pyridine unit
ca.	Circa/approximately
cm^{-1}	Per centimetre
DAC	Diamond anvil cell
DCM	Dichloromethane
DFT	Density function theory
dm^{-3}	Per decimeter^3
E	Normalised structure factor
e^-	Electron
E_{ox}	Oxidation peak
E_{red}	Reduction peak
et al.	Et alii/and others
Et_2O	Diethyl ether
F	Face centred cell
f	Atomic scattering factor
Fc	Ferrocene
F_{calc}	Structure factor (calculated)
F_{hkl}	Structure factor (for given hkl)
F_{obs}	Structure factor (observed)
g	Grams
GPa	Gigapascals
h	Hours
hkl	Miller set
HOCO	Highest occupied crystal orbital
HOMO	Highest occupied molecular orbital
Hz	Hertz
I	Body centred cell
I	Transmitted light
I	Current
I_{hkl}	Diffraction intensity (for given hkl)
IR	Infrared
ITO	Indium Tin Oxide
j	Total angular momentum (individual)
J	Total angular momentum (total)
j_{x-y}	j-coupling (NMR(nuclei))
K	Degrees Kelvin
l	Azimuthal quantum number (individual)

L	Azimuthal quantum number (total)
LC	Ligand-centred (excitation)
LED	Light emitting diode
LUCO	Lowest unnocupied crystal orbital
LUMO	Lowest unnocupied molecular orbital
mg	Milligrams
MHz	Megahertz
MLCT	Metal to ligand charge transfer (excitation)
mm	Millimeter
mM	Millimole
MMLCT	Metal-metal to ligand charge transfer (excitation)
mol^{-1}	Per mole
mV	Millivolts
N^C^N	Pincer ligand based on 3,5-di(2-pyridyl)benzoate unit
N^N^C	Pincer ligand based on 6-Phenyl-2,2'-bipyridine unit
nm	Nanometers
NMR	Nuclear magnetic resonance
Θ	Angle
OLED	Organic light emitting diode
OTTLE	Optically transparent thin layer electrochemical (cell)
P	Primitive cell
ppy	2-phenylpyridine
R	Coordinated group
s	Seconds
s	Spin quantum number (individual)
S	Spin quantum number (total)
SCE	Saturated calomel electrode
(Sh)	Shoulder (of peak)
S_n	Singlet state
TD-DFT	Time dependent density function theory
TGA	Thermogravimetric analysis
THF	Tetrahydrofuran
TMEDA	Tetramethylethylenediamine
T_n	Triplet state
tpy	Terpyridine
UV	Ultraviolet
UV-Vis	UV-Visible (light)
V	Volts
Δ_{sq}	Crystal field splitting energy (Square planar)
η	Refractive index
η	Hapticity
λ	Wavelength
λ_{max}	Wavelength of maximum absorption/emission
µm	Micrometer
ξ	Spin-orbit coupling constant
ρ	Electron density
φ	Phase
φ_{lum}	Quantum yield

Acknowledgements

Firstly I would like to thank my supervisor Paul Raithby for his support, advice, and kind generosity throughout my PhD, and for all the opportunities he has provided me with. I would also like to thank the Raithby group, both past and present, for all their help and guidance.

Particular thanks to Dr. Sara Fuertes who introduced me to platinum pincers and whose work and ideas have contributed enormously to the development of this project.

Many thanks to everyone at the University of Bath, and elsewhere, who have helped me along the way, particularly Dr. Mark Warren, Dr. Robin Owen and Dr. Pierre Aller at the Diamond Light Source for taking the time to help me with various solid state spectroscopy experiments.

I would like to thank Dr. Simon Teat and Dr. Christine Beavers for granting me the use of Beamline 11.3.1 at the ALS and for all their help, without which my inability to grow crystals of a useful size would have been a far larger problem!

I would also like to express my gratitude to the University of Bath for providing me with the funding to carry out this research.

Finally I would like to thank my family for all their encouragement, particularly my wife Elina, whose constant support during my PhD made this thesis possible.

Abstract

The research presented within this thesis is concerned with the design, synthesis, characterisation, and analysis of a series of new compounds of platinum (II), with aims to produce compounds possessing switchable optical properties, and with potential applications as "smart-materials" for use as highly selective sensors.

Chapter 1 contains a brief review of the interaction of light with matter and the phenomena of fluorescence and phosphorescence. This is followed by an introduction to the chemistry and electronic properties of platinum(II) pincer complexes. The chapter is completed by a description of the instrumental methods used to structurally and spectroscopically analyse the new complexes synthesised in this thesis, and focuses on x-ray crystallographic and optical spectroscopy techniques.

Chapter 2 involves a spectroscopic and computational study into three new platinum N^C^N pincer complexes, in order to more fully understand and explain the mechanisms behind the photophysical properties of this class of compound. In doing so, attempting to achieve some control over the system's colour and/or luminescent emission, could then be more easily directed.

Chapter 3 builds on the knowledge gained through the work of **Chapter 2**, whereby stabilisation of the d_{xz} and d_{xy} orbitals was attempted in order to facilitate possible colour changes from intermetallic d_z^2 interactions. This was achieved through substitution with the strong-field cyanide ligand, and resulted in three highly selective and sensitive vapochromic materials, along with one thermochromic material. These were investigated spectroscopically, crystallographically and computationally, and show excellent promise in application as sensing materials.

Chapter 4 concerns the serendipitous discovery of mechanochromic properties in another new platinum pincer complex. Through crystallographic and spectroscopic analysis it was determined that a strong red-shifting in the luminescent emission as a result of grinding was due to amorphisation of the microcrystalline powder producing excimeric emission. The complex was also found to transition from yellow to red under hydrostatic pressure, and was studied crystallographically and computationally in order to explain this phenomenon.

The work of **Chapter 5** explores a second strategy for introducing controlled visual responses to applied stimuli. Again directed by the work of **Chapter 2** it was determined that using an acetylide as a bridge, a coordinating ligand with inherent switchability could potentially be used to manipulate the HOMO orbitals of the metal. The ligand chosen for this role was ferrocene, and a material that showed a reversible electrochromic response was produced.

Chapter 1: Introduction

Part 1. Photophysics

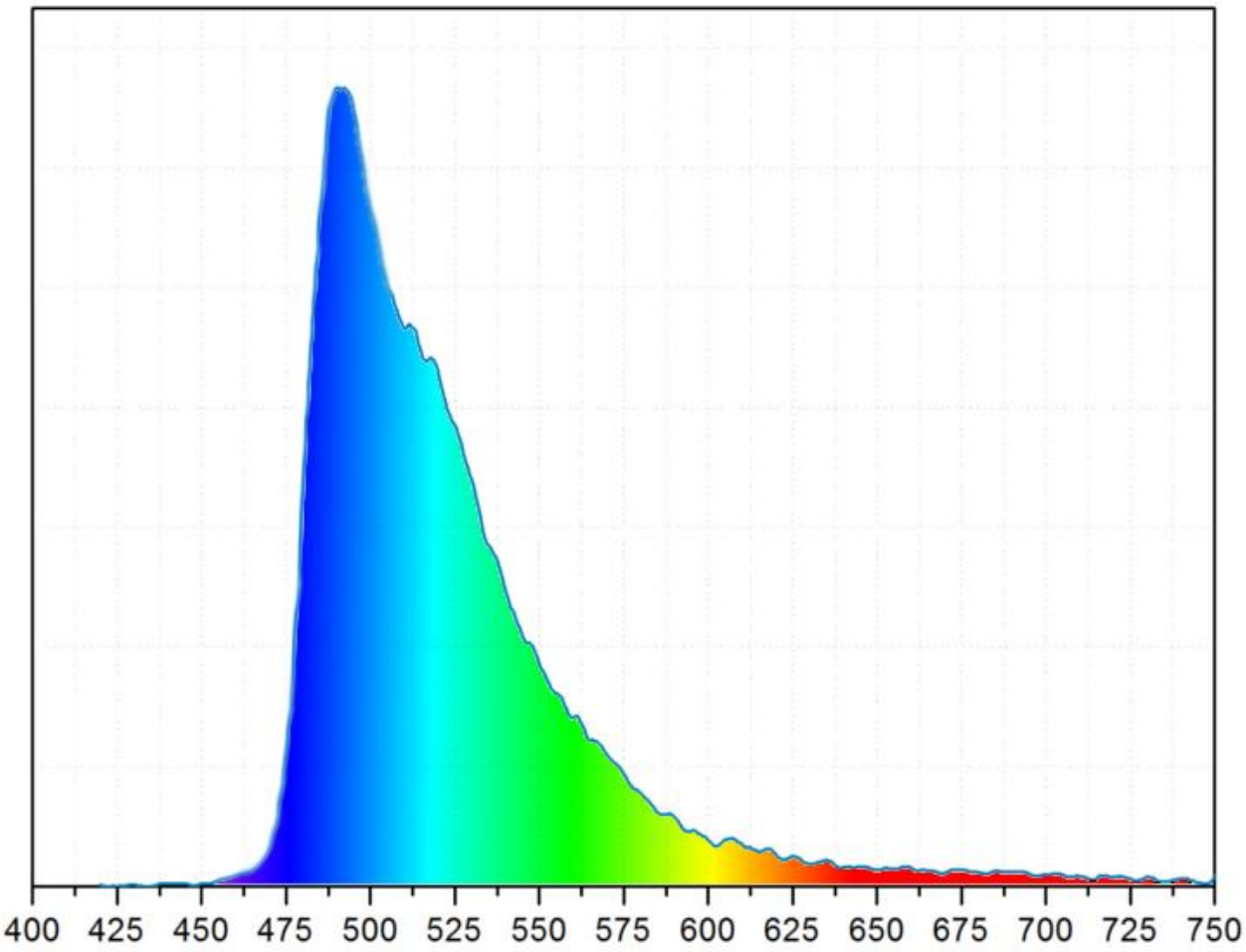

1. Introduction

1.1 Electronic transitions- light and electrons

The ways in which electromagnetic radiation can interact with matter is dependent on its wavelength, and therefore the energy it is able to impart. When a photon is absorbed by matter its energy is transferred, resulting in some form of energetic excitation. Low frequency microwave radiation for example, can impart its energy through excitation of molecules into new quantised rotational energy states proportional to the energy of that photon, and absorption of mid-IR frequencies can induce vibrational excitation of the bonds between atoms. As we ascend the electromagnetic spectrum further we reach the visible and UV regions, and this portion of the spectrum has sufficient energy to interact with electrons in the atoms themselves.[1]

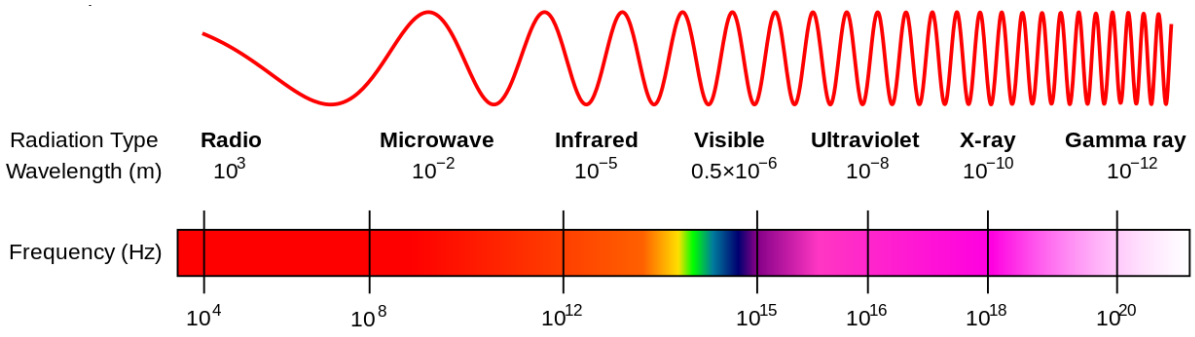

Figure 1.1. The electromagnetic spectrum. [2]

1.1.1 Colour in compounds

The colour of a compound is an attribute of its electronic properties. More specifically it is how a compound's electrons interact with visible light. In a typical compound at room temperature, electrons mostly exist in the lowest available energy state, or electronic ground state. If photons with an energy proportional to the gap between the ground and an excited state come into contact with a material, there is a chance that each photon will be absorbed, along with the promotion of an electron into this excited state.

As the electron is now in an energetically excited state, it is thermodynamically favourable for it to return to its ground state. For this to occur, the molecule needs to lose some energy to the surroundings, and this can happen in a variety of ways. Typically this energy is lost through vibrational modes, or phonons. The end result of this is the expulsion of energy as heat, and the

return of excited electrons into lower energy states. This method of electrons returning to the ground state is called internal conversion, or non-radiative relaxation.

The overall result of this process is that the frequency of light absorbed is removed from the spectrum falling upon the compound and converted to heat. If a portion of the visible spectrum (white light) is absorbed in this fashion by a compound, the result will be the transmittance of the remainder as coloured light. For example, a compound with ground state to excited state transitions matching blue/green frequencies will remove these frequencies from white light and so will visibly appear orange/red.[3]

1.1.2 Luminescence

Vibration is not the only way in which electrons may return energy to the surroundings. If a vibrational relaxation pathway is not available to an electron, it may return to the ground state by the re-emission of a photon, which is known as luminescence.[4] Photon absorption as a way of achieving the excited states required for luminescence is known as photoluminescence, however there are other ways of exciting electrons to this end, for example luminescence as a result of direct excitation using electric current is known as electroluminescence (as seen in LEDs).

Light emitted via photoluminescence is typically of lower frequency than that of the incident light (excitation energy) and this separation in absorption and emission maxima is called Stokes shift. An explanation for this can be derived from the Franck-Condon principle, which states that in an electronically excited state, a molecule tends not to have the same equilibrium inter-nuclear separations as in its ground state (i.e. excitation causes some molecular distortion). Also stated is that the electronic transition itself is near instantaneous in relation to the rate at which nuclei can adjust to their new equilibrium positions. Due to this, it can be said that upon excitation, the nuclei will initially remain at their ground state equilibrium positions, and therefore the electronically excited state is generated in a vibrationally excited state. The vibrational structure of the electronic states can be approximated using Morse potentials, and the electronic excitation can be represented as a vertical excitation between the ground and excited states (**Figure 1.2**). This essentially means that the most likely electronic transition is to the vibrational level of the excited state that has its classical turning point (in the oscillator) at the equilibrium nuclear positions of the ground state (r_e). After the initial excitation, the nuclei then relax to their new equilibrium position within the electronically excited state by internal conversion, and so this energy is lost non-radiatively to thermal phonons. The vibrational relaxation within the excited state usually happens within about

10^{-12} s – several orders of magnitude faster than the typical lifetime of the excited state, and as a result, electronic decay by photon emission is generally from the vibrational ground state of an electronic excited state.[5]

Emission will also follow the Franck-Condon principle, whereby decay will occur initially to the vibrationally excited state of the ground state that has its turning point at the equilibrium nuclear positions of the excited state (r_e'). Once again this will decay via internal conversion to the vibrational ground state. The combined loss of energy, non-radiatively through internal conversion for both these processes, explains the disparity in the excitation and emission energies in luminescent processes, i.e. Stokes shift. A large Stokes shift is also therefore associated with a large structural change in the excited state.[5,6]

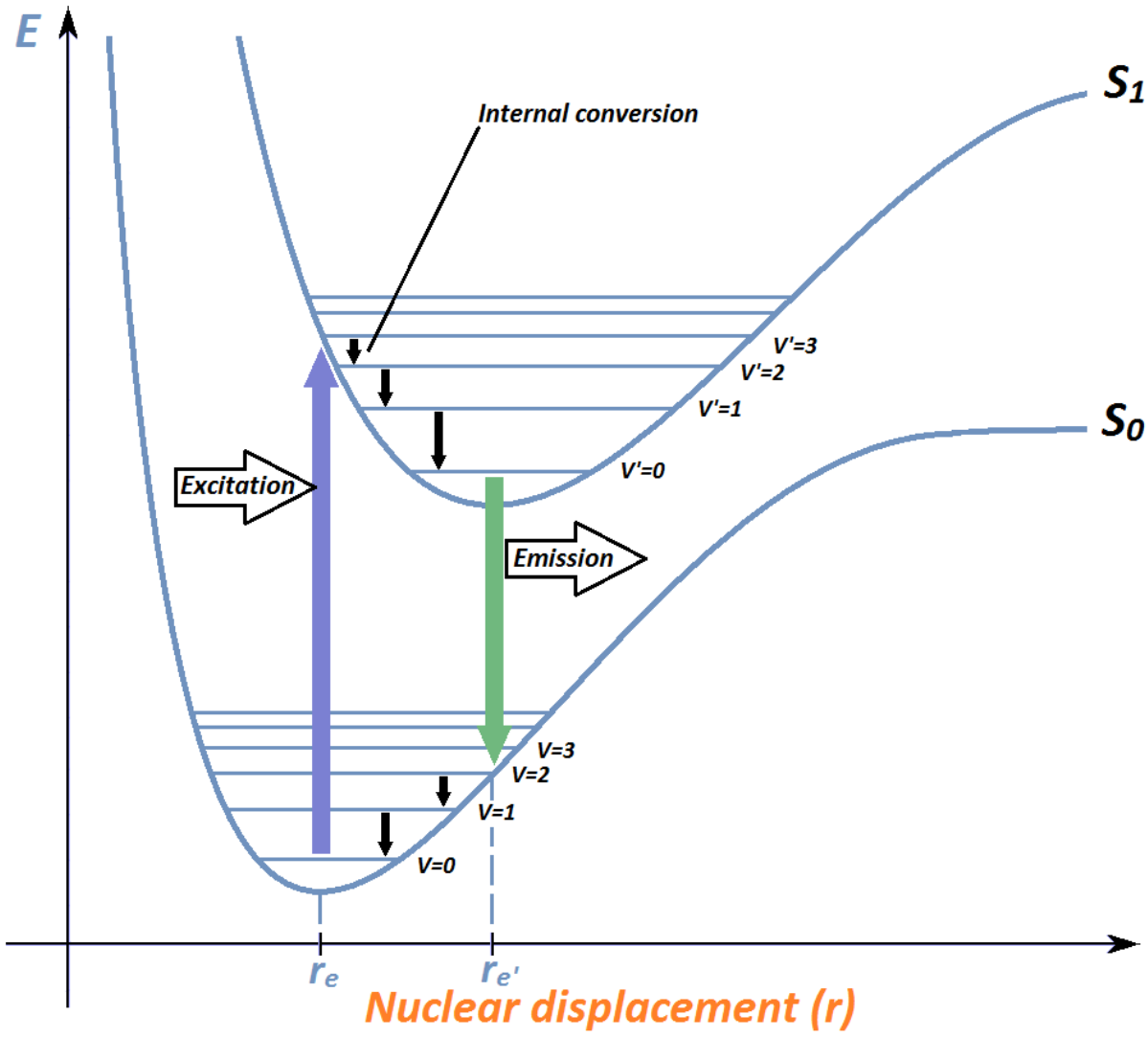

Figure 1.2. Morse Potentials demonstrating vertical electronic transitions signifying the near instantaneous nature of light absorption when compared to molecular motion (Franck-Condon Principle).

Luminescence is a very useful phenomenon as it is an inherently more efficient means of light production than incandescence. This is because it has the ability to operate independently of high temperatures, with LEDs and fluorescent tubes being good examples of highly energy efficient light producing technology that utilises luminescence.

1.1.2.1 Fluorescence and phosphorescence

Depending on the spin-symmetry of electrically excited states in relation to the ground state, luminescent emission can be categorised as either fluorescence or phosphorescence.[7] The spin symmetry of an electronic state is essentially a way of describing the alignment of electronic spin in the system. All electrons have spin quantum number s=1/2, and so in a system where all the electrons are paired, angular spin momentum S=0. This is known as a spin-antisymmetric state (non-parallel spins), and has a multiplicity of 1 (given that the spin magnetic quantum number m_s may only take values of [-S, (-S+1),...+S] or more concisely, the spin multiplicity is given by 2S+1) and is hence known as a **singlet state**.

Conversely, a spin-symmetric (parallel spins) excited state is a system where two electrons are unpaired and thus has an angular spin momentum S=1, giving a multiplicity of three. This is known as a **triplet state**.

States of other multiplicities also exist, but only the simplest cases of singlet and triplet states will discussed.

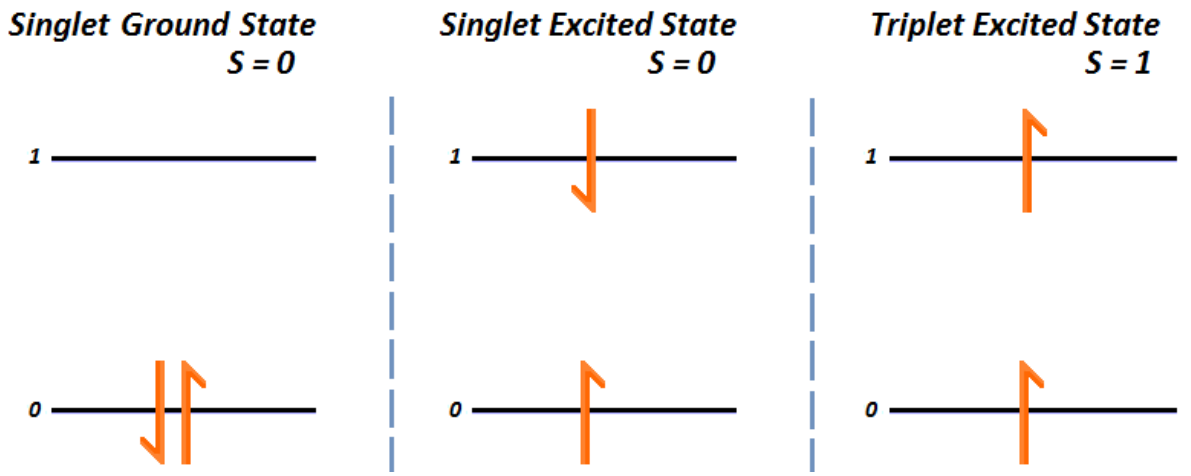

Figure 1.3. Diagram of spin antisymmetric (singlet) ground and excited states, and a spin symmetric (triplet) excited state.

Depending on the multiplicity of the ground state electronic configuration, direct relaxation of electrons (and hence luminescence) from excited states of any multiplicity can happen readily, however an electronic excitation or decay involving a spin flip (i.e triplet-singlet or singlet-triplet) is formally forbidden by the spin selection rule $\Delta S=0$.

For the sake of clarity, in this section it will be assumed that the ground state is always a singlet state, although this is not always the case.

Following population of an electronically excited state, spin-allowed emissive decay ($\Delta S=0$) to a ground state with the same multiplicity e.g. ($S_1 \rightarrow S_0$), is known as **fluorescence**. This is seen in **Figure 1.2**. Due to the spin allowed nature of this transition, decay via fluorescence for a typical organic molecule is rapid at room temperature with excited state lifetimes of roughly 10^{-9} to 10^{-7}s.[8]

Luminescent emission as a result of a spin forbidden decay to a lower energy state of different multiplicity (i.e. involving a spin flip) is known as **phosphorescence** e.g. ($T_1 \rightarrow S_0$). Due to the spin-forbidden nature of this decay, for a typical organic molecule, excited states leading to phosphorescence can have a lifetime many orders of magnitude longer than that of fluorescence, usually being between 10^{-3} and 10^{2}s.[8]

In order for this phenomenon to occur, the population of an excited state with different multiplicity to that of the ground state must first be achieved. Excitation to a triplet excited state (T_1) directly from a singlet ground state (S_0) is also a spin forbidden process as ($\Delta S\neq0$), and this combined with movement to a more thermodynamically unstable state means such a transition is highly unlikely to occur (with the probability of occupation in this manner being approximately 0.0001% that of the corresponding singlet excited state forming).[9] Direct population of triplet states from a singlet ground state can therefore be seen as insignificant. However, there is a more efficient mechanism of spin-flipping, and thus populating triplet excited states. In certain cases, it is possible for singlet excited state to decay non-radiatively to a lower energy triplet state through vibrational coupling. This is known as intersystem crossing. Intersystem crossing, still involving a spin-flip, is typically a kinetically unfavourable, slow process (10^{-2}-10^{-6}s)[6], and so in many systems cannot usually compete with fluorescent emission. However, as the triplet state is of a lower energy than the singlet excited state from which it came, the process is now thermodynamically favourable, making it far more likely to occur than through direct population via excitation. For this reason, phosphorescent emission also tends to have a longer wavelength than corresponding fluorescent emission. Emission from this lower energy triplet state back to the singlet ground state is a common origin of phosphorescent emission. This is the process described in **Figure 1.4**. [5,8]

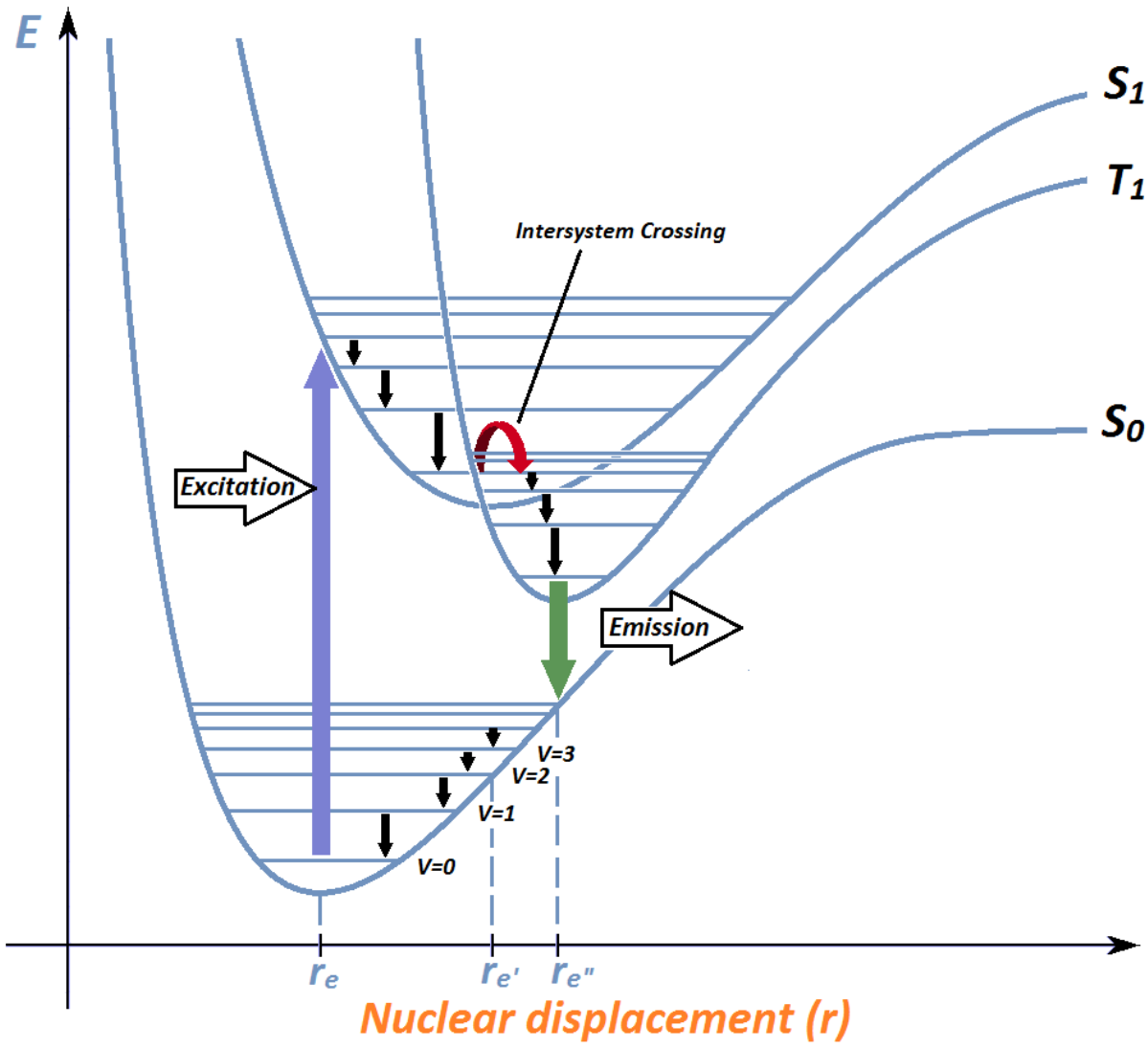

Figure 1.4. Diagram showing intersystem-crossing from a singlet excited state to a triplet, followed by phosphorescent emission to a singlet ground state.

1.1.2.1.1 Why study Phosphorescence?

As the demand for energy in today's society rises, so too does the necessity for energy efficiency in newly developed technology. Concerning potential light production and visual display applications, luminescence via fluorescence of organic molecules offers significant improvements in performance and efficiency when compared to current competing technology (such as LCDs), with OLED or "organic LED" displays currently available in mobile phone technology and in the most modern televisions.[10] Such a system however remains intrinsically inefficient, due to the mechanism by which fluorescent emission is produced. Because of their different multiplicities, the theoretical ratio of singlet excited states to forbidden triplet excited states in any system is 1:3 (i.e. a triplet contains

three degenerate states, as when S=1, (2S+1)=3) and there is good evidence to suggest that electronically excited states in small organic molecules are fairly well constrained by this ratio.[11,12]

This is easily rationalised by looking back at what multiplicity actually describes. As explained in **1.1.2.1**, a singlet state has a spin angular momentum S=0. This results in one possible set of quantum numbers as m_s can only equal 0 (2S+1), hence the multiplicity of 1 and designation as "singlet". A triplet state has spin angular momentum S=1, and this results in three otherwise degenerate states, differing only in the quantum number m_s, taking values of -1, 0, and 1.

As fluorescence occurs via the spin allowed decay of a singlet excited state into a lower energy singlet state (where intersystem crossing and phosphorescence are highly forbidden due to the low atomic number of organic materials), triplet emission from these compounds is highly unfavourable.

Since singlet states only account for 25% of possible emissive states, the maximum efficiency achievable by a device utilising only fluorescence is 25% purely from statistics. This leaves room for huge improvements in efficiency.

By utilising the triplet excited states for emissive decay, the theoretical maximum efficiency rises to 100%, and while this is an unrealistic target, it does provide scope for vastly improved efficiency in future devices and in lighting applications (including the efficient production of white light), and this provides a good incentive for research into triplet emitting compounds. As phosphorescence is a spin forbidden process, in order to utilise phosphorescent emission the spin selection rule needs to be relaxed. This can be achieved via the spin-orbit effect, with the inclusion of heavy atoms.[13,14,15,16]

1.1.2.2 Spin-Orbit coupling

Because electrons are charged, the motion of electrons (as with all moving charges) generates magnetic fields.

Spin orbit coupling is the interaction of an individual electron's intrinsic spin angular momentum (s) and its own orbital angular momentum (l) through the magnetic moments generated by these two forms of motion (by being both a spinning charge (μ_s) and being a charged particle possessing orbital motion (μ_l)). The two angular momenta of an electron combined describe its total angular momentum (j).

In light elements, such as carbon, the dominant interaction of electron momenta is between the individual orbital angular momenta (l) of all the electrons to give a total orbital momentum (L) for

the system, and likewise, between all the electrons' individual spin angular momenta (s) to give a total spin angular momentum for the system (S) (which is the value in question in the spin selection rule ΔS=0). For this reason the total angular momentum for the whole system (J) can be approximated to L+S, where L is the sum of all the orbital angular momenta of the individual electrons, and likewise S is the sum of all the individual electrons' spin angular momenta – this model is known as LS-coupling or Russell-Saunders Coupling, and accurately describes electronic momentum in low molecular weight systems.

The magnetic field produced by the movement of any charge is proportional to its velocity, and thus the faster an electron travels, the greater the associated orbital magnetic moment. In atoms with higher nuclear charge, electrons accelerate to much higher (often relativistic) speeds when approaching the nucleus. The result of this is that the coupling between the spin magnetic moment and the orbital component of individual electrons (spin-orbit coupling) will be higher in systems with larger nuclei.

This means that for heavy elements, the system is usually better described by the coupling of the spin and orbital angular momenta of individual electrons, each forming their own individual total angular momenta (j), the sum of which now best describes J for the system. This model is known as jj-coupling.

Due to these effects, it is clearly now no longer possible to accurately describe this system in terms of its total orbital (L), or total spin (S) angular momentum - thus the spin selection rule (ΔS=0) loses meaning, and may not necessarily hold true for heavy atoms.[17] This phenomenon is experimentally perceived as a relaxation the spin selection rule, in turn allowing previously "spin forbidden" processes such as intersystem crossing and phosphorescent decay to happen more readily in a luminescent system (although there are in fact rare cases where the opposite is true, whereby the rate constant for reverse intersystem crossing T→S is more affected by the heavy atom than the rate for phosphorescent decay [18]).

The inclusion of heavy elements, especially heavy transition metals, into luminescent systems therefore tends to have the effect of enhancing spin-orbit coupling, and relaxing the spin selection rule. This allows the thermodynamically favourable, but previously kinetically hindered process of intersystem crossing to dominate a luminescent system, along with phosphorescent emission. [19,20]

Part 2.

Platinum (II) (N^C^N) pincer compounds

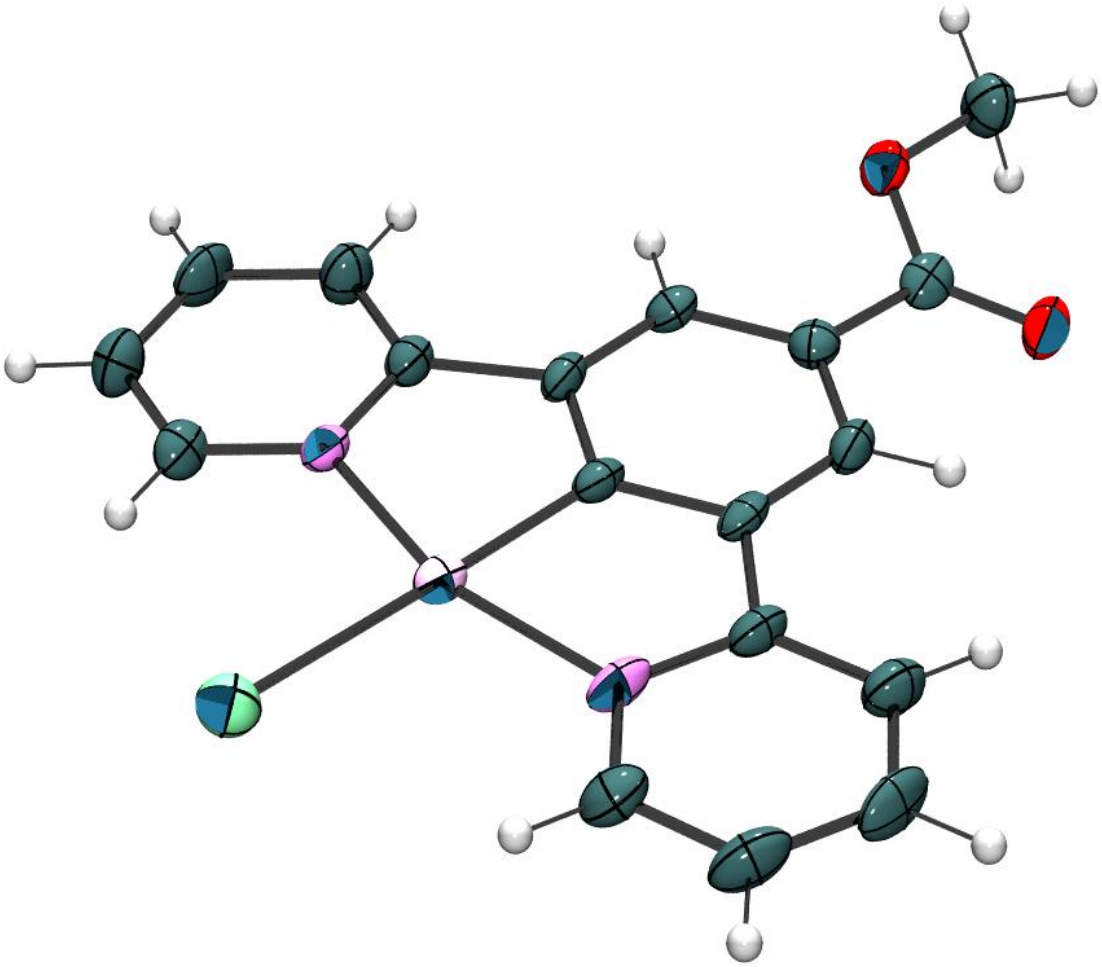

1.2 Organometallic compounds of platinum (II)

1.2.1 Platinum (II) and square planarity

The chemistry of platinum is dominated by the 2+ oxidation state, which is a d^8 ion, and a result it tends to form complexes with a square planar geometry. The tendency of d^8 ions to form this geometry is easily rationalised by a simple ligand field splitting diagram (Figure **1.5**). The best way to understand this is to imagine the effect on the orbital energies in a d^8 octahedral structure if the axial ligands (along the z-axis) were removed. The orbitals with components in the z-direction will see significant reduction in repulsion, and the contraction of the equatorial ligands in response to this will increase repulsion seen by orbitals in the xy-plane. The greater the orbital contribution in said axis/plane, the greater the effect. As a result the formerly high energy d_z^2 is greatly reduced in energy, with the d_{xz} and d_{yz} reduced to a lesser extent. Likewise, the energy of the $d_{x^2-y^2}$ and to a lesser extent the d_{xy} orbital energetically increase.

Overall this results in a high energy, unoccupied $d_{x^2-y^2}$ orbital along with significant overall stabilisation of the molecule, providing the additional Coulombic-repulsion from pairing of two previously unpaired electrons is low enough (i.e. if Δ_{sq} > pairing energy).

Due to the degree of Δ splitting increasing down the group (Ni - Pd - Pt) and the metal centre's inherently low pairing energy, four-coordinate compounds of platinum (II) are invariably square planar.

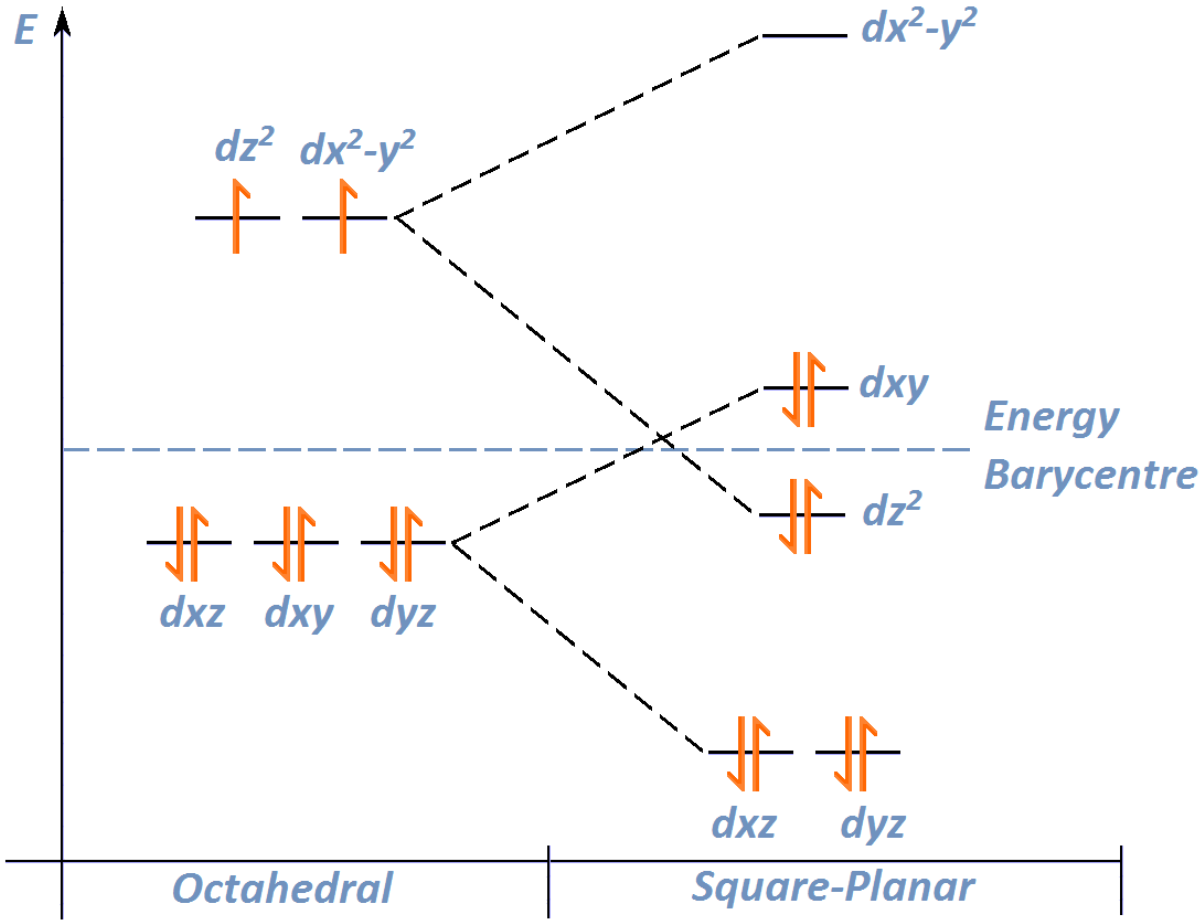

Figure 1.5. d^8 Square planar ligand field splitting diagram.

1.2.2 Luminescence in compounds of Pt(II)

As mentioned in **1.1.2.1.1**, the study of systems exhibiting phosphorescent emission is desirable, due to their intrinsic efficiency advantages over fluorescent systems. In order to introduce this property to a system, the inclusion of an atom with a high spin-orbit coupling constant (ξ) is very much a requirement, but also one that exhibits good orbital mixing with its surrounding ligands. This is to create a large orbital contribution into the electronic transitions, ensuring the chromophore/luminophore is not electronically isolated from the effects of the spin orbit effect, allowing for efficient phosphorescent emission.

Square planar platinum (II) compounds are an excellent candidate for such an application firstly due to their high spin-orbit coupling constant (ξ) resulting in fast intersystem crossing, and low triplet excited state lifetimes. [15,21,22,23,24,25] Organometallic compounds of platinum have also been shown to exhibit good orbital overlap with ligands, resulting in high metal contributions to electronic transitions. [21]

The importance of good orbital mixing is seen experimentally whereby compounds of platinum (II) tend to have stronger luminescence intensity than analogous palladium (II) compounds. In addition, the stronger ligand field splitting effects in platinum compounds make deleterious d-d transitions (into the vacant $d_{x^2-y^2}$ orbital) generally less thermally available (this is explained further in **1.2.2.1**). [14,26,27,28,29]

1.2.2.1 Excited state electronics of Pt(II) compounds

As explained in **1.2.1**, due to the square planarity of complexes of platinum (II), the $d_{x^2-y^2}$ orbital is very high in energy, and is only ever involved in antibonding interactions. As a result, excited states in which electrons are promoted to the $d_{x^2-y^2}$ orbital causes a large reduction in the metal to ligand bond order accompanied by significant geometric distortion.

This nuclear distortion of the excited state relative to the ground state can be represented as the displacement of the potential energy surface significantly away from that of the ground state (**Figure 1.6**) resulting in the emergence of an isoenergetic crossing point with the potential energy surface of the ground state. Emissive decay from this excited state is therefore unlikely due to the easy access to the ground state non-radiatively through this point (internal conversion).

The Laporte-forbidden nature of emissive decay through d-d transition also hinders luminescence and so overall, the rate constant for non-radiative decay is large, and the rate constant for radiative decay is small. It is clear that for platinum compounds to be luminescent to any significant degree, occupation of the $d_{x^2-y^2}$ state must be avoided.

It is also the case that other excited states within platinum complexes, such as π-π* LC (ligand centred) or n-π* MLCT (metal-ligand charge transfer) states between conjugated aromatic ligands and the metal may have poor luminescence too, even if they are lower in energy and have intrinsically better rate constants for luminescent decay (less forbidden). This is due to thermally activated depopulation to (and non-radiative decay from) the $d_{x^2-y^2}$ state - essentially funnelling the excited state electrons back down to the ground state.

The result of this is that simple platinum-ligand complexes in solution are rarely luminescent to any significant degree. The molecular distortion responsible for this quenching however may sometimes be restricted in the solid state, or in frozen "glassy solutions" preventing the formation of an isoenergetic crossing point. This prevents non-radiative depopulation, resulting in better luminescence quantum yields.

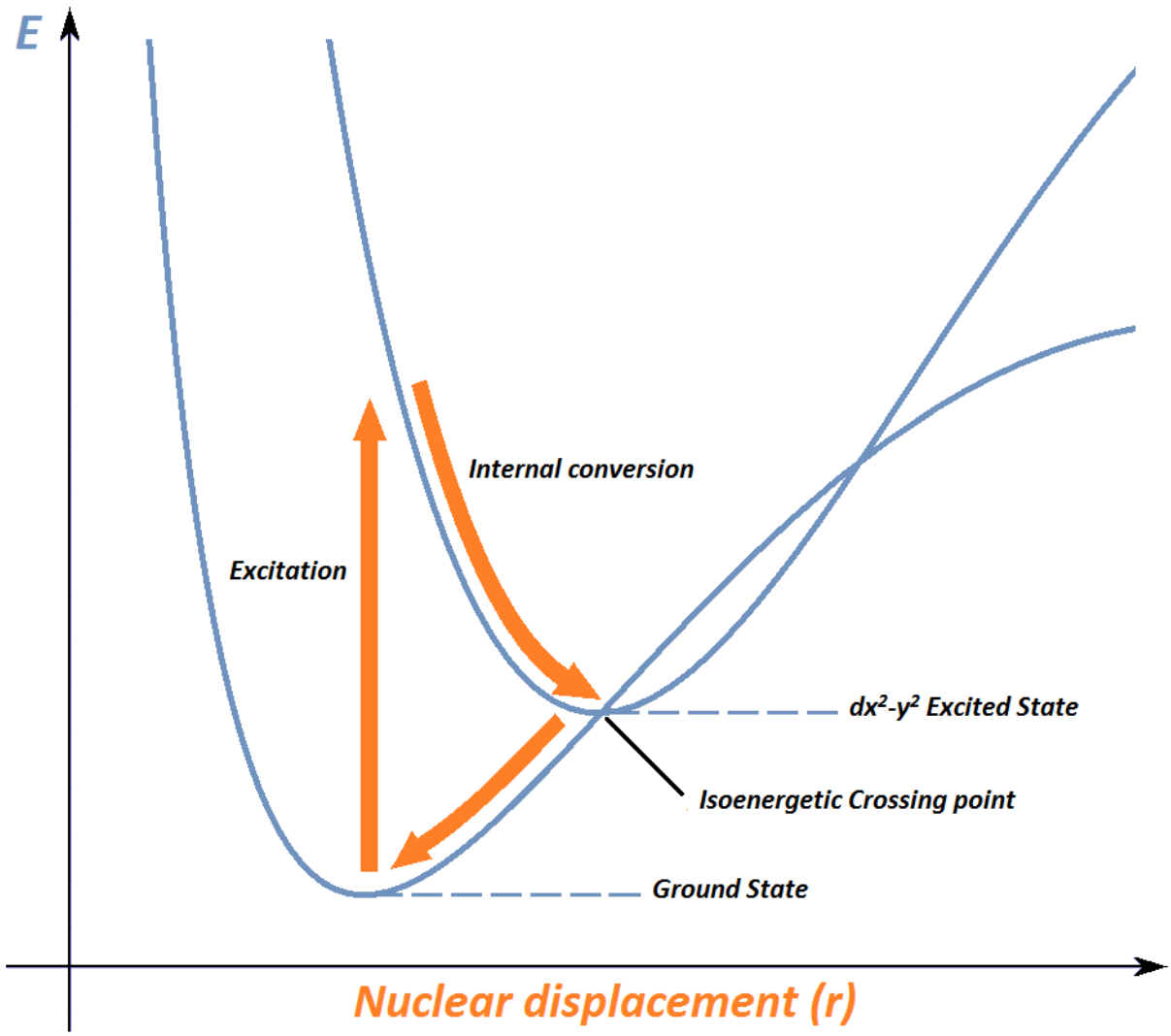

Figure 1.6. Representation of the displacement observed in the $d_{x^2-y^2}$ excited state energy surface upon occupation.

Platinum would appear then to be a poor choice of metal when designing organometallic compounds, if one aim is to study possible phosphorescent emissive properties. However through careful design, accessing excellent luminescence in conjunction with the other useful properties unique to square planar geometries is possible, and the choice of ligands is critical in this. [30,31,32]

1.2.2.2 Ligand effects

As discussed in **1.2.2.1** a low lying $d_{x^2-y^2}$ that is thermally accessible will often quench luminescent emission. Highly emissive complexes of platinum (II) therefore tend to exhibit excited states sufficiently energetically displaced from the $d_{x^2-y^2}$ to render it thermally inaccessible.

As metal contribution to the excited states from other d-orbitals is important in order to induce phosphorescent emission, applying methods to keep the emissive excited states energetically away from the $d_{x^2-y^2}$ state while retaining metal character need to be implemented. One possible way to do this is to lower the energy of the emissive state away from the $d_{x^2-y^2}$ by using ligands with low lying orbitals. Examples of this are Pt(II) porphyrins - a porphyrin ligand-based π-π* state is normally sufficiently low in energy to avoid depopulation to the $d_{x^2-y^2}$. Also the addition of electron donor groups to the ligands can encourage low energy intra-ligand excited states. Emission from these compounds is consequently low energy too, emitting in the red region of the spectrum.[33]

Lowering the energy of the excited state in this way is satisfactory for creating low energy emissive species, but this principle clearly cannot be extended to species where high energy emissions such as blue light is desired. Additionally, due to the energy gap law, which states that the rate of non-radiative decay processes exponentially increases with reduction in the separation of ground and excited states, this method can result in poor emissive efficiency. In order for emission to be possible in any part of the visible spectrum desired (and thus making platinum compounds feasible for wider luminescence applications), the energy of the vacant $d_{x^2-y^2}$ orbital must instead be raised. This may be achieved through the use of strong field ligands in the square planar environment, providing large ligand field splitting energy, and thus enlarging the energy gap between the upper and lower orbitals of the square planar configuration. Following this principle, many highly phosphorescent compounds of platinum (II) have been synthesised. [34,35]

1.2.2.3 Intermolecular d_{z^2} interactions

Another potentially interesting property resulting from the square planarity of platinum (II) centres, is that the geometry of the molecule is often fairly flat (particularly if the surrounding ligands are also flat, as with an sp^2 organic ligand system), and so may be stacked more closely than equivalent octahedral complexes. As seen in **Figure 1.7**, the d_{z^2} orbital lies perpendicular to the plane of a square planar molecule. If these molecules experience stacking interactions, providing an intermetallic separation of 3-3.5 Å, this may result in significant ground state metal-metal (d-d) σ-overlap of corresponding d_{z^2}, resulting in the formation of dσ and dσ* molecular orbitals (The unoccupied $6p_z$ levels also overlap to give pσ and pσ*orbitals). There is no formal Pt-Pt bonding

since both the dσ* and dσ levels remain fully occupied, however, configuration interaction with the pσ and pσ* orbitals results in net favourable interactions.

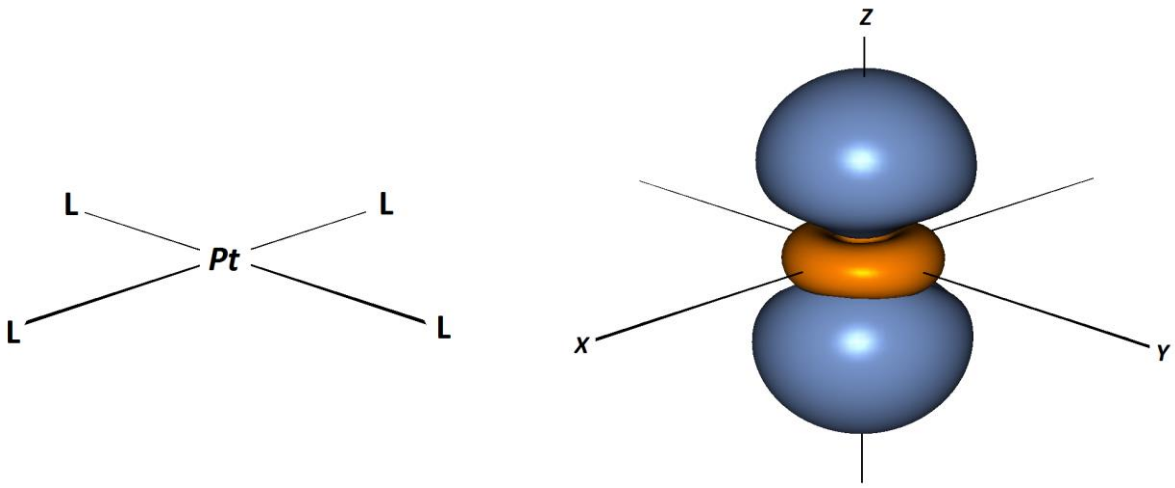

Figure 1.7. Diagram of the d_z^2-orbital's orientation perpendicular to the x-y plane of the coordinated ligand environment.

This is an important effect to take into account, as these interactions are highly effective in altering the energy of electronic transitions in platinum coordination compounds in particular, with high sensitivity of the absorption/emission spectra to this interaction. [26,36]

The reason for this becomes clear if we observe the molecular orbital diagrams for the single and aggregated molecules (**Figure 1.8**). If in a given Pt(II) molecule, the non-bonding d_z^2 orbital lies close in energy to that of the frontier orbitals (which is often the case), upon intermetallic d_z^2 overlap the higher energy occupied σ* state can often exceed the HOMO in energy (becoming the new HOMO). This essentially shrinks the HOMO-LUMO gap, leading to a new lowest energy excitation - a metal-metal bond to ligand charge transfer and excimer formation upon excitation.

As the energy of the new d_z^2+ d_z^2 molecular orbital depends on the degree of overlap, the shorter the inter-metal distance, the higher the σ* orbital, resulting in a further reduction in the excitation energy. [37]

The interaction therefore provides a highly sensitive mechanism by which altering or tuning the electronic properties may be achieved.

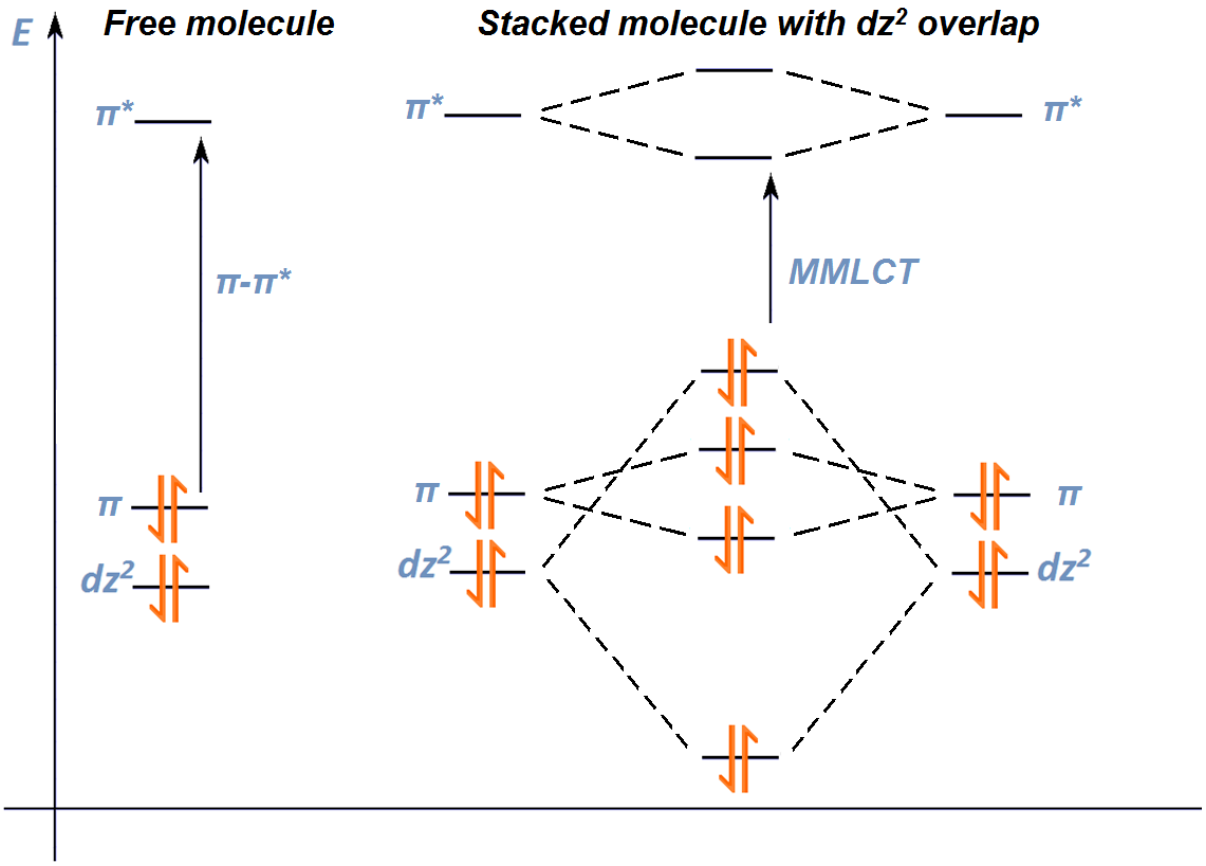

Figure 1.8. Simplified MO-diagram explaining the red-shift of absorption/emission often encountered upon significant intermolecular d_z^2-d_z^2 σ-overlap.

It can also be seen in **Figure 1.8** that even in the absence of metallic overlap, π-stacking interactions of ligands may also have the effect of reducing the HOMO-LUMO gap, and hence red-shifting the emission in a square planar transition metal compound. This can be seen in solutions with concentration-dependent emission wavelength,[38] and also in the fact that many such compounds still have red-shifted emission from solution to the solid state in examples with no Pt-Pt interactions in the solid form. [39]

1.3 The choice of platinum N^C^N pincer compounds as a building fragment

1.3.1 Polyaromatic coordinating ligands in platinum compounds

As explained in **1.2.2.2** the choice of ligands in designing new platinum (II) organometallics is very important in order to maximise the possibility of producing functional and interesting new materials. Not only do ligands need to incorporate strong field effects to avoid populating the $d_{x^2-y^2}$ excited state, but ideally they should resist distortion away from planar geometry around the platinum (II) centre, as this contributes to non radiative depopulation and is highly detrimental to the luminescence.

Basing the systems on a rigid polyaromatic Pt(II) ligand environment as a base fragment is a good way of ensuring good luminescent properties, along with providing good electronic communication between the chromo/luminophore and the metal centre. One such ligand type, suitable for producing highly luminescent species are the tridentate, cyclometallating, aromatic "pincer ligands".

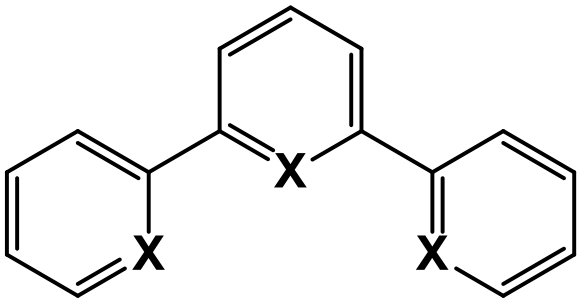

Figure 1.9. General structure of a tridentate polyaromatic coordinating ligand.

The general form of these ligands can be seen in **Figure 1.9**, and are structurally analogous to terpyridine. The positions marked **X** indicate the binding sites to metals centres, and at least one of which one must be carbon in order for the ligand to be cyclometallating (explained further in **1.3.1.1**), with the remainder usually consisting of nitrogen. Many variations of this ligand are known, some with a variety of substitutions on the non-binding sites of the rings in order to influence the electronics, solubility and stacking.[40-42,43]

1.3.1.1 Cyclometallation

A cyclometallating ligand is a ligand that upon coordination to a metal centre results in a ring of atoms incorporating the metal, and forming at least one metal-carbon *σ*-bond (metallacycle).[44] Pincer ligands with cyclometallating binding sites are typically both good σ-donors through the metal carbon bond and good π-acceptors by means of the aromatic heterocycles.[43]

Metals bound in this way experience a very strong ligand-field environment, and thus large d-orbital splitting, due to this σ-interaction with the carbon. In the case of organometallic platinum complexes, this often results in enhancement of luminescent emission properties by displacing antibonding metal-metal excited states to inaccessible energies, where they are unable to negatively affect emission. An example of this effect can be seen in the exchange of a bidentate bipyridine (bpy) ligand with a 2-phenylpyridine (ppy) in the platinum bis-(bpy) compound seen in **Figure 1.10.**

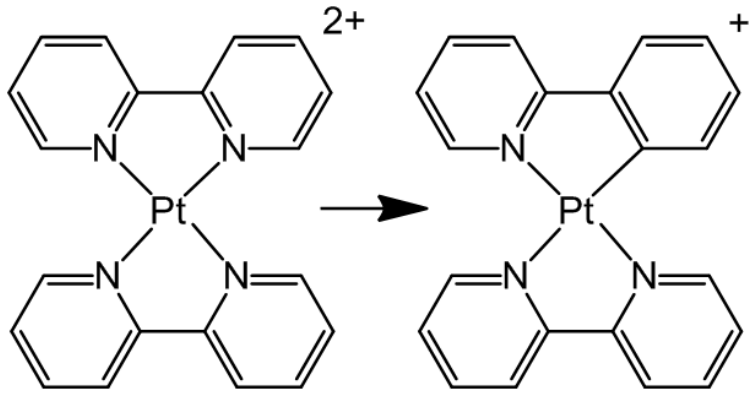

Figure 1.10. [Pt(bpy)2] (left) and [Pt(bpy)(ppy)] (right).

The (bpy) compound on the left is barely luminescent at room temperature due to a low lying $d_{x^2-y^2}$ orbital as discussed. The (ppy) compound on the right however shows strong luminescence with a high quantum yield.[45-47]

1.3.1.2 Tridentate pincers

By extending the cyclometallating ligand to a tridentate pincer, significant stabilisation of this metal-carbon *σ*-bond is achieved, particularly if the cyclometallating site is on the central position of the ligand. This allows for easy functionalisation of the phenyl ring at the 4-position, to which the electronics of the organometallic system are very sensitive, allowing for the ligand and metal complex's electronic properties to be tuned.[48]

A further advantage of using tridentate aromatic pincers when designing organometallic phosphors is that the rigid binding mode forces the aromatic rings into a co-planar arrangement with the square planar platinum centre. This results in unusual orbital overlap of the filled d_{xz} orbital on the Pt(II) and the antibonding orbitals of the aromatic π-system, extending the metal into the conjugated π-system of the organic fluorophore.[49] Due to this effect, there is good "communication" between the metal centre through to the conjugated π-system of the molecule, which is needed in order to relax the spin selection rule for the whole aromatic system, and promote phosphorescence over fluorescence.[50] The effect of a totally planar molecule extends beyond intramolecular electronics however. The ability for the molecules to stack in a planar fashion with intermolecular π-π interactions, along with the vacant axial d_z^2 orbital of the platinum extending perpendicular to this plane, allows for some very interesting potential intermolecular stacking interactions in new molecules.

1.3.2 Platinum NCN pincers

The first platinum polyaromatic N^C^N pincer compound of this type was synthesised by Cárdenas *et al*. in 1999,[51] building on previous work by van Koten *et al*. developing tridentate platinum pincer complexes containing C_{aryl}-Pt σ-bonds. [52 53]

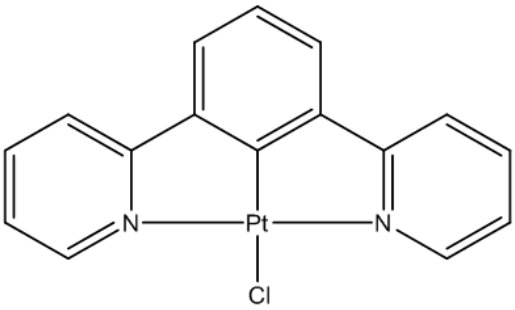

Figure 1.11. The first Pt(II) N^C^N pincer compound.

It was not until 2003, however, that the remarkable optical properties of N^C^N-Pt(II) complexes were studied. A series of compounds based on the R-N^C^N-Pt-Cl fragment (with R being substitution at the *para*-position of the central phenyl ring (see **Figure 1.12**)) was synthesised by Williams *et al.* and intense colours and surprisingly high luminescence quantum yields were reported. Subsequently it has been demonstrated that they also outperform analogous N^N^C and C^N^C complexes.[54-56] The complex, were also acknowledged to be potentially useful for a variety of applications such as molecular sensors, and luminescent devices.

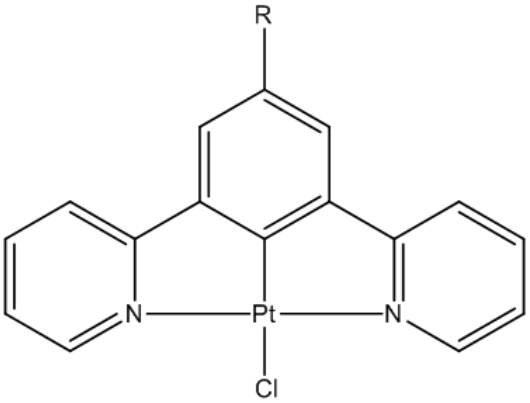

Figure 1.12. General formula of the compounds studied by Williams *et al.* in 2003.

The chemistry and optical properties of this class of compound has recently been expanded enormously, with the compounds becoming known for the ease with which the optical properties may be tuned, or manipulated.[54,57-62]

Various substitutions and variations on both the pincer ligand, and the fourth coordination site of the platinum have resulted in compounds with absorptions and emissions spanning the entire visible spectrum and beyond.[32,63-66,46]

Electronic transitions are reported to typically originate from $^3\pi$-π^* transitions based on ligand centred (LC) excited states, but also contain significant metal d-π^* MLCT character. A significant transition from the HOMO to LUMO is also often observed. [63,64,67,68,69]

Typically for this class of compounds, the LUMO and low lying unoccupied orbitals consist of π^* states of the pincer ligand, and often situated mainly over the pyridyl rings.[65] Due to the extended conjugation providing good electronic communication across the ligand, and onto the metal centre, functionalisation of the pincer at various points with different electron withdrawing or donating groups, particularly the position of the phenyl *para* to the metal, has been shown to produce compounds with emissive frequencies across the visible spectrum, by altering the energy of these orbitals.[32,55]

The HOMO and occupied orbitals lying near the frontier are typically based around the π^*-interactions between the filled platinum d-orbitals and the component of the ligand environment with the correct symmetry to interact in this way. Through variation of the ligand occupying the fourth coordination site, significant shifts in the energy of these occupied orbitals have been observed, offering a further method to control the energy of electronic transitions (see **Figure 1.13**). [65,69,70]

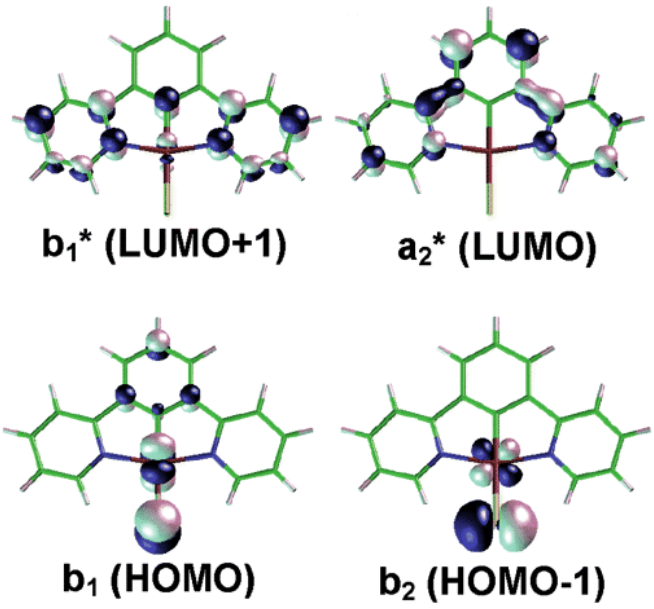

Figure 1.13. Contour plots of the frontier orbitals in a simple Pt-N^C^N compound. [70]

The ligand at the non-pincer binding position has also shown significant influence both in altering the solid state aggregation of the compounds, and in facilitating intermolecular Pt-Pt interactions.[71,72] As explained in **1.2.2.3**, The planar conjugation of the platinum pincer moiety often induces stacking in the solid state, which can result in favourable Pt-Pt d_z^2 overlap and π-π stacking interactions. This can result in low energy electronic transitions (metal-metal-to-ligand charge transfer or MMLCT), and red shifted phosphorescence.[71,73,74] This new excited state often exhibits enormous sensitivity to minor changes in Pt-Pt separation, which can be affected by changing environmental conditions. Examples of sensitivity to a variety of stimuli in these compounds are known, where variation in temperature,[73] pressure,[75,76] exposure to small amounts of solvent vapour or liquid,[77-79] or gentle mechanical crushing[80] are seen to induce dramatic changes to both absorption and emission spectra.

1.3.3 σ-acetylide compounds

Along with the many simple ligands that are able to bind to platinum which may offer interesting variations in π-interactions to the vacant Pt-orbitals, it may also be interesting to look at potentially bridging the platinum pincer fragment to more complex pendants. As the molecule HOMOs tend to consist of the platinum-ligand π* state, in order to impart some influence over the optical properties of a system through the metal centre, π-interaction from the pendant to the platinum extended via the bridge would likely be needed. One possible group of ligands, that may perhaps be useful in fulfilling the role of π-system bridge to platinum are acetylides.

First synthesised by Hagihara *et al* in 1978,[81] platinum acetylide compounds are now a relatively well studied class of compounds owing to their general stability, and often interesting properties. Platinum acetylide complexes can be essentially regarded as complexes of the $R\text{-}C{\equiv}C^-$ ligand (possessing similar complexing behaviour to the CN^- ligand, with an isoelectronic bridgehead carbon) [82], due to its relatively high proton acidity compared to most other hydrocarbons. [83]

This acidity of the alkyne unit means addition to the coordination plane of a platinum centre and hence incorporation of a platinum centre into the π-system of a pendant molecule is relatively simple.

Syntheses of this kind are typically achieved through a dehydrohalogenation reaction between the terminal alkyne and chlorides of platinum, using a strong base (typically diisopropyl amine), and in the presence of a CuI catalyst. [84,85,86]

Due to the rigid linear nature of the acetylide linkers, platinum acetylide compounds are often rod like, taking the general form seen in (**Figure 1.14**). It is also seen that Pt(II) can form neutral bis-acetylide polymers, and both *trans*- and *cis*- forms may be synthesised, however in the absence of chelating groups, *trans*- forms are favoured. This rigid linear morphology often imparts liquid crystalline properties into the molecules.[87]

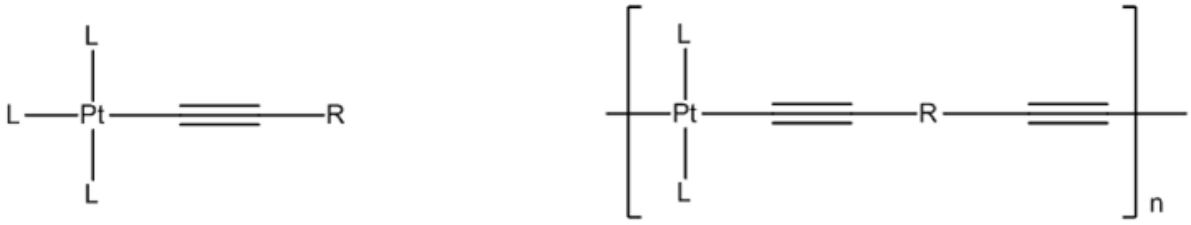

Figure 1.14. General formula of platinum acetylide rods and polymers.

The stability of this class of compounds can be attributed to the platinum-carbon σ-bond receiving stabilising effects through dπ-pπ interaction, and the absence of β-hydride elimination as a decomposition pathway. This unique combination σ-donor, π-donor and π-acceptor properties seen between metal and acetylide ligands results in good general orbital overlap between the filled s-p hybrid orbitals of the unsaturated carbon and the filled d-orbitals of the metal, providing an effective bridge between the metal centre and the functionalisation of the acetylide. This may allow for an enormous variety of functionalisation to be achieved, while still maintaining good electronic communication to the metal and its ligand environment, and it has been demonstrated with a variety of complexes that metal functionalisation using σ-acetylides as electronic bridges to different ligands has significant impact on the resultant optical and emissive properties, having strong effects on both emission energy (colour), intensity and the excited state lifetimes.[88]

1.4 General aims and objectives

The aim of this thesis is to synthesise and characterise a set of new luminescent and/or strongly coloured complexes of platinum (II), with the aim to first study the relationship between their chemical structure and molecular electronics, and progressing towards potentially using this knowledge to create compounds with tuneable properties through structural changes, external manipulation, and through the manipulation of intermolecular interactions.

The molecules synthesised in this body of research will all be based on the cyclometallated Platinum 1,3-di(2-pyridyl)benzene system (**Figure 1.15**) which was selected for reasons outlined in the preceding section, and several synthetic approaches will be employed, primarily in order to influence the occupied metallic d-orbitals (d_{zx}, d_{yz}, d_{xy}, d_z^2), of which the π* combinations with their ligand environment make up most of the HOMOs. These orbitals are likely to be sensitive to the degree, strength and nature of the π-interactions and intermolecular interactions, and so will be used as the site of manipulation, and as the mechanism though which variation/control over the optical properties of these chromo/luminophores will be attempted.

First σ-acetylide linkers will be employed as a bridging ligand, with the aim to study the effect of systematic variation of π-interactions via extending conjugation, in order to study the nature of the excited states and the effects that this variation will have on each of the occupied frontier orbitals.

Moving forward with this knowledge, attempts will be made to try to develop new systems in which the occupied metal orbitals will be in a favourable state to induce platinum stacking interactions, and this will be studied as a method for manipulation of optical properties.

Beyond this, new systems will be designed and manipulated combining both these strategies in order to try and create switchable molecules with potential sensing applications, where external conditions and stimuli can be used to influence either the π* metal ligand interactions, the intermetallic interactions, or both and in doing so create colour or luminescence changing switches.

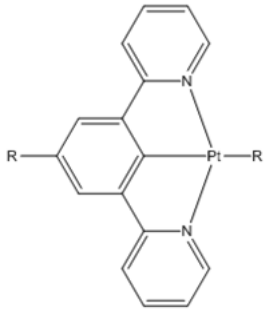

Figure 1.15. General structure of the cyclometallated 1,3-di(2-pyridyl)benzene system where: R = sites of variation.

Part 3. Analytical techniques

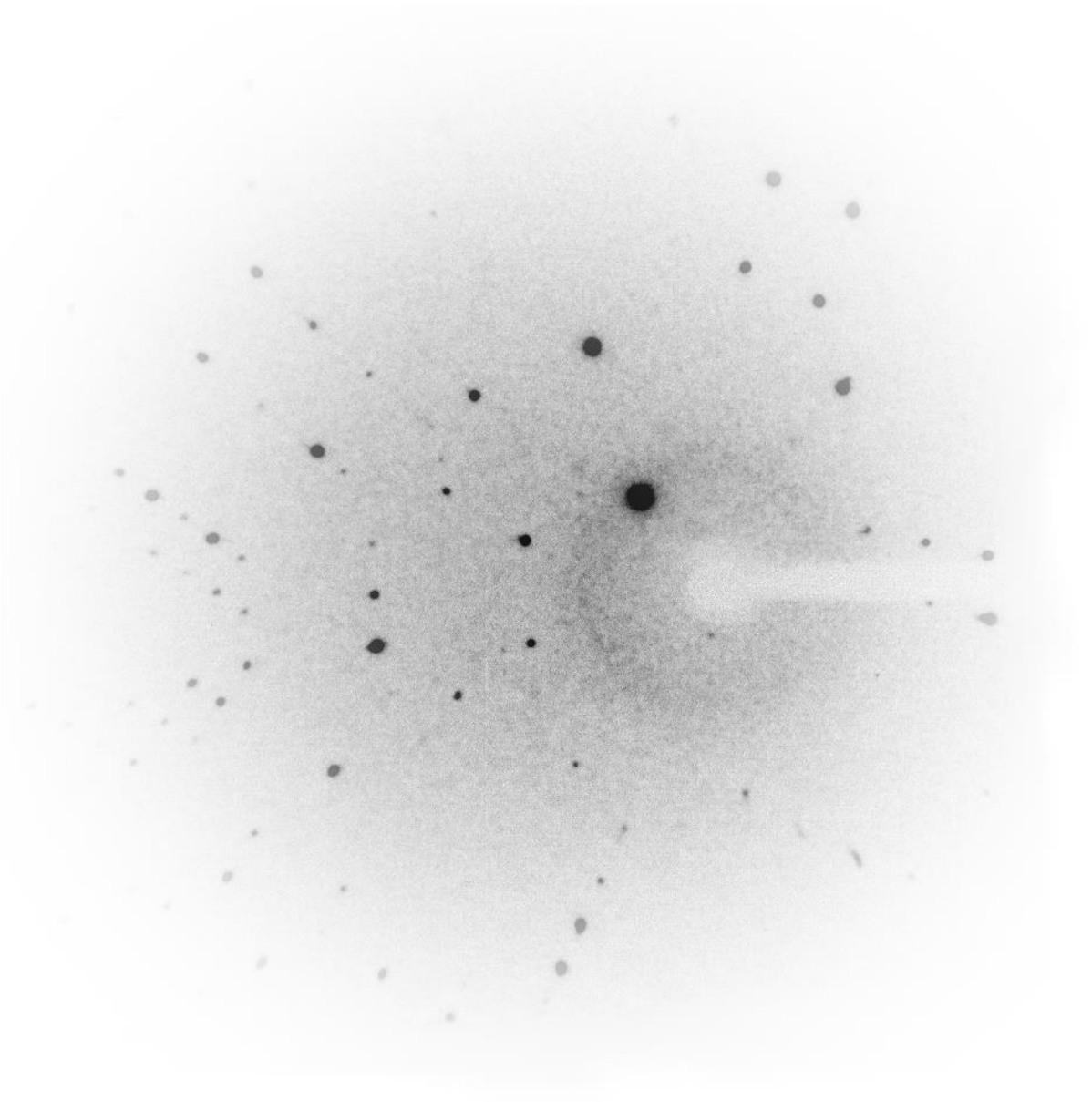

1.5 X-ray crystallography

X-ray crystallography is a key analytical method used in understanding the nature of materials in the crystalline state. For this body of research, crystallographic analysis has been indispensable in providing a detailed analysis and explanation of the various new compounds and their behaviour in the solid state, and so in the following sections the technique is discussed in some detail.[89,90]

1.5.1 Crystals, unit cells and the Bravais lattices

A crystal is a periodic arrangement of matter whereby molecules, atoms or ions are arranged with regular distribution and long range order [91] (with the rare exception of quasi-periodic crystals, which show order without periodicity [92]). Because of the periodic nature of a crystal, any structure can be simplified to a series of repeating equivalent environments known as lattice points.

These lattice points do not have to represent an atom or molecule or ion; they hold no information on the contents of the crystal, they are simply a marker that indicates identical environments and hence periodicity throughout the crystal. The joining of these lattice points in three dimensions creates an infinite array of boxes called unit cells, which as a whole, is known as the lattice. Again, no information regarding the content of the crystal is known from the lattice alone as it is simply a representation of the translational symmetry (or periodicity) of the crystal, but it does allow us to create the entire crystal structure, if the content of one unit cell is known.[93]

As a unit cell is essentially a box, it can be described by three side lengths and three angles: a,b,c and α,β,γ. This gives rise to seven possible cell types, and these are known as the seven crystal systems [94] (**Figure 1.16**).

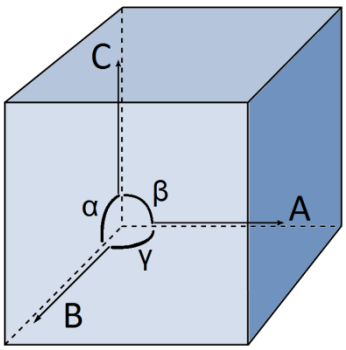

Cubic	***a = b = c***	***α = β = γ = 90°***
Tetragonal	***a = b ≠ c***	***α = β = γ = 90°***
Orthorhombic	***a ≠ b ≠ c***	***α = β = γ = 90°***
Hexagonal	***a = b ≠ c***	***α = β = 90, γ = 120°***
Trigonal (Hexagonal lattice) ***(Rhombohedral lattice)***	***a = b ≠ c*** ***a = b = c***	***α = β = 90, γ = 120°*** ***α = β = γ ≠ 90°***
Monoclinic	***a ≠ b ≠ c***	***α = γ = 90, β ≠ 90°***
Triclinic	***a ≠ b ≠ c***	***α ≠ β ≠ γ ≠ 90°***

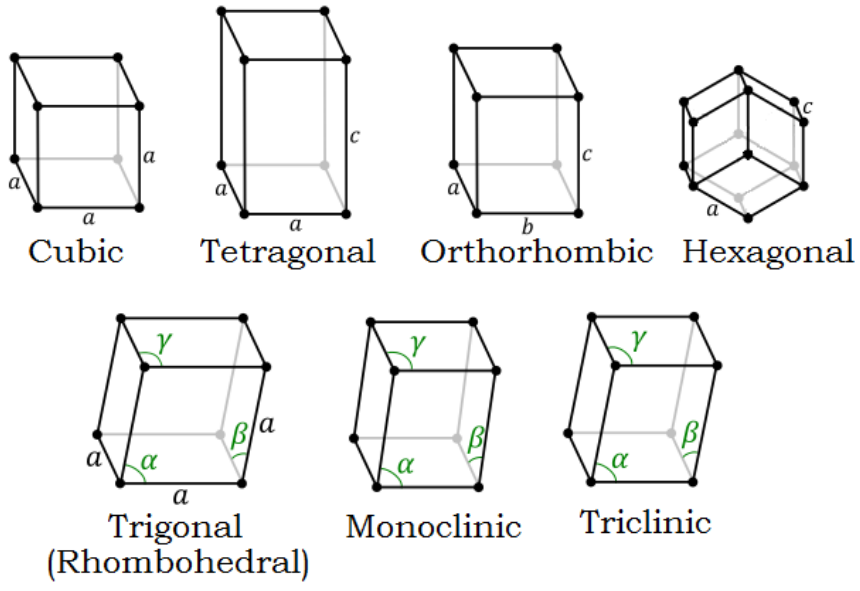

Figure 1.16. The seven crystal systems. [94]

When creating the lattice, if all the lattice points are included in order to create a minimum sized cell (i.e. the smallest repeating unit cell), we have what is known as the primitive cell (P). However, other larger cells that contain additional lattice points within them are also possible. By convention, the smallest unit cell that represents the full symmetry of the crystal is chosen. In some cases, where the full symmetry cannot be fully represented by a primitive cell, the smallest cell that does is chosen; this is called a centred cell.

Along with the primitive cell, three types of centred cell exist, giving us four lattice types (*Fig. 11*).

- Body centred (I) which contains an additional lattice point at its centre
- Face centred (F) which contains an additional lattice point in the centre of each face of the cell
- Side centred (A, B or C), which contains an additional lattice point in the centre of one set of opposite faces, with the axis this is orientated on deciding whether it is A, B or C centred.

Combining the seven crystal systems and the four lattice types gives us fourteen possible unique combinations - the Bravais lattices (**Figure 1.17**).[93]

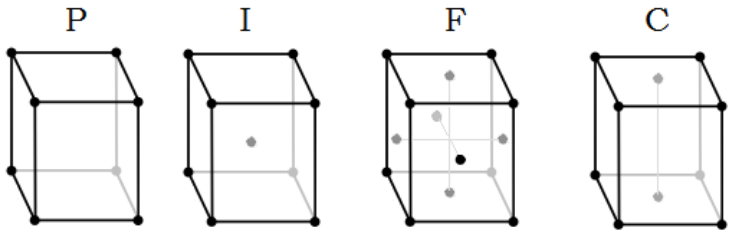

Cubic	***P I F***
Tetragonal	***P I***
Orthorhombic	***P I F C***
Hexagonal	***P***
Trigonal	***P***
Monoclinic	***P C***
Triclinic	***P***

Figure 1.17. The four basic lattice types and the fourteen Bravais lattices.

1.5.2 Lattice planes

It can also be useful to describe crystal lattices as a series of lattice planes, where the lattice points are connected in slices at varying angles through the crystal.

There are two conventions used when indexing these planes.[95]

- Weiss indices are a set of three coordinates, indicating the point of intersection of each axis by the plane. Using this convention however, planes that pass through the origin, or lie within an axis are not indexable.

- Miller indices are the reciprocals of the Weiss indices, with the fractions cleared (where $1/\infty = 0$).

Miller indices are given in the format (h,k,l) corresponding to the a, b and c axes, respectively, and each (h,k,l) corresponds to a series of parallel planes known as a Miller set (examples can be seen in **Figure 1.18**). The spacing between these planes within each set is known as the d-spacing.[96]

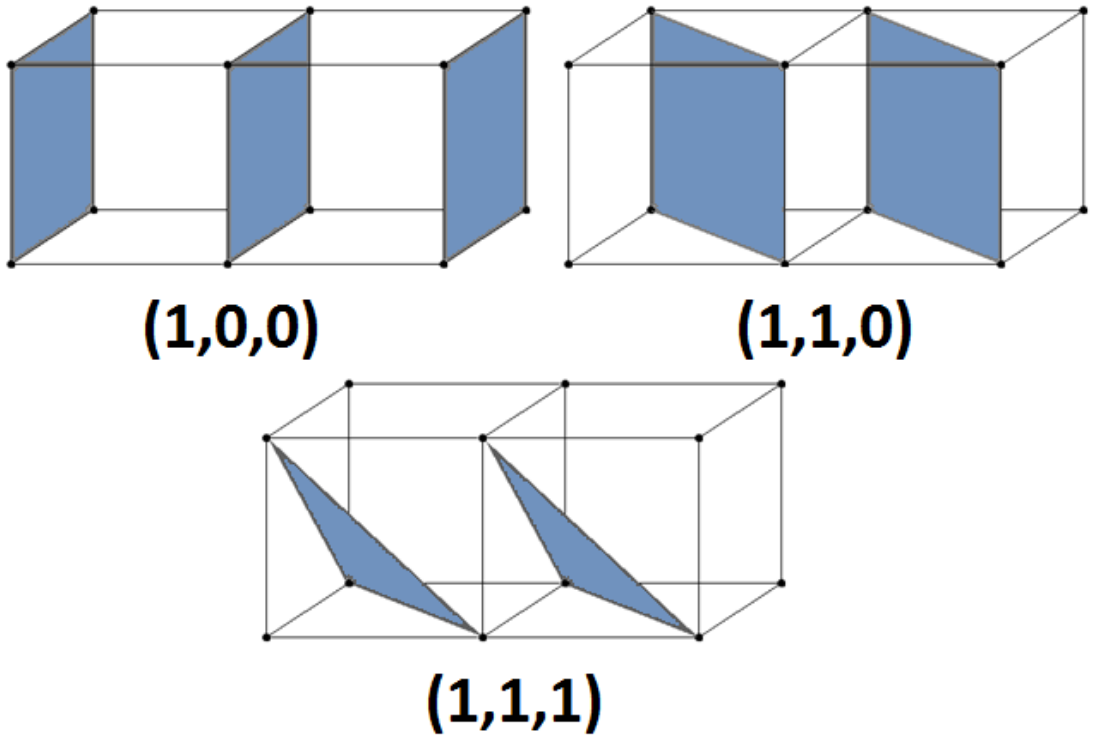

Figure 1.18. Three examples of Miller sets.

1.5.3 X-ray diffraction and Bragg's law

X-ray crystallographic experiments are used to determine the nature and arrangement of atoms within a crystal by using x-ray diffraction. X-ray crystallography is used for a huge range of applications, most notably as an unambiguous and accurate characterisation technique of molecules and macromolecules, and to understand the nature and arrangement of a material in its solid state.

It is well known that light waves can be scattered and diffracted, and that a grating of similar spacing size to that of the radiation wavelength will produce a diffraction pattern of constructive and destructive interference.[97] Given that a crystal is a periodic arrangement of matter, with comparable inter-atomic or inter-molecular spacing to the wavelength of the x-rays, upon radiation a single crystal behaves as a diffraction grating, with the resultant scattering building into a pattern of interference.

X-rays are a penetrating form of electromagnetic radiation and so during a crystallographic experiment, about 98% of the beam will pass through the crystal with no interaction at all, and be absorbed by the beam stop. Of the 2% that does interact with the crystal there are three possibilities:

- The x-rays may be absorbed via the photoelectric effect. This interaction accounts for about 84% of the interacting photons, and is the source of "radiation damage" to a crystal.
- They may be scattered inelastically (Compton scattering), which accounts for 8%
- They may be scattered elastically (Thomson scattering), which accounts for the final 8%

It is the relatively small amount of elastic scattering that is useful to us for an x-ray diffraction experiment.[98] The elastic scattering of x-rays is produced by their interaction with electrons, and they do so in a spherical manner [99] (**Figure 1.19**). The majority of the scattered radiation will interfere destructively, however due to the periodicity of the electron density within a crystal, in certain directions (determined by Bragg's law (**Figure 1.20**)) we may observe constructive interference. This results in a three dimensional diffraction pattern of discrete spots. This pattern is useful to us, as it is essentially a reciprocal space representation of the lattice.

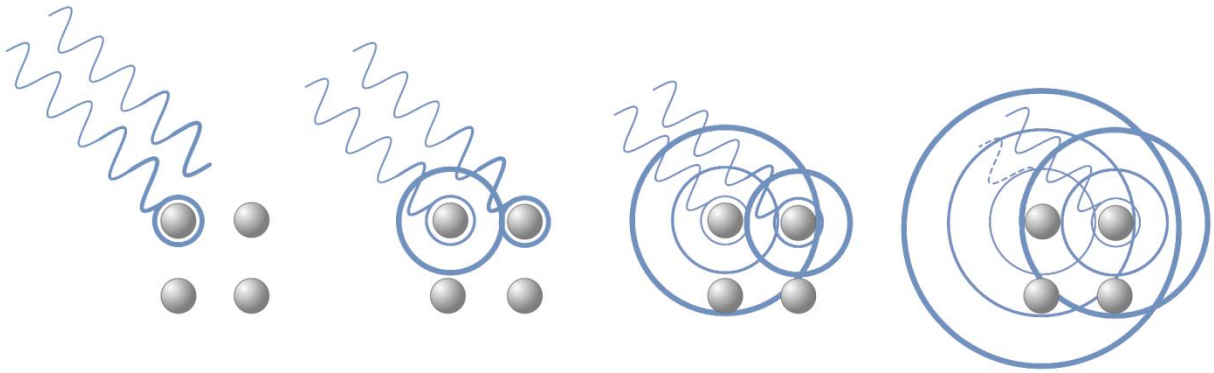

Figure 1.19. Spherical scattering of X-rays from electron clouds. [100]

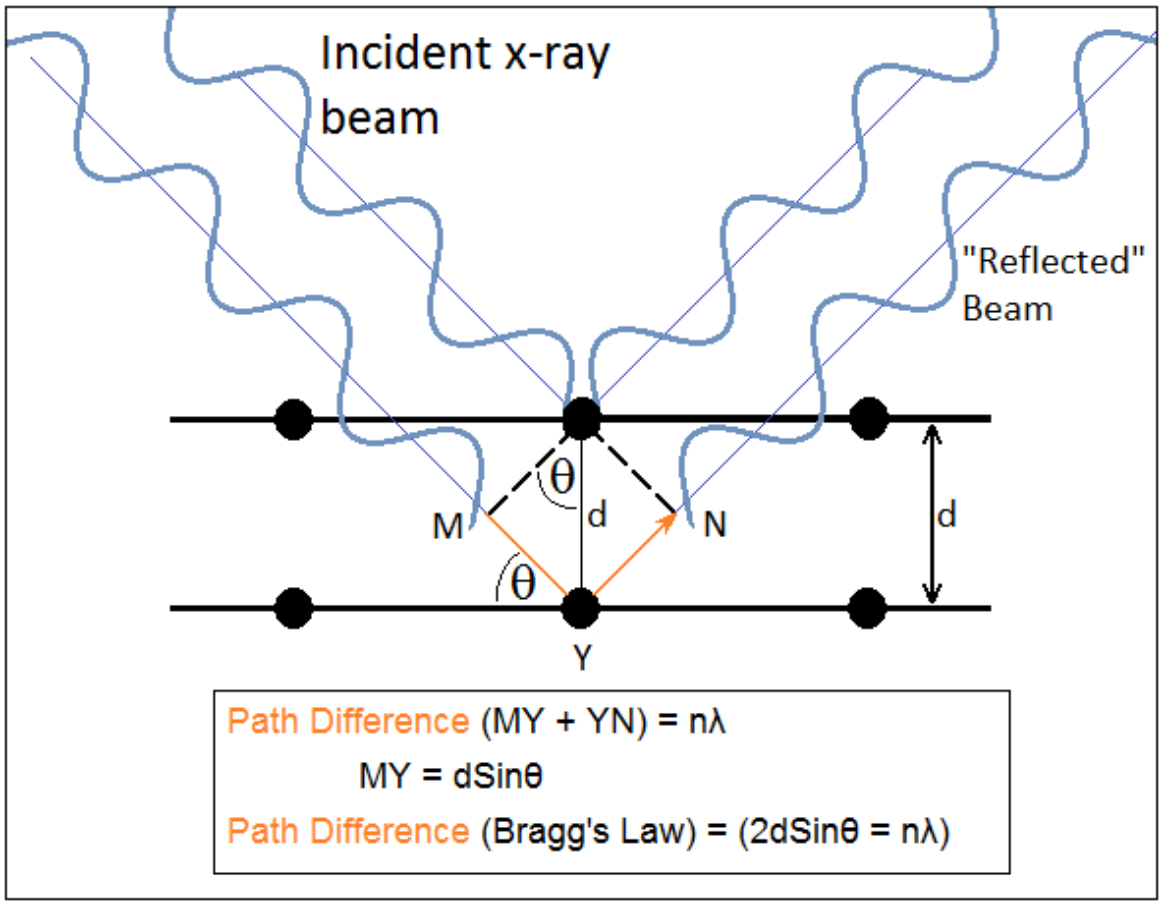

Figure 1.20. The reflection model, explaining Bragg's law and the derivation of the Bragg equation.

Bragg's law treats each diffraction spot of the resulting diffraction pattern as a reflection, with each reflection corresponding to one Miller set (h,k,l). In order to satisfy Bragg's law, the path difference (seen in orange) must equal an integer multiple of the wavelength λ, otherwise the reflected beam from each layer will be out of phase with the others and will interfere destructively, hence:

$$2d \sin\theta = n\lambda$$

-The Bragg Equation

During an x-ray diffraction experiment the incident beam is of fixed wavelength, so the only variables in this formula are the d-spacing and the angle (Θ). By observing the angle at which each reflection (spot) appears we can calculate the d-spacing of each Miller set.[96]

1.5.4 Space groups, symmetry elements, and absences

When performing an x-ray crystallography experiment, the desired end result is usually to obtain a full structural model of the crystal. An important prerequisite to doing this is a full description of how the atoms/molecules are packed relative to each other. These relative spatial positions are governed by symmetry, and the total symmetry of an periodic crystal can by described by combinations of 6 symmetry elements consisting of four non-translational and two translational. The symmetry of every unit cell can be described using these elements, with a total of 230 possible combinations of these elements existing.

These are known as the 230 space groups, which are spread out over the Bravais lattices and refer to the 230 possible ways to arrange identical objects (asymmetric units) in space, periodically. Knowing the space group of a crystal is an essential step in solving a crystal structure as it allows us to locate all equivalent positions within the crystal, and therefore assign an "asymmetric unit". An asymmetric unit is the smallest unit of matter within the unit cell that which, by application of the crystal symmetry, can recreate all the contents of the crystal. In other words because a crystal structure is periodic, knowing the contents of a unit cell allows us to recreate the entire structure, and knowing the internal symmetry and equivalent positions of the unit cell reduces this even further, simplifying the problem of crystal structure solution.

1.5.4.1 Symmetry elements

The types of symmetry elements are as follows:

Non-translational:

1. Rotational: This is fairly self explanatory, but it needs to be noted that only 2, 3, 4 and 6 fold rotation symmetry is possible in a periodic single crystal environment, and that all rotation is anticlockwise. Examples of objects with only rotational symmetry can be seen in **Figure 1.21**.

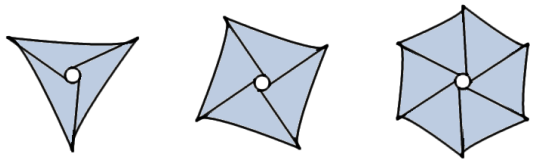

Figure 1.21. Examples of objects with three, four and six fold rotational symmetry .

2. Mirror symmetry: An object that possesses mirror symmetry will be unchanged by reflection about that axis. An example of an object with two mirror planes can be seen in **Figure 1.22.**

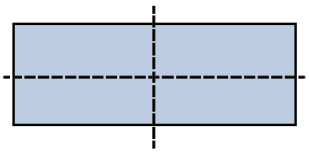

Figure 1.22. An example of mirror symmetry. Mirror planes represented by dotted lines.

3. Inversion: Simply inversion through a central point (see **Figure 1.23**.)

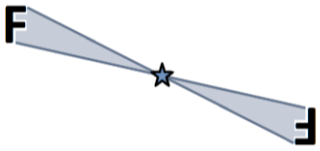

Figure 1.23. An example of an asymmetric unit (F) undergoing inversion through a point.

4. Rotary Inversion: A rotation about an axis, followed by an inversion through that point. An example of this can be seen in the staggered ethane molecule (**Figure 1.24**).

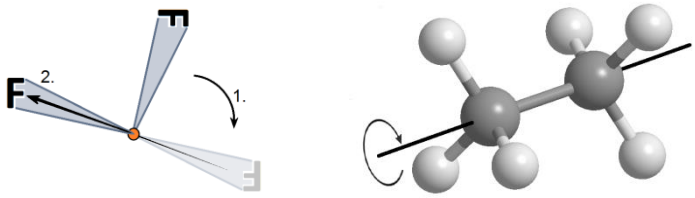

Figure 1.24. Left: an example of asymmetric unit undergoing rotary-inversion.
Right: an ethane molecule with rotary-inversion axis highlighted.

Translational:

Translational symmetry elements involve periodic translations of an object in space.

1. Glide: Objects are related to each other through a ½ unit cell translation, followed by a reflection in a mirror plane parallel to the translation axis. Glide planes are possible along a, b, c, n (diagonal), and d (body diagonal) axes (see **Figure 1.25** for example).

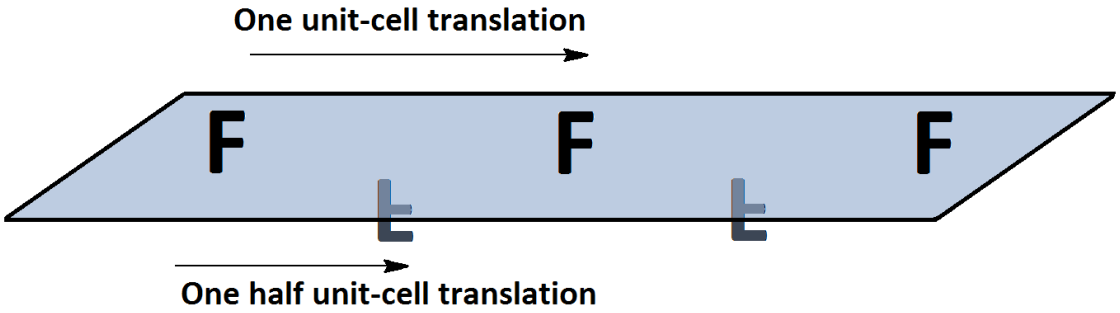

Figure 1.25. Example of an asymmetric unit being translated via a glide plane.

2. Screw: A rotation about an axis of 360/n°, followed by a translation of 1/n unit cell lengths. Screw axes can be along a, b and c. Screws that involve clockwise rotation with each step (i.e. the enantiomer) are denoted as having anticlockwise rotation, but for an additional translation step per rotation (see **Figure 1.26** for an example.)

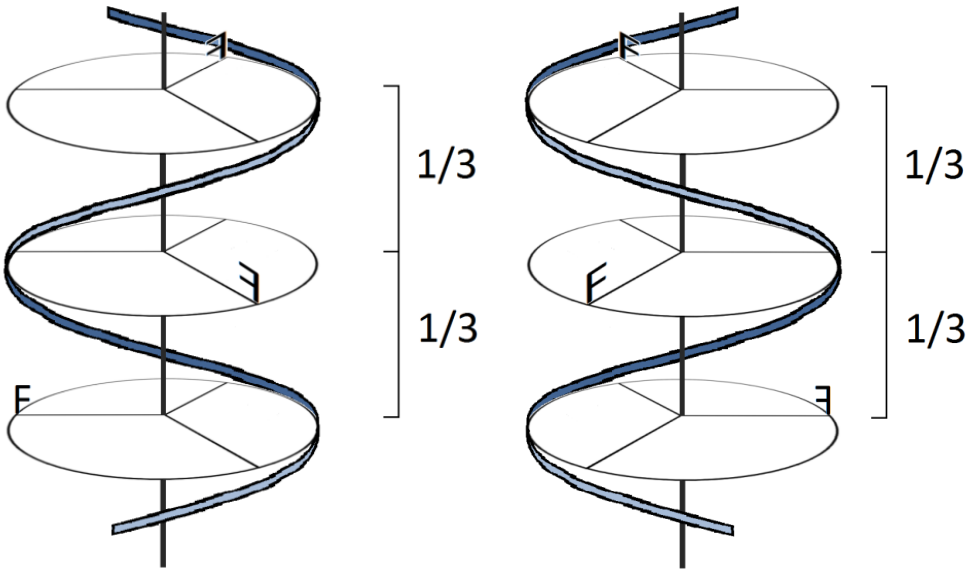

Figure 1.26. Examples of two enantiomeric screw axes. Left: 3_1 and right: 3_2.

1.5.4.2 Determining the space group

In order to determine the space group of a crystal from the diffraction experiment, we must first examine the systematic absences. Absences refer to conditions under which certain Miller sets will produce a reflection with I_{hkl}=0, and are hence absent from the diffraction pattern. There are two kinds of absence: General and Systematic.

General absences result from the centering of the lattice, and are therefore not present in a primitive lattice (see **Table 1.1.**).

Table 1.1. General absences

Lattice type	Conditions for general absences
P	None
A	k + l = 2n + 1 (i.e., the sum of k and l is odd)
B	h + l = 2n + 1 (i.e., the sum of h and l is odd)
C	h + k = 2n + 1 (i.e., the sum of h and k is odd)
F	Reflections must have either all even or all odd indices to be observed: Mixed odd and even indices are not allowed
I	h + k + l = 2n + 1 (i.e., the sum of the indices is odd)

Systematic absences are reflections not present in the diffraction pattern as a result of translational symmetry elements being present in the lattice. This is caused by destructive interference of the diffracted radiation as a result of certain symmetric arrangements of species within the crystal. This results in a specific set of (h,k,l) values for each translational symmetry operation, where the intensity is mathematically zero (the solution to the forward Fourier-transform, F_{hkl}, and thus I_{hkl} = 0 - **See section 1.5.5**), and hence the reflection is not seen in the diffraction pattern. By locating these absent reflections we can therefore infer the types of translational symmetry operation present in the crystal, and this will lead us towards identifying the space group (see **Table 1.2.** and **Table 1.3.**).[96]

Table 1.2. Systematic absences- Screw axes

Symmetry element		Conditions for systematic absence	
Screw axis along a	2_1, 4_2	(h, 0, 0)	h = 2n + 1
	4_1, 4_3	(h, 0, 0)	h = 4n + 1
Screw axis along b	2_1, 4_2	(0, k, 0)	k = 2n + 1
	4_1, 4_3	(0, k, 0)	k = 4n + 1
Screw axis along c	2_1, 4_2, 6_3	(0, 0, l)	l = 2n + 1
	3_1, 3_2, 6_2, 6_4	(0, 0, l)	l = 3n + 1
	4_1, 4_3	(0, 0, l)	l = 4n + 1
	6_1, 6_5	(0, 0, l)	l = 6n + 1

Table 1.3. Systematic absences - Glide planes

b glide perpendicular a	(0, k, l)	k = 2n + 1
c glide perpendicular a	(0, k, l)	l = 2n + 1
a glide perpendicular b	(h, 0, l)	h = 2n + 1
c glide perpendicular b	(h, 0, l)	l = 2n + 1
a glide perpendicular c	(h, k, 0)	h = 2n + 1
b glide perpendicular c	(h, k, 0)	k = 2n + 1

Although non-translational symmetry elements do not result in systematic absences, techniques exist that can be used to further refine space group determination. The tests compare equivalent intensities and their distribution about their mean value, with certain distributions hinting at the presence of certain symmetry elements. The statistical analysis is carried out on the E-values, which are essentially normalised amplitudes, corrected for vibrational motion (**See section 1.5.5**).

These tests are frequently unreliable however, and consequently the only routinely used test is that for centrosymmetry, which is the $|E^2-1|$ value (The entire data set can be used in this analysis, improving its reliability over the others). Values close to 0.736 indicate no centrosymmetry, and values close to 0.968 indicate centrosymmetric space groups.

This test only hints at the presence of an inversion centre however, and should not be taken as a certainty.[101,102]

With all these techniques employed together, many common space groups can be identified straightforwardly, though it is not uncommon for more than one possibility to be identified. In such a case, structure solution would have to be attempted in multiple space groups in order to identify the correct one.[103]

1.5.5 Crystal structure solution

1.5.5.1 Constructing the Fourier map

By recording all the positions that reflections are found at during the experiment, the crystal lattice (and therefore the unit cell of the crystal) can be determined, and the space group through systematic absence analysis. What observing the relative positions of the reflections does not do however, is give us any information regarding the contents of the cell, and thus the atomic structure of the crystal. This information is in fact present in the diffraction pattern, but is contained in the actual spots themselves. By integrating each reflection, we can calculate its intensity (I_{hkl}), and because it is the electron density that determines the scattering strength of the X-rays, we can relate this intensity back to the electron density. Once a correct map of electron density can be placed within the unit cell (and hence the whole crystal by symmetry), atomic positions can be derived.

Because electron density is periodic throughout the lattice, a Fourier series can be produced that describes the electron density at any location (**Equation 1.1**).

Equation 1.1.

$$\rho(xyz) = \frac{1}{V} \sum F(hkl) \exp[-2\pi i(hx + ky + lz)]$$

Where V= the volume of the unit cell ($Å^3$) and ρ=electron density ($e^- Å^{-3}$)

To generate such a map we need a parameter known as the structure factor (F_{hkl}) for each Miller set, which is essentially a mathematical description of how all the atoms of the unit cell scatter X-rays.

Equation 1.2.

$$F(hkl) = \sum_{j=1}^{N} f_j \exp[2\pi i(hx_j + ky_j + lz_j)]$$

f_j being the atomic scattering factor of atom j, (x_j, y_j, z_j) its location, and (h, k, l) the Miller index.

The structure factors are described by **Equation 1.2.**

Equation 1.2 essentially describes the principle that the diffraction pattern is the Fourier transform of the crystal structure, and that each reflection consists of the sum of the scattered waves from each of the component atoms, with its electron density contribution described by its element type and hence its atomic scattering factor (*f*). In order to add these components up, we also need to take into account the atoms' positions relative to each other (hence the xyz term), and both their amplitudes and phases.

If we know all of these parameters, we can calculate a predicted diffraction pattern for the structure, and this is give as a set of "calculated" structure factors (F^{calc}). This is known as the forward Fourier transform.

By knowing all of the structure factors (i.e all the individual reflections' intensities and phases), we can calculate the atomic positions using **Equation 1.1**. The problem with this is that we can only measure the amplitudes of the structure factors (observed structure factors (F^{obs})), and know nothing of the phases, and so the equation appears to be unsolvable. This is known as the "phase problem".

The difficulty in solving a crystal structure is therefore essentially the recovery of the missing phase data, and this can be achieved through a variety of methods. Another way of understanding the phase problem is noting that each structure factor equals the square root of the observed intensity [$I_{hkl} = (F_{hkl})^2$] and so from the diffraction experiment we may easily calculate the magnitude of each structure factor, while the phase is not directly attainable because $\sqrt{I_{hkl}} = \pm F_{hkl}$ and no definitive answer can be given.

1.5.5.2 Direct methods.

The majority of structures, including all of the ones in this thesis, are solved using techniques called direct methods, which seek to directly derive the phases of the structure factors from a single set of reflection intensities.

If the amplitudes and phases of structure factors (**F**) were totally independent it would not be possible to calculate phases directly. Thankfully they are linked, in that we have an understanding of electron density, and by correctly applying this knowledge to the problem the phases may be directly calculated from the amplitudes. Without this knowledge, and by treating it as a purely abstract problem, it would be mathematically impossible to get one from the other. We are, however, describing a real, physical system, about which we can make certain assumptions, and this is what allows us to make the connection. These characteristics of electron density that we already know, enable us to place certain mathematical constraints on the problem, and thus restrict the possible structure factor values calculated after applying the forward Fourier-transform, leading us towards approximating the phases.

The first of these constraints arises from the fact that we know a crystal contains real, discrete atoms, and we can therefore infer that the electron density within the crystal will be far from homogenous, possessing peaks at the atomic positions, and falling to low values elsewhere. In order to apply this constraint we assume that all the atoms are points, with no thermal motion, by converting the structure factors (**F**) to normalised structure factors (**E**). E-values represent the structure factors that would be calculated from a stationary point-atom crystal diffraction pattern. Treating it as such essentially exaggerates this property of the corresponding Fourier-map, and assumes all the peaks are the same shape (which is a reasonable assumption to a degree in an atomic crystal). From the application of this assumption we may infer that for **Equation 1.1**, only for values of x,y,z that are close to the actual atomic locations (x_j y_j z_z) will they give a significant contribution to the value of the structure factor.

Another constraint that we may add through knowledge of real electrons, is that that negative electron density (i.e. negative atoms) cannot be present at any point in the structure, as this makes no physical sense. This leads to a set of requirements that the structure factors must satisfy, restricting their outcome further.

By combining these first two constraints we arrive at a constraint that treats the whole structure as a series of atoms, randomly distributed. The result of this is that we obtain a probability distribution for the phases, as opposed to a set of allowed and disallowed values.

A statistical approach to assigning phases can then be developed, whereby groups of reflections can be said to have related phases. This phase relationship essentially states that for certain groups of strong reflections, the phases can be related by **Equation 1.3.**

Equation 1.3.

$$\varphi(-h) + \varphi(h-k) + \varphi(k) \approx 0$$

Where the φ term represents the phase

And by applying the further constraint that maximises the value $\int\rho^3(x)dV$ in order to enhance the discrete, atomic nature of the electron density and produce distinct peaks, we arrive at the tangent formula (**Equation 1.4**).

Equation 1.4.

$$\tan(\varphi(-h)) \approx \frac{\sum_k |E(k)E(h-k)| \sin(\varphi(k)+\varphi(h-k))}{\sum_k |E(k)E(h-k)| \cos(\varphi(k)+\varphi(h-k))}$$

Or more concisely

$$(\varphi(-h)) \approx \text{The phase of } \left\{ \sum_k E(k)E(h-k) \right\}$$

By implementing these principles, a set of phase relationships between the E-values can be determined, which is then applied to the strongest E-values. An iterative process may then be used to determine the correct set of phases from an initial, randomly assigned set, whereby the phases are cycled through the tangent formula to receive new sets of phases until a stable point is reached. Each new set of phases is assigned what is known as figures of merit, in order to sort the correct set of phases from the many incorrect sets.

1.5.5.3 Refinement

Once the phases have been assigned, we are left with a set of atomic positions that reasonably describe the peak positions in the electron density of the crystal, essentially the electron density is used to produce a more simple atomic model for ease of visualisation. This model however may not be perfect, and the atom positions need to be refined to best fit the now phased electron density data. This model refinement is typically performed through least squares iterative refinement of the estimated values of F^{calc} obtained from the solution to obtain an improved fit to the experimental data. the first step of this is to use the F^{calc} values to generate a Fourier series (ρ_{xyz}), and this calculated map is compared to that of the measured F^{obs} values. In this comparison, the positions of missing atoms can be seen as contours of electron density. These new atomic positions are then added to those derived previously, and new F^{calc} values are generated. This process, is then cycled until all the atomic locations have been generated, and each of their positions are refined. Throughout, a value known as the refinement factor or "R factor" is produced. This is essentially a measure of the difference between the calculated structure factors, and those observed, indicating how accurately the model matches the experimental data. A value below 7% is generally considered to be an acceptable value, and considered a complete structure.[96,99,104,105,89]

Equation 1.5

$$R = \frac{\sum(|F^{obs}| - |F^{calc}|)}{\sum|F^{obs}|}$$

The R-Factor

There are many other factors that determine the quality of a solved structure, and whether the model produced is an accurate representation. Firstly the degree of data coverage and completeness

in the actual data collection should be as high as is practical to collect, and the resolution should be appropriate (typically < 0.8 Å), a lack of high angle data in a collection will restrict the accuracy achievable. Small ESDs on atom positions, and sensible looking displacement on thermal ellipsoids is often a good indicator of an accurate structure. Finally, the presence of residual electron density in a structure is often an indicator that the structure is wrong or incomplete.

1.5.6 Summary of a single crystal x-ray diffraction experiment

1. Sample Preparation: Suitable crystal is selected, mounted on the diffractometer (goniometer head) and centred.
2. A pre-experiment is run; a small set of frames covering several regions of diffraction space are collected to determine the unit cell and Bravais lattice.
3. Full collection of intensity data is then run.
4. Space group of the crystal is determined through absence analysis, and the structure is solved, normally using Patterson or Direct methods.
5. Structure is completed by locating the remaining atoms, and refining their positions using least squares iterations.

In **Figure 1.27** the set up of a typical x-ray diffraction experiment can be seen. X-rays are generated by bombarding a metal target with high energy electrons. The target is typically made of molybdenum or copper (many other metals may also be used) and has to be water cooled.

These two metals are commonly used as the resulting wavelengths are suitable for probing small molecules at good resolution, with molybdenum being preferred for strongly absorbing species such as organometallics. The beam is then refined to a narrow wavelength range either with filters or using a monochromator (separation via diffraction from a crystal), and narrowed to a specific beam size using a collimator (tube to filter stray radiation).[106] The goniometer is a device used to rotate the crystal to a precise angular position, allowing data from each Miller set of planes to be observed without moving the x-ray tube.

A cold nitrogen or helium gas stream is typically used to cool the crystals accurately, and temperatures of 100-150K are routinely used in order to reduce the effects of thermal motion within the crystal, and therefore reduce the uncertainty of measured atomic positions. The beam-stop is essentially a small piece of metal used to block the non-diffracted radiation of the incident beam

from reaching the detector; this radiation is far more intense than the diffracted radiation, and would damage the detector, along with potentially drowning-out useful reflections. The detector used is often a charge-coupled device (similar to that used in a digital camera) with a phosphor screen mounted on a fibre-optic taper, although there are other detector types.

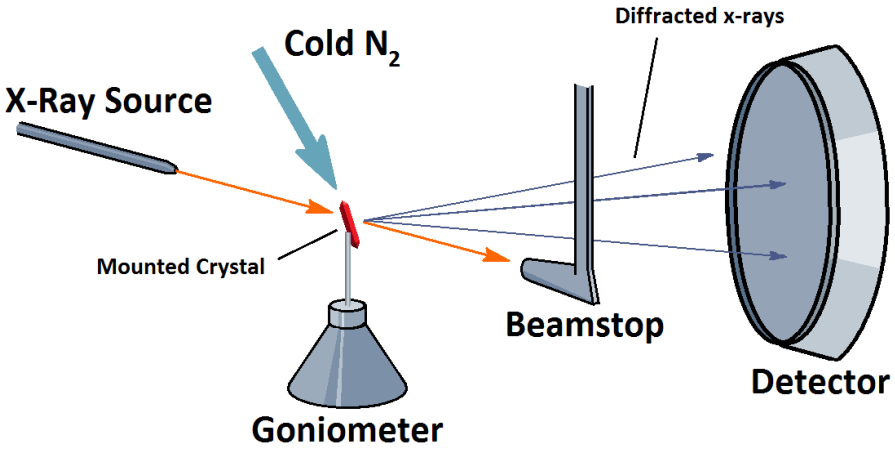

Figure 1.27. Schematic of a standard, single crystal x-ray diffraction experiment.

1.6 Optical spectroscopy

The study of a compound's interaction with light is essential for this body of work, particularly if the nature of their colour and/or luminescence is a primary concern. The physics underlying light's interaction with electrons has been described in **section 1.1**, and this section will simply focus on the underlying principles and practical application of absorption and emission spectroscopy.

1.6.1 UV-Visible absorption spectroscopy

For this body of work a significant objective is to understand, influence and potentially manipulate colour in a set of new compounds. When describing compounds as having colour, or containing a chromophore, we are essentially saying that the compound absorbs photons in the visible spectrum. It is important therefore that we are able to quantify specifically what wavelengths are absorbed, not only so that we have a quantitative measure of each compound's "colour" in a way that simplifies comparison and is more reliable/sensitive than simple observation, but also because this information in turn tells us something about the behaviour of electrons within the compound. This information can then be applied in directing the project towards its goals.

The technique used to measure this property is known as UV-visible absorption spectroscopy, or UV-Vis, and is measured using a UV-Vis spectrophotometer.

1.6.1.1 Instrumentation

UV-Vis spectroscopy is generally a simple spectroscopic technique where the intensity of light is measured before and after interacting with the sample, for a spectrum of wavelengths between about 200 and 900 nm. The ratio between the intensities of the incident and transmitted light ($\mathbf{I/I_0}$) is known as the transmittance (**%T**), and this value is plotted for each wavelength in the spectrum. The result is essentially a plot of the degree to which each wavelength is absorbed by the compound, and provides us with a quantitative measure of its colour. As mentioned, this also informs us of the excited state properties of the compound in question, and this may be used to direct further experiments studying luminescent emission. This is often why UV frequencies are probed along with the visible, as due to the Stokes' shift, when studying luminescent emission in the visible region it is often important to look at excitations that extend into the UV region. This is particularly important for phosphorescent emission.

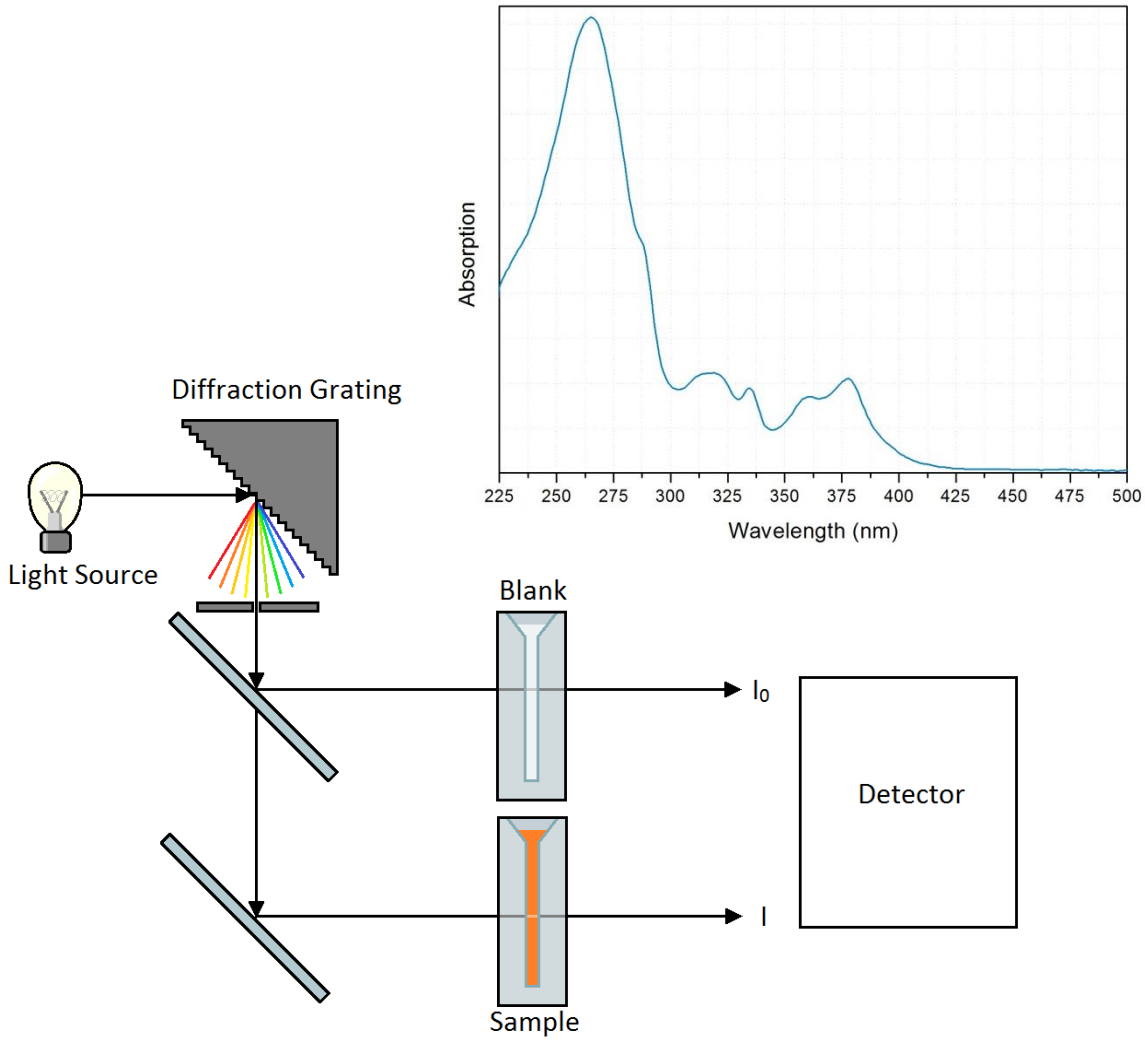

Figure 1.28. Schematic of a typical solution state transmittance spectroscopy experiment, and an example spectrum.

UV-Vis spectroscopy is a versatile technique and it is possible to use samples in a variety of forms. Typically samples are measured either in solution or the solid state. A standard solution state experiment involves measuring the transmitted light (**I**) through a transparent sample, and comparing this with the light transmitted through an identical sample environment containing only the carrier solvent ($\mathbf{I_0}$). A simple schematic of this type of experiment can be seen in **Figure 1.28** where a rotating diffraction grating is used to scan the wavelengths provided by a broad-band light source. Transmittance can also be used for solid samples in the form of thin films or as single crystals. However, for most solid samples this is not possible due to low transparency, and so diffuse reflectance is often used instead. For this technique, an incident beam is placed upon the sample, within an integrating sphere. This is essentially a sphere coated with a highly diffusely-reflective coating (normally barium sulphate). The sphere then directs all the non-specularly reflected light from the sample towards the detector, where it is compared to that of a white plate and thus, and absorption can be determined. For these experiments $\mathbf{I/I_0}$ is expressed as % reflectance or **%R**.

All the UV-Vis absorption spectra recorded in this body of work are performed in transmission mode.

1.6.2 Photoluminescent emission spectroscopy.

Along with attempting to understand, measure and potentially manipulate the colour of a series of new compounds, another aim of this project was to attempt to do the same for luminescent emission. Luminescent emission spectroscopy is a complimentary technique to UV-Vis absorption spectroscopy, and can shed further light on the nature of electronic excited states within a compound.

1.6.2.1 Instrumentation

Luminescence measurements are generally carried out using a fluorometer. A simple description of how this device works can be seen in **Figure 1.29**. As with UV-Vis spectroscopy an incident light is selected, typically with a diffraction grating, and the sample irradiated, however this wavelength remains fixed for the duration of the experiment. The detector is usually placed at 90° to the incident beam, in order to prevent any incident light reaching the detector. A filter or a second diffraction grating monochromator is also usually placed in front of the detector. Upon irradiation with the incident beam, the sample will emit in all directions, and so it is this light that is measured by the detector. A plot of the intensity of emission at each wavelength is then generated, giving a photoluminescent-emission spectrum. As with UV-Vis spectroscopy, many sample states and environments can be used to generate such spectra, however it is very difficult to gain useful

standalone intensity data, and therefore accurate quantum yields, from any sample type. This is due to the way the emission is measured, whereby instrumentation, optics, sample environment, reabsorption effects and many other factors need to be carefully corrected for. As such quantum yields are usually measured by referencing to a known standard.

Quantum yield is defined by the following equation:

$$\Phi = \frac{K_r}{K_r + K_{nr}}$$

Where K_r is the radiative rate constant, and K_{nr} is the rate of non-radiative processes.

Excited state lifetimes (τ) can also be described by the following equations:

$$n(t) = n_0 e^{-\kappa t}$$
$$\tau = k^{-1}$$

Where n is the number of populated excited states, t is time, and the rate constant of all decay processes is k.

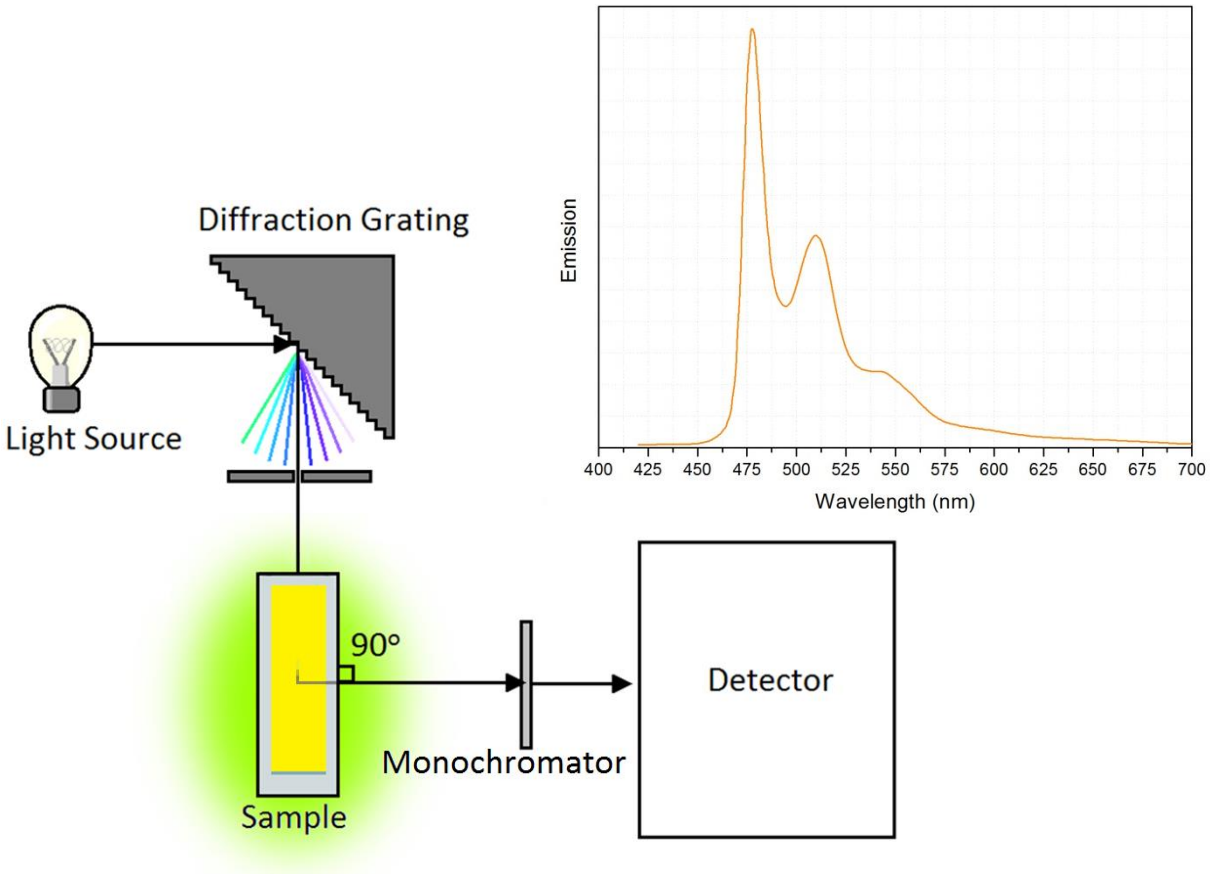

Figure 1.29. Schematic of a typical solution state filter fluorometer set up, and an example spectrum.

1.7 References

(1) Svanberg, S. *Atomic and Molecular Spectroscopy: Basic Aspects and Practical Applications*; 4th ed.; Springer Science & Business Media, **2003**.
(2) Inductiveload/NASA; EM_Spectrum_Properties_edit(modified), Ed. Wikimedia Commons.
(3) Burrows, A.; Holman, J.; Parsons, A.; G., P.; Price, G. *Chemistry*^{3}, **2013**.
(4) Kitai, A.; Wiley: **2001**.
(5) Lakowicz, J. R. *Principles of Fluorescence Spectroscopy*; Springer, **2006**; Vol. 1.
(6) Robert A., Alberty, R. J. S. *Physical Chemistry*; Wiley, **1992**.
(7) Wulfsberg, G. *Inorganic Chemistry*; University Science Books: Sausalito- CA, **2000**.
(8) Roberts, M. W., Thomas, J.M; Royal Society of Chemistry: **1973**; Vol. 2.
(9) Allen, N. S., Edge, M.; Springer: **1992**, p 63.
(10) Mertens, R. Herzelia, **2011**, p Oled Information.
(11) Pina, J., Burrows, H.D., de Melo, J.S.S *Photochemistry* **2011**, *39*, 30.
(12) Baldo, M. A., O'brien, D.F, Thompson, M.E, Forrest, S.R *Phys. Rev. B* **1999**, *60*, 14422.
(13) Yersin, H. *Highly Efficient OLEDS with Phosphorescent Materials*; Wiley-VCH: weinheim, **2008**.
(14) Baldo, M. A., Thompson, M.E, Forrest, S.R. *Nature* **1999**, *403*, 750.
(15) Furuta, P. T.; Deng, L.; Garon, S.; Thompson, M. E.; Fréchet, J. M. J. *Journal of the American Chemical Society* **2004**, *126*, 15388.
(16) Lu, W.; Mi, B.-X.; Chan, M. C. W.; Hui, Z.; Che, C.-M.; Zhu, N.; Lee, S.-T. *Journal of the American Chemical Society* **2004**, *126*, 4958.
(17) Williams, D. *Molecular physics* Academic Press inc., **1962**; Vol. 3.
(18) Turro, N. J. *Modern Molecular Photochemistry*; University Science Books: Sausalito, **1991**.
(19) Nave, C. R. **2010**; Vol. 2011, p Physics.
(20) Turro, N. J.; Ramamurthy, V.; Scaiano, J. C. *Principles of Molecular Photochemistry, An Introduction*; University Science Books, **2009**.
(21) Yersin, H.; Donges, D. *Low-Lying Electronic States and Photophysical Properties of Organometallic Pd(II) and Pt(II) Compounds. Modern Research Trends Presented in Detailed Case Studies*, **2001**; Vol. 214.
(22) Massimo Cocchi; Dalia Virgili; Valeria Fattori; David L. Rochester; Williams, J. A. G. *Adv. Funct. Mater.* **2007**, *17*, 285.
(23) Sheng, C. X.; Singh, S.; Gambetta, A.; Drori, T.; Tong, M.; Tretiak, S.; Vardeny, Z. V. *Sci. Rep.* **2013**, *3*.
(24) Ho, C.-L.; Wong, W.-Y. *Coordination Chemistry Reviews* **2011**, *255*, 2469.
(25) Montalti, M.; Credi, A.; Prodi, L.; Gandolfi, M. T. *Handbook of Photochemistry*; 3rd ed.; CRC Press, Taylor and Francis Group, **2006**.
(26) Rochester, D. L. Doctoral Thesis, Durham University, **2007**.
(27) Lai, S.-W.; Cheung, T.-C.; Chan, M. C. W.; Cheung, K.-K.; Peng, S.-M.; Che, C.-M. *Inorg. Chem.* **2000**, *39*, 255.
(28) Mao, L.; Moriuchi, T.; Sakurai, H.; Fujii, H.; Hirao, T. *Tetrahedron Letters* **2005**, *46*, 8419.
(29) Barigelletti, F.; Sandrini, D.; Maestri, M.; Balzani, V.; Zelewsky, A. v.; Chassot, L.; Jolliet, P.; Maederlc, U. *inorg. Chem.* **1988**, *27*, 3644.
(30) Williams, J. A. G. *Top Curr Chem* **2007**, *281*, 205.
(31) Connick, W. B., Schaefer, W.P, Marsh, R.E, Gray, H.B *Inorg. Chem.* **1997**, *36*, 913.
(32) Farley, S. J.; Rochester, D. L.; Thompson, A. L.; Howard, J. A. K.; Williams, J. A. G. *Inorg. Chem.* **2005**, *44*, 9690.
(33) de Haas, R. R., van Gijlswick, R.P.M, van der Tol, E.B, Zijlmans, H.J.M.A.A, Bakker-Schut, T, Bonnet, J, Verwoerd, N.P, Tanke, H.J *The Journal of Histochemistry & Cytochemistry* **1997**, *45*, 1279.

(34) Cîrcu, V., Micutz, M. *X-Ray Structural Characterization of Cyclometalated Luminescent Pt(II) Complexes*; University of Bucharest, **2011**.
(35) Murphy, L., Williams, J.A.G *Top Organomet Chem* **2010**, *28*, 75.
(36) Pucci, D.; Barberio, G.; Crispini, A.; Francescangeli, O.; Ghedini, M.; Deda, M. L. *Eur. J. Inorg. Chem.* **2003**, 3649.
(37) Connick, W. B., Henling, L.M, Marsh, R.E, Gray, H.B *Inorg. Chem.* **1996**, *35*, 6261.
(38) Bronner, C., Wenger, O. S. *Dalton Trans.* **2011**, *40*, 12409.
(39) Bryant, M. J.; University of Bath: **2011**.
(40) Yam, V. W., Tang, R.P., Wong, K.M., Lu, X., Cheung, K., Zhu, N. *Chem. Eur. J.* **2002**, *8*, 4066.
(41) Schneider, J., Du, P., Wang, X., Brennessel, W., Eisenberg, R. *Inorg. Chem.* **2009**, *48*, 1498.
(42) Rochester, D. L., Develay, S., Zalis, S., Williams, J.A.G. *Dalton Trans.* **2009**, 1728.
(43) Hofmann, A.; Dahlenburg, L.; van Eldik, R. *Inorg. Chem.*, *42*, 6528.
(44) Hill, A. F. *Organotransition metal chemistry*; RSC, **2002**.
(45) Miskowski, W. M.; Houlding, V. H. *Inorg. Chem.* **1989**, *28*, 1529.
(46) Kvam, P. I., Songstad, J. *Acta. Chem. Scand.* **1995**, *49*, 313.
(47) Kvam, P. I., Puzyk, M. V., Balashev, K. P., Songstad, J. *Acta. Chem. Scand.* **1995**, *49*, 335.
(48) Cardenas, D. J., Echavarren, A. M., Ramírez de Arellano, M. C. *Organometallics* **1999**, *18*, 3337.
(49) Ortiz, J. V., Havlas, Z., Hoffmann, R. *Helv. Chim. Acta* **1984**, *67*, 1.
(50) Baldo, M. A., O'Brien, D.F, You, Y, Shoustikov, A, Sibley, S, Thompson, M.E, Forrest, S.R *Nature* **1998**, *395*, 151.
(51) Cardenas, D. J.; Echavarren, A. M. *Organometallics* **1999**, *18*, 3337.
(52) Koten, G. v. *Pure & Appl. Chem.* **1989**, *61*, 1681.
(53) Lagunas, M. L.; Gossage, R. A.; Smeets, W. J. J.; Spek, A. J.; van Koten, G. *Eur. J. Inorg. Chem.* **1998**, 163.
(54) Williams, J. A. G.; Beeby, A.; Davies, E. S.; Weinstein, J. A.; Wilson, C. *Inorg. Chem.* **2003**, *42*, 8609.
(55) Williams, J. A. G. *Chemical Society Reviews* **2009**, *38*, 1783.
(56) Tong, G. S.-M.; Che, C.-M. *Chemistry – A European Journal* **2009**, *15*, 7225.
(57) Lu, W.; Chan, M. C. W.; Zhu, N.; Che, C.-M.; Li, C.; Hui, Z. *J. Am. Chem. Soc.* **2004**, *126*, 7639.
(58) Schneider, J.; Du, P.; Wang, X.; Brennessel, W. W.; Eisenberg, R. *Inorg. Chem.* **2009**, *48*, 1498.
(59) Lu, W.; Chui, S. S.-Y.; Ng, K.-M.; Che, C.-M. *Angew. Chem. Int. Ed.* **2008**, *47*, 4568.
(60) Garner, K. L.; Parkes, L. F.; Piper, J. D.; Williams, J. A. G. *Inorg. Chem.* **2010**, *49*, 476.
(61) Fuertes, S.; Brayshaw, S. K.; Raithby, P. R.; Schiffers, S.; Warren, M. R. *Organometallics* **2011**, *31*, 105.
(62) Fuertes, S.; Woodall, C. H.; Raithby, P. R.; Sicilia, V. *Organometallics* **2012**, *31*, 4228.
(63) Williams, J. A. G.; Develay, S.; Rochester, D. L.; Murphy, L. *Coordination Chemistry Reviews* **2008**, *252*, 2596.
(64) Williams, J. A. G., Beeby, A., Davies, E.S., Weinstein, J.A., Wilson, C. *Inorg. Chem.* **2003**, *42*, 8609.
(65) William A. Tarran; Gemma R. Freeman; Lisa Murphy; Adam M. Benham; Ritu Kataky; Williams, J. A. G. *Inorg. Chem.* **2014**, *53*, 5738.
(66) Yam, V. W.-W.; Chan, K. H.-Y.; Wong, K. M.-C.; Zhu, N. *Chemistry – A European Journal* **2005**, *11*, 4535.
(67) Williams, J. G. *Chemical Society Reviews* **2009**, *38*, 1783.
(68) Nisic, F.; Colombo, A.; Dragonetti, C.; Roberto, D.; Valore, A.; Malicka, J. M.; Cocchi, M.; Freeman, G. R.; Williams, J. A. G. *Journal of Materials Chemistry C* **2014**, *2*, 1791.
(69) Rochester, D. L.; Develay, S.; Zalis, S.; Williams, J. A. G. *Dalton Transactions* **2009**, 1728.
(70) Sotoyama, W.; Satoh, T.; Sato, H.; Matsuura, A.; Sawatari, N. *The Journal of Physical Chemistry A* **2005**, *109*, 9760.

(71) Rossi, E.; Colombo, A.; Dragonetti, C.; Roberto, D.; Demartin, F.; Cocchi, M.; Brulatti, P.; Fattori, V.; Williams, J. A. G. *Chemical Communications* **2012**, *48*, 3182.
(72) Chen, Y.; Li, K.; Lu, W.; Chui, S. S.-Y.; Ma, C.-W.; Che, C.-M. *Angewandte Chemie International Edition* **2009**, *48*, 9909.
(73) Connick, W. B.; Henling, L. M.; Marsh, R. E.; Gray, H. B. *Inorg. Chem.* **1996**, *35*, 6261.
(74) Chen, Y.; Lu, W.; Che, C.-M. *Organometallics* **2012**, *32*, 350.
(75) Shirotani, I.; Inagaki, Y.; Utsumi, W.; Yagi, T. *J. Mater. Chem* **1991**, *1*, 1041.
(76) Williams, J. A. G. *Top. Curr. Chem.* **2007**, *281*, 205.
(77) Kato, M. *Bull. Chem. Soc. Jpn.* **2007**, *80*, 287.
(78) Kunugi, Y.; Mann, K. R.; Miller, L. L.; Exstrom, C. L. *J. Am. Chem. Soc.* **1998**, *120*, 589.
(79) Kobayashi, A.; Yonemura, T.; Kato, M. *Eur. J. Inorg. Chem.* **2010**, 2465.
(80) Ni, J.; Zhang, X.; Wu, Y.-H.; Zhang, L.-Y.; Chen, Z.-N. *Chem. Eur. J.* **2011**, *17*, 1171.
(81) Takahashi, S.; Kariya, M.; Yatake, T.; Sonogashira, K.; Hagihara, N. *Macromolecules* **1978**, *11*, 1063.
(82) Nast, R. *Coordination chemistry reviews* **1982**, *47*, 89.
(83) Willian Johnson, A. *Invitation to Organic Chemistry*; Jones and Bartlett Publishers, **1999**.
(84) Zhang, H., Lee, A.W.M, Wong, W, Yuen, M.S.M *J. Chem. Soc., Dalton Trans.* **2000**, 3675.
(85) Takahashi, S., Kariya, M, Yatake, T, Sonogashira, K, Hagihara, N *Macromolecules* **1978**, *11*, 1063.
(86) Long, N. J., Williams C.K *Angewandte Chemie International edition* **2003**, *42*, 2586.
(87) Kaharu, T.; Matsubara, H.; Takahashi, S. *J. Mater. Chem.* **1991**, *1*, 145.
(88) Yam, V. W. W., Wong, K.M.C *Top Curr Chem* **2005**, *257*, 1.
(89) Blake, A. J.; Clegg, W.; Cole, J. M. *Crystal structure analysis: principles and practice*; Oxford University Press, **2009**.
(90) Giacovazzo, C.; Monaco, H. L.; Artoli, G.; Viterbo, D.; Milanseio, M.; Ferraris, G.; Gilli, G.; Gilli, P.; Zanotti, G.; Catti, M. *Fundamentals of Crystallography*; Third ed.; OxfordScience Publications.
(91) Helmenstine, A. M. In *Chemistry.about.com*; The New York Times Company: **2012**.
(92) Shechtman, D., Blech, I. *Phys. rev . lett.* **1984**, *53*, 1951.
(93) Sands, D. E. *Introduction to Crystallography*; Courier Dover Publications, **1994**.
(94) Goel, A. *Crystallography*; Discovery Publishing House, **2006**.
(95) Vaĭnshteĭn, B. K. *Modern Crystallography: Fundamentals of crystals, symmetry and methods of structural crystallography*; Springer, **1994**.
(96) Hammond, C. *The Basics of Crystallography and Diffraction*; third ed.; Oxford University Press, **2009**.
(97) Crowell, B. **2010**.
(98) Murray, J. W., Rudino-Pinera, E., Owen, R.L., Grininger, M., Ravelli, R.B.G, Garman, E.F. *J. Synchrotron Rad.* **2005**, *12*, 268.
(99) Kasai, N., Kakudo, M. *X-Ray Diffraction by Macromolecules*; Springer, **2005**.
(100) Chan, C. D. N. **2004**.
(101) Snow, M. R., Tiekink, E.R.T *Acta Cryst.* **1988**, *B44*, 676.
(102) Hall, S., Subramanian, V. In *The Gnu Xtal System User's Manual: Chapter 4.25* **2002**.
(103) Stout, G. H., Jensen, L.H. *X-ray Structure Determination- A Practical Guide*; Wiley, **1989**.
(104) Woolfson, M. M., Hai-Fu, F. *Physical and non-physical methods of solving crystal structures*; Cambridge University Press, **2005**.
(105) A., H. H. *Rep. Prog. Phys.* **1991**, 1427.
(106) Jezierski, G.; The University of Oklahoma: **2011**.

Chapter 2: Aromatic ethynyl platinum pincer compounds

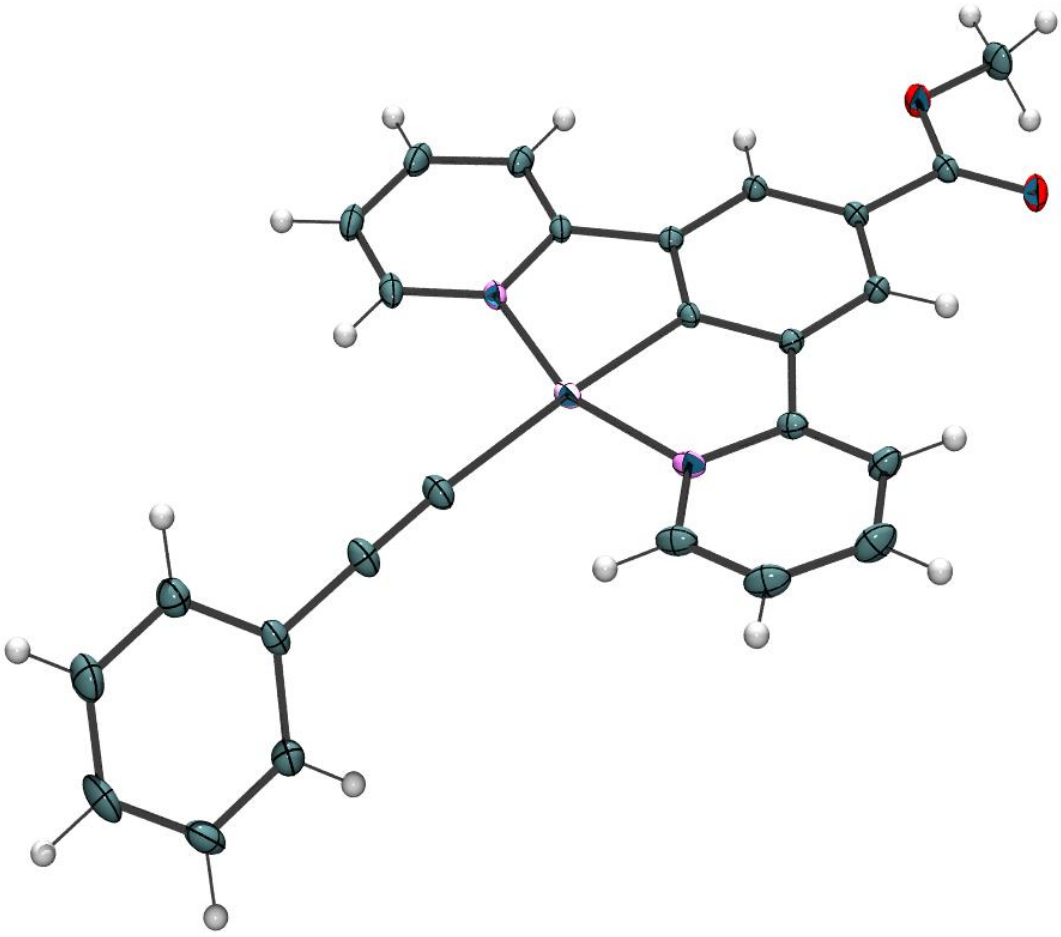

Abstract.

The work presented in this chapter was undertaken in order to establish a more complete understanding of the electronic properties of the platinum N^C^N pincer system by creating a series of systematically varied analogues. It was hypothesised that changing the π-interactions of the surrounding ligand environment may provide a convenient route to alter the energies of the metal d-orbital containing HOMOs without affecting LUMOs, and thus changing the colour in a controllable way. A simple way to test this was devised whereby progressively more conjugated substituents would be bridged to the metal centre via acetylide groups, which are known to allow for good electronic communication.

The hypothesis proved to be correct, whereby transitioning to ligands with progressively more π-donor properties lead to increasingly red-shifted absorptions by destabilising platinum d-orbital containing HOMOs. It was also confirmed that the acetylide group effectively transfers the interaction of the ligand to the metal centre through both xy and xz planes.

The orientation of the fourth ligand substituent was also shown to be important, with the plane through which π-interactions exist to the metal centre having the ability to change the ordering and energies of HOMO orbitals.

The spectroscopic and computational analysis presented in this chapter led to aquiring a far more detailed understanding of the arrangement of orbitals within these systems, and helped to direct further research into producing switchable materials.

2. Aromatic ethynyl platinum pincer compounds

2.1 Introduction

2.1.1 Conjugation and aromaticity

A conjugated molecular system can be defined as a series of atoms covalently bonded in a way that allows for delocalisation of electrons along the length of the molecule via parallel overlapping p-orbitals. This is most typically seen in chains of sp^2 hybridised carbons in an alternating double-single bond arrangement (polyenes), whereby the p-orbitals that are left uninvolved in sigma-bonding overlap to form π-π interactions (**Figure 2.1)**. This allows the electrons of these orbitals to delocalise across the molecule, with the effect of increasing the stability, and lowering the energy of the molecule.

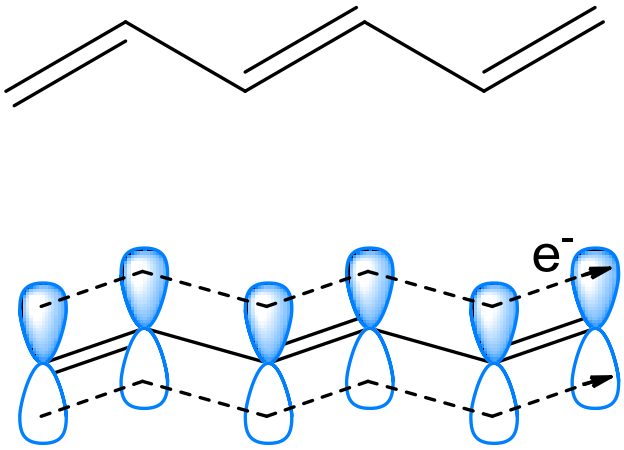

Figure 2.1.2 Diagram showing the delocalisation of electrons through π-interacting p-orbitals in a conjugated system.

Another property of conjugation is that it often has a large effect on the optical properties of the compound. The electronic absorption energy of a conjugated system is correlated to the size of the delocalised system (i.e. the number of p-orbitals available for delocalisation), with the larger systems absorbing longer wavelengths. This effect can be explained by looking at the way the p-orbitals combine to form π and π* interactions. For every p-orbital involved, one molecular π-orbital exists that is delocalised over all the atoms. This is a product of the various possible in and out of phase combinations of the p-orbitals, each with an increasing number of nodes as their energy increases (**Figure 2.2**). When two double bonds are conjugated, the MOs arrange in such a way that the HOMO-LUMO gap is lessened. If the number of double bonds (and hence the extent of the conjugation) is increased, the number of MOs is also increased, and the HOMO-LUMO gap is further decreased. The result of this is that as the degree of conjugation increases we see a red-shift to

lower energy in the absorption spectrum, due to the shrinking HOMO-LUMO gap. This can be seen in the simple case shown in **Figure 2.3** whereby a red-shifted absorption from ethene through to hexatriene has been measured using UV-Vis absorption spectroscopy, with the λ_{max} for the three compounds being 165nm, 217nm and 258nm respectively.[1,2]

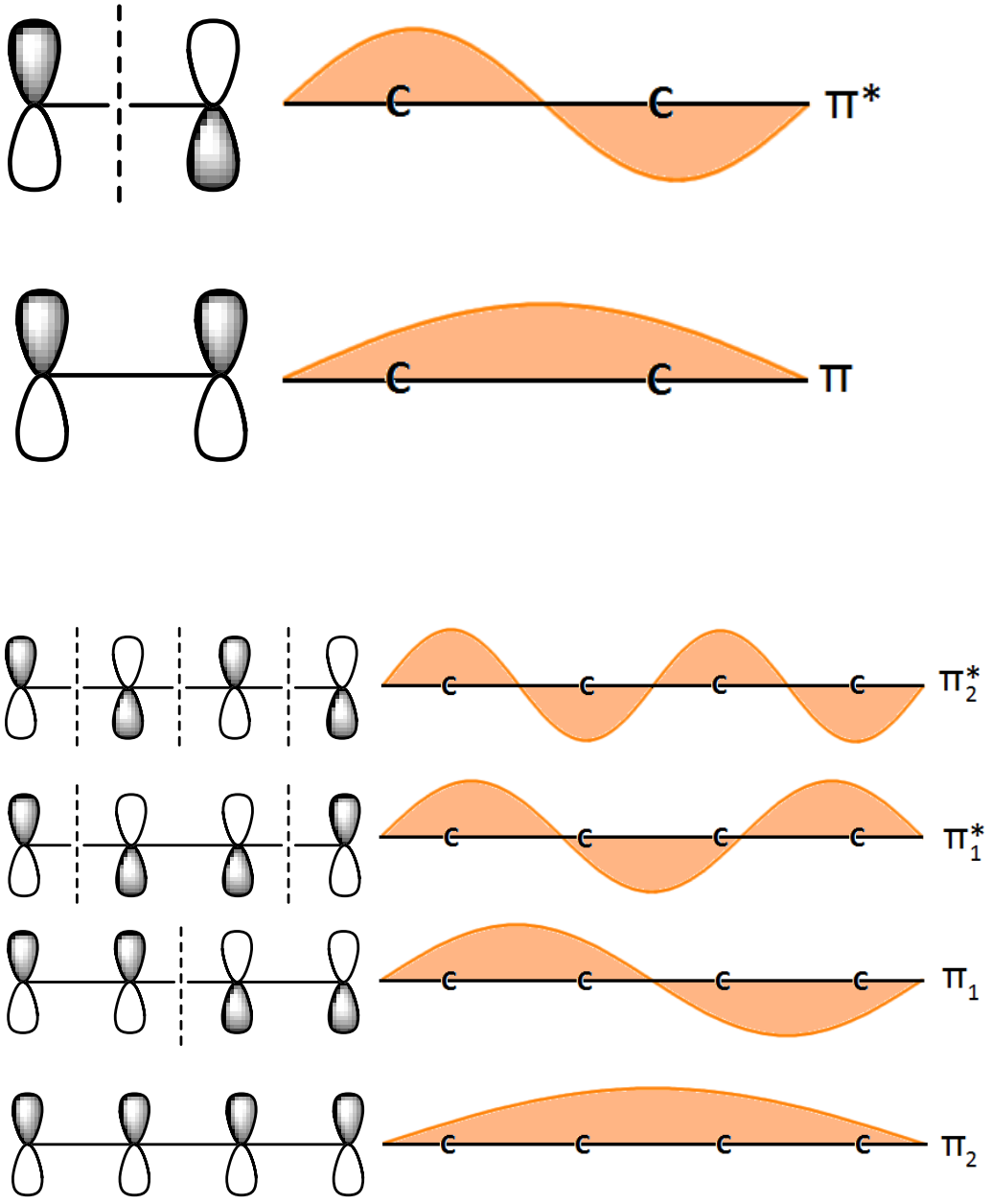

Figure 2.2. Diagram detailing the in and out of phase combinations of π-orbitals in a conjugated alkene chain, along with the increase in nodes seen with increasing chain length.

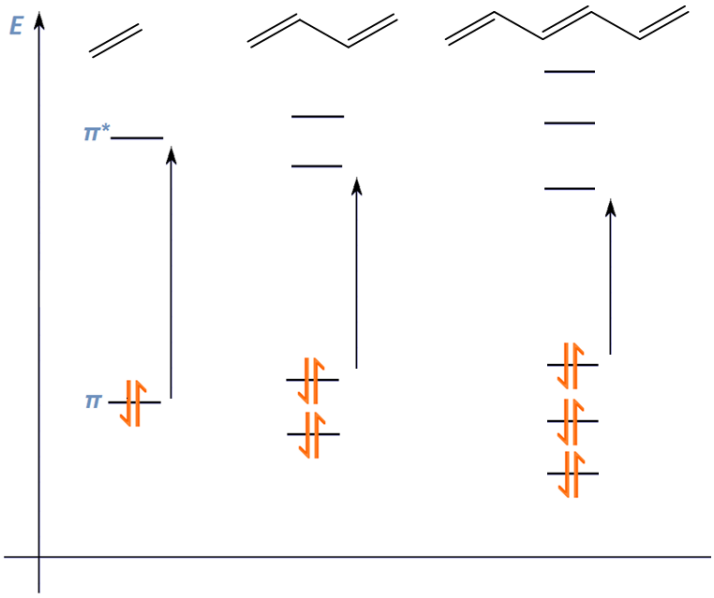

Figure 2.3. Energy level diagram showing how the HOMO-LUMO gap is reduced by increased conjugated alkene chain length.

Aromaticity is a property gained where a conjugated system is enclosed into a planar ring that follows Hückel's rules (4n+2 π-electrons) allowing the delocalised electrons to circulate. The result of this is additional stabilisation on top of that expected from conjugation alone. Similar trends to simple conjugation are also observed regarding the effect of extending the delocalisation of aromatics on absorption energies and colour. For example the λ_{max} of benzene, naphthalene and anthracene are 255nm 314nm and 380nm, respectively.[3]

2.1.2 Frontier orbital composition of N^C^N Pt(II) pincer compounds

As mentioned in **Chapter 1.** one of the aims of this thesis was to synthesise and characterise a set of new complexes based around the N^C^N Pt(II) pincer fragment in order to study how alteration to the chemical structure may be used to drive changes in optical properties in a controlled and predictable manner.

In order to achieve this, it was first important to understand in detail the nature of the electronic transitions, along with the frontier orbital composition for compounds of this type. Using this information it was then possible to derive a strategy through which these properties may be altered systematically.

As explained in **Chapter 1**, ligand field theory predicts that upon interaction with square planar coordinating ligands, metal d-orbitals will split in such a way as seen in **Figure 2.4** for simple compounds. This diagram is lacking, however, in that it only describes σ-interactions. Ligand π-interaction with the occupied, non-bonding metal d-orbitals in square planar systems gives rise to further splitting of these states to π and π* states, and depending on the specific ligands and the orientations and interactions involved, there may be re-ordering of the energies of the metal d-orbitals in a way that differs from the purely σ-bonding model.

π-donor ligands, with occupied orbitals of the correct symmetry are likely to induce large splitting upon combination with occupied metal d-orbitals, resulting in low energy π and high energy π* occupied orbitals. Such ligands are typically low on the spectrochemical series. As a result, metal compounds with such ligands often have HOMOs comprised of the π* states of these combinations.

Conversely, π-acceptor ligands, high on the spectrochemical series, often interact with metal d-orbitals through π-interaction with high energy vacant orbitals. The result of this combination is typically a split into an occupied π-orbital with low energy, and an unoccupied π*-orbital with high energy.[4]

By applying this principle to N^C^N Pt(II) pincers, predictions can be made about their orbital structure.

Because of the planarity of the pincer ligand itself, and the square planar nature of the compounds it forms, it would be expected that little π-interaction will occur between the pincer and the d_{xy} and d_{z^2} orbitals due to the incorrect symmetry.[5]

Additionally, the specific points of contact to the platinum centre are one phenyl and two pyridyl rings. These ligands possess different π-donating/accepting abilities, so one would expect a divergence in energies for the d-orbitals based on their orientations relative to these groups. The d_{xz} for example should have π-interaction with the π-donor phenyl bridgehead carbon atom, while the d_{yz} should have π-interaction with the less π-donating pyridyl nitrogen donor atoms. The resulting hybrid orbital from the d_{yz} should be the lower energy of the two (see **Figure 2.5** for details).

Looking at π-interactions of these orbitals now with those of the ligand occupying the fourth coordination site (**L**) (**Figure 2.6**), we can see that the d_{xz} orbital also possesses the correct symmetry to interact with this ligand, while no such interaction is to be expected for the d_{yz}. The d_{xy} orbital however, despite showing no π-interaction with the pincer, does have the correct symmetry to interact with the ligand **L**, dependent of course on the ligand possessing corresponding orbitals in the xy-plane. Due to this fact, the energy of this orbital is likely to be highly dependent on the π-donor/accepter nature of this ligand.

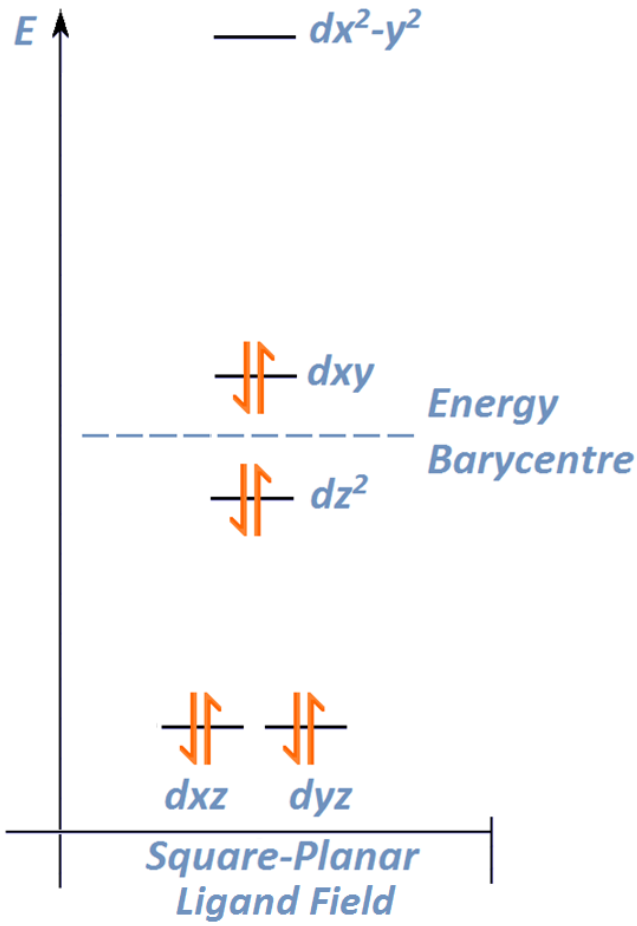

Figure 2.4. σ-only Ligand field splitting diagram for a square planar complex.

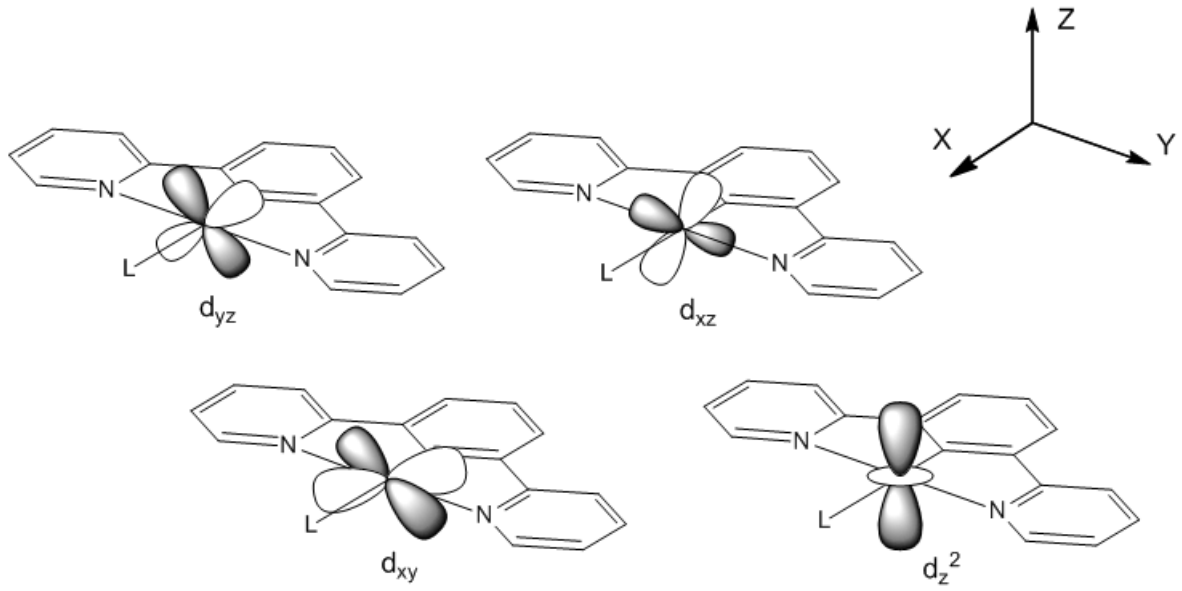

Figure 2.5. Schematic showing the orientations of the four occupied metal d-orbitals relative to the pincer ligand. Note that only the d_{yz} and d_{xz} possess the correct symmetry to interact with the ligand's π-system.

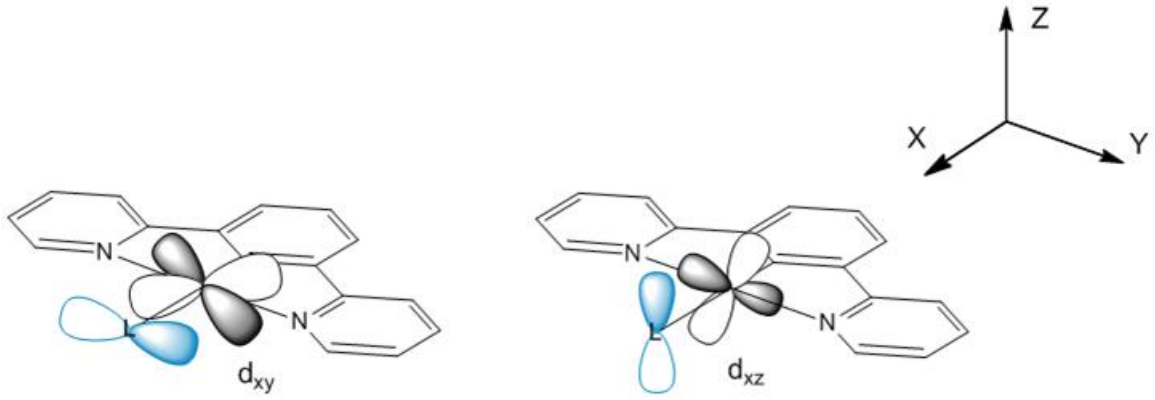

Figure 2.6. Schematic detailing the two possible π-interactions of occupied platinum d-orbitals with a ligand occupying the fourth coordination site of the platinum.

In previous studies on a series of related compounds by Sotoyama *et al.* ,[6] the arrangement of frontier orbitals for a simple variant (with the fourth ligand as a chloride) was calculated, and the predictions given by ligand field theory and the orbital symmetries are supported, as can be seen in **Figure 2.7**. The HOMOs of the compound, as expected consist of the platinum d-orbitals in various combinations with the ligand environment.

The HOMO was calculated to be a π* combination of the d_{xz} and occupied orbitals of the phenyl and chloride ligand. This is the highest energy occupied orbital, most likely due to both phenyl and chloride being good π-donor ligands. The HOMO-1 was calculated to be comprised of a π* combination between the d_{xy} and the occupied p_x of the chloride. Chloride is a good π-donor ligand, occupying a low position on the spectrochemical series, and so this offers an explanation as to why this orbital can be reasonably high in energy, despite lacking any pincer π-interaction.

The HOMO-2 was calculated to be the non-bonding d_z^2 orbital.

The HOMO-3 was calculated to be a π* combination of the d_{yz} and occupied pyridyl orbitals. While this does not represent a π-acceptor interaction, the position of the pyridyl ligand higher up the spectrochemical series indicates poor π-donation, and along with having incorrect symmetry to interact with the strongly π-donating chloride ligand, the lower energy of this orbital can be rationalised.

The LUMOs consisted of π* orbitals almost entirely based on the pincer ligand, which is in line with previous descriptions of similar compounds.

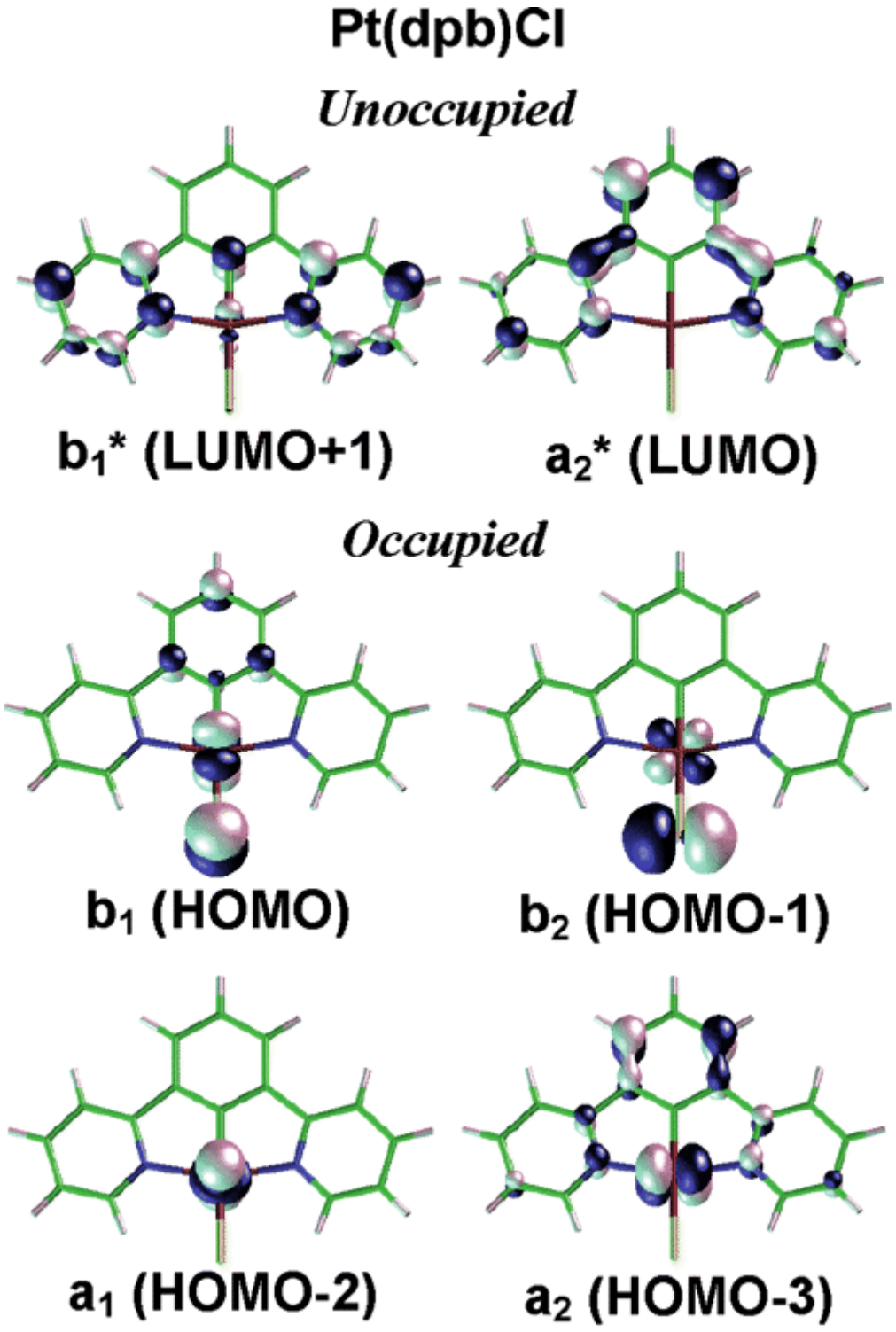

Figure 2.7. Contour plots of the frontier orbitals in a Pt-N^C^N chloride compound calculated by Sotoyama et al.[6]

2.2 Objectives and strategy

From the background research described in this chapter, the research strategy developed was to use synthetic modification in an attempt to manipulate the optical properties of the platinum pincer fragment in a systematic way. The desired outcome of this was to see if the platinum pincer chromophore's optical properties behave in agreement with the predictions informed by ligand field theory and computational calculations on similar systems, under the systematic variation. The useful understanding of the optical properties a positive result would provide could then be used to direct more ambitious lines of modification.

Looking at the frontier orbitals described for the related system seen in **2.1.2** it may be possible to make some specific predictions as to how various synthetic modifications can be made in order to affect the energies of these orbitals.

It would appear that the highest energy occupied molecular orbitals for Pt-N^C^N pincer compounds are likely to be comprised of π* interactions between the non σ-bonding metal d-orbitals and the higher energy occupied π-orbitals of the surrounding ligand environment (particularly the d_{xz}, and with the d_{xy} corresponding mainly to the fourth ligand due to its symmetry).

In the attempt to predictably manipulate the optical properties (i.e the frontier orbitals) of these systems via synthetic alteration, the approach taken was to produce a systematic variation to the π-interactions of the ligand environment with the platinum d_{xz} and d_{xy} orbitals, with the aim of affecting the energy of the HOMO.

There are many ways in which the π-interactions may be varied synthetically though choice of ligands, but for this study given that a systematic approach was desired, the idea of using variable degrees of conjugation was chosen. A series of aromatic ligands with systematically increasing conjugation were selected to occupy the fourth coordination site, with the aim to electronically connect their delocalised π-systems to the metal d-orbitals through π-interaction. The predicted result of this was that the systematic increase conjugation/delocalisation of the ligand would result in destabilisation of the ligand-metal π* hybrids (complex HOMOS) due to the increased energy of the ligand HOMOs.

In order to achieve this connection while also ensuring good π-orbital overlap a σ-acetylide was to be used as a "bridging ligand". As mentioned in **Chapter 1** the acetylide ligand possesses the ability to accept and donate via π-interactions, and to allow π-overlap to d-orbitals in both the xy and xz planes,[7] making it an ideal candidate for electronically connecting a variety of ligands' delocalised π-systems to the platinum centre, and hopefully imparting their effects on the frontier orbitals.

It was therefore decided that the synthesis of the new systems would involve substituting the fourth platinum coordination site with a variety of acetylides functionalised with varying degrees of extended conjugation.[5]

The reason for choosing this line of synthetic modification is two-fold. Firstly, as mentioned, the series will offer information on whether the orbitals can be manipulated in a predictable way, but more importantly, it should be noted that for the intended series of compounds, the coordination environment is identical. It can be assumed that substituting new ligands directly onto the metal may exert some effect on the orbital energies, however, what the work in this chapter attempts to find out is whether ligand changes can still exert their affect on the metal through the conjugated acetylide bridge. If this is the case, then this opens up the system to a wide array of more complex substitutions that can be bridged to the metal centre in order to create switchable materials, sensitive to a variety of stimuli.

As was explained in **section 2.1**, the effect of increasing conjugation on simple organic species is a general shrinking of the HOMO-LUMO gap, contributed to by both a stabilisation of the LUMO and a destabilisation of the HOMO. For the compounds in this study, it is to be expected that the LUMO will be comprised of remote pincer ligand π*-orbitals,[8] and so the expected effect of increasing conjugation (providing there is π-interaction with the metal as desired) is a destabilisation of the HOMO, but leaving the LUMO relatively unaffected.

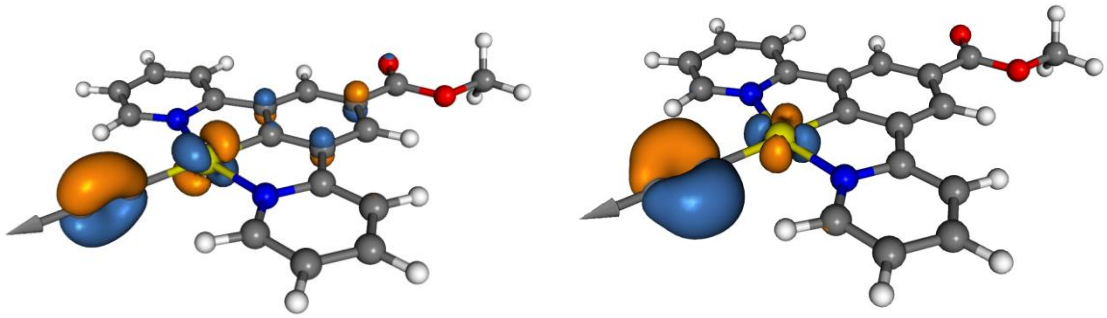

Figure 2.8. Simple Orbital simulation, showing a ways in which acetylides may be able to bridge the platinum centre electronically to various ligands through π-interactions.

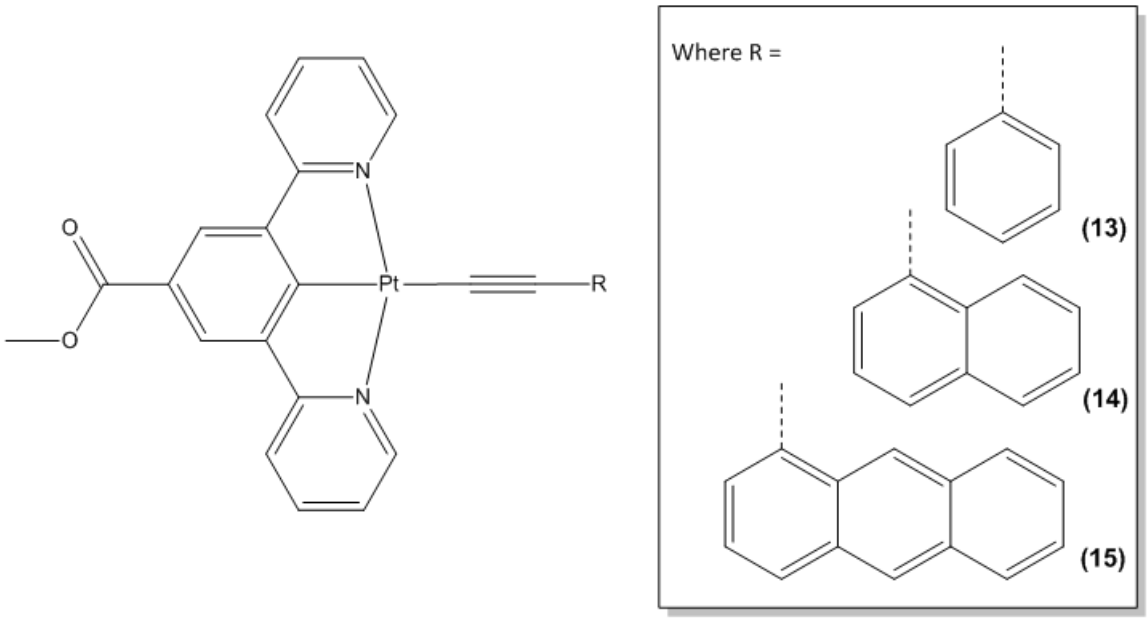

Figure 2.9. Synthetic targets for this chapter.

2.3 General synthetic strategy

In this chapter we report the syntheses of a series of new platinum N^C^N pincer compounds based on the **methyl 3,5-di(2-pyridyl)benzoate (5)** ligand which has a methyl-ester group occupying the *trans*-position of the central arene ring. The fourth coordination site of the platinum is occupied by a series of polyaromatic acetylides with systematically varied π-systems (**Figure 2.9**).

The synthetic strategy employed to create this series of compounds is broken down into a series of steps.

2.3.1 Ligand Synthesis

Firstly, the aromatic fragments of choice needed to be synthesised to include acetylide "bridge" ligands, as a way to link the delocalised π-electrons to the orbitals of the platinum centre.

All the polyaromatic ligands were synthesised as trimethylsilyl-protected alkynes, from brominated starting materials, using an adapted Sonogashira reaction, and follow the general steps shown in **Scheme 2.1**.[9]

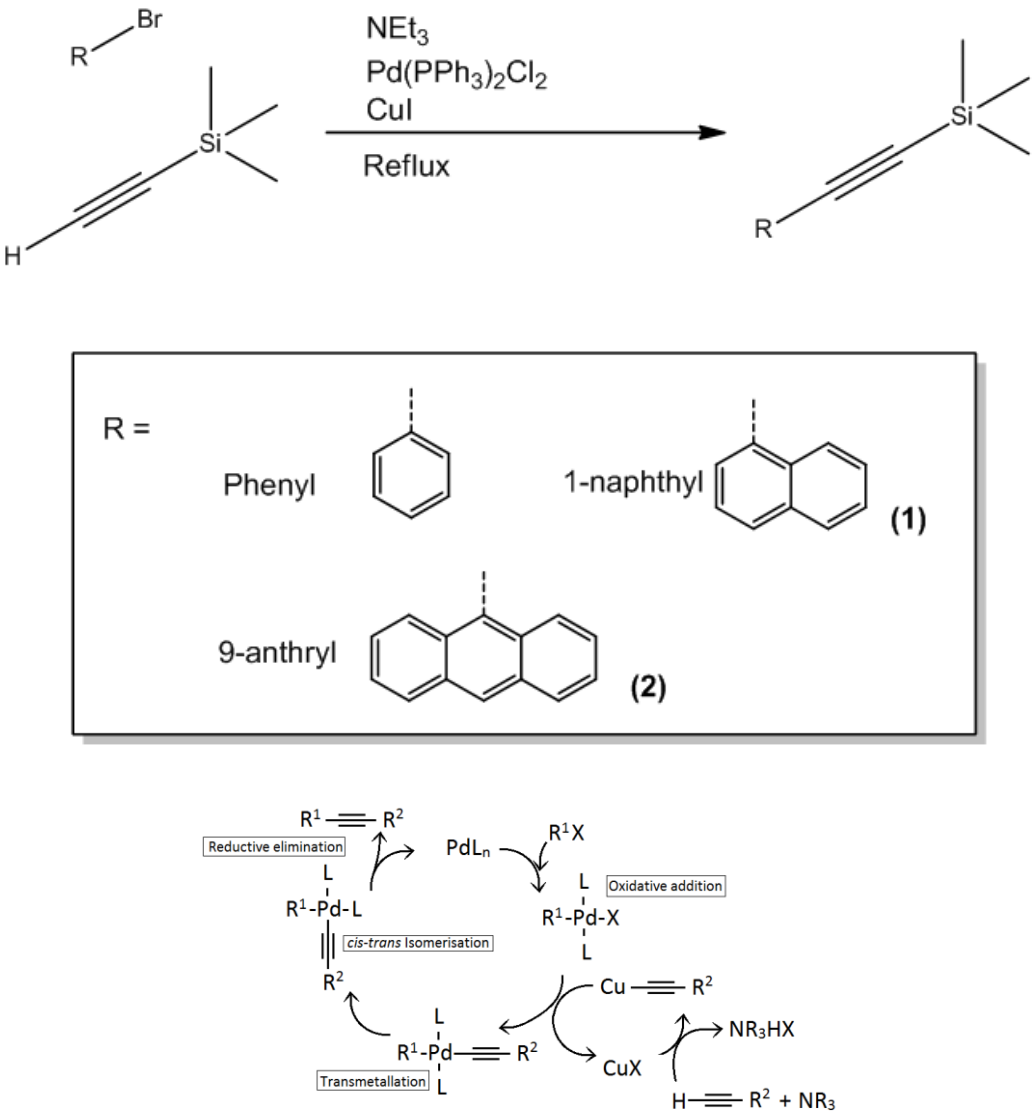

Scheme 2.1. Reaction scheme for the three ligand substitutions (Sonogashira cross-coupling).

2.3.2 Pt-NCN pincer system synthesis

The next step in the synthesis of this series of compounds is the synthesis of the platinum (II) N^C^N pincer fragment **methyl 3,5-di(2-pyridyl)benzoate (5)**, to which the aromatic acetylides are to be connected. This process can be broken down into two steps.

2.3.2.1 Pincer ligands

The N^C^N pincer ligand used was synthesised first, using a standard Stille cross-coupling reaction [10] between methyl-(3,5-dibromo)benzoate and 2-(tri-n-butylstannyl)pyridine in triethylamine using Bis(triphenylphosphine)palladium(II) dichloride catalyst. The ligand was purified by column chromatography on silica, using hexanes and diethyl ether as an eluent. Pure **(5)** was produced with 79% yield (**Scheme 2.2**).

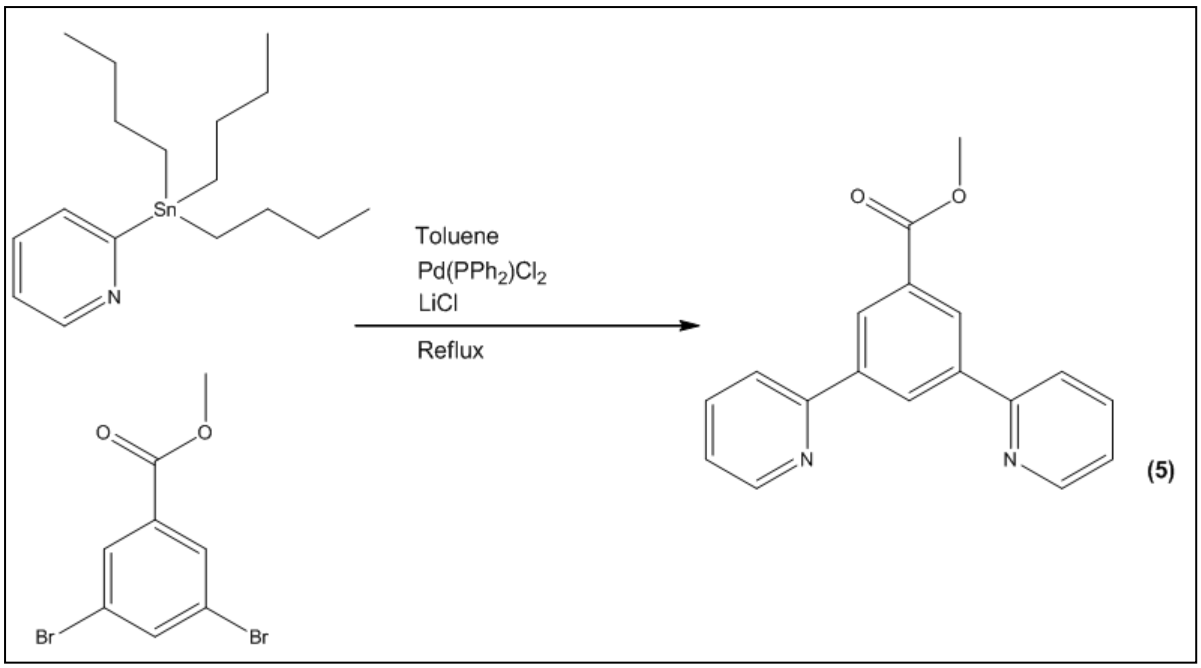

Scheme 2.2. Stille-coupling pincer ligand synthesis.

2.3.2.2 Incorporation of platinum

The pincer ligand was then cyclometallated to incorporate platinum. The purified ligand was reacted with potassium tetrachloroplatinate in a minimum quantity of solvent (acetonitrile/water) and heated at reflux for 72 h. This resulted in cyclometallation in good yield, leaving chloride occupying the fourth coordination site of the metal. The precipitated product was then filtered out and simply washed with water, ethanol, acetonitrile and diethyl ether to produce pure **chloro[methyl 3,5-di(2-pyridyl)benzoato]platinum (9)** (**Scheme 2.3**).[11]

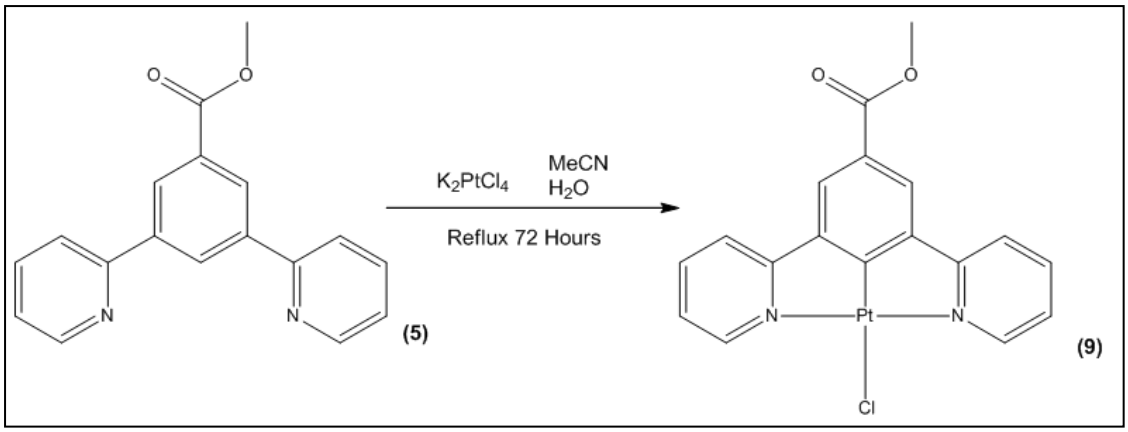

Scheme 2.3. Cyclometallation reaction.

2.3.3 Synthesis of the platinum (II) alkyne complex

The final step is to react each of the aromatic acetylides with the resulting Pt(II)N^C^N pincer chloride, to produce the series of new compounds with this ligand occupying the fourth coordination site of the metal, with the acetylide ligand linking the metal and the aromatic organic fragments. This was carried out using a salt metathesis reaction, whereby the trimethylsilyl-protected polyaromatic acetylides were deprotected with sodium hydroxide and methanol, and then the chloro[methyl 3,5-di(2-pyridyl)benzoato]platinum **(9)** was introduced and allowed to react. [12] The resulting final products were purified by recrystallisation, and were all produced in yields exceeding 49%

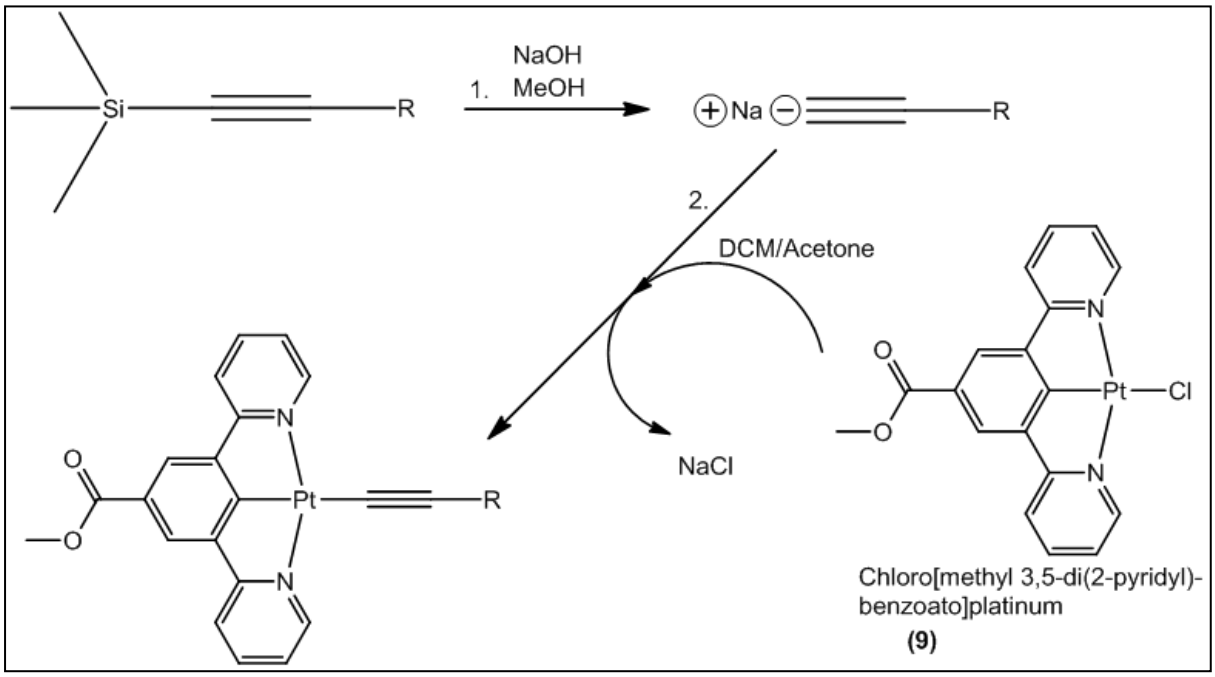

Scheme 2.4. General salt metathesis reaction to produce final products.

Detailed syntheses, and characterisations of all compounds can be found in the experimental section.

2.4 Phenylethynyl[methyl 3,5-di(2-pyridyl)benzoato]platinum (13)

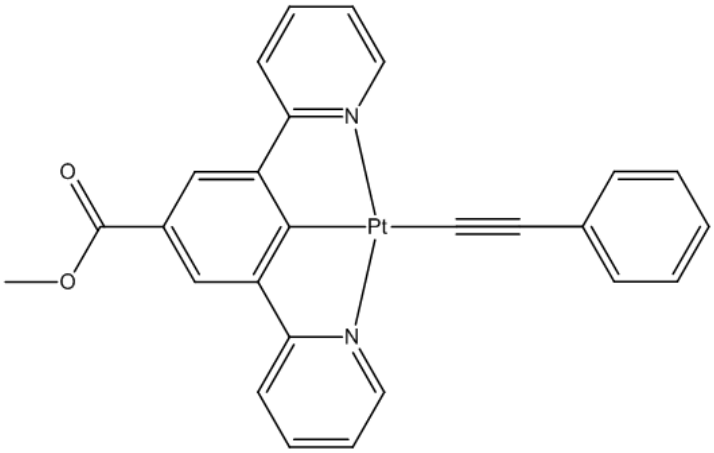

(13) was fully characterised by NMR and solid-state IR spectroscopy, Mass spectrometry and X-Ray crystallography. (See experimental section)

The IR spectrum shows a strong, sharp absorption at 2077 cm^{-1}, assignable to the $\nu_{C\equiv C}$ of a σ-alkynyl group. This value is consistent with those recorded for a series of related compounds.[13,14] Also seen is a single strong absorption at 1696 cm^{-1} assignable to the $\nu_{C=O}$ of the ester group, which is a typical value for a methyl benzoate ester.[15,16]

^{1}H NMR, and $^{13}C\{^{1}H\}$ NMR spectra of **(13)** were obtained for the product dissolved in deuterated dichloromethane. The correct assignment of hydrogen atoms was supported with the use of a 2-dimensional HCOSY experiment.

All spectra corresponded with the structure proposed for **(13)**.

NMR data are included in this chapter for **(13)** only, to provide a demonstration of the methods used to assign peaks (**Figure 2.10**). Data for remaining compounds, along with further characterisation can be found in the experimental section.

^{1}H NMR (500 MHz, CD_2Cl_2) δ_H: 9.51 (d, $^{3}J_{H\text{-}H}$= 5.6 Hz, $^{3}J_{H\text{-}Pt}$= 47.3 Hz, 2H, *ortho-Py*), 8.27 (s, 2H, *pincer-Ph*), 8.07 (t, $^{3}J_{H\text{-}H}$= 7.8 Hz, 2H, *para-Py*), 7.88 (d, $^{3}J_{H\text{-}H}$= 7.5 Hz, 2H, *meta-Py*), 7.55 (d, $^{3}J_{H\text{-}H}$= 8 Hz, 2H, *ortho-pendant Ph*), 7.33 (m, 4H, *meta-Py* + *meta-pendant Ph*), 7.23 (t, $^{3}J_{H\text{-}H}$= 7.4 Hz, 1H, *para-pendant Ph*), 3.98 (s, 3H, CO_2CH_3)

$^{13}C\{^{1}H\}$ NMR (400 MHz, CD_2Cl_2) δ_C: 185.65, 169.20, 167.95, 155.96, 152.17, 143.75, 137.09, 131.97, 129.00, 128.59, 125.86, 125.59, 124.71, 120.54, 112.588, 52.56, 1.33

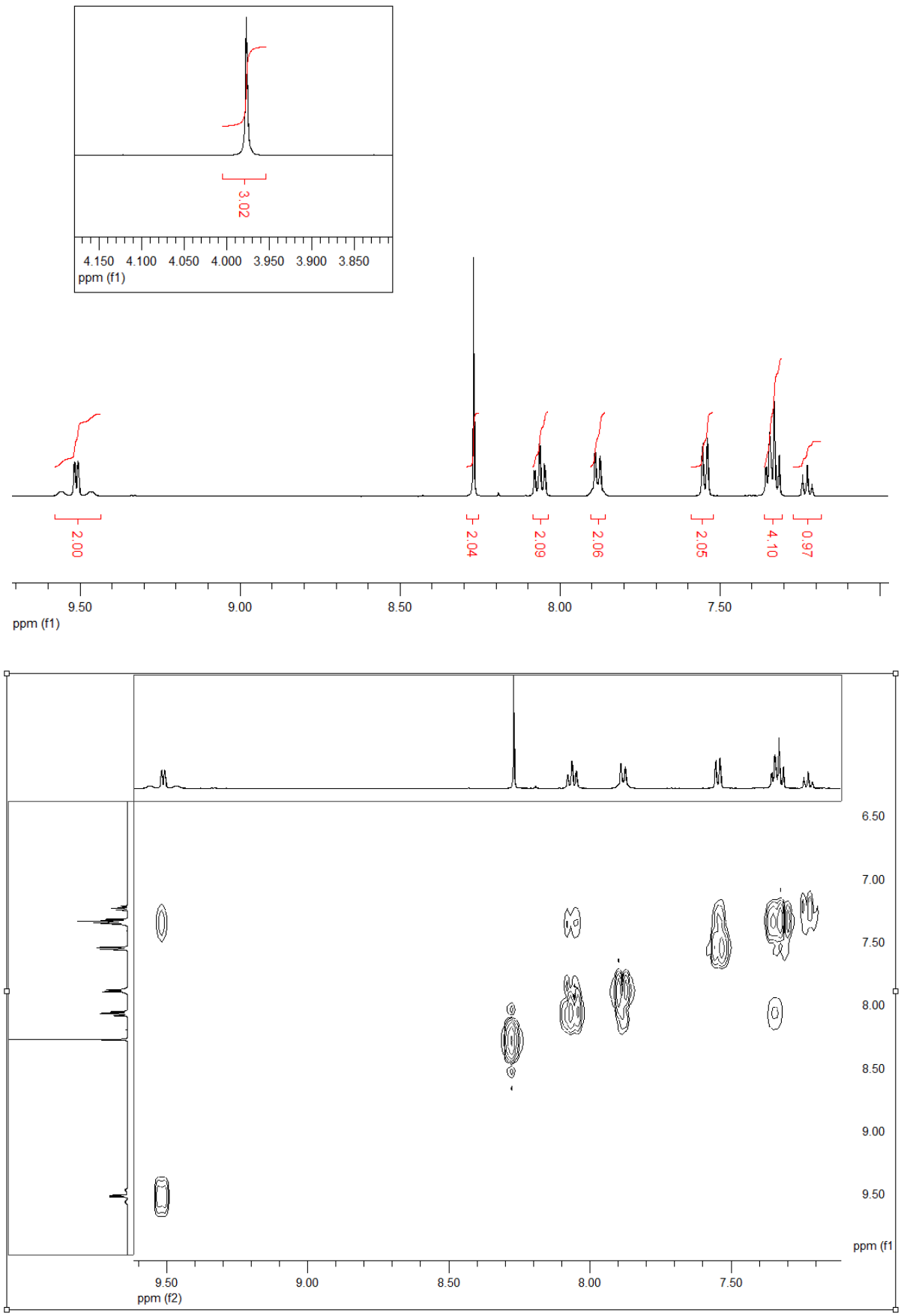

Figure 2.10. Top: ^{1}HNMR spectrum of (13). Bottom: COSY spectrum used to assign peaks.

2.4.1 Crystallography

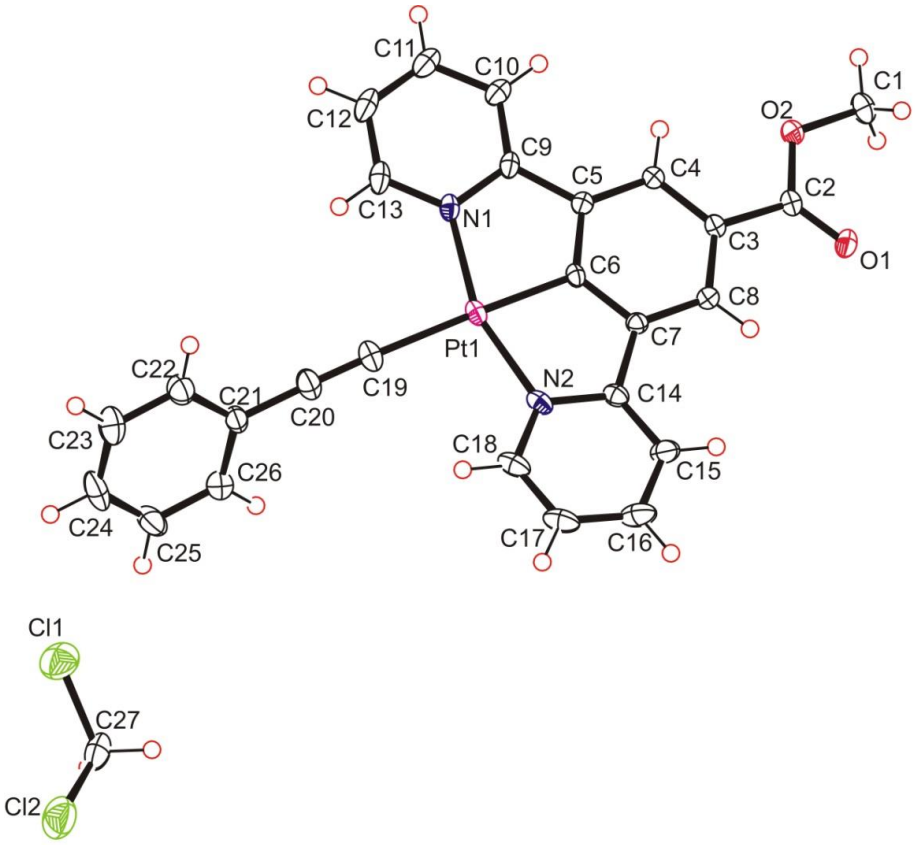

(13) crystallised as relatively large yellow blocks obtained by layering n-hexane onto a concentrated DCM solution and allowing the solvents to phase together slowly at -20°C. **(13)** crystallises in the monoclinic space group $P2_1/n$, with the asymmetric unit consisting of one neutral molecule of the complex, and one molecule of dichloromethane. The acetylide group is slightly bent down away from the plane of the molecule, and the average plane of the phenyl ring is twisted by 57.10 (12) ° from the average plane of [Pt1, C5, C6, C7, C9, C14, N1 and N2]. The Platinum centre adopts the expected square planar geometry with minor distortion (N1-Pt1-N2 angle 159.96 (14) °) due to the pincer bite angle, with bond parameters in the expected ranges. The C≡C bond distance, 1.203 (6) Å is also typical (**Table 2.1**).[17,18,12]

Table 2.1. Selected bonds and angles for (13)

Bond	Length (Å)
Pt1-N1	2.025 (4)
Pt1-N2	2.032 (4)
Pt1-C6	1.931 (4)
Pt1-C19	2.056 (5)
C19-C20	1.203 (6)

Bonds	Angle (°)
Pt1-C19-C20	174.37 (4)
C19-C20-C21	179.39 (6)

The crystal structure as a whole consists of two staggered orientations of stacked planar pairs of the neutral platinum pincer complexes at a shallow angle to each other in a herringbone configuration (**Figure 2.11**). Four main types of interactions are present within each planar pair which are separated by a plane to plane distance of 3.58 (2) Å (taken as separation of Pt1 to symmetry equivalent plane of Pt1, C5, C6, C7, C9, C14, N1 and N2), indicating π-π stacking is present within the pairs.

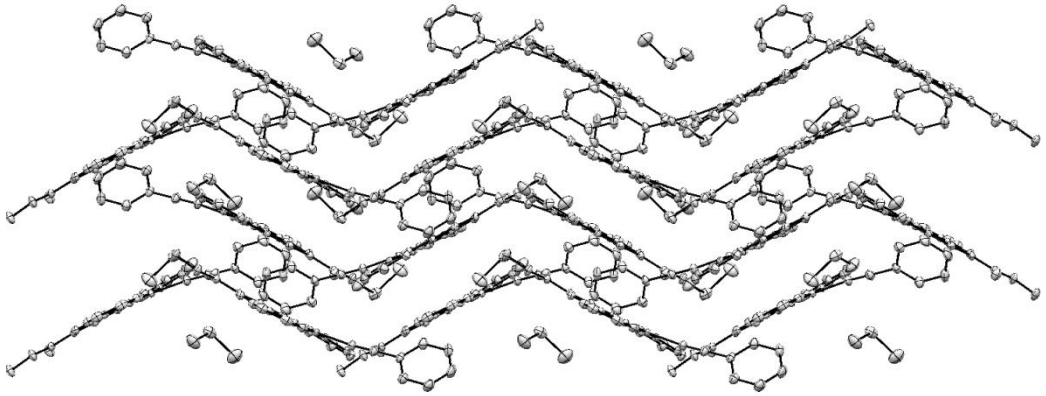

Figure 2.11. Extended structure of (13) to show herringbone stacking configuration.

The twisting of the auxiliary phenyl away from the plane in the solid state, and the bending of the acetylide linker differ from the calculated minimum energy configuration (Detail in section **2.71**) and this appears to be a result of void filling in the crystal, along with stabilisation via weak C-H---O hydrogen bonding interactions with the ester of adjacent molecule. The adjacent stacks also appear to be held together with weak hydrogen bonding interactions (C-H---Cl and C-H---O) to the dichloromethane molecule. Details of these interactions can be seen in and **Figure 2.12** and **Table 2.2**.

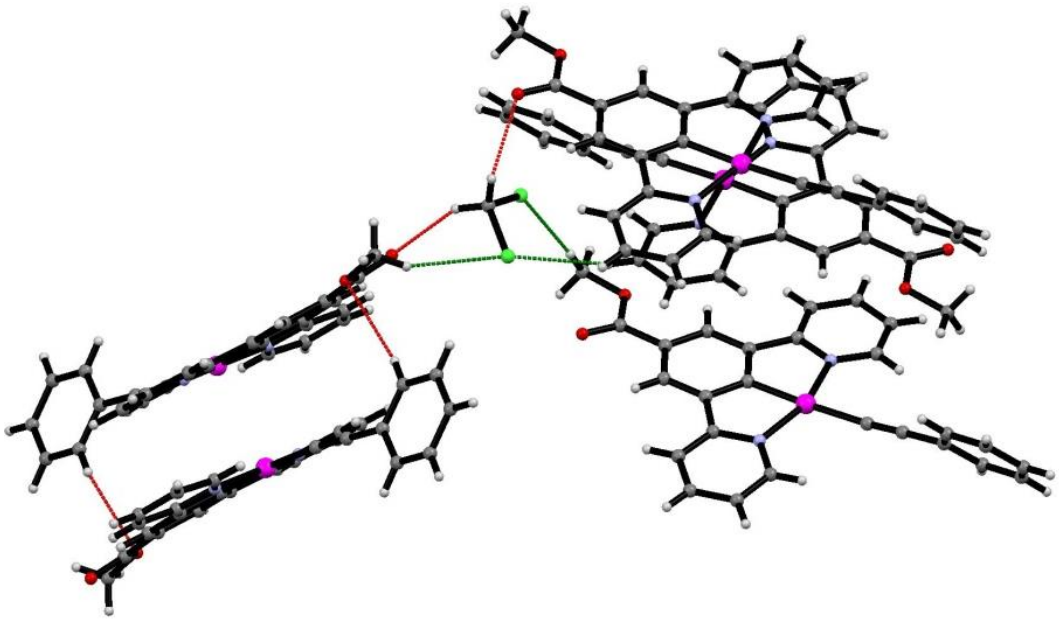

Figure 2.12. Weak carbon donor hydrogen bonding interactions to chlorine (green) and oxygen (red) acceptors

Table 2.2. Weak hydrogen bonding interactions for (13)

Bond	Distance (D..A) (Å)	Distance (H..A) (Å)	Angle (D..H..A) (°)
C22 -H22-O2[1]	3.676 (6)	2.816	154.2
C25-H25-O1[2]	3.797 (6)	3.130	130.2
C12-H12-Cl2[1]	3.841 (5)	2.924	168.79
C1-H1B-Cl1[3]	3.809 (5)	2.863	168.79
C1-H1C-Cl2[4]	3.885 (5)	3.025	149.85
C27-H27A-O1	3.323 (6)	2.540	137.80
C27-H27B-O1[5]	3.245 (6)	2.362	151.03
C16- H16-O2[6]	3.549 (6)	2.680	155.85

1 = (1-x, -y, -z), 2 = (1.5-x, -1/2+y, 1/2-z), 3 = (x, 1+y, z), 4 = (1/2-x, 1/2+y, 1/2-z), 5 = (1/2-x, -1/2+y, 1/2-z), 6 = (1/2+x, 1/2-y, 1/2+z)

2.5 1-naphthylethynyl[methyl 3,5-di(2-pyridyl)benzoato]platinum (14)

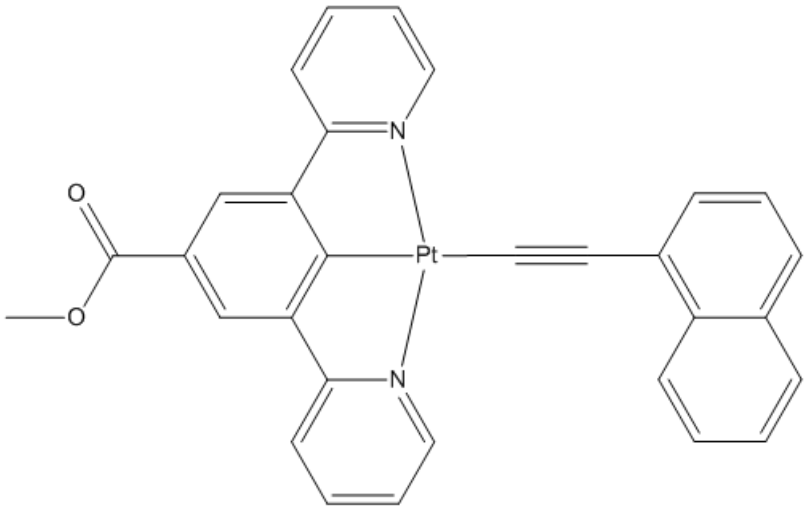

(14) was fully characterised by NMR and solid-state IR spectroscopy, Mass spectrometry and X-Ray crystallography.

The IR spectrum shows a strong, sharp absorption at 2074 cm^{-1}, assignable to the $\nu_{C\equiv C}$ of a σ-alkynyl group. This value is consistent with those recorded for a series of related compounds.[13,14] Also seen is a single strong absorption at 1697 cm^{-1} assignable to the $\nu_{C=O}$ of the ester group, which is a typical value for a methyl benzoate ester.[15,16]

^{1}H NMR, and $^{13}C\{^{1}H\}$ NMR experiments on **(14)** were run on the product in deuterated chloroform. The correct assignment of hydrogen atoms was supported with the use of a 2-dimensional HCOSY experiment.

All spectra corresponded with the structure proposed for **(14)**. See experimental section for details.

2.5.1 Crystallography

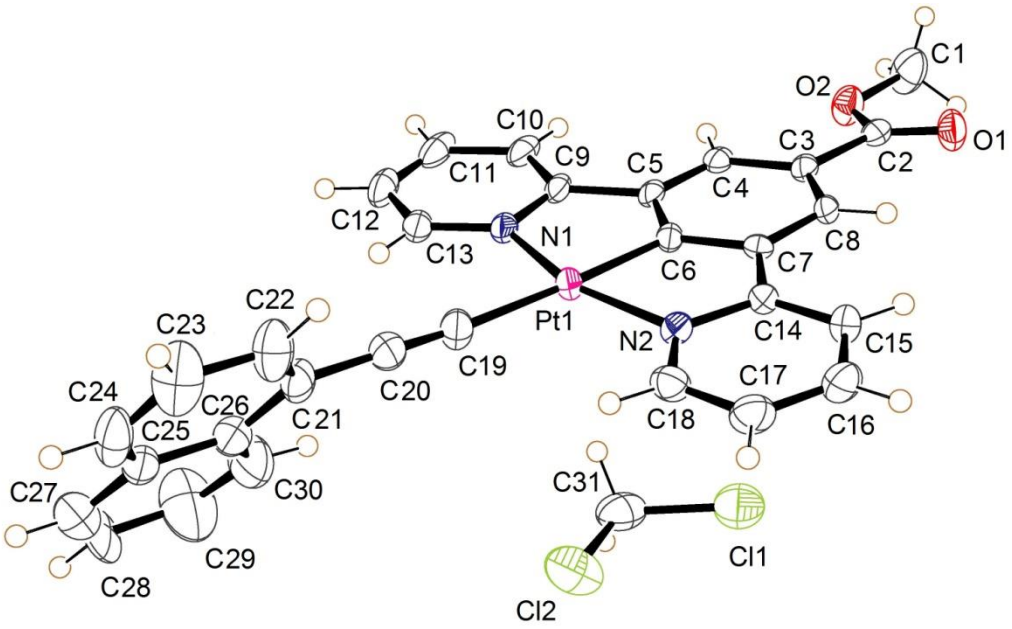

(14) crystallised as orange/yellow plates obtained by layering methanol onto a concentrated DCM solution and allowing the solvents to phase together slowly at -20°C. As with **(13)**, **(14)** crystallises with the asymmetric unit consisting of one neutral molecule of the complex, and one molecule of dichloromethane, this time in the monoclinic space group $P2_1/c$.

Overall the configuration in the molecule is close to that of **(13)**. In this structure the average plane of the naphthyl fragment is twisted by 54.6 (16) ° from the average plane of [Pt1, C5, C6, C7, C9, C14, N1 and N2] and this configuration is closer to the calculated minimum energy position of 79.45°. The acetylene is closer to linear than **(13)**. The platinum centre adopts the expected square planar geometry with minor distortion (N1-Pt1-N2 angle 160.4° (3)) due to the pincer bite angle, with bond parameters in the expected ranges. The C≡C bond distance, 1.210(3) Å is also typical (**Table 2.3**).[17,18,12]

Table 2.3. Selected bonds and angles for (14)

Bond	Length (Å)
Pt1-N1	2.040 (7)
Pt1-N2	2.034 (7)
Pt1-C6	1.932 (8)
Pt1-C19	2.050 (9)
C19-C20	1.217 (13)

Bonds	Angle (°)
Pt1-C19-C20	175.8 (6)
C19-C20-C21	176.1 (8)

Like **(13)**, the crystal structure of adopts a herringbone extended structure of end-to end planar pairs of **(14)**, with the planes separated by 3.449 (9) Å (taken as separation of Pt1 to symmetry equivalent plane of Pt1, C5, C6, C7, C9, C14, N1 and N2) (**Figure 2.13**).

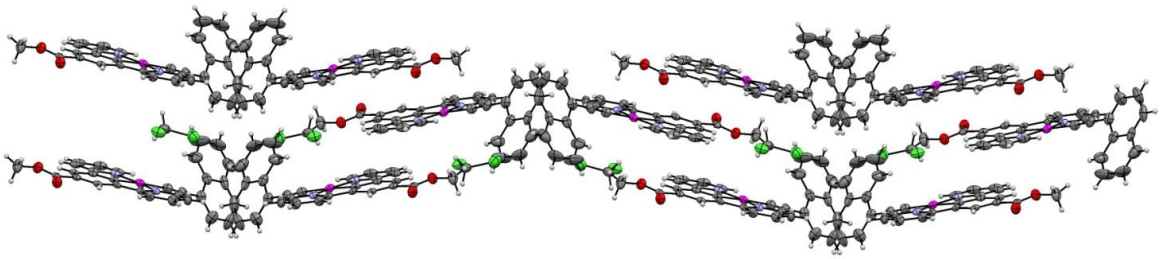

Figure 2.13. Extended structure of (14) to show herringbone stacking configuration.

The structure is held together with weak hydrogen bonds consisting of carbon donors to either oxygen or chlorine. In **Figure 2.14** the C-H---O bonds are highlighted, and in **Figure 2.15** the C-H---Cl interactions are highlighted. **Table 2.4** gives the details of these interactions.

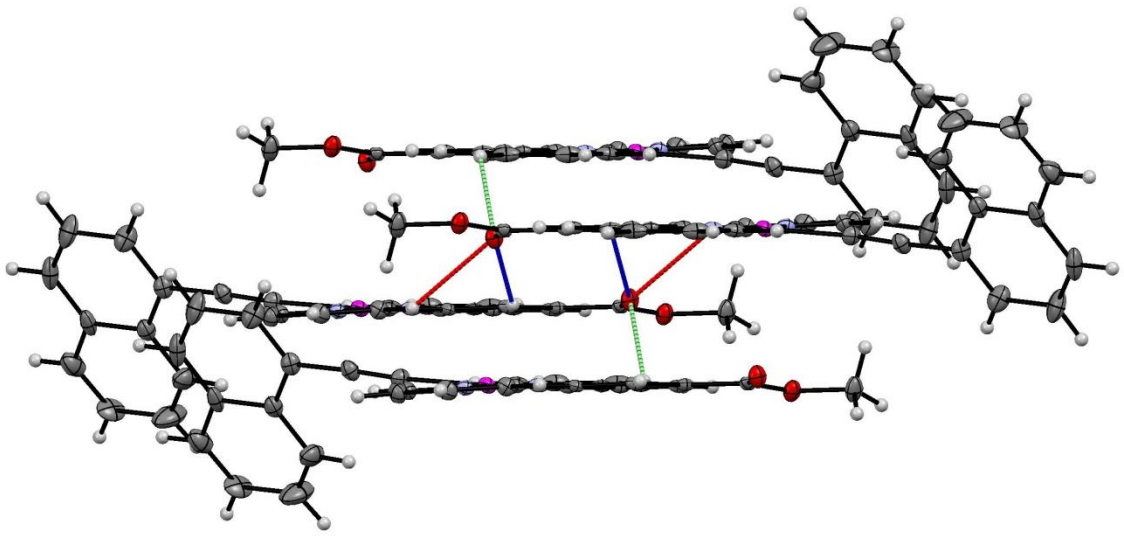

Figure 2.14. Interactions between molecules of (14) via C-H---O interactions to the carbonyl. Like-coloured interactions are symmetry equivalents.

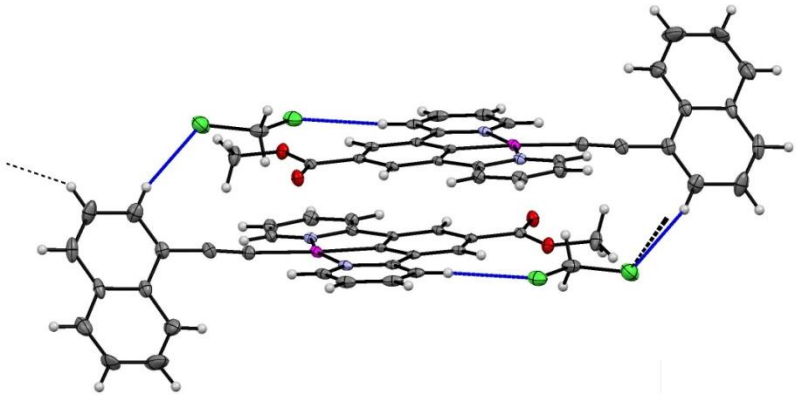

Figure 2.15. C-H---Cl interactions to the chlorines of dichloromethane. The black interactions show how the pairs of the other planar orientation in the herringbone connect to this via Cl2 and C23 (H30).

Table 2.4. Weak hydrogen bonding interactions for (14)

Bond	Distance (D..A) (Å)	Distance (H..A) (Å)	Angle (D..H..A) (°)
C16-H16-O1[1]	3.320 (11)	2.727	122.52
C4-H4-O1[2]	3.731 (10)	2.910	147.96
C10-H10-O1[2]	3.493 (11)	2.663	149.12
C15-H15-Cl1[3]	3.772 (10)	2.913	154.48
C22-H22-Cl2	3.887 (11)	2.975	163.76
C23-H23-Cl2[4]	3.777 (12)	3.016	140.11

1 = (x, y, 1+z), 2 = (1-x, -y,-1 -z), 3 = (1-x, -y, -z), 4 = (x,1/2-y, 1/2+z)

2.6 9-anthrylethynyl[methyl 3,5-di(2-pyridyl)benzoato]platinum (15)

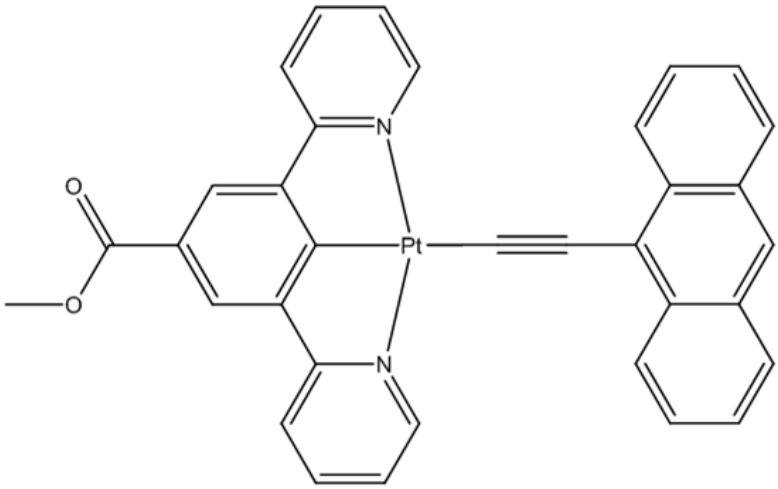

(15) was fully characterised by NMR and solid-state IR spectroscopy, Mass spectrometry, and X-Ray crystallography.

The IR spectrum shows a strong, sharp absorption at 2065 cm^{-1}, assignable to the $\nu_{C\equiv C}$ of a σ-alkynyl group. This value is consistent with those recorded for a series of related compounds.[13,14] Also seen is a single strong absorption at 1706 cm^{-1} assignable to the $\nu_{C=O}$ of the ester group, which is a typical value for a methyl benzoate ester.[15,16]

^{1}H NMR, and $^{13}C\{^{1}H\}$ NMR experiments of **(15)** were run on the product in deuterated dichloromethane. The correct assignment of hydrogen atoms was supported with the use of a 2-dimensional HCOSY experiment.

All spectra corresponded with the structure proposed for **(15)**. See experimental section for details.

2.6.1 Crystallography

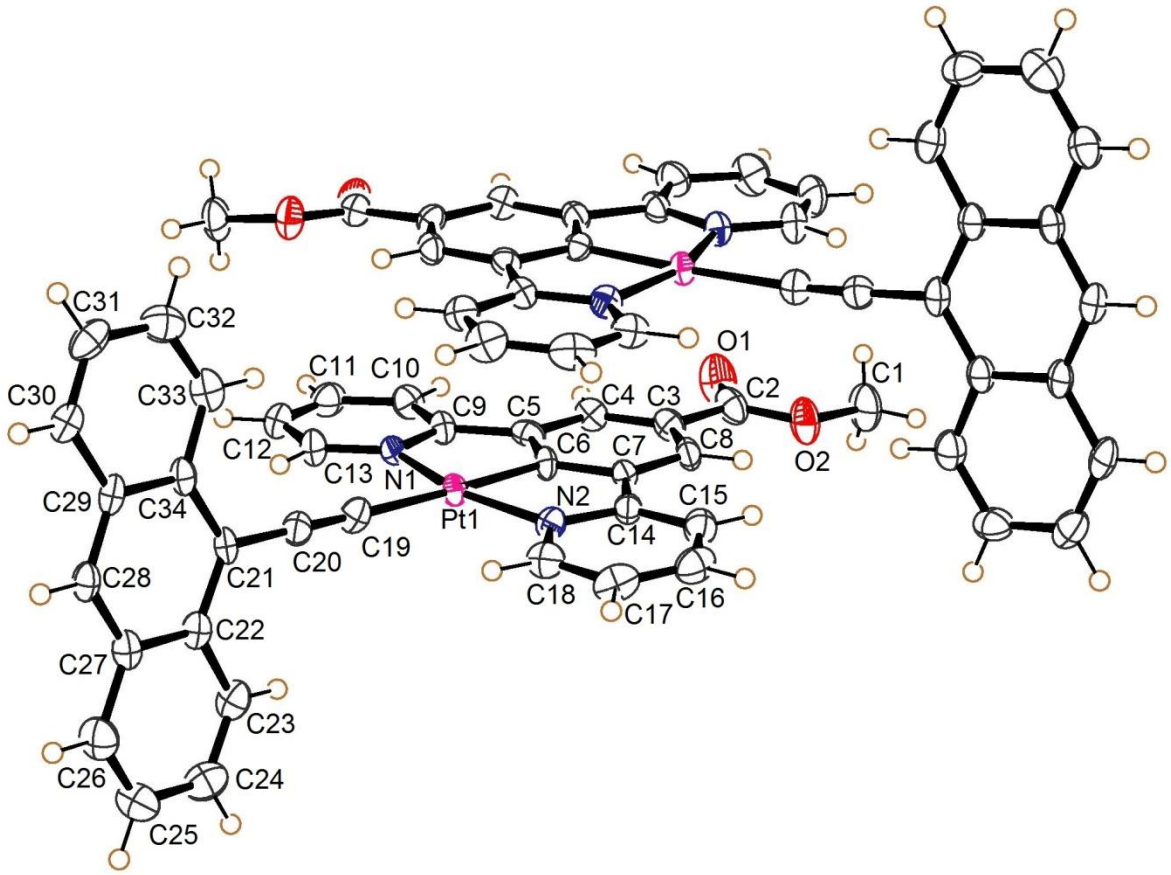

(15) crystallised as orange/yellow blocks obtained by layering hexane onto a concentrated DCM solution and allowing the solvents to phase together slowly at -20°C. In contrast to the other two compounds, **(15)** crystallises with the asymmetric unit consisting of two neutral molecules of the compound with no solvent (to be referred to as molecule 1, and molecule 2- whose atom labels are the same as molecule one with a prime (') symbol). The compound again crystallised in the monoclinic space group $P2_1/c$.

In this structure the average plane of the anthryl fragments are twisted by 78.43 (9) ° for molecule 1 (from average plane of Pt1, C5, C6, C7, C9, C14, N1 and N2), and 84.72 (9) ° for molecule 2 (from average plane of Pt1', C5', C6', C7', C9', C14', N1' and N2'). These configurations are now close to the calculated minimum energy position of 82.36°. The acetylene of molecule 1 is close to linear with molecule 2 slightly more distorted. The platinum centres adopt the expected geometry with minor distortions (N1-Pt1-N2 angle 159.86 (19) °, and N1'-Pt1'-N2' angle 159.93 (20) °) due to the pincer bite angle, with bond parameters in the expected ranges. The C≡C bond distances, 1.200 (9) Å (molecule 1) and 1.189 (8) Å (molecule 2) are also typical (**Table 2.5**).[17,18,12]

Table 2.5. Selected bonds and angles for (15)

Bond	Length (Å)
Pt1-N1	2.038 (5)
Pt1-N2	2.032 (5)
Pt1-C6	1.945 (6)
Pt1-C19	2.061 (6)
C19-C20	1.200 (9)

Bond	Length (Å)
Pt1'-N1'	2.036 (5)
Pt1'-N2'	2.031 (5)
Pt1'-C6'	1.925 (6)
Pt1'-C19'	2.063 (6)
C19'-C20'	1.189 (8)

Bonds	Angle (°)
Pt1-C19-C20	177.8 (6)
C19-C20-C21	179.1 (7)

Bonds	Angle (°)
Pt1'-C19'-C20'	172.0 (6)
C19'-C20'-C21'	178.0 (7)

Interactions between the two molecules in the asymmetric unit are essentially limited to simple π-π stacking interactions, however, contact between the platinum centres and the π-system of the adjacent pincers also exists. Between adjacent pairs there is also π-π stacking based on interaction between anthracene groups (**Figure 2.16** and **Table 2.6**). There are further interactions between adjacent pairs in which C-H---O weak hydrogen bonding interactions between the pincer ligands and ester carbonyls occur. Details of these interactions can be seen in **Figure 2.17**, and **Table 2.7**.

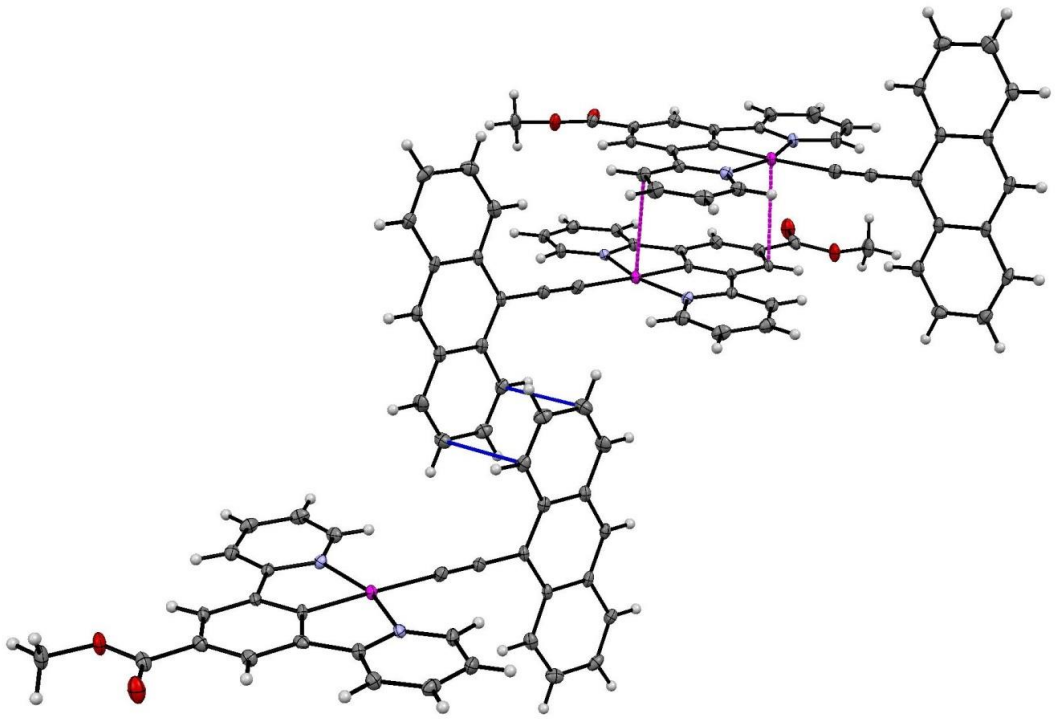

Figure 2.16. Platinum-π-system interactions shown in pink, and π-π interactions between anthracene groups in blue (details in Table 2.6).

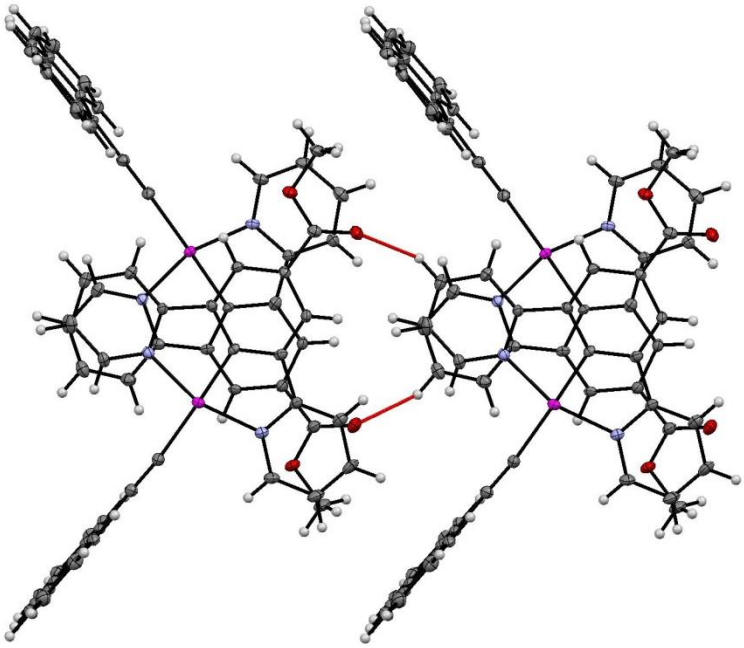

Figure 2.17. Weak hydrogen bonding interactions that exist between adjacent pairs of molecules.

Table 2.6. π-stacking interactions for (15)

Bond	Distance (D..A) (Å)
Pt1'-C8	3.370 (7)
Pt1-C10'	3.522 (7)
C23-C25[1]	3.254 (10)

1 = (1-x, 1-y, 1-z)

Table 2.7. Weak hydrogen bonding interactions for (15)

Bond	Distance (D..A) (Å)	Distance (H..A) (Å)	Angle (D..H..A) (°)
C16-H11-O1[1]	3.168 (9)	2.587	123.07
C11'-H7'-O1'[1]	3.191 (8)	2.461	121.07

1 = (x, 1+y, z)

2.7 UV-Vis absorption spectra

By synthetically altering the ligand environment of the platinum through replacement of the chloride with increasingly conjugated aromatic acetylides, it was the aim of the research in this chapter to attempt to manipulate the energy of the HOMO through π-splitting of the d-orbitals using conjugated aromatic ligands, linked to the metal through acetylide bridges.

The lowest energy electronic absorption band for these compounds can yield information about the frontier orbitals, and electronic transitions that potentially contain metal orbital character. The effect of the polyaromatic ligand on these transitions can be studied by comparing the absorptions in this region for each compound, and by comparing to the starting material with only a chloride substituted at this position which acts as a control. (See **Figure 2.18**)

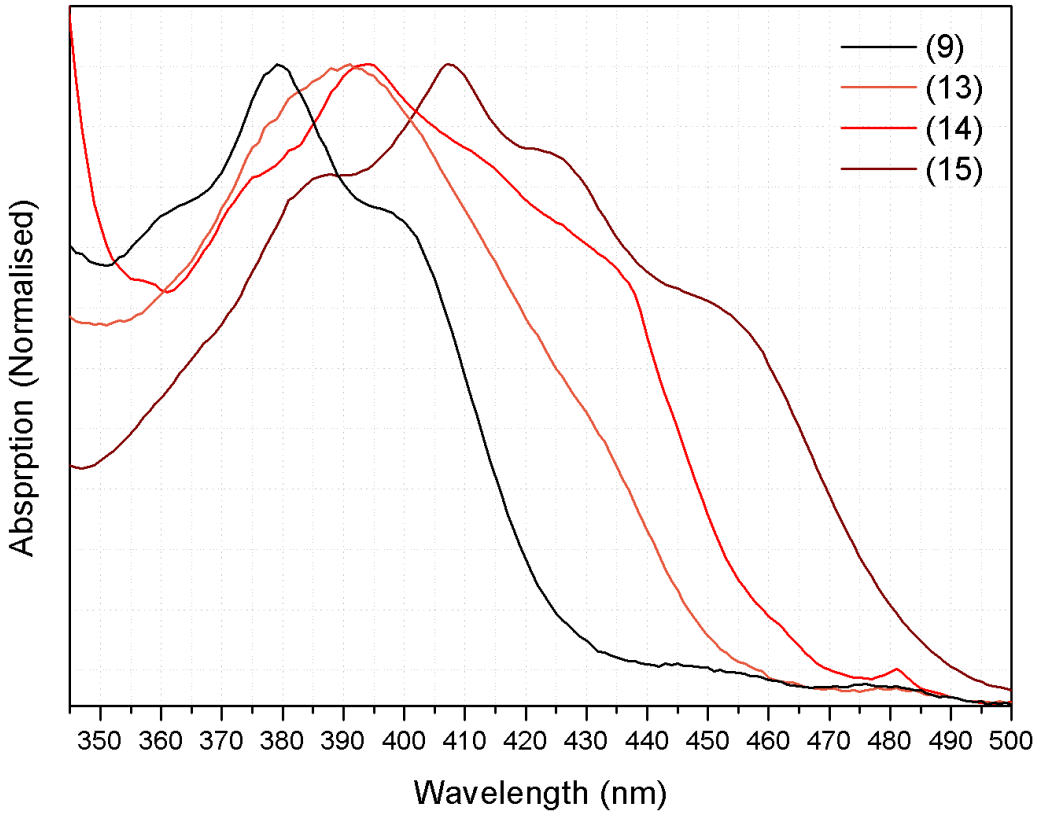

Figure 2.18. Normalised spectrum of the low energy absorption of $5x10^{-6}$ mol dm^{-3} dichloromethane solutions of the compounds. peaks = 379nm (9), 392nm (13), 394 (14), 408 (15).

Spectra were recorded for each compound in dichloromethane at concentrations $1x10^{-7}$ to $1x10^{-4}$. No aggregation was observed with increasing concentration as evidenced by unchanged UV-Vis and linear Beer-Lambert plots. These additional spectra and plots can be found in the supporting information.

(13)

Looking first at the phenylacetylide compound, **(13)**, it can be seen immediately that while the profile of the absorption resembles that of the chloride derivative, the peak of this absorption has red-shifted to 392 nm. The profile of the peak, while less defined in its vibrational structure, has broadened with the general absorption extending beyond 440nm.

(14)

The next compound in the series is the naphthylacetylene substituted compound, **(14)**. The absorption maximum can be seen to have red-shifted again, but this time only slightly relative to the phenyl substituted compound, to 394nm. The peak has broadened further however, with the tail of the absorption extending past 455nm, and shows additional vibrational structure that is characteristic of naphthalene, suggesting that this transition involves orbitals situated on the naphthalene.

(15)

Finally the anthrylacetylene compound, **(15),** shows a much larger red-shifting of its absorption maximum again, to 408nm. The peak has once again broadened, with absorption extending past 480nm, and the further addition of vibrational structure to the peak suggesting involvement of anthracene orbitals in this absorption.

It is clear from these results that there is a trend in the optical properties, whereby a red shift is observed with the increasing degree of conjugation, however it is not a uniform trend with the **(14)** absorbing almost at the same maximum frequency as **(13)**, followed by a further shift for **(15)**. The fine structure and peak profiles seem to suggest the involvement of the aromatic fragments in each transition, so why is there such a small shift when substituting phenyl for naphthalene?

In order to understand this it was required that the nature of the excited states was established. To determine the cause to the shift in optical properties between these complexes DFT calculations were performed.

2.7.1 DFT calculations

Calculations were performed in the gas phase. Details of the experimental methods used can be found in the supporting information.

2.7.1.1 Energy minimisation

The first calculation performed for each compound was an energy minimisation in order to establish the most stable configuration for the aromatic fragments relative to the metallo-pincer in the non-aggregated molecules. It was shown that for the phenyl group, lying in the plane of the pincer offered the highest stability. For the naphthyl and anthryl fragments however, a position close to perpendicular to the plane of the pincer offered the lowest energy configuration with angles of 79.45° and 82.36° respectively to the plane of the pincer.

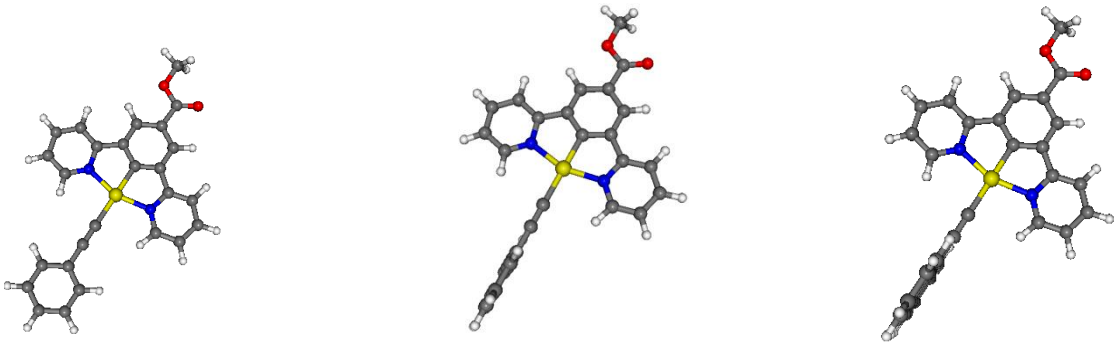

Figure 2.19. Calculated minimum energy configurations. Left to right – (13), (14), and (15).

Both of these configurations (in-plane or perpendicular) allow for mixing of the conjugated ligand π-systems with platinum d-orbitals, and so the intention of affecting the energy of the HOMO in this manner is still viable.

2.7.1.2 Orbital calculations

The frontier orbitals and excited states associated with these configurations were then calculated for these minimised energy structures to get an approximation of their behaviour in non aggregated states, such as in dilute solutions, and hopefully help to explain the pattern of red-shifting seen spectroscopically, and how the variation of the ligands affects the orbital composition and energy.

DFT studies were performed in the gas phase for each compound, as an approximation of an unaggregated molecule, and to get an approximation of each compound's internal orbital structure free from external influence. It is known that pure DFT (in this work, B3LYP is used) will often

underestimate HOMO-LUMO gaps (due to inherent inaccuracy in describing unoccupied orbital energies), and so the actual transition energies calculated using this method are unlikely to accurately predict those recorded spectroscopically. They should however be proportionate, and show accurate trends between the compounds. This method should also give a good indication as to the orbital transitions involved, and help to explain the optical properties of the compounds.[19,20]

(9)

Calculations were first performed on the chloride starting material **(9)** as a way to verify validity of the methods used on the other compounds. The compound is known to the literature, and its orbital transitions have been extensively studied. The calculations performed revealed the lowest energy excited state being calculated almost exclusively to be a transition between HOMO and LUMO (97.12% contribution). The HOMO of **(9)** consists of the platinum d_{xz} orbital (36%) in a π-interaction with the phenyl of the pincer (18%) and the p_z-orbital of the chloride (37%), and the LUMO being mainly found on the pyridyls (69%), with some arene (22%), and a small contribution of metal d_{xz} character (7%).

So it is established that for **(9)**, as expected, the lowest energy excited state measured spectroscopically can be assigned as primarily an electronic transition from an occupied MO based on a π* interaction of the platinum d_{xz} with its ligand environment (Cl and arene π-system), to vacant orbitals situated primarily on the pincer ligand pyridyl orbitals.

The arylacetylene compounds

For all three of the new compounds, it was calculated that the lowest energy absorption remains a HOMO-LUMO transition. The LUMO for all three compounds appears relatively unchanged in nature, being situated primarily on the pincer ligand pyridyl groups, but also showing some pincer-phenyl and metal character. The energy of this orbital for each of the compounds remains virtually unchanged from that of **(9)**, with all four being calculated as approximately -2eV.

(9): -2.060 eV, **(13)**: -1.999 eV, **(14)**: -2.016 eV, **(15)**: -2.051 eV.

The HOMOs of each compound however are far more greatly affected by the ligand substitution.

As predicted, the π-interaction of the conjugated ligands, bridged by the acetylides appears to have the effect of enhancing the splitting of the metal d-orbital with which it is interacting, pushing the highest energy occupied π* component further into the frontier (i.e. reducing the HOMO-LUMO gap), and increasing the number of states into which it is split.

For **(13)**, due to the xy-plane orientation of the ring we can see the HOMO still consists of the platinum d_{xz}-orbital (19%) this time in a π* interaction with the delocalised phenylacetylene π-system (contribution 71%).

The higher energy of this orbital in relation to **(9)** offers an explanation for the red-shift measured spectroscopically, and this can be attributed to increased splitting of the d_{xz} ligand hybrid orbital through stronger π-interaction with the phenylacetylene than with the chloride. An increase in the energy of the π* orbital containing the d_{xy} is also seen to a lesser extent, potentially due to the π-interaction with the p_y-orbitals of the acetylide component. The energies of the occupied orbitals containing the d-orbitals that do not have the correct orientation for π-interaction with the phenylacetylide ligand (d_z^2 and d_{yz}) are relatively energetically unchanged, supporting that it is the π-interaction that is responsible for the orbital shifts observed.

Progressing to **(14)** and we see can see an explanation for the relatively small shift observed (**Figure 2.20** and **Figure 2.21**). Due to the orientation of the aromatic component of the ligand being in the xz-plane, the effect of the ligand π-system (84% of HOMO) interaction is now entirely upon the previously lower energy (due to lack of pincer π-interactions) platinum d_{xy}-orbital (9%). As a result, it is this orbital that is now most extensively split and has now become the HOMO (as opposed to the d_{xz}). The extent to which it has split (and hence extent to which the HOMO has risen) has indeed markedly increased due to the increased conjugation of the naphthalene fragment, but due to its lower energy pincer-ligand environment (and thus lower initial energy), the overall HOMO-LUMO gap decrease is only slight.

Concurrently we also see only a minor increase in energy for the d_{xz} ligand π* orbital, compared to what was seen for the arene, due to the now incorrect symmetry of this orbital to interact with the conjugated π-system.

The trend continues for **(15)**, with the orbital again containing the π*-interaction of the ligand (91%) with the d_{xy}-orbital (5%) (due to the xz-ligand orientation) becoming the HOMO, and being extensively split. Once more we see the extent of the conjugation having an effect, whereby for this compound the energy of the HOMO has increased again compared to the naphthalene.

As with the previous two compounds, the metal orbitals that lack the correct orientation to form π* interactions with the ligand remain relatively unchanged, and other than the d_{xy}, the orbitals of the anthryl and naphthyl compounds are very similar.

As a result of these interactions, a reasonable explanation for the spectroscopically observed pattern of red-shifting can be seen for these compounds, and fulfils the aim for this chapter, in improving our understanding of the occupied d-orbital-containing frontier-orbital energy levels to direct further manipulation. Substituting the fourth ligand position with aromatic acetylides appears to have the effect of causing π-interactions with the σ-non bonding d-orbitals with the correct symmetry-orientation. The result of this is a splitting of this orbital into various π and π* states, the highest energy of which is likely to form the HOMO. The greater the extent of delocalisation of the aromatic alkyne, the greater the degree of splitting in the resulting orbitals, and the higher the energy of the HOMO. For this series of compounds, a consistent LUMO energy is observed, and so the vast majority of the Red-shift can be assigned to the increasing HOMO energy.

HOMO Energies: (9): -5.689 eV, **(13)**: -4.961 eV, **(14)**: -4.816 eV, **(15)**: -4.476 eV

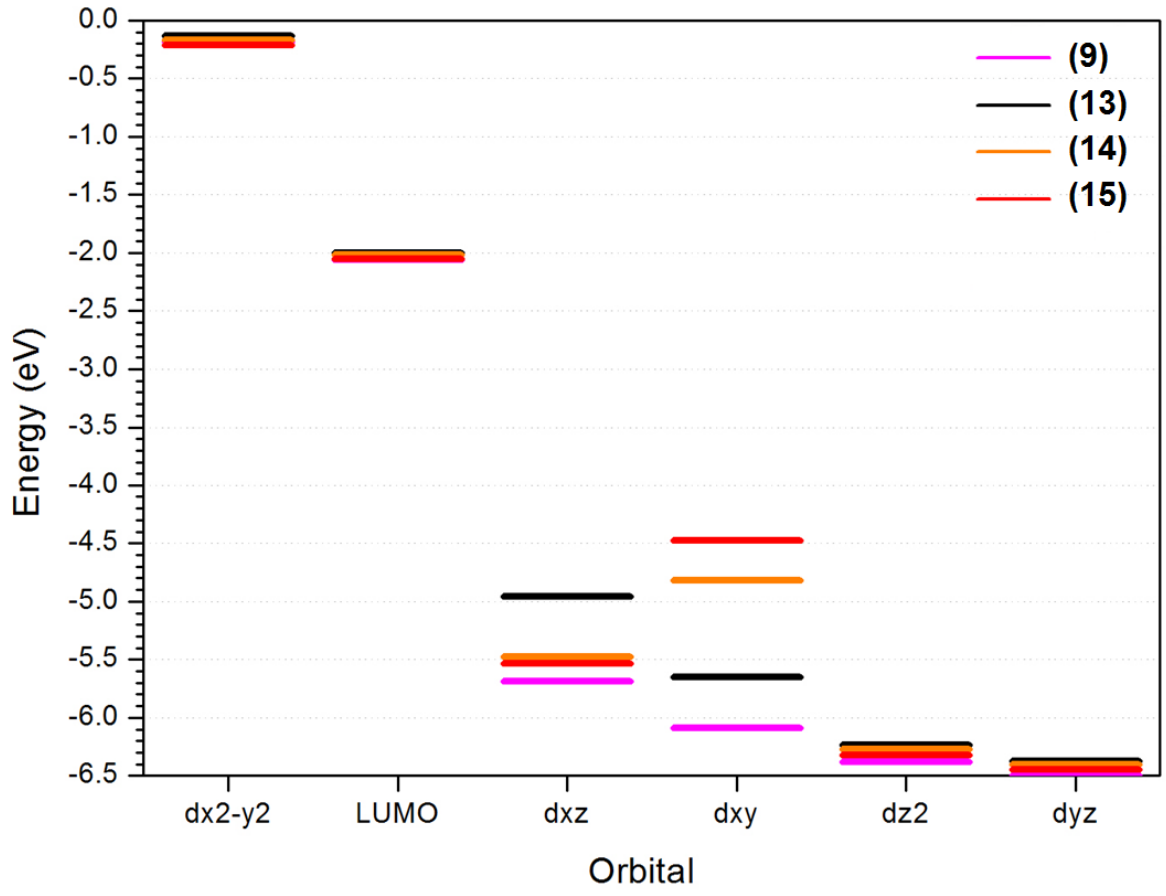

Figure 2.20. Energy diagram showing the energies of the highest energy metal-ligand π*-orbitals (+ LUMO). Labels dictate metal d-orbital component of orbital.

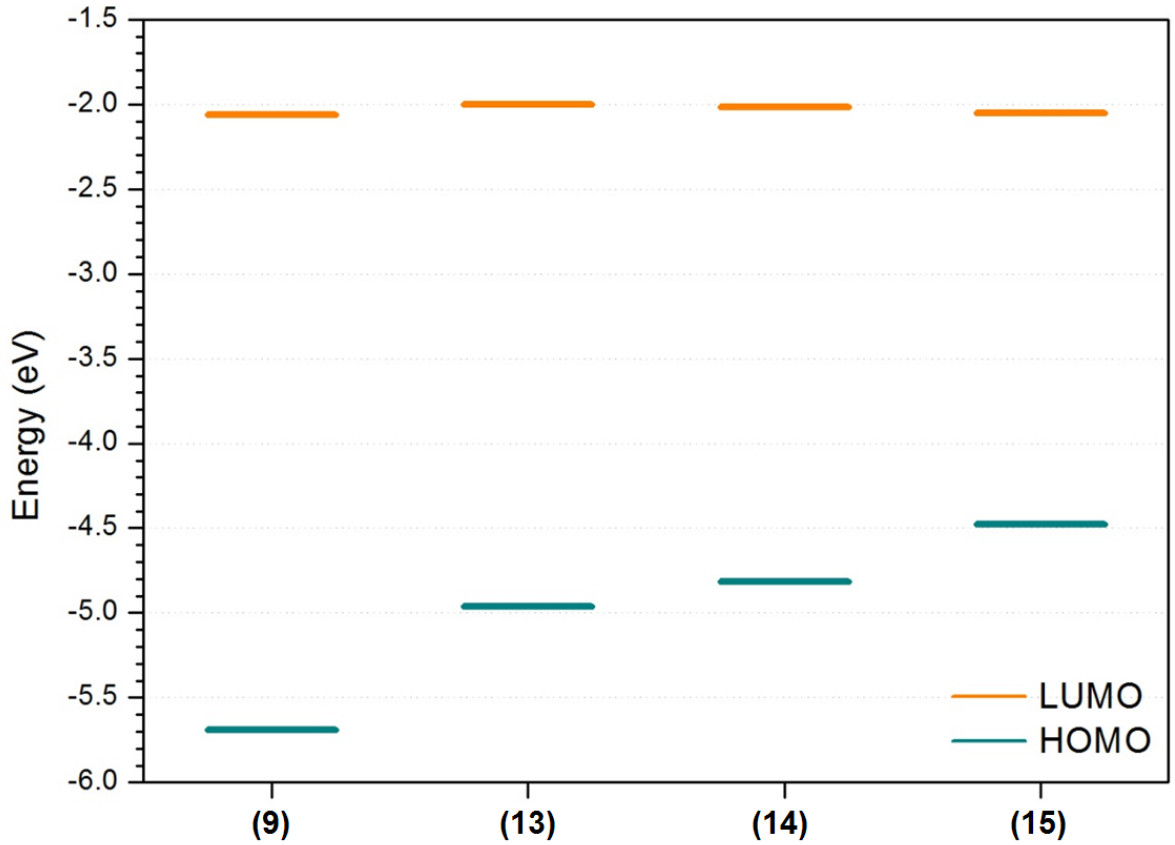

Figure 2.21. Energy diagram showing the HOMO-LUMO transitions of the four compounds.

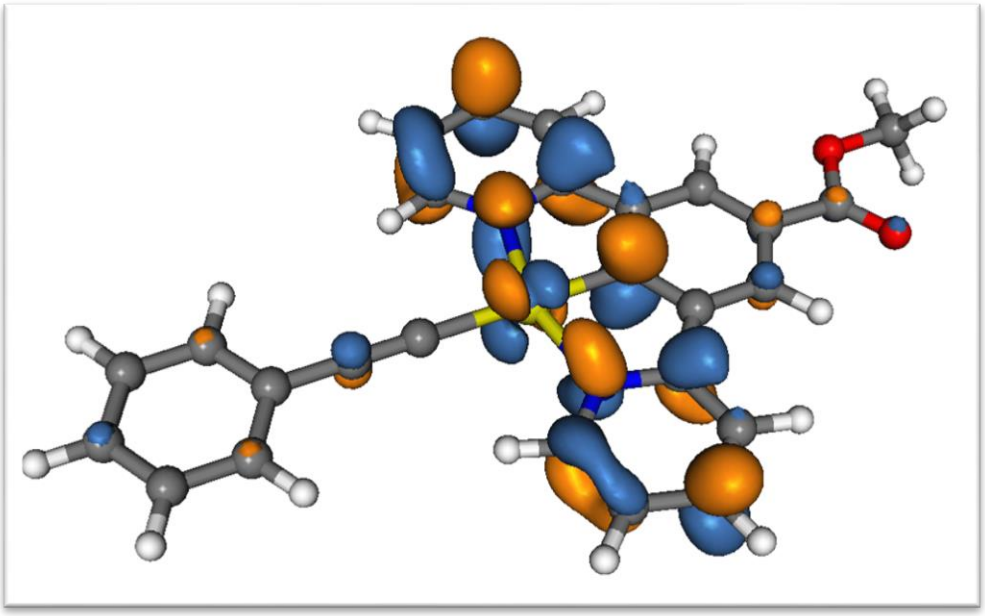

LUMO

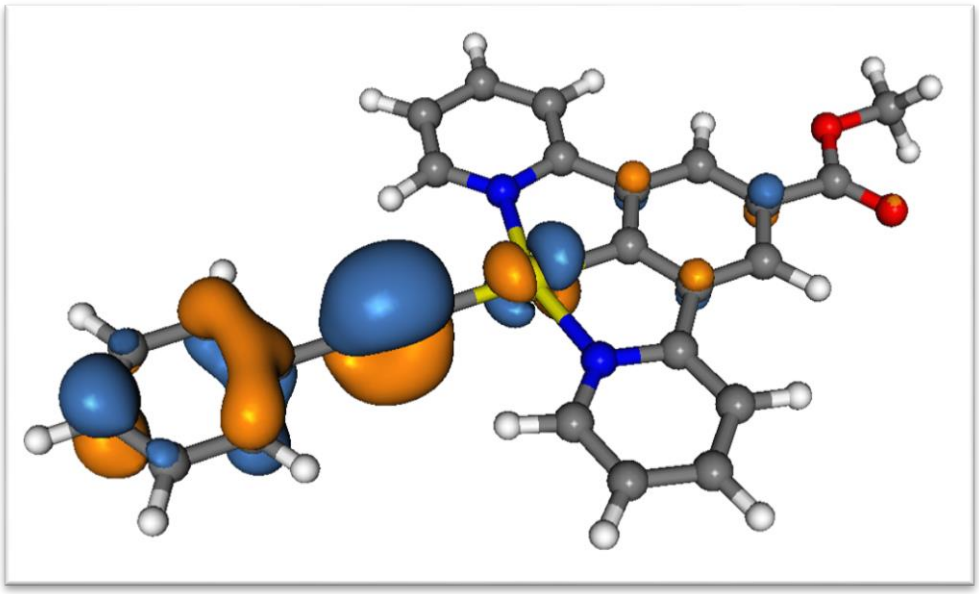

HOMO

Figure 2.22. Calculated HOMO and LUMO for 13.

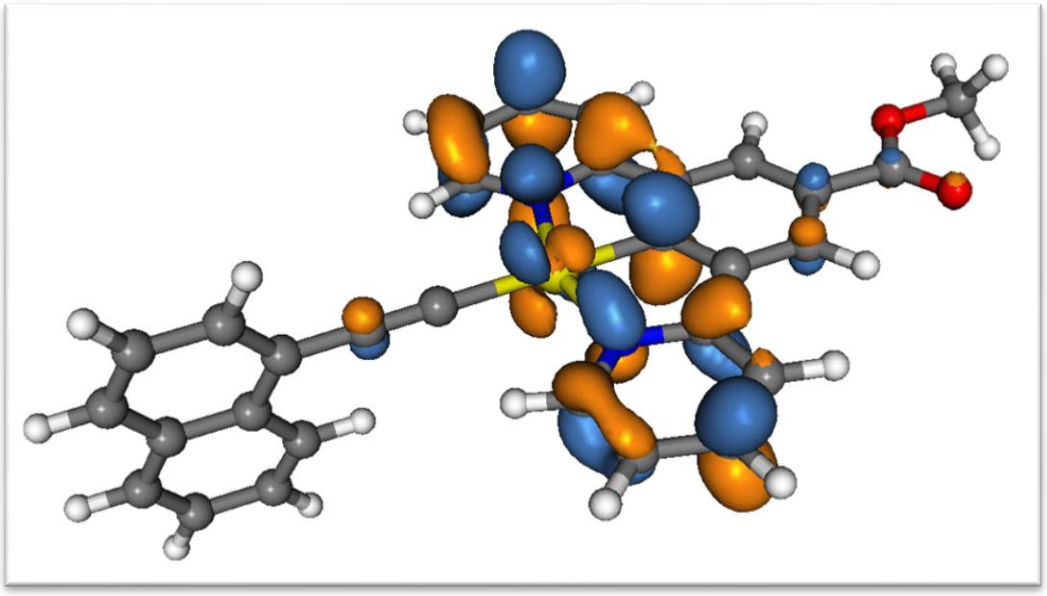

LUMO

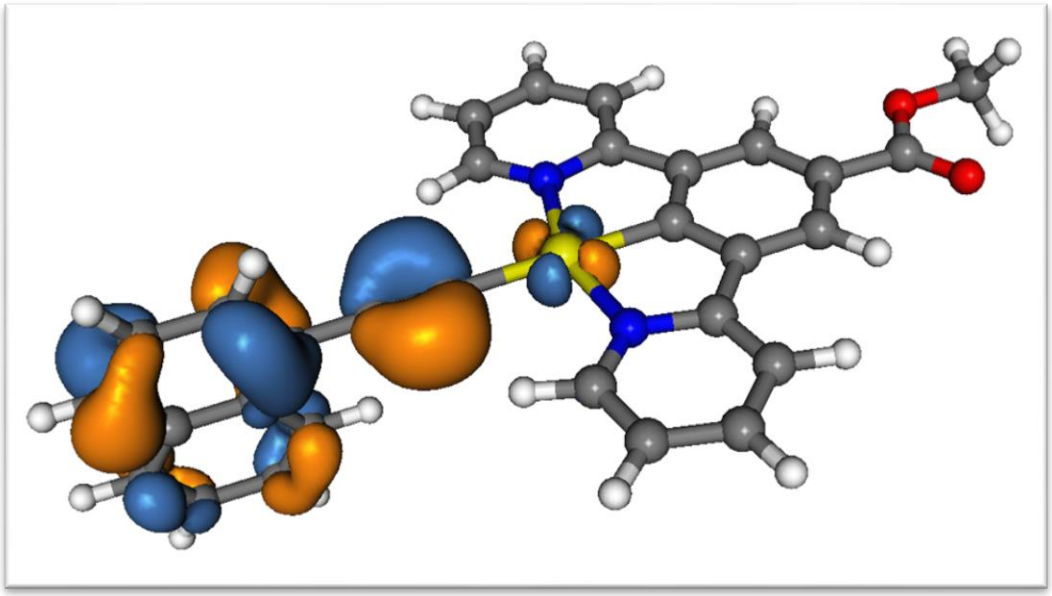

HOMO

Figure 2.23 Calculated HOMO and LUMO for 14.

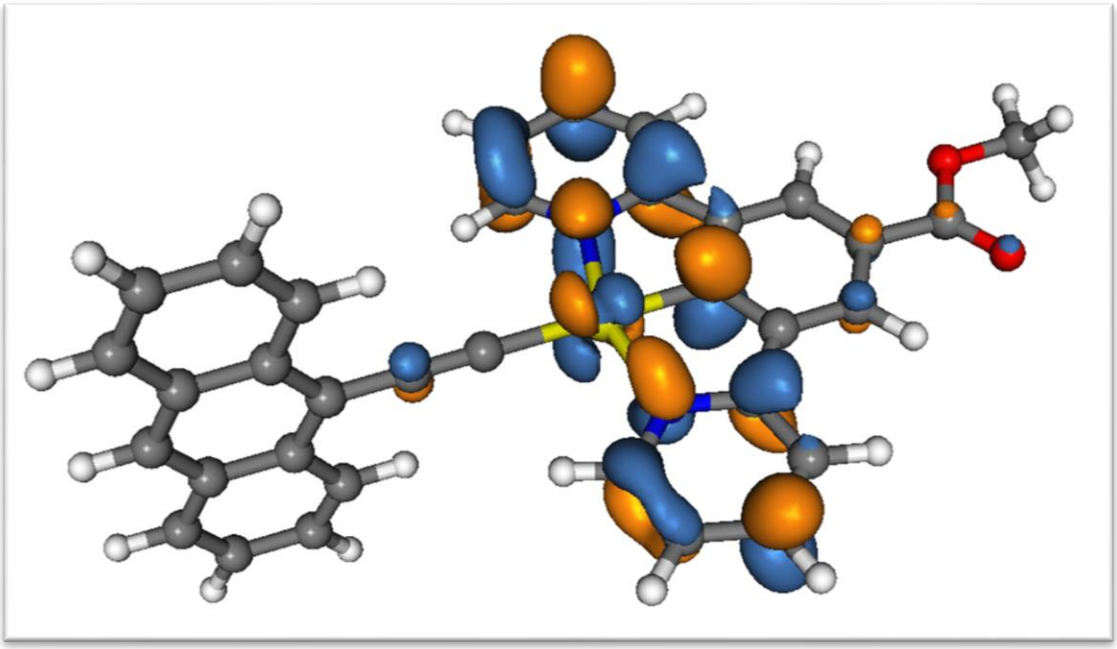

LUMO

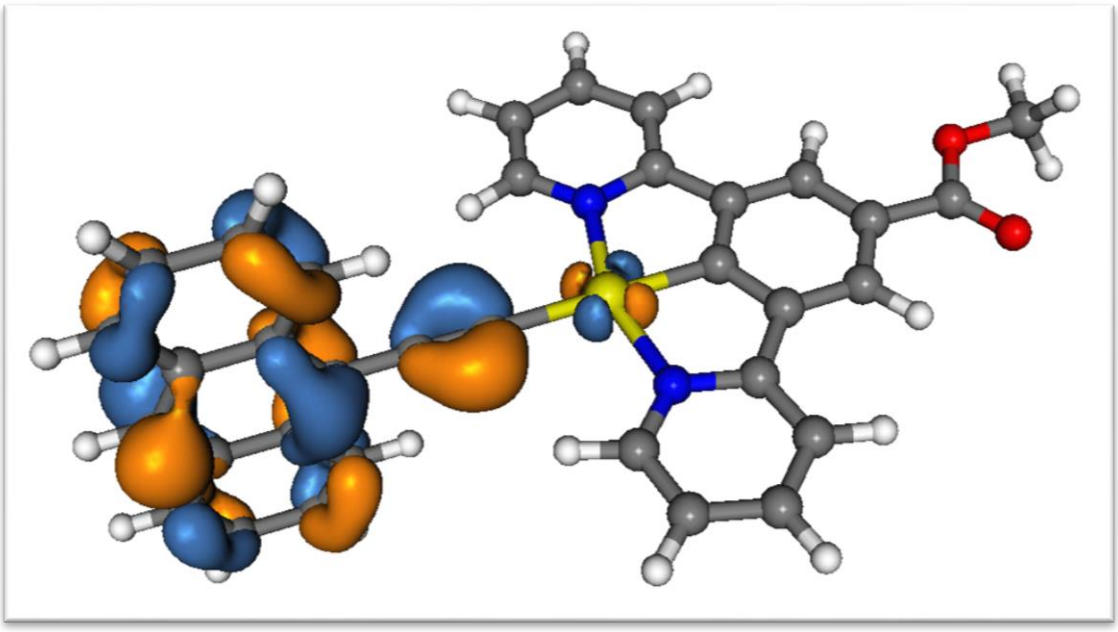

HOMO

Figure 2.24. Calculated HOMO and LUMO for 15.

2.8. Luminescence

The compounds are all luminescent at room temperature in solution (see quantum yields section), however, the spectra are rather more complex than for the absorption. It is immediately clear from the emission maxima that the simple trend of red-shifting with conjugation that is observed with the absorption spectra is not present.

In order to make a comparison between the compounds, the nature of the emission for each compound needs to be better understood, as the spectra show very different profiles, and so the spectra of each compound will be discussed individually to begin with.

Looking firstly again at **(9)** as an already well understood comparison (dashed line in **Figure 2.25**), the luminescence of this compound along with other variations have been assigned as originating from a ligand centred $^{3}\pi$-π^* state, and so essentially following the excitation of electrons onto the pincer ligand, the emissive stage of the decay occurs mainly within the ligand orbitals rather than in a transfer to the metal. This leads to a pronounced vibrational structure.[11,21] Also present in this compound and in other chloride derivatives is the formation of a low energy, broad, featureless excimer peak with increasing concentrations. This was also seen to become increasingly bright at the expense of the higher energy emission.

2.8.1 (13)

Moving to **(13)** from **(9)** (orange line in **Figure 2.25**), firstly, the emission maximum is red-shifted, and the peak profile is broader and less structurally defined, with a tail that extends further into low frequencies. Because many related examples have assigned emissive states as purely pincer based LC $^{3}\pi$-π^* character, it could be expected that the emission for this complex would be more closely related to that of **(9)** (with which it shares a pincer ligand), but it appears that the addition of the phenylacetylene fragment is in fact contributing to the emissive state. It was hypothesised that a return to the ^{3}MLCT emissive states assigned to analogous N^N^C compounds [22] may be a possible explanation for this shift, as this would allow for inclusion of the platinum-acetylide fragment. However, the emission proved to show a very weak and somewhat negative solvatochromic response (in THF, DCM, acetone and acetonitrile), which is highly indicative of a LC state.[21] It would appear, therefore, that the ^{3}LC state is retained, but is experiencing some contribution from the phenylacetylene fragment. The spectrum also differs in that no excimer peak is present in this compound with increasing concentration. This provides additional evidence that the nature of the emissive state has changed somewhat for this complex.

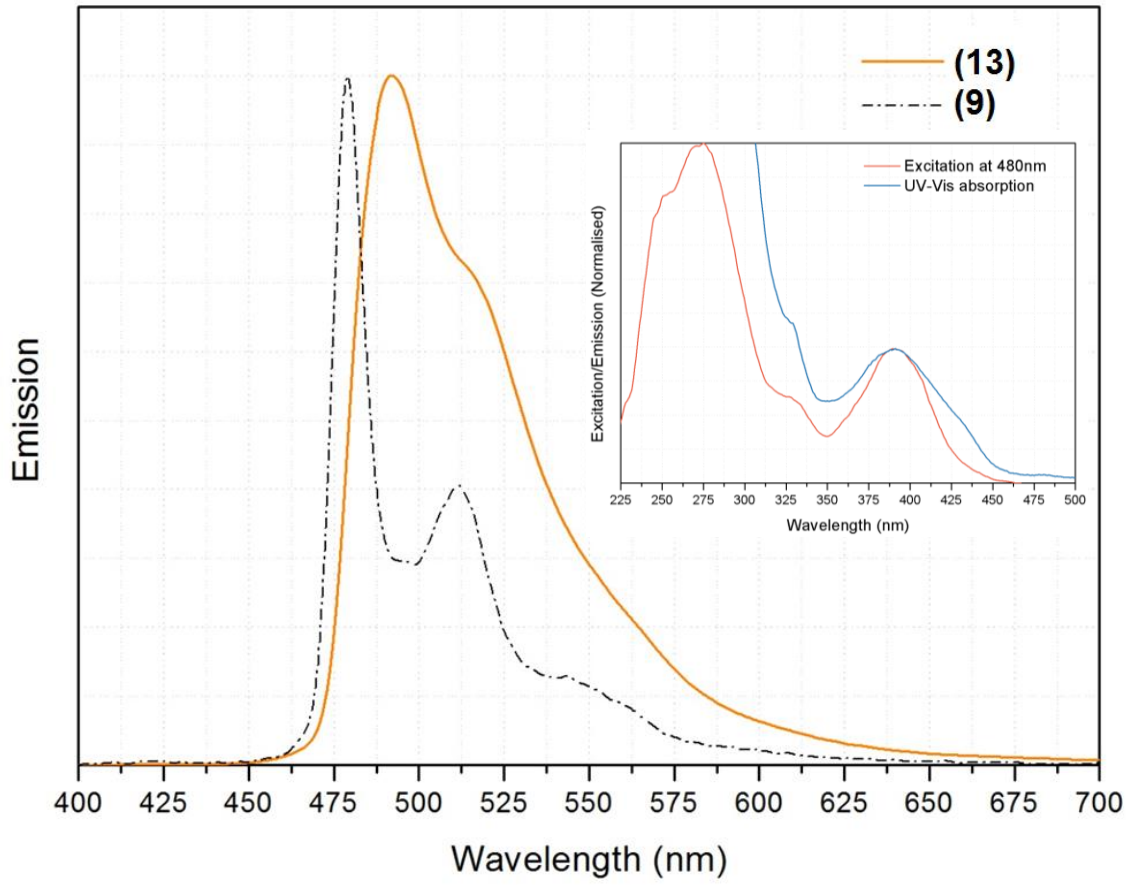

Figure 2.25. Emission spectrum of (13) (orange) and (9) (dashed) in dilute dichloromethane solution ($1x10^{-7}$ mol dm^{-3})

2.8.2 (14)

From **Figure 2.26** it can be seen that the emission of **(14)** has returned to almost the same frequency to that of **(9)**, and regained the defined structural features, seeming to indicate a return to a pure pincer based ^{3}LC emission. The reason the transition from phenylacetylene to naphthylacetylene causes the emissive state to revert back in this way is not immediately clear, though it may be a steric issue. As discussed previously, the lowest energy position for the phenyl ring is in-plane with the pincer. The naphthalene, however, is too sterically bulky to adopt this position, instead preferring a perpendicular orientation. This lack of co-planarity with the pincer may be the driving force behind the lack of contribution to the emissive state seen for this complex.

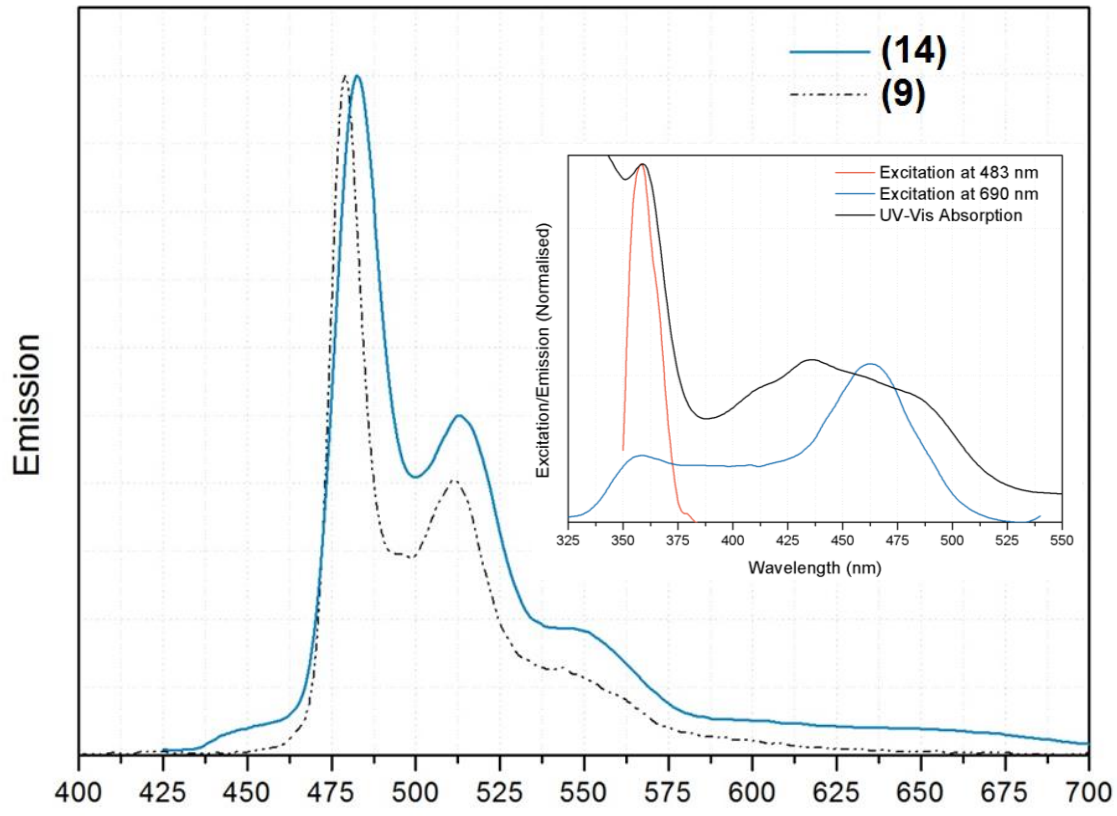

Figure 2.26. Emission spectrum of (14) (blue) and chloride starting material (dashed) in dilute dichloromethane solution ($1x10^{-7}$ mol dm^{-3}). Excitation at 375nm, λ_{max} = 482.5nm.

Similarly, a return to excimeric behaviour with increasing concentrations is also observed (**Figure 2.27** and **Figure 2.28**). In thoroughly degassed dichloromethane solution an intense broad featureless peak at λ_{max} = 685nm appears at the expense of the monomeric emission with increasing concentration, and extends well into IR frequencies. Because of this slow transition between purely monomeric (blue/green) and purely eximeric (red) with concentration, an interesting result of this is the ability to essentially tune the emissive frequency of the solution with concentration to almost any position in the visible spectrum. There is also a significant inner filter effect observed with increasing concentration. While the emission at 483 and 690 nm appear from the excitation spectra to be of different origin, both match well with part of the absorption spectrum.

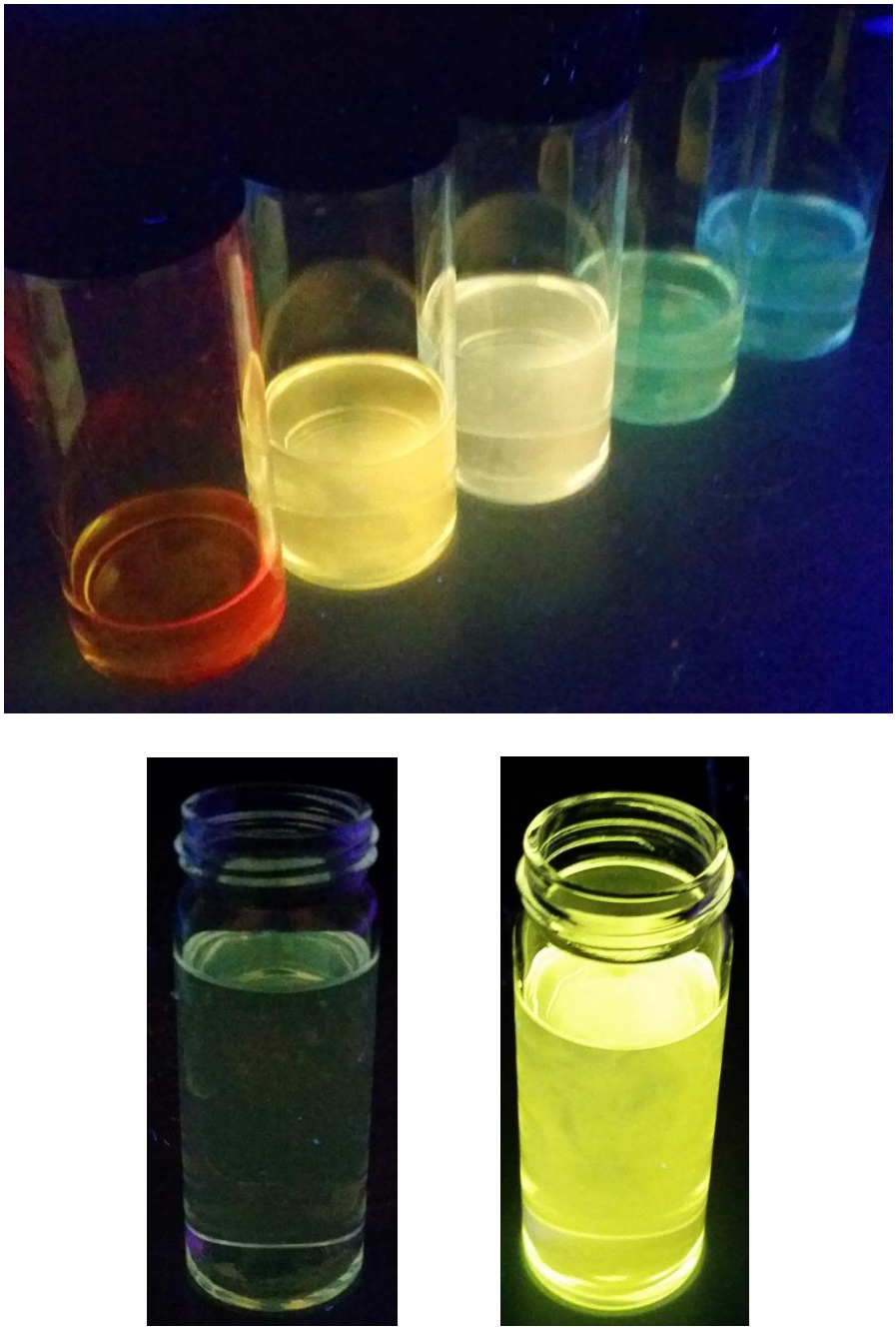

Figure 2.27. Top: Dichloromethane solutions of (14), in decreasing concentration from left to right. Bottom: Dichloromethane solution of the compound before (left) and after (right) degassing, demonstrating the emission's sensitivity to oxygen.

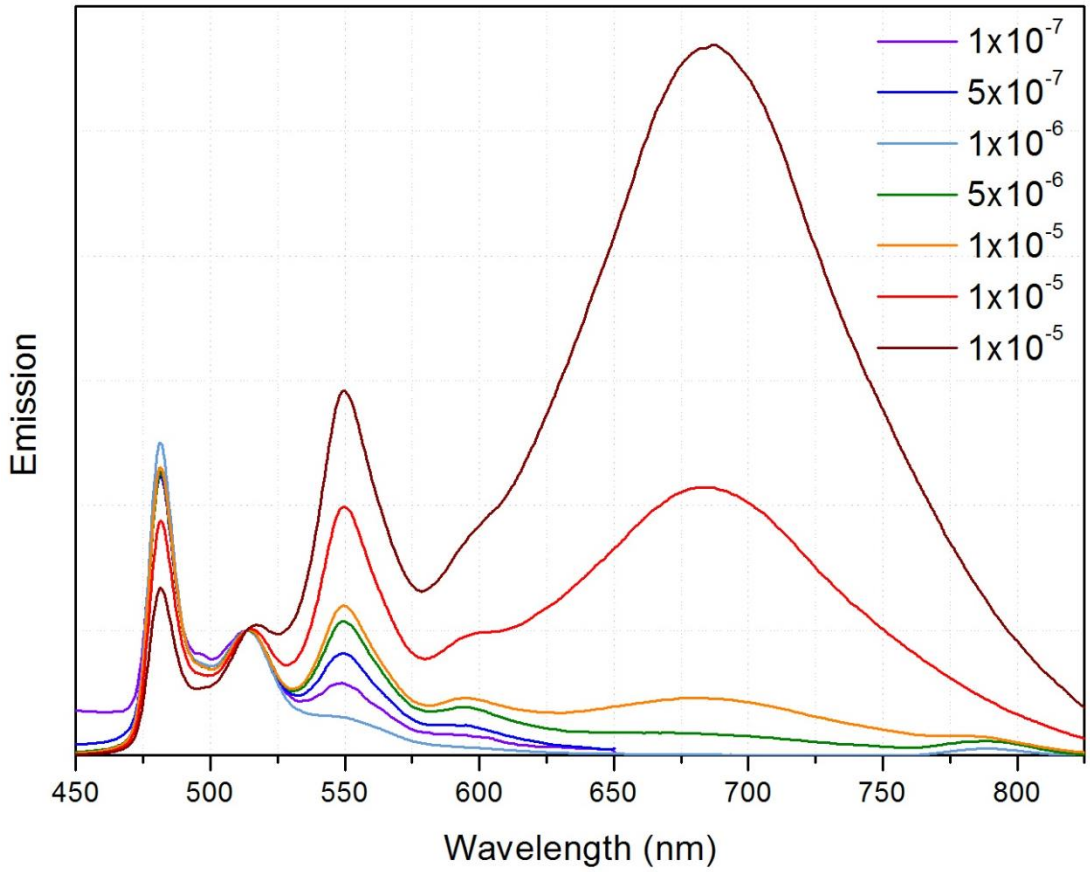

Figure 2.28 - Emission spectrum of (14) at 400nm excitation, with variable concentrations demonstrating excimer formation. Normalised to peak at 550nm.

2.8.3 (15)

The emissive properties of **(15)** (red line in **Figure 2.29**) in dilute dichloromethane solution again shows a similar profile to that of **(9)**, and λ_{max} at essentially the same energy as **(14)**. However, there is a significant set of higher energy peaks present at 409nm and 433nm, which could perhaps be assigned to an isolated ^{1}LC state on the ethynyl anthracene fragment itself. Evidence for this lies in the comparison to the spectrum of free trimethylsilylethynylanthracene, which has a very similar emission energy and structural profile, also indicating that the emission is likely to be fluorescent in origin. Additionally by observing the excitation spectra for the peaks at 410 and 482 nm it can clearly be seen that not only do the emissions originate from the same absorption, but that these correspond to the lowest energy absorption present in the UV-Vis, eliminating the possibility of the fluorescence peaks resulting from impurity in the sample.

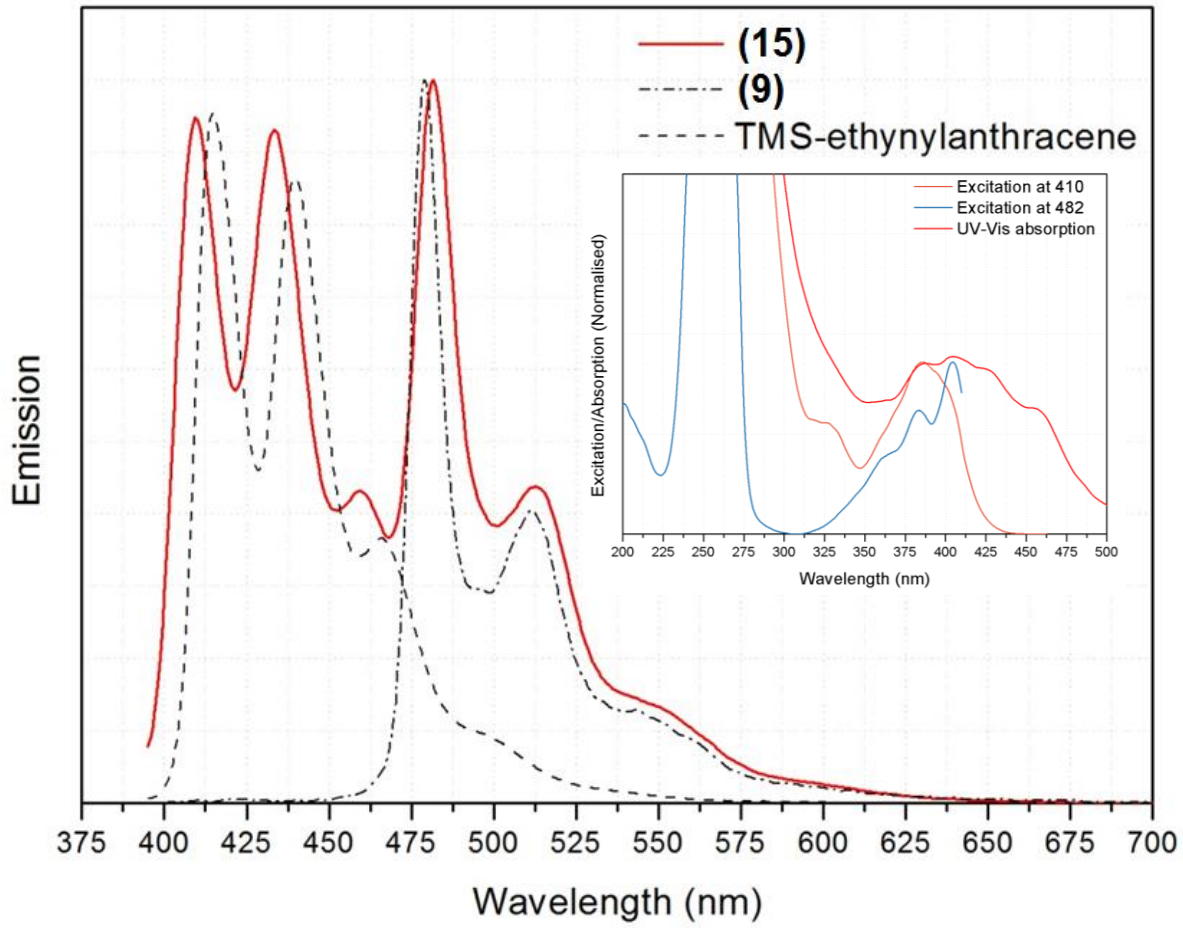

Figure 2.29. Emission spectrum of (15) (red), (9) (dot-dashed), and free trimethylsilylethynylanthracene in dilute dichloromethane solution ($1x10^{-7}$ mol dm^{-3}).

Excitation at 375nm, λmax = 482nm (compound).

No excimeric emission is observed with concentration increase, although the fluorescent emission peaks fall off steeply in favour of the ^{3}LC pincer emission, due to inner filter effects. The lack of excimer here is potentially due to the steric bulk of the anthracene fragment preventing effective intermolecular interaction.

Variable concentration emission spectroscopy of **(15)** can be seen in **Figure 2.30**.

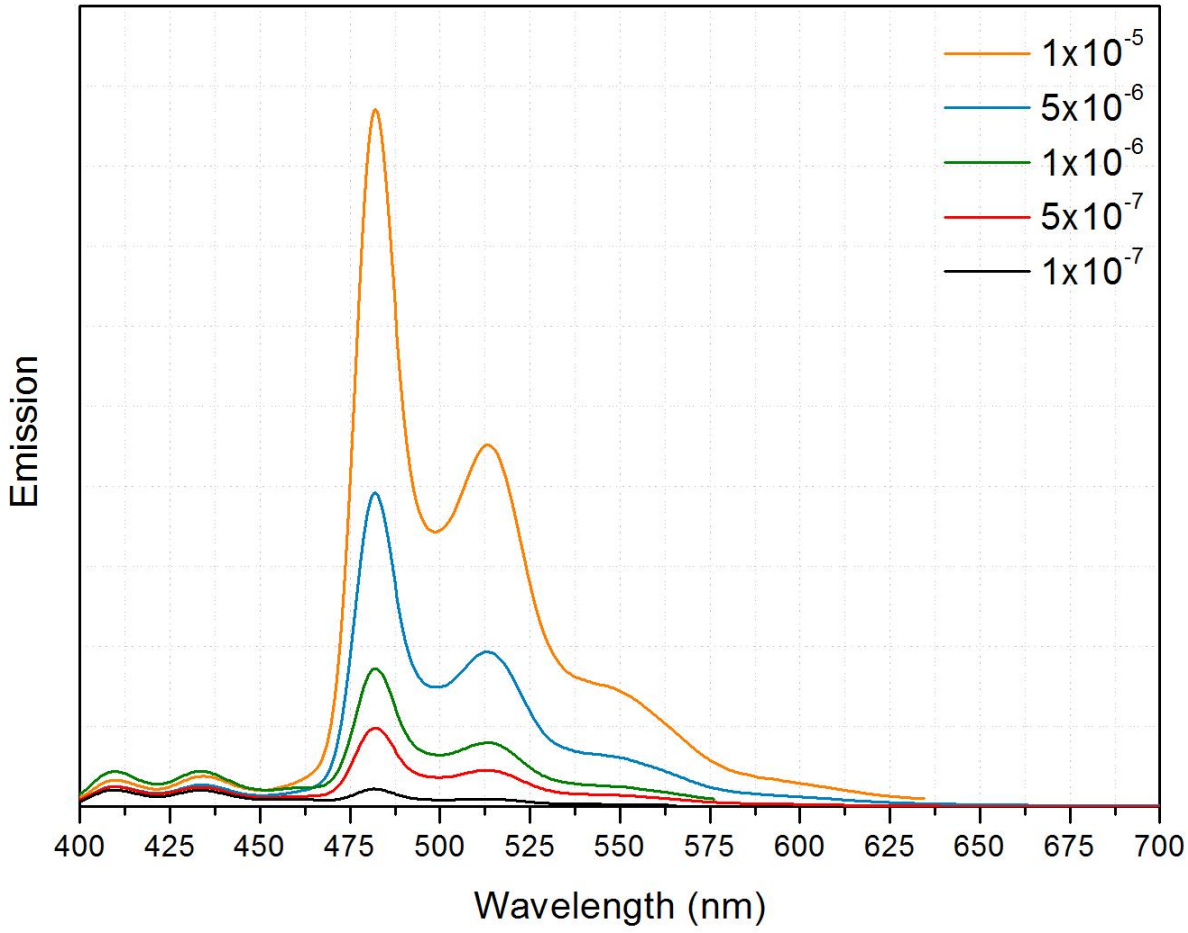

Figure 2.30. Emission spectrum of (15) at 375nm excitation, with variable concentrations demonstrating suppression of fluorescence peaks.

2.8.4 Quantum yields.

Measuring quantum yields accurately is a very difficult procedure, and with the limited equipment available, the measurements in this section are only approximate estimates with low confidence in their accuracy. What they can do is provide a simple comparison between the complexes and give a general feel to their emissive efficiencies. The approximations were made by using a graphical comparison method with a known standard. Due to its similarity to the compounds (both physically and spectroscopically) a comparison to **(9)** was chosen as opposed to a more traditional standard such as fluorecein in 1M $NaOH_{(aq)}$. This was essentially in attempt to eliminate cumulative errors produced by having highly different excitation and emission frequencies (all the compounds, including the chosen standard emit within a relatively tight band, and from the same excitation frequency) and from different solvent absorption and refractive indices. **(9)** is highly emissive and has been previously accurately assigned φ_{lum} = 0.56 in degassed dichloromethane.[11]

The procedure used to approximate the quantum yields was to record absorption and emission spectra for a set of degassed dichloromethane solutions of each compound through a concentration series, while keeping the instruments in identical settings for each compound. The integral of each emission spectrum was then calculated, and this was plotted against the absorption at the shared excitation frequency of (395nm). This produced a series of straight line plots for the compounds along with the standard. The gradients of these linear plots for the compounds were then used to calculate the approximate quantum yields by comparing to that of the standard using **Equation 1**.

$$\varphi_x = \varphi_{st} \left(\frac{Gradient_x}{Gradient_{st}} \right) \left(\frac{\eta_x^2}{\eta_{st}^2} \right)$$

Equation 1. Formula used for calculating quantum yields, where ϕ_x and ϕ_x = the quantum yields of the compound and standard respectively, and η_x and η_{st} = the refractive index of the solvents.

(9)	Φ= 0.56
(13)	Φ= 0.16
(14)	Φ=N/A
(15)	Φ=0.08

Some problems were encountered while carrying out this comparison however.

Firstly, no quantum yield has been provided for **(14)**. This was due to excimeric behaviour of the compound, and as such the quantum yields for the two emissive mechanisms need to be determined. However due to strong inner-filter problems this was not possible without acquiring low path-length cuvettes, and re-recording data.

The second problem encountered was the slight self-quenching/inner filter effect seen in **(15)**, leading to a gentle curve away from the straight line after concentrations of $1x10^{-6}$ mol dm^{-3}. In response to this, the initial slope was taken to provide the quantum yield, although this factor needs to be taken into account when analysing the compound's emissive properties.

As stated earlier the quantum yields given are an approximation only due to the limitations of the method and equipment used, however they do show that the compounds are indeed fairly emissive, and show a trend towards lower efficiency with bulkier substitutions.

2.9 Summary of results and conclusions

The aim for the work presented in this chapter was to establish a thorough understanding of the electronic properties of the platinum N^C^N pincer system, so that this knowledge could be used to direct the design of potentially useful systems in which there is some external control over the optical properties.

It has been established that π-interactions of the surrounding ligand environment offers a convenient way in which changes can be made to the occupied metal d-orbital containing HOMO orbital energies. As predicted by ligand field theory, the d_{xz} and d_{xy} orbitals in out-of-phase combination with the surrounding ligand environment made up the HOMOs for the new compounds synthesised, and it has been shown that by influencing the π-donor properties of the fourth coordinating ligand, changes can be made to the energies of these orbitals, without affecting the LUMO.

It has also been confirmed that that the orientation of this ligand is important, in that the π-system will influence the orbital with the corresponding symmetry, and as such to influence a particular orbital, steric hindrance and minimum energy position need to be taken into account to ensure π-donation occurs in the desired plane.

The result of the knowledge gained is that some control over the HOMO-LUMO gap has been established, and using π-interactions as a method of explicitly manipulating HOMO orbitals of these systems in order to produce functional materials seems plausible.

It has also been confirmed that these orbitals can be affected at a distance via an acetylide "bridging ligand". This result opens up a useful protocol in directing future synthetic routes to introduce tunablility into these systems. Given that changes to π-donor properties of substituent ligands may be spread onto the HOMO orbitals through these bridges, a whole host of potential ligands with inherent switchability could be proposed to impart tuneable functionality to the HOMO orbitals across this bridge, and as a result provide a visual or luminescent response to a variety of stimuli.

Other routes to potential optical property manipulation may also be targeted using the knowledge gained . As mentioned in **Chapter 1**, d_z^2 - d_z^2 intermolecular interactions have been shown to induce large shifts in optical properties, with HOMO-LUMO gaps having a high sensitivity to overlap. In order to facilitate such interactions however, the non-bonding d_z^2 orbitals need to lie close to the frontier orbitals, such that linear combinations create new higher energy MMLCT HOMOs.

In this chapter we have established that the two highest lying occupied orbitals (d_{xz} and d_{xy}) have a significant sensitivity to the π-donor properties of the ligand environment, and so it is proposed that by incorporating a ligand with poor π-donor properties, or π-acceptor properties into the fourth coordination site of the metal, we may stabilise these orbitals, and in doing so bring the frontier towards the d_z^2 orbital (typically the HOMO-2). This may then facilitate intermolecular interactions as a route towards colour tuning.

It is this route that was attempted first, the results of which can be seen in **Chapter 3**.

2.10 References

(1) Soderberg, T.; Larsen, D.; Larsen, P. D., Ed. University of California Davis; Vol. **2014**.

(2) Fleming, I.; Williams, D. *Spectroscopic Methods in Organic Chemistry*; 6th ed.; McGraw-Hill Education, **2008**.

(3) Roberts, J. D.; Caserio, M. C. *Basic Priciples of Organic Chemistry*; 2 ed.; W. A. Benjamin, **1977**.

(4) Atkins, P.; Overton, T.; Rourke, J.; Weller, M.; Armstrong, F.; 4th ed.; Oxford University Press: **2006**, p 468.

(5) Belijonne, D.; Wittmann, H. F.; Kohler, A.; Graham, S.; Younus, M.; Lewis, J.; Raithby, P. R.; Khan, M. S.; Friend, R. H.; Bredas, J. L. *J. Chem. Phys.* **1996**, *105*, 3868.

(6) Sotoyama, W.; Satoh, T.; Sato, H.; Matsuura, A.; Sawatari, N. *The Journal of Physical Chemistry A* **2005**, *109*, 9760.

(7) Yam, V. W. W., Wong, K.M.C *Top Curr Chem* **2005**, *257*, 1.

(8) Castellano, F. N.; Pomestchenko, I. E.; Shikhova, E.; Hua, F.; Muro, M. L.; Rajapakse, N. *Coordination Chemistry Reviews* **2006**, *250*.

(9) Sonogashira, K.; Tohda, Y.; Hagihara, N. *Tetrahedron Letters* **1975**, *16*, 4467.

(10) Stille, J. K. *Angewandte Chemie International Edition* **1986**, *25*, 508.

(11) Williams, J. A. G., Beeby, A., Davies, E.S., Weinstein, J.A., Wilson, C. *Inorg. Chem.* **2003**, *42*, 8609.

(12) Chen, Y.; Li, K.; Lu, W.; Chui, S. S.-Y.; Ma, C.-W.; Che, C.-M. *Angewandte Chemie International Edition* **2009**, *48*, 9909.

(13) Devi, L. S., Al-Suti, M.K, Zhang, N, Teat, S.J, Male, L, Sparkes, H.A, Raithby, P.R, Khan, M.S, Kohler, A. *Macromolecules* **2009**, *42*, 1131.

(14) Khan, M. S., Al-Suti, M.K, Al-Mandhary, M.R.A, Ahrens, B, Bjernemose, J.K, Mahon, M.F, Male, L, Raithby, P.R, Friend, R.H, Kohler, A, Wilson, J.S *Dalton Trans.* **2002**, 65.

(15) Bio-Rad; Bio-Rad/Sadtler IR Data Collection: Philadelphia, p FTIR.

(16) Sigma-aldrich **2011**.

(17) Khan, M. S., Al-Suti, M.K, Al-Mandhary, M.R.A, Ahrens, B, Bjernemose, J.K, Mahon, M.F, Male, L, Raithby, P.R, Friend, R.H, Kohler, A, Wilson, J.S. *Dalton Trans.* **2002**, 65.

(18) Berenguer, J. R., Lalinde, E, Torroba, J. *Inorg. Chem.* **2007**, *46*, 9919.

(19) Rengifo, E. A.; Murillo, G. *Revista de ciencias* **2012**, *16*, 117.

(20) Wheeler, D. E.; Rodriguez, J. H.; McCusker, K. *J. Phys. Chem. A* **1999**, *103*, 4101.

(21) Farley, S. J.; Rochester, D. L.; Thompson, A. L.; Howard, J. A. K.; Williams, J. A. G. *Inorg. Chem.* **2005**, *44*, 9690.

(22) Lu, W.; Mi, B.-X.; Chan, M. C. W.; Hui, Z.; Che, C.-M.; Zhu, N.; Lee, S.-T. *Journal of the American Chemical Society* **2004**, *126*, 4958.

Chapter 3: Platinum N^C^N pincer cyanides

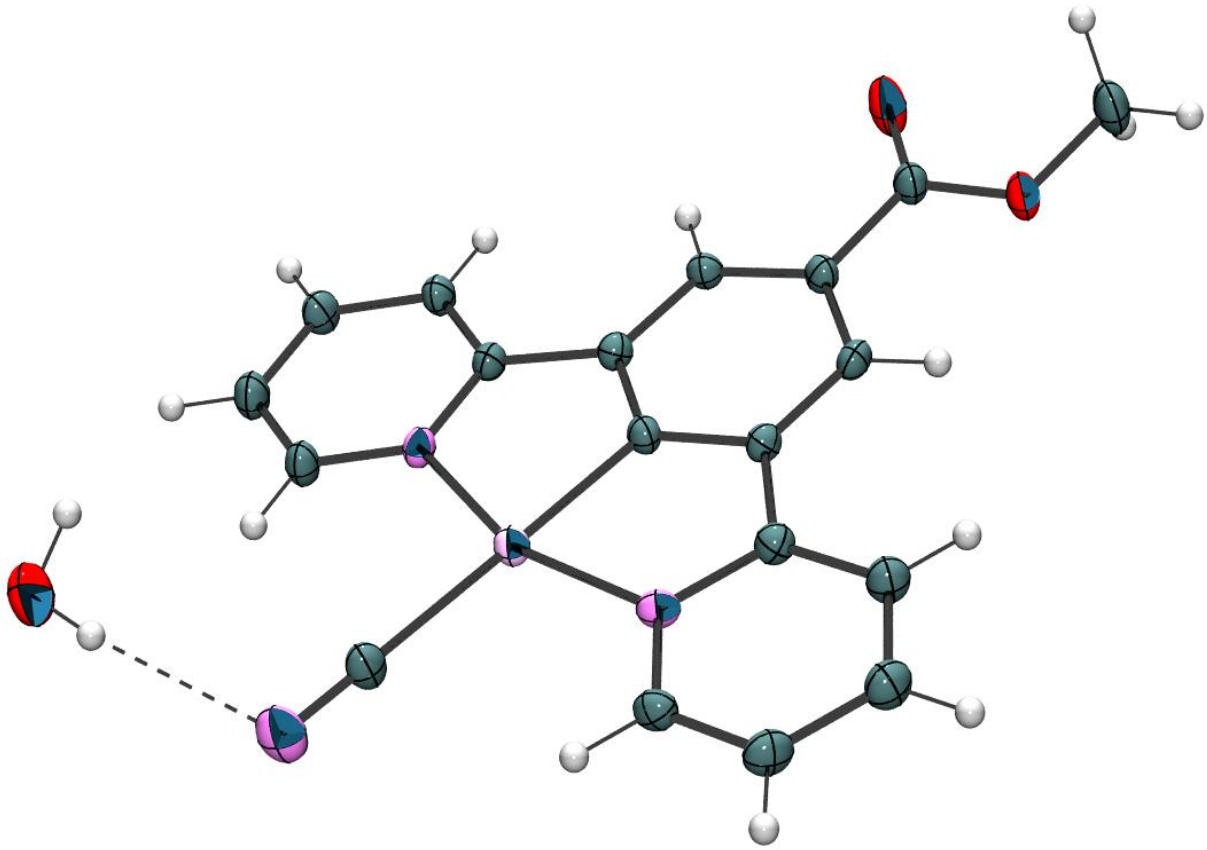

Abstract.

At the end of **Chapter 2** it was discussed that a possible route towards developing switchable platinum pincer systems would be to try and facilitate d_z^2 - d_z^2 intermolecular interactions with poor π-donor ligands.

In the work presented in this chapter, a series of new platinum N^C^N pincer compounds incorporating the small, strong field, cyanide ligand, into the fourth coordination site was synthesised in the hope that d_z^2 -d_z^2 interactions could be facilitated.

This proved to be the case, and four new strongly coloured complexes with optical properties highly sensitive to the degree of intermetallic interaction was the result. Three of these compounds exhibited a rapid vapochromic response with unprecedented speed of transition, and one thermochromic compound also resulted from this study.

By analysing these compounds in the solid-state using spectroscopic, crystallographic and computational techniques, evidence has been presented that the cyanide ligand serves as both a hydrogen bonding site for solvent uptake, resulting in structural rearrangement, and as a facilitator for colour switching resulting from d_z^2-d_z^2 interactions by allowing for a prominent non-bonding d_z^2 orbital relative to the frontier.

All the systems studied crystallographically have shown a proportional response in the absorption and emission spectra (in the form of a red-shift) to the degree of intermetallic d_z^2 - d_z^2 overlap, and that the degree of overlap can be influenced by crystal structure changes upon absorption/desorption of solvent vapours. These findings have also been confirmed using solid state TD-DFT calculations.

Alongside the cyanide ligand, the importance of the functionalisation of the pincer ligand in directing crystal packing has also been investigated. It has been established that the weak intermolecular interactions provided by an ester group appear to contribute to rapid, and reversible transitions for these compounds

These findings have produced a possible protocol for developing highly selective, and rapidly responding solvent/vapour sensors.

3. Platinum N^C^N pincer cyanides

3.1 Introduction.

3.1.1 The cyano-ligand

The cyano-ligand is simply an sp-hybridised carbon triply bound to a nitrogen. For a closed shell configuration the cyanide requires a negative charge on the carbon atom, and is thus an ionic ligand. Cyano-ligands are small, strong-field ligands and are both highly basic and nucleophillic. Cyano ligands also tend to have strong π-backbonding interactions with late transition metals, usually resulting in stable compounds with strong bonds to the metal centres.[1]

3.2 Objectives and strategy

As mentioned in **Chapter 1**, one of the potential routes by which a new platinum pincer compound may be made tuneable, or have its optical properties altered, is to exploit intermolecular interactions in the solid state. In related systems the planarity and conjugation of the platinum pincer moiety has induced stacking in the solid state leading to π-π interactions, and has also produced structures exhibiting various degrees of Pt-Pt d_z^2 overlap, resulting in new low-energy electronic transitions (metal-metal-to-ligand charge transfer or MMLCT) and red shifted phosphorescence.[2-4] Minor changes in Pt-Pt overlap have been shown to be highly effective in altering frontier-orbital energies, offering a promising route for the creation of tuneable optical properties, and compounds with potential applications as optical/luminescent sensors for a variety of conditions/environmental variables.[5,6]

In **Chapter 2**, direct manipulation of the HOMO through varying π-interactions of the R-group with the platinum orbitals was studied as a potential means to tune the colour of the systems.

The work in this chapter investigates using Pt-Pt d_z^2 intermolecular interactions in the solid-state as a route to achieving the target of producing materials with alterable optical properties in platinum pincer complexes.

As also mentioned in **Chapter 1**, the ligand occupying the fourth coordination site of the platinum has been shown to have a significant influence both in altering the solid state aggregation in related compounds, and in facilitating intermolecular Pt-Pt interactions. For this reason it was decided that selecting an appropriate ligand for this site in order to try to direct intermolecular interaction was a sensible approach.[4,7]

The cyanide group was selected as a target ligand for several reasons:

- The cyanide is a small ligand, and so unlike the polyaromatic alkyne ligands discussed in **Chapter 2**, steric hindrance to intermolecular/planar/stacking arrangements is not likely be an issue.

- The cyanide unit, like the acetylide ligands described in **Chapter 2** is sp-hybridised and thus we can expect to see π-interaction with the platinum to continue to occur through both xz and xy planes.

- The ligand exhibits an extremely strong ligand-field, and as such is likely to continue to promote luminescence in the compound by displacing the antibonding $d_{x^2-y^2}$ orbital (known to quench emissive states) to inaccessible energies. [8,9,10,11]

- The second consequence of the cyanide's position in the spectrochemical series, and most important reason for choosing this ligand, is its lack of π-donor properties and strong π-accepting nature. As discussed in **Chapter 2**, depending on the nature and symmetry of the ligand environment of transition metal coordination complexes, the non-bonding occupied metal d-orbitals of the σ-only ligand field model may be shifted and reshuffled by further π-interactions, given that the interacting orbitals have the correct symmetry (example in **Figure 3.1**). It was also discussed that the coordination of the pincer ligand alone provides the platinum with an asymmetric environment with respect to the degree of π-donor/π-acceptor interactions, resulting in the different d-orbitals interacting differently with the fourth ligand substitution position. We have already seen that the result of π-overlap between a metal d-orbital and an increasingly conjugated aromatic π-system causes an increasing destabilisation of the π* hybrid orbital formed, red-shifting the lowest energy absorption. We have also seen that only the d_{xz} and d_{xy} orbitals possess the correct symmetry to interact with the ligand at the fourth position, and that the π* hybrids formed through this interaction with the occupied ligand π-orbitals tend to exist as the HOMO as a result.
  The cyanide however, is likely to provide far less destabilisation to these orbitals due to its position in the spectrochemical series, and may, in fact, act to stabilise them somewhat. The result of stabilising these orbitals would be firstly to blue-shift the lowest energy transition, but this would also serve to bring the frontier closer to the relatively ligand independent d_{z^2}-orbital, which is an orbital that, as mentioned previously, can have significant effects on the optical properties of such compounds through intermolecular interactions.

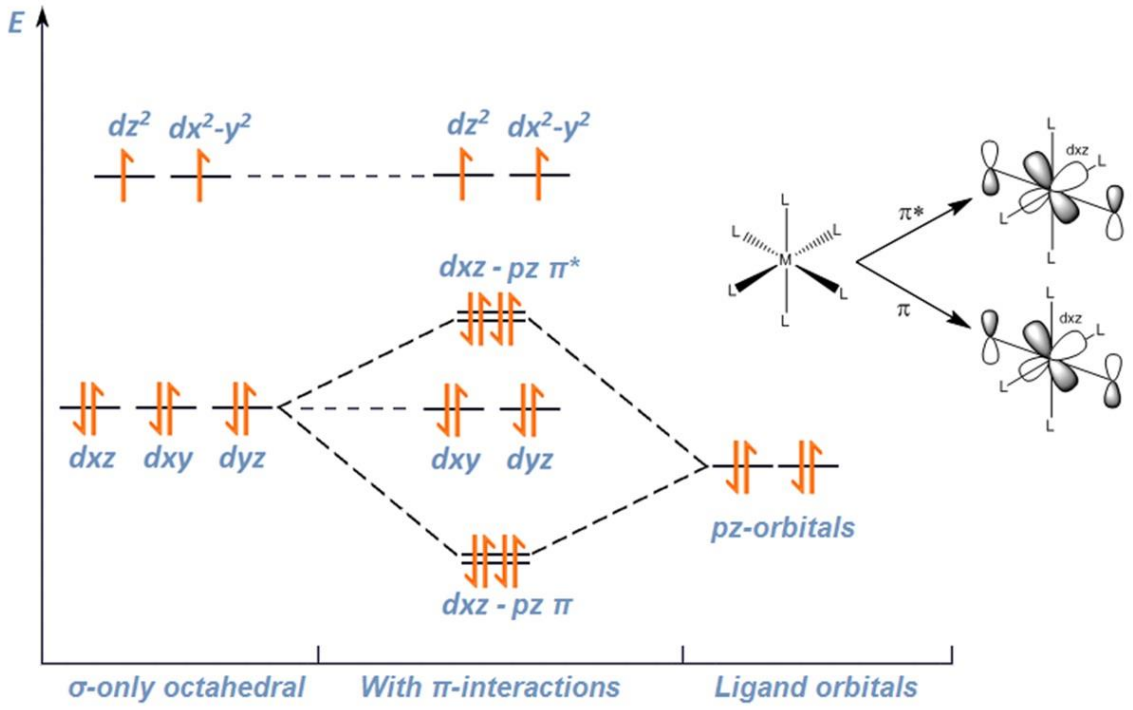

Figure 3.1. Simplified diagram detailing the effect π-interaction would have on an octahedral system if the ligands only had the correct orbital symmetry for π-interaction with the metal d_{xz} orbital.

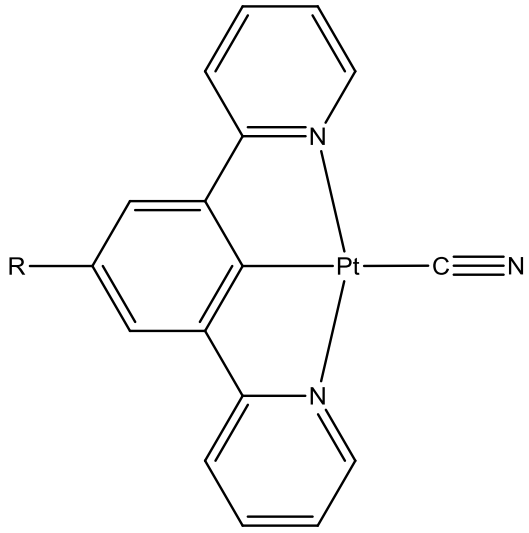

Figure 3.2. General formula of the Pt(II) N^C^N pincer cyanide compounds of this chapter.

3.3 General synthetic strategy

For the research in this chapter, a series of new compounds were synthesised consisting of a platinum N^C^N pincer fragment with various substitutions (R) at the *trans*-position of the central phenyl ring, and a cyanide group occupying the fourth coordination site of the square planar Pt(II) centre (see **Figure 3.2**).

3.3.1 Compound synthesis

The cyanide compounds were synthesised using Pt(II)N^C^N pincer chloride starting materials, for which the synthesis was developed in the work presented in **Chapter 2.** Detailed syntheses of the specific pincer ligands, and their resultant platinum chloride complexes can be found in the experimental section.

To produce the final series of Pt(II)N^C^N cyanide compounds a salt metathesis reaction was performed, which differs slightly for each compound. Generally, AgCN or KCN was heated with the equivalent Pt pincer chloride, until complete reaction has occurred (**Figure 3.3**). If AgCN is used, it also needs to be freshly prepared from $AgNO_3$ and KCN in water for the reaction to progress in acceptable yields. Acids should not be used in these reactions due to the potential production of highly toxic HCN gas. The reactions are generally poor yielding due to an apparent competing reaction whereby one pyridine ring is displaced from its metal coordination site, presumably upon formation of a bi- substituted cyanide side product as a result of the cyanide ligand's strong affinity for the metal. Solvents and conditions are varied to try and prevent this occurring. Silver cyanide is generally used as opposed to direct reaction with the potassium salt to prevent this side reaction, as the higher solubility of the potassium cyanide allows the reaction to progress too quickly, favouring the formation of the side product. There is, however, a case where the opposite appears to be true. There is also difficulty in purifying the resulting compounds due to their low solubility in solvents at room temperature, and similarities in solubility to the starting materials.

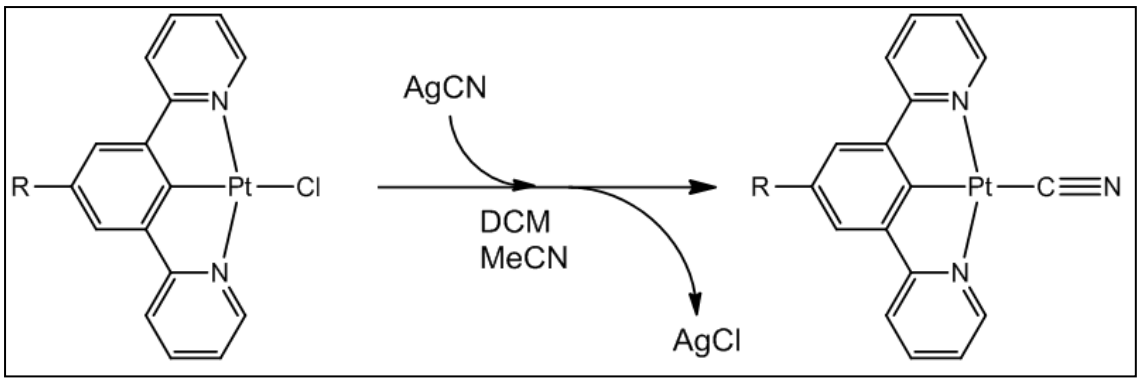

Figure 3.3. General reaction pathway.

3.4 Cyano[methyl 3,5-di(2-pyridyl)benzoato]platinum (16)

The first compound synthesised, and the most comprehensively studied compound to be discussed in this chapter is **Cyano[methyl 3,5-di(2-pyridyl)benzoato]platinum (16)**.

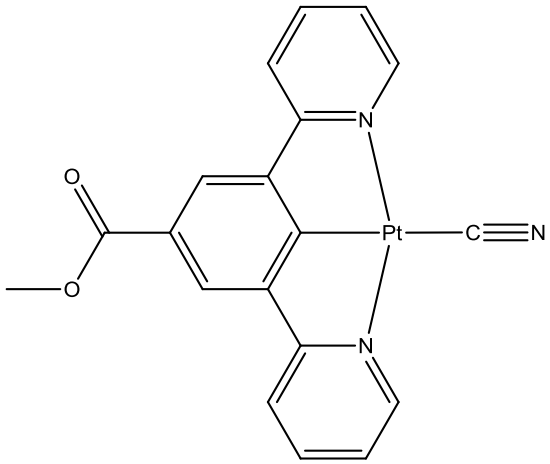

(16) was characterised by NMR and solid-state IR spectroscopy, mass spectrometry and x-ray crystallography.

The IR spectrum shows a single absorption at 2118 cm^{-1} assignable to the $\nu_{C\equiv N}$ of a cyanide group. This value is consistent with those recorded for a series of transition metal cyanide compounds.[12,13] Also seen is a single strong absorption at 1698 cm^{-1} assignable to the $\nu_{C=O}$ of the ester group, which is a typical value for an methyl benzoate ester.[14,15]

^{1}H NMR, and $^{13}C\{^{1}H\}$ NMR spectra of **(16)** were obtained on the product dissolved in deuterated dichloromethane. The correct assignment of hydrogen atoms was supported with the use of a 2-dimensional HCOSY experiment. Due to low solubility, the ^{13}C spectrum is of low resolution.

All recorded spectra correspond to the structure proposed for **(16)**.

3.4.1 Vapochromic behaviour

(16) under standard conditions exists as a deep red solid. However, the colour was revealed to be highly sensitive to exposure from a variety of environmental stimuli. A dramatic colour change was observed in the compound upon exposure to a flow of dry inert gas, whereby the entirety of the bulk crystalline solid in the path of the gas switched from the red **form-I** to a bright yellow colour (**form-II**) on a sub-second timescale. Photography of this transformation can be seen in **Figure 3.4** (videos of the transition can be found on the supplementary information CD). This phenomenon was observed to be completely reversible, almost instantaneously reverting from yellow back to red upon interruption of the flow of dry nitrogen/argon. Other stimuli such as gentle heating, application of vacuum, and exposure to ethanol or diethyl ether were also found to repeat this same transition to the yellow **form-II**, and likewise upon re-exposure to standard atmospheric conditions, an instantaneous transition back to the red **form-I** was observed. It was determined by controlling the environmental conditions that the transition was a response to exposure to water vapour, and that atmospheric humidity was sufficient to cause this transition extremely rapidly simply through exposure to air.

Further investigation into these properties revealed an equally dramatic colour change to deep blue (**form-III**) upon exposure to methanol vapour or liquid. This transition can be seen in **Figure 3.5** and **Figure 3.6** (and again videos are on the supplementary CD). The change is again fully reversible upon returning to standard conditions, and it was demonstrated that the compound could be rapidly switched back and forth between all three forms indefinitely, without decomposition (**Figure 3.7**).

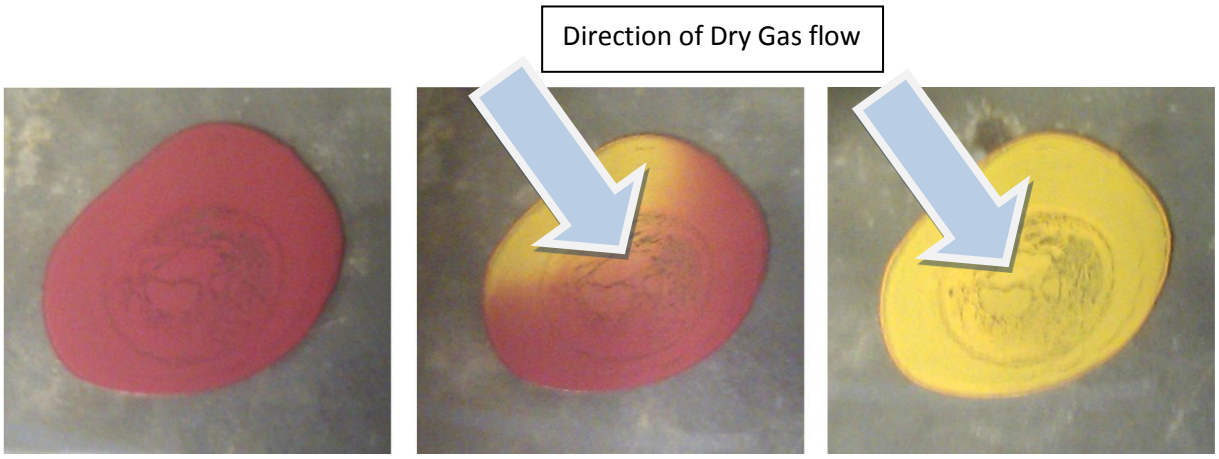

Figure 3.4. Solid state transition of a drop-cast thin film (from DCM solution) (ca. 2cm in diameter) of (16) on a glass slide, from form-I to form-II, using dry argon flow.

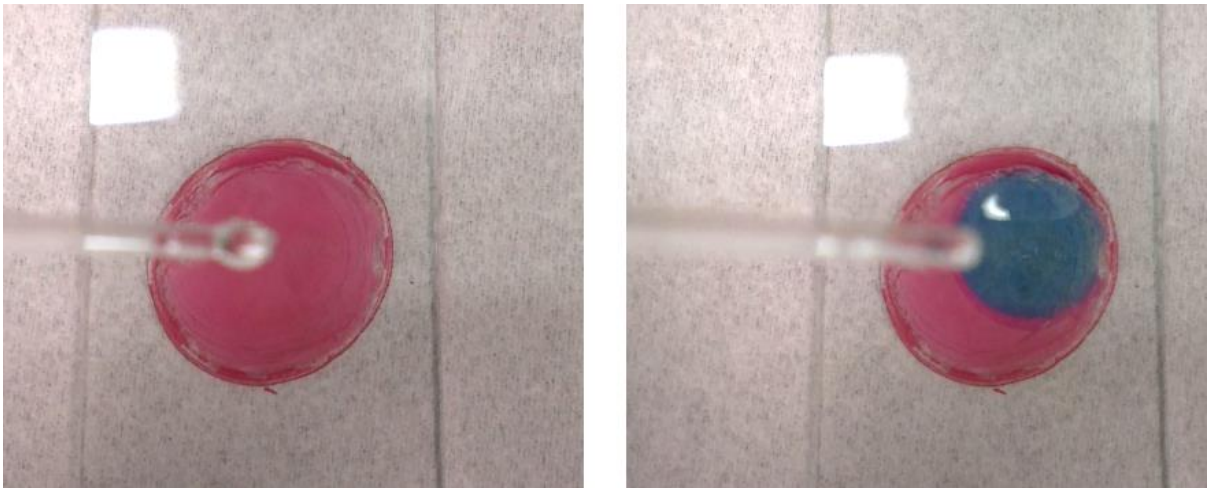

Figure 3.5. Solid state transition of a drop-cast thin film (from DCM solution) (ca. 2cm in diameter) of (16) on a glass slide, from form-I to form-III by direct application of a drop of methanol.

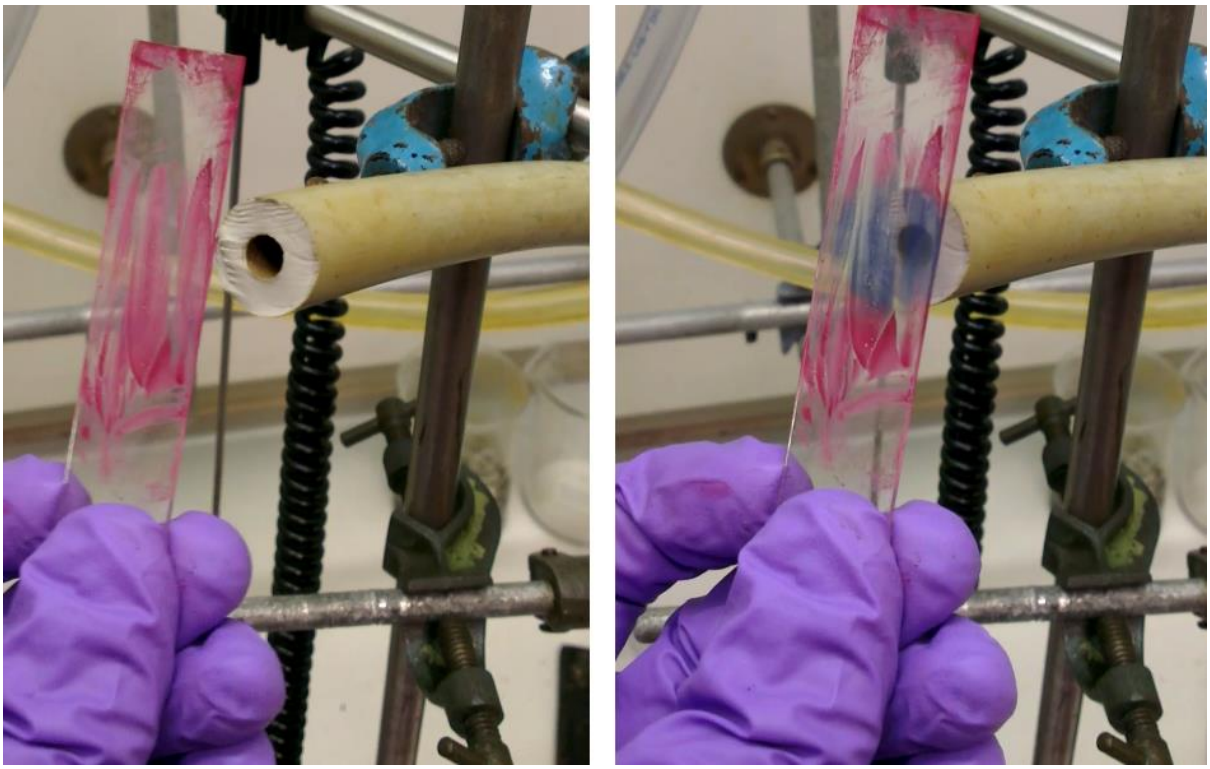

Figure 3.6. Solid state transition of a rough, drop-cast film (from DCM solution) of (16) on a glass slide, from form-I to form-III by exposure to methanol vapour (argon carrier gas through methanol bubbler).

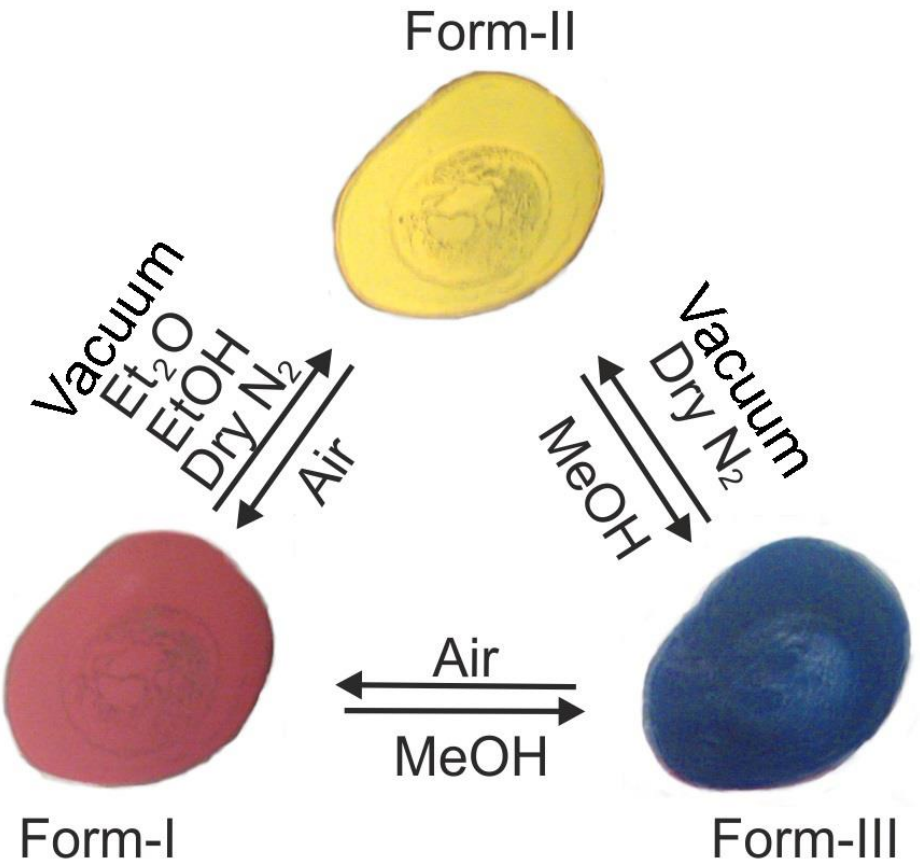

Figure 3.7. Photographs summarising the three coloured forms (ca. 2cm diameter, drop-cast from DCM solution), and the environmental conditions needed to transfer the sample between them.

3.4.2 UV-Vis spectroscopy

3.4.2.1 Solution state spectroscopy

The rapid colour changing properties of **(16)** are seen only in the solid state, pointing towards intermolecular interaction as the likely cause. In order to confirm that no unusual behaviour is seen intra-molecularly, spectroscopy in dilute solution was carried out. This would also provide information regarding the frontier orbitals of the discrete molecules and help to direct an explanation for the properties.

(16)	Absorptions: **[λ (nm)]**
Dichloromethane Solution ($1x10^{-5}$ mol dm^{-3})	[265], [287(sh)], [319], [334], [359], [378)]

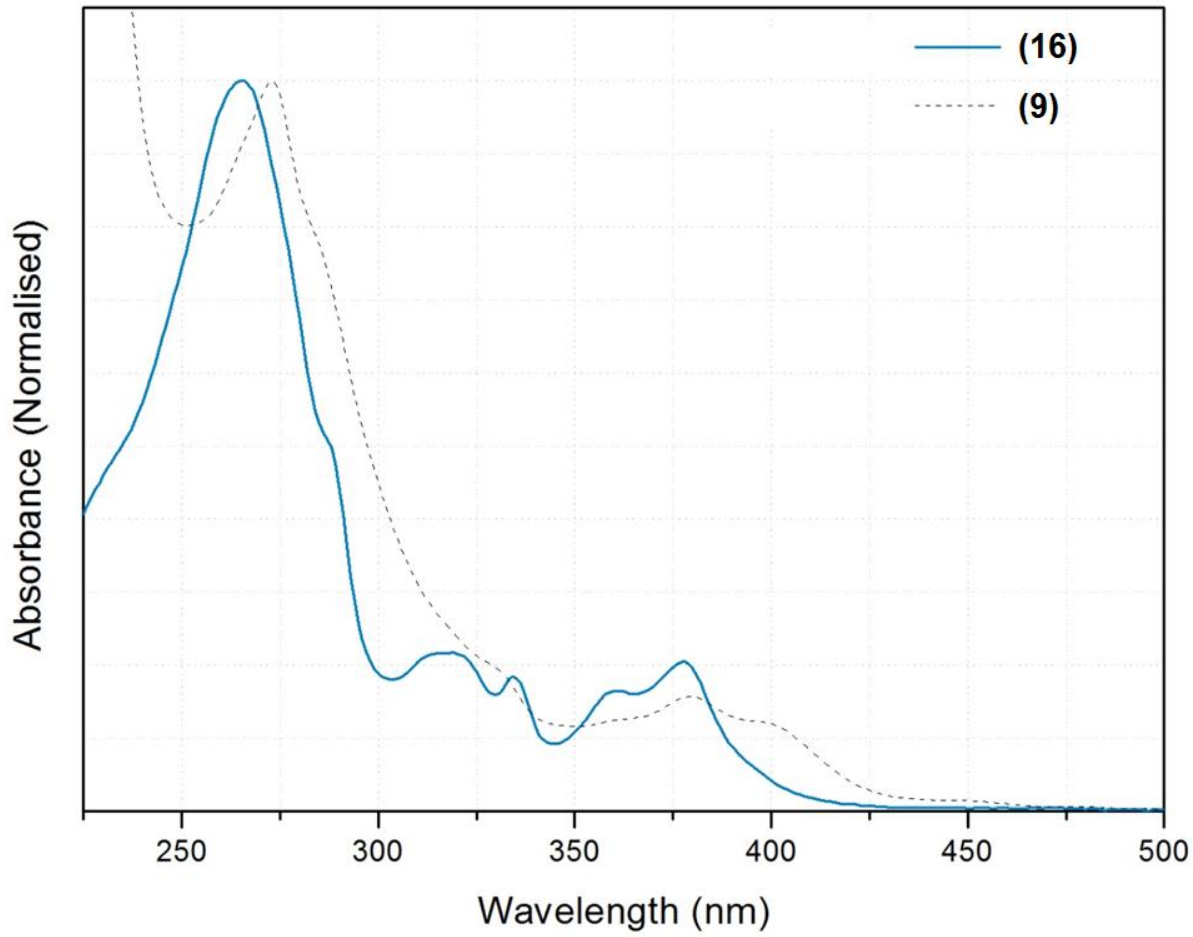

Figure 3.8. UV-Vis absorption spectrum for compound 18 in dichloromethane solution ($1x10^{-5}$ mol dm^{-3}).

The solution state absorption spectroscopy for **(16)** can be seen in **Figure 3.8** and shows a broadly analogous profile to that of the chloride starting material **(9)**, with an expected small blue-shift in the lowest energy absorption with λ_{max} = 378nm. It appears that in the solution state, the frontier orbitals may be similar in the two compounds. The lowest energy absorption for the chloride compound has been previously attributed to a $^{1}\pi$-π^* electronic transition from an occupied MO based on a π^* interaction of the platinum d_{xz} with its ligand environment (Cl and arene π-system), to vacant orbitals situated primarily on the pincer ligand pyridyl orbitals.

3.4.2.1.1 Gas phase DFT calculations

It was discussed in **3.2.1**, that the inclusion of the strong-field cyanide ligand may have the effect of facilitating d_z^2 intermolecular interactions, by drawing the d_{xz} and d_{xy} down in energy, and therefore bringing the d_z^2 closer to the frontier. In order to determine the nature of the rapid colour changes of the compound, gas-phase DFT calculations were first performed in order to establish whether this may be a contributing factor, along with gaining a better understanding of its absorption spectrum in dilute solution.

The Frontier orbitals for **(16)** are as predicted, quite similar to those of **(9)** (See **Figure 3.9**, **Figure 3.10**, and **Figure 3.11**). Like **(9)**, the HOMO still consists mainly of the platinum d_{xz} orbital (43%) in a similar π*-interaction with the arene of the pincer (30%) and a π*-interaction with the occupied p_z-p_z orbtial of the cyanide ligand (13%) replacing that to the p_z of the chloride. However, for reasons discussed in **3.2.1**, the orbital is indeed less destabilised by the cyanide- hence the small reduction in energy and the blue-shift measured spectroscopically in comparison to **(9)**. In **Chapter 2**, it was concluded that possessing the correct symmetry allows orbitals containing the platinum d_{xz} and d_{xy} to be influenced to the greatest degree by the nature of the fourth ligand. For the d_{xz}-orbital, however, a fixed interaction with the π-donating arene ring of the pincer means it is less sensitive to the fourth ligand's nature than the d_{xy}, which possesses incorrect symmetry to interact with the pincer ligand and therefore only experiences π-interactions with the fourth ligand.

The differences between the compounds' orbitals begin with the HOMO-1.
For **(9)**, the HOMO-1 consists of the π*-hybrid of the platinum d_{xy} and the p_y-orbitals of the chloride. This is not the case for **(16)**. As the energy of the d_{xy} containing orbital is highly sensitive to the nature of the fourth ligand (its sole π-interaction being with this ligand, in the xy plane), we can see that the d_{xy} of compound **(16)** receives far less destabilisation from its π*-interaction with the cyanide (due to the cyanide's position in the spectrochemical series), and hence is found at much lower energies in this case as the HOMO -3.

Because the other filled metal d-orbitals possess incorrect symmetry for π-interaction with the fourth ligand, relatively little change is observed in them between the two compounds. The highest energy of these, the platinum d_z^2-orbital, has therefore become the HOMO-1 for **(16)**. In essence, what we see by changing the chloride ligand to the less π-donating cyanide, results in a

reduction in the energies of the HOMOs containing the metal d-orbitals with correct symmetry for π-interactions with the ligand at this position (d_{xz} and d_{xy}). The largest change is seen in the d_{xy}, due to the d_{xz} retaining its π-interaction with the similarly destabilising pincer arene. As a result of this, these two frontier orbitals are brought down in energy, while the filled metal orbitals that lack the symmetry to π-interact with this ligand remain at relatively similar energies between the two compounds. The d_z^2 orbital, being the highest energy of these, now lies just below the frontier as the HOMO-1 for **(16)** (the d_{yz} is stabilised by interaction with the pincer pyridyls, and is thus inherently lower in energy).

As mentioned in **Chapter 1**, and in section **3.2.1**, intermolecular interaction of the platinum d_z^2 orbital is known to induce large displacement of its energy, and so it was hypothesised that the unusual optical behaviour observed by this compound in the solid state may be due to the proximity of this orbital to the frontier.

The phenomenon of orbital stabilisation by π-interaction with cyanide ligands was noted in similar systems studied by Williams *et al.*[11] During work on improving the efficiency of platinum based OLEDs, it was found that for the compounds $[Pt(tpy)CN]^+$ and $Pt(5,5'\text{-}Me_2\text{-}bpy)(CN)_2$, the contraction of platinum d-orbitals away from the frontier as a result of the cyanide ligands was large enough to introduce more ligand centred transitions, and the reduction in MLCT states proved a detriment to the quantum efficiencies. In fact they suggested using acetylides as a more strongly π-donating alternative to maintain a density of filled metal orbitals at the frontier to overcome this issue, highlighting the different responses observed from these two seemingly similar ligands.

For the research presented in this chapter however, the reduction in energy of the d_{xy} and d_{xz}, and the subsequent exposure of the d_z^2 orbital is intentional, with the aim of creating tuneable/switchable optical properties intrinsic to compounds, and for this aim the cyanide appears to be a good choice of ligand.

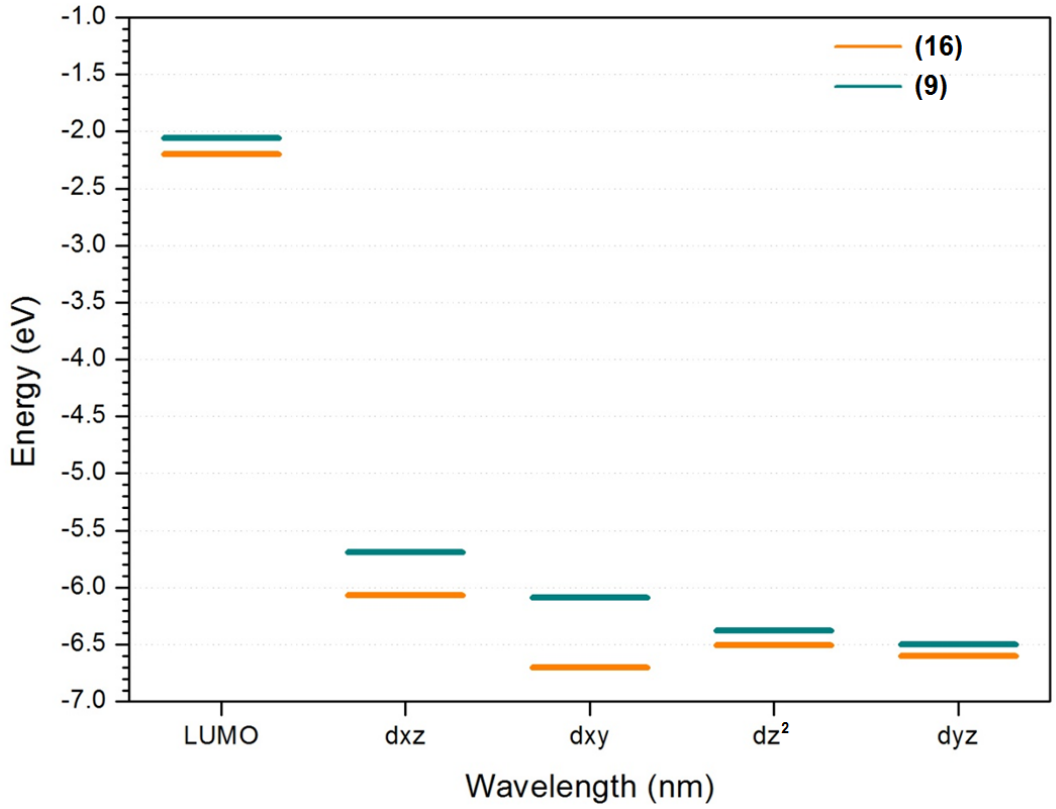

Figure 3.9. Energy level diagram comparing the HOMOs and LUMO of (16) and (9). The reduction in energy of d-orbitals possessing π-interaction with cyanide is clearly observed (d_{xz}, d_{xy}). For clarity the orbitals have been labelled after the metal orbital involved, although they represent highest energy π* hybrid of the stated d-orbital with the ligand environment, which make up the orbitals HOMO-HOMO-4.

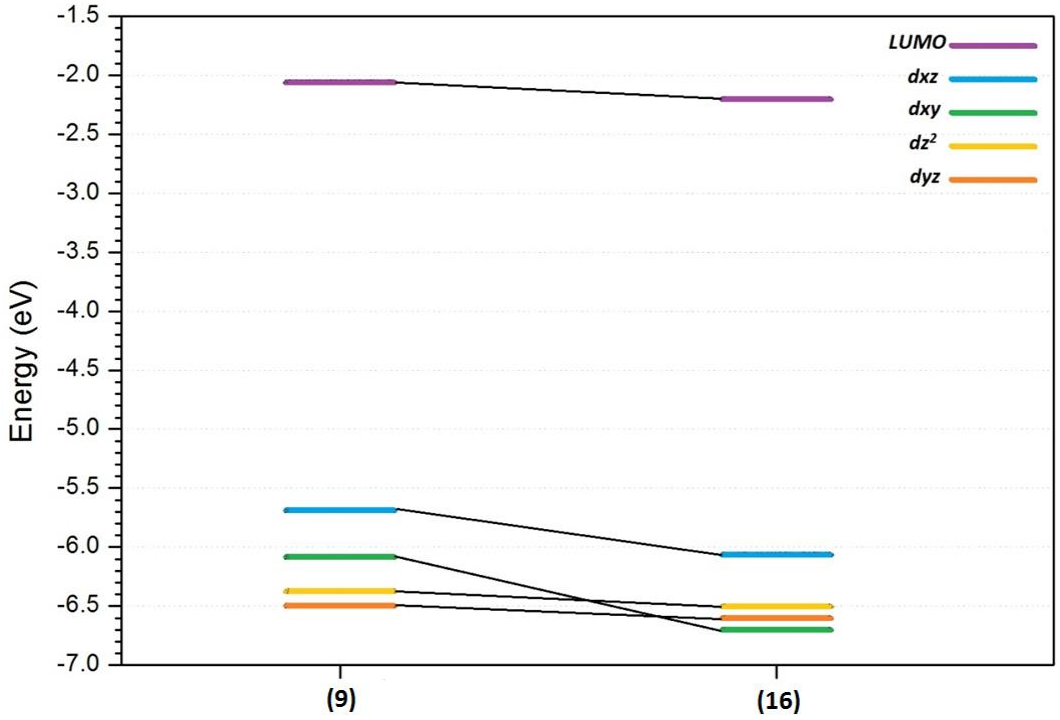

Figure 3.10. Further energy level diagram detailing the disproportionate reduction in energy of the d_{xz} and d_{xy} orbitals in (16) relative to (9). Labels adopt same convention as Figure 3.9.

(9) HOMOs	(16) HOMOS
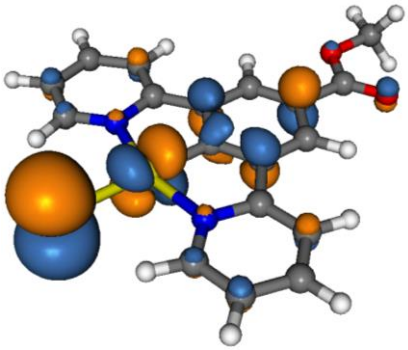	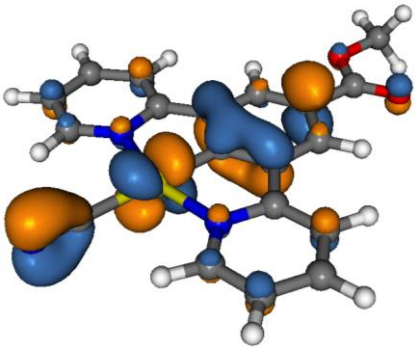
d_{xz} (HOMO)	d_{xz} (HOMO)
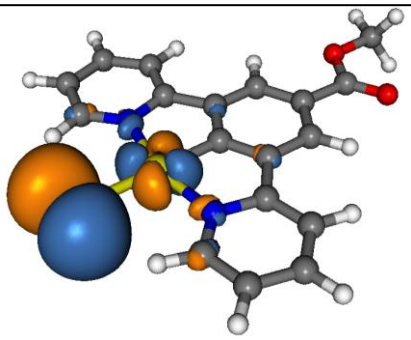	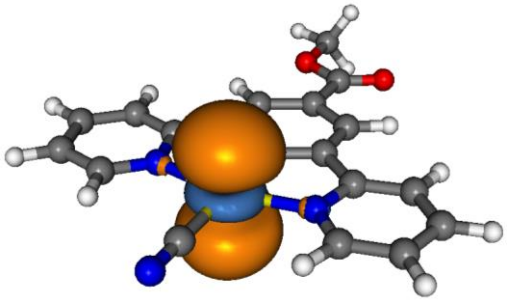
d_{xy} (HOMO -1)	d_{z}^{2} (HOMO -1)
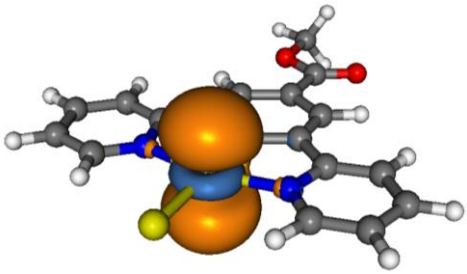	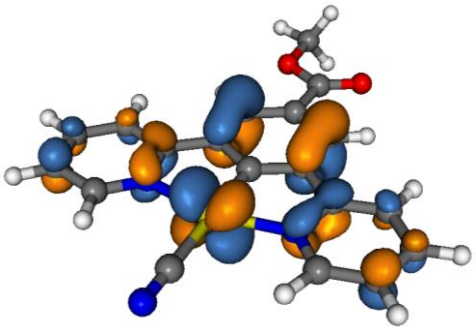
d_{z}^{2} (HOMO -2)	d_{yz} (HOMO -2)
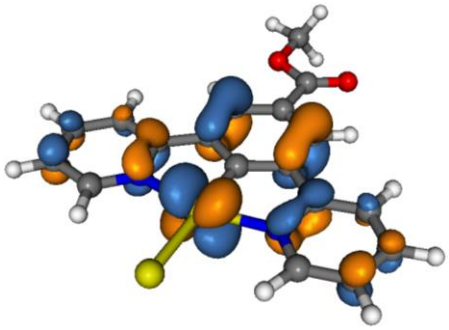	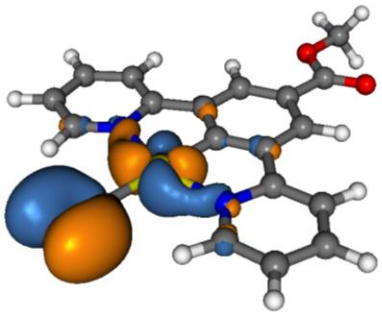
d_{yz} (HOMO -3)	d_{xy} (HOMO -3)

Figure 3.11. Comparison of the calculated HOMOs for a single molecule of (16) and (9). Note the change in order, due to d_{xy} stabilisation, bringing d_{z}^{2} to HOMO-1.

3.4.2.1.2 π-donor calculation test

In order to further test whether the extent of the fourth ligand's π-donor ability was indeed responsible for the reduction in energy of the d_{xz} and d_{xy} containing orbitals, a simple test was derived whereby orbitals energies were simulated for analogous compounds containing iodide, bromide, chloride and fluoride as the fourth ligand. π-donor ability diminishes from high for iodide to practically zero for fluoride across this series, and so it should provide a reasonable standard to which comparisons can be made.[16]

What was found was that the calculations suggest all the orbitals of the molecule (including the LUMO and unoccupied orbitals) tended to migrate to higher energies in the calculations going from the iodide through to the fluoride ($d_{x^2-y^2}$, d_{yz} and d_{z^2}), and all the orbitals remained in the same order, however the π* orbitals involving the d_{xz} and d_{xy} and the halogen were indeed, proportionately, greatly reduced in energy across this series.

In **Figure 3.12**, for ease of comparison the energies of the orbitals have been scaled in relation to the d_{yz} orbital, as this orbital sees the least influence from the fourth ligand (even iodide forms no interaction). It can be seen that the d_{z^2} containing orbital and LUMO stay relatively constant, although there is some side-on σ-type interaction observed from the very diffuse Iodide p_x orbital and the d_{z^2}, hence the slight energetic increase seen for this compound.

The d_{xz} combination however experiences notable contraction across the series to a point, and then it tails off. This is presumably due to the continuation of π-donor influence from the pincer arene, competing with the reduction in π-donation from the halogen.

But as predicted, the d_{xy} orbital which benefits from no such pincer interaction sees a consistent reduction in absolute energy across the series.

The cyanide ligand **(16)** has been included in **Figure 3.12** for comparison, and it it appears that the trend continues with progression to stronger-field ligands.

Iodide HOMO	Bromide HOMO	Chloride HOMO	Fluoride HOMO
19% Pt d_{xz} 70% Iodine p_z 11% Pincer π-system	29% Pt d_{xz} 52% Bromine p_z 19% Pincer π-system	36% Pt d_{xz} 37% Cl p_z 27% Pincer π-system	46% Pt d_{xz} 16% F p_z 38% Pincer π-system

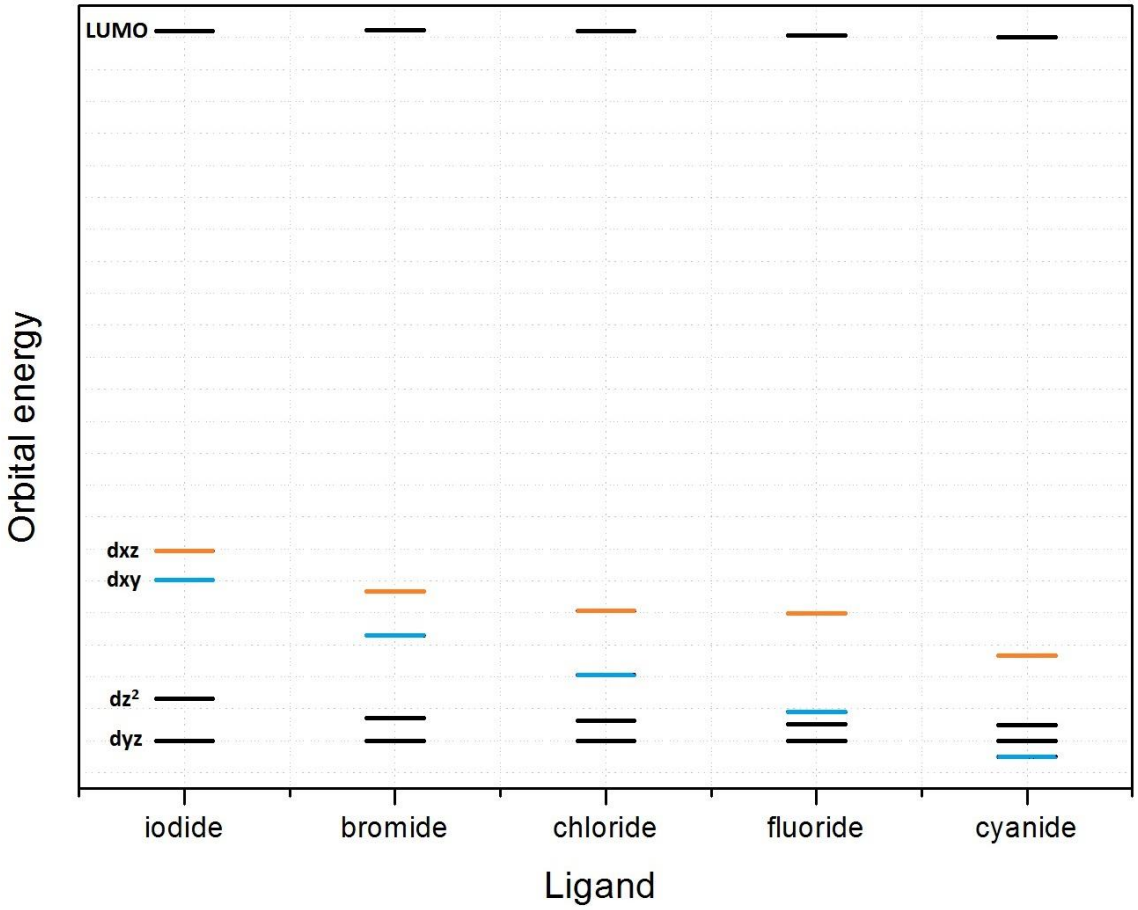

Figure 3.12. Orbital calculations showing the highest energy occupied combinations for each highest energy π* hybrid of the stated d-orbital for compounds containing the halogens. This was to test the hypothesis that reducing π-donation will disproportionately stabilise the π*-hybrids containing the d_{xz} and particularly the d_{xy} orbital due to their symmetry. π-donor ability reduces from left to right. Energies scaled to d_{yz} level form ease of comparison.

3.4.2.2 Solid state spectroscopy

The three distinctly coloured solid forms of **(16)** were next investigated using solid state UV/Vis spectroscopy, in order to better understand the origin of such a significant divergence in optical properties between the three forms. (**Figure 3.13**). This experiment was performed with a microspectrophotometer via transmission of a 50 µm diameter probe beam through a thin film of the compound (*ca.* 5 x 5mm) drop cast from dichloromethane solution onto a glass substrate.

Spectra were collected using mirrored lenses (Bruker) mounted in an off-axis geometry with a deuterium halogen light as the light source (Ocean Optics). Absorption was monitored over the 200-750 nm wavelength range using a Shamrock 303 imaging spectrograph (Andor).

Once the spectrum for **form-I** was collected, the sample was converted to form-II in-situ, using a room-temperature flow of dry nitrogen provided by an Oxford-Cryosystems cryostream. **Form-III** was then generated by direct application of methanol to the sample.

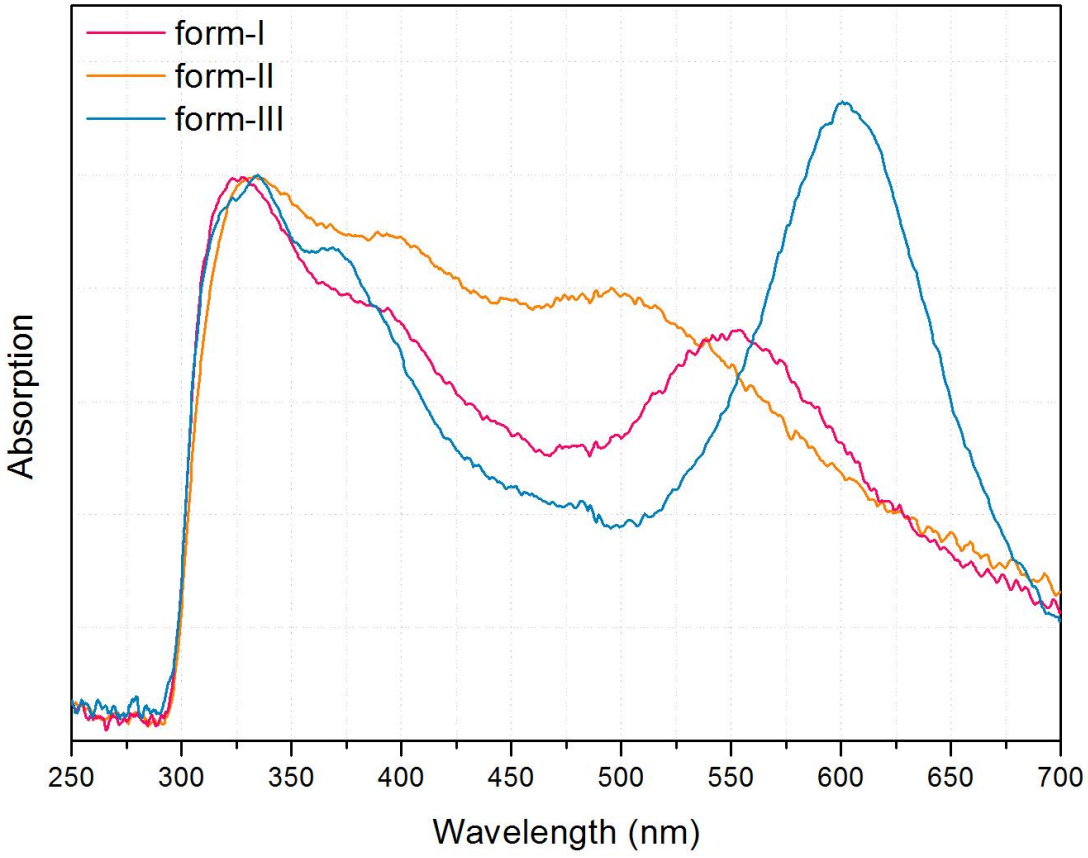

Figure 3.13. Normalised solid-state UV-Vis absorption spectrum of the three coloured forms of (16). Recorded at room temperature, on a thin-layer powder sample of 1 ca. 5 x 5 mm deposited on a glass slide.

The individual spectra display structural similarity, showing strong broad absorption bands in the UV region, along with a second absorption in the visible region with varying wavelength that distinguishes the three forms, and provides the visible differences. The similarity of the structural form between the three spectra seems to suggest that the absorptions are derived from the same origin, but that the energy of the lowest energy absorption appears to be shifting in response to the presence of water or methanol.

A blue shift in absorption wavelength of this peak is observed from the red **form-I** ($\lambda \approx 540$ nm) to the yellow **form-II** ($\lambda \approx 500$ nm) while a red shift is observed through to the methanol blue **form-III** ($\lambda \approx 600$ nm).

3.4.2.2.1 Solid state time-resolved spectroscopy

One of the main features of interest in the switching ability observed in this compound is the speed at which it is able to do so. In order to quantify this property, time resolved UV-Vis experiments were also performed (**Figure 3.14**).

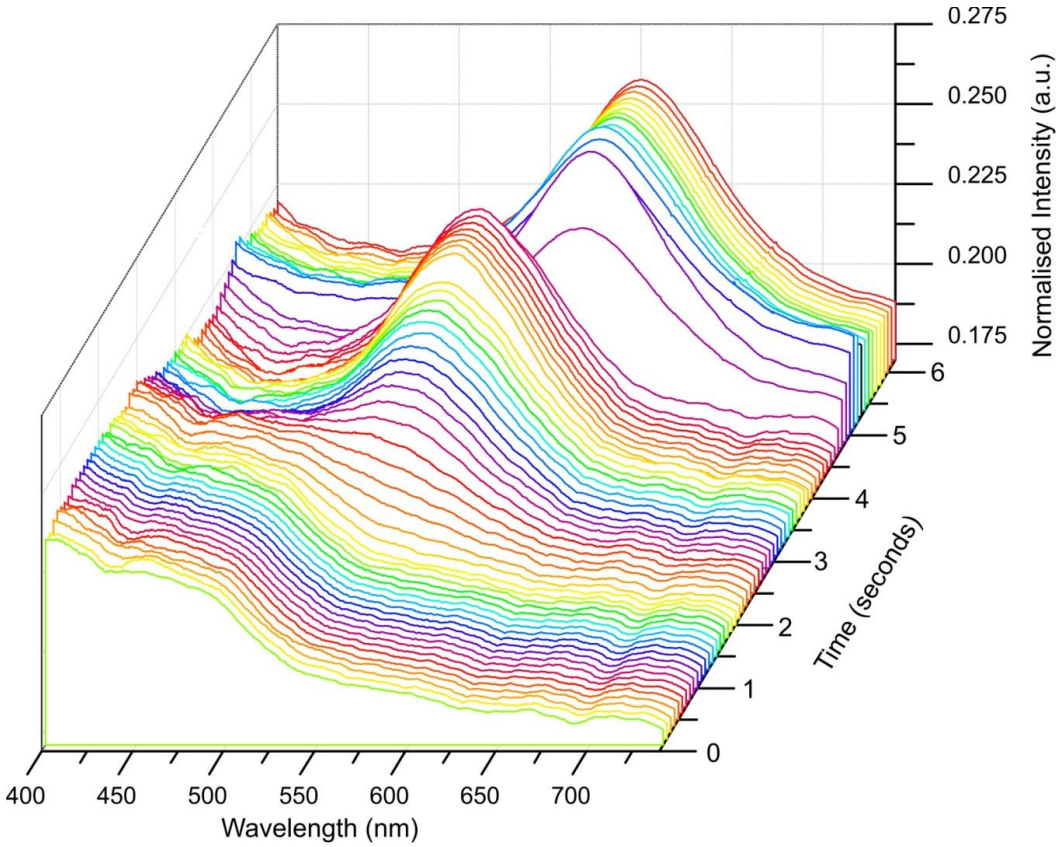

Figure 3.14. Solid-state time-resolved UV-Vis spectrum of (16) transitioning from form-II to form-I to form-III. Recorded on a thin-layer powder sample of 1 ca. 5 x 5 mm deposited on a glass slide. At T = 0 s the sample was under a nitrogen atmosphere, the transition at ca. T = 2.5 s was induced by the removal of the nitrogen jet. The transition at ca. T = 4.5 s was induced by the application of liquid methanol directly to the sample.

The experiments were performed using the same technique as with the single solid-state spectra, however multiple spectra where recorded at a rate of 10Hz, and conditions were changed *in situ* to attempt to record the transition between forms.

It was shown that the shift between forms occur on the sub-second timescale both back and forth between all three forms. A 3-dimensional graph showing transition from **form-II** to **form-I** to **form-III** can be seen in **Figure 3.14**, and serves as a summary of the results obtained.

It is important to mention that this experiment was limited to the speed at which the conditions were changeable, and so only qualitative conclusions may be drawn from this, however it does offer some perspective into the optical response time to changes in environmental conditions that are achievable by this compound.

3.4.3 Emission Spectroscopy

(16) is also a highly emissive species, exhibiting intense luminescence in solution and the solid state. In addition to its colour switching properties, a similar switching of the emissive frequencies is observed.

3.4.3.1 Solution-state spectroscopy

As with absorption spectroscopy, the spectroscopic properties of the un-aggregated compound (i.e. dilute solution) were first studied.

The resultant emission spectrum is shown in **Figure 3.15**.

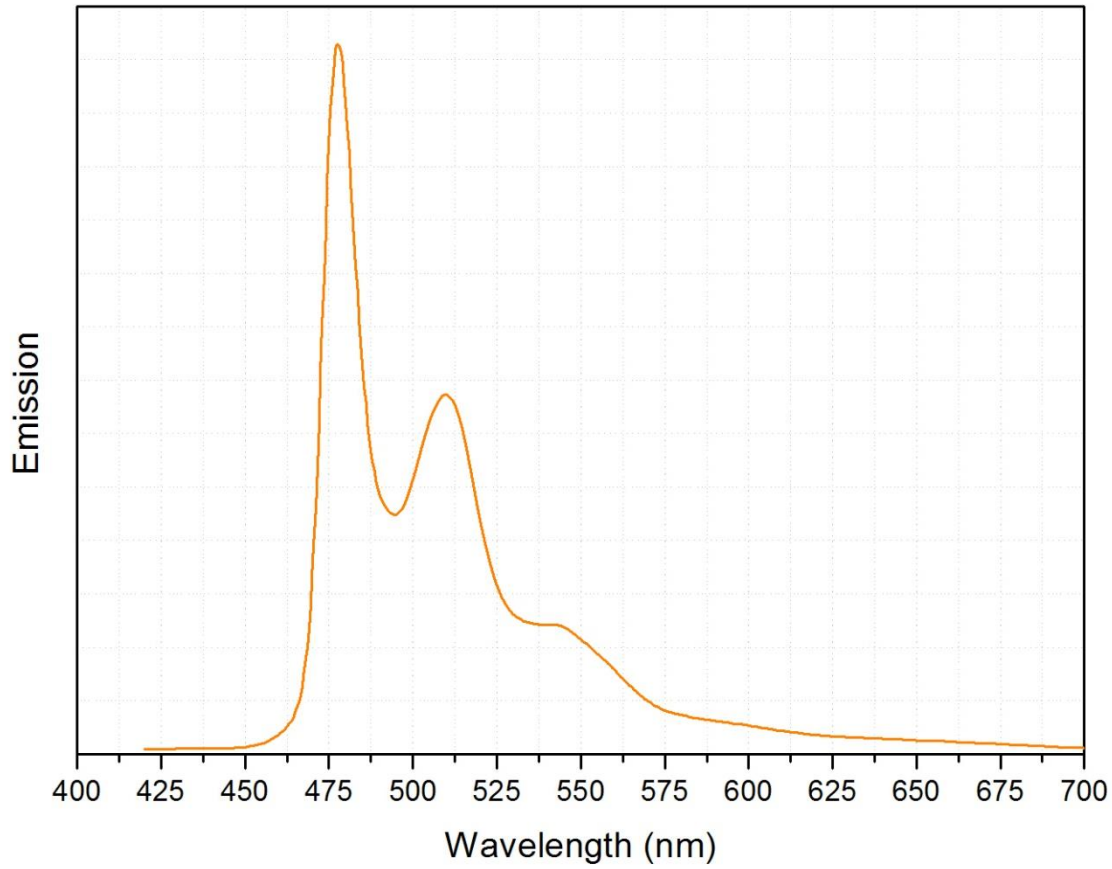

Figure 3.15. Emission spectra for (16) in dichloromethane solution ($5x10^{-6}$ mol dm^{-3}), excitation at 395nm, λ_{max} = 477nm

As with the solution state absorption spectrum, the emission spectrum of **(16)** in solution is very similar to that of the chloride compound, but slightly blue shifted (λ_{max} chloride = 482nm), offering further support to the evidence that the molecule's opto-electronic properties remain largely unchanged in dilute solution by exchanging the chloride for cyanide. The solution state emission can be assigned as originating from a ^{3}LC state.[10,17]

3.4.3.2 Quantum yield

As stated in **chapter 2**, measuring accurate quantum yields with the equipment available proved challenging, however approximations were made by comparison of emission maxima through concentration scales with the previously determined chloride starting material **(9)** as a standard (φ_{lum} = 0.56 in degassed dichloromethane).[17]

The quantum yield was calculated by plotting the integrated emission intensity at a series of concentrations in degassed dichloromethane (concentrations ranged from $1x10^{-7}$ to $1x10^{-5}$) vs. absorbance measured at the probe frequency (for the same set of solutions).

The gradients of this linear plot were then used to calculate the approximate quantum yields using **Equation 3.1**, whereby a comparison is made to the corresponding plot created for the chloride standard.

$$\varphi_x = \varphi_{st} \left(\frac{Gradient_x}{Gradient_{st}} \right) \left(\frac{\eta_x^2}{\eta_{st}^2} \right)$$

Equation 3.1. Formula used for calculating quantum yields, where ϕ_x and ϕ_x = the quantum yields of the compound and standard respectively, and η_x and η_{st} = the refractive index of the solvents.

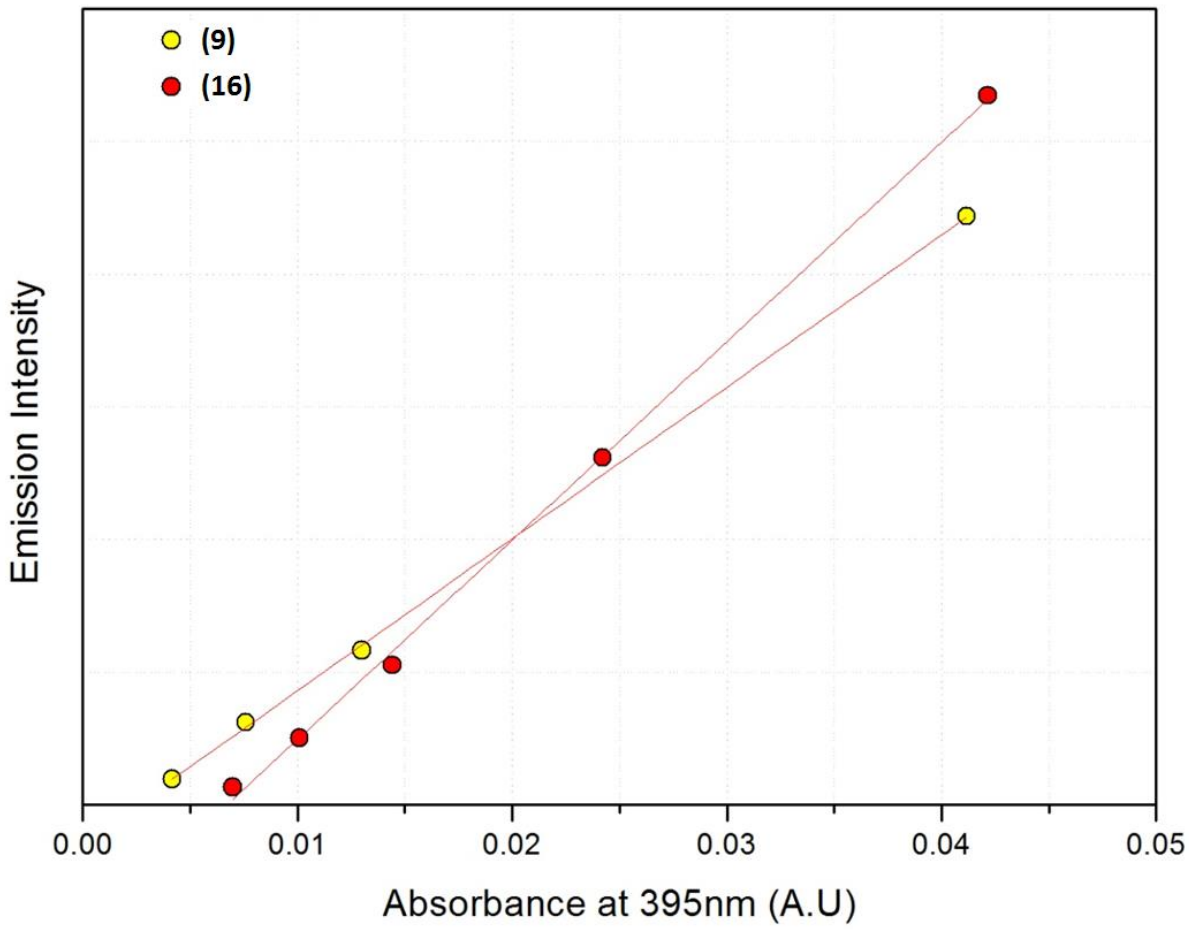

Figure 3.16. Emission intensity vs. Absorbance at 395nm for (16) and the chloride standard.

Through this method the approximate quantum yield in degassed dichloromethane was determined to be $\varphi_{lum} \approx 0.73$.

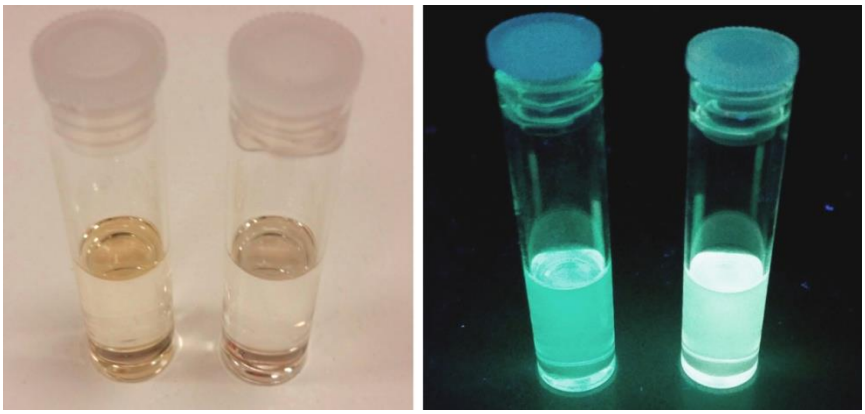

Figure 3.17. Photographs of $1x10^{-4}$ mol dm^{-3} solutions of the chloride-standard (left vial) and (16) (right vial) under ambient and UV light.

While the quantum yield calculated should not be taken as an accurate value, the assignment of the compound as being extremely emissive with a quantum yield higher than the standard is likely to be reliable. Looking at **Figure 3.17.** it can be seen in the left hand image that for high concentrations, the standard **(9)** is slightly more absorbent of visible frequencies, appearing more yellow, with **(16)** appearing less coloured at the same concentration. The right hand image shows the same two vials irradiated at 365 nm, and **(16)** can be seen to visibly emit comparably, despite its lower absorption at high frequencies (**Figure 3.16**). This is only a qualitative comparison, but it shows that while an approximation, the designation of the compound as extremely emissive is an accurate one.

3.4.3.3 Solid-state spectroscopy

As mentioned previously, in addition to the switching of optical absorption spectra, the compound exhibits a similar ability regarding its luminescent emission.

Transitions occur under the same set of environmental stimuli, with each of the three forms possessing a discrete emission spectrum.

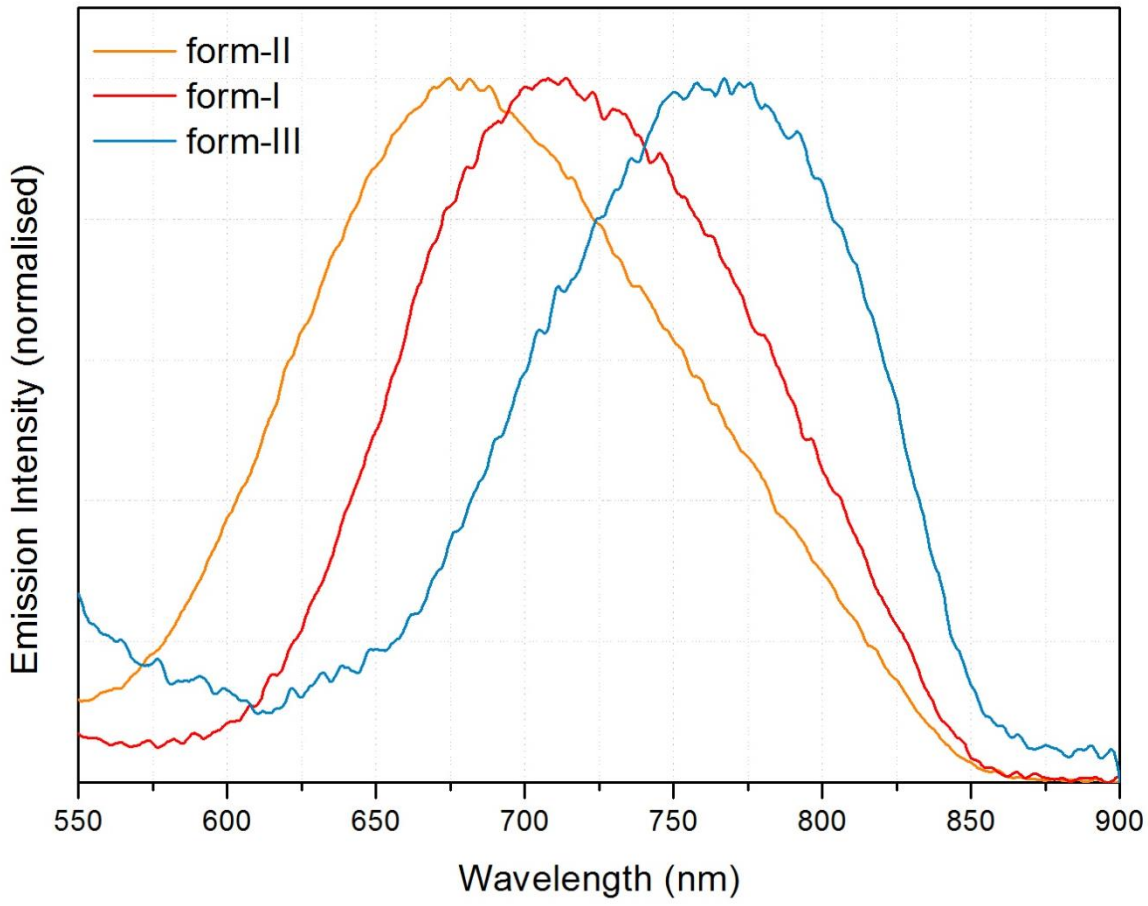

Figure 3.18. Normalised solid state emission spectra of (16) recorded in a sealed quartz vial under dry argon, air (water-vapour), and argon + methanol-vapour atmospheres (to give II, I and III respectively).
Spectrum recorded at 500nm excitation.

It can be seen in **Figure 3.18** that the solid state emission differs greatly from that of the solution state emission, where we can see broad featureless peaks that are significantly red-shifted. **Form-I** emits a broad band of frequencies encompassing the lowest visible energies (λ_{max} ≈ 710 nm) and extending into the near IR as far as 850nm. Visibly this emission appears deep red. As seen with the UV-Vis absorption spectra, a clear blue-shift is observed upon transition to **Form-II**, emitting a similarly broad band of frequencies this time encompassing the visible spectrum from yellow frequencies through to near-IR with emission λ_{max} ≈ 675 nm. This emission visually appears bright orange.

Again mimicking the trend observed for the absorption spectra a clear red-shift is seen upon transitioning to **form-III**. Emission from **form-III** peaks almost in the near infra red region with λ_{max} ≈ 765 nm, and appears only slightly emissive at visible frequencies. Visually, emission from this species is undetectable.

Phosphorescent emission in the near-IR region is fairly rare, particularly at room temperature, and is an inherently inefficient process due to the ease at which excited states with low energy gaps can be quenched by high frequency vibration coupling (C-H) (O-H), however **form-III** created using deuterated methanol (d4) produced no change to the intensity or frequency of emission for **(16)** to that of regular methanol. Absolute quantum yields were not measured for this compound in the solid state due to lack of the appropriate equipment, and the spectra in **Figure 3.18** are normalised for ease of comparison. The intensities do show the characteristic reduction in intensity towards the IR region, and approximate intensities can be provided relative to that of form-II (the most intense emitter). Form-I emits at λ_{max} with *c.a.* 73% intensity and form-III emits at λ_{max} with *c.a.* 12% intensity relative to form-II.

Near IR emitters have many potential applications such as night vision readable displays, and in the telecommunications industry.[18-20]

Near IR emission was observed by Rossi *et al.* in a related compound whereby a large red shift in emission originated from an aggregated excited state of MMLCT character, as a direct result of platinum - platinum interactions.[4]

3.4.4 Structural analysis - explaining the colour change

By using spectroscopic techniques, the rapid solid-state optical switching seen in **(16)** has been accurately described, and alongside DFT calculations has offered evidence that platinum d_z^2-d_z^2 interactions may be driving the change. However, for a complete mechanism and full explanation for how this compound achieves such distinct property shifts in reaction to environmental conditions, the three forms of the compound needed to be structurally analysed in the solid state. In order to do this x-ray diffraction techniques were employed.

3.4.4.1 Powder x-ray diffraction

The aim of the research presented in this chapter was to attempt to produce a novel compound where intermolecular interactions could potentially affect optical properties through π-π stacking, or through intermetallic interactions *via* the perpendicular d_z^2 orbitals. Due to the highly divergent optical properties observed between solid-state and solution, it appeared to be the case that intermolecular interactions are a driving force.

In order to establish whether ordered solid-state structural differences were responsible for the optical switching in the thee forms, powder x-ray diffraction experiments were performed (**Figure 3.19**). Three capillary tubes were prepared containing a sample of each of the three forms of **(16)**. First, **form-I** was prepared simply by loading sample into the capillary under standard atmospheric conditions. **Form-II** was produced by converting a sample from **form-I** using dry argon gas, and preparing and sealing the capillary with epoxy-resin under dry inert argon inside a glovebox. **Form-III** was prepared by converting from **form-I** with an excess of liquid methanol, and filling the capillary with the resulting suspension. Once the solid **form-III** had settled to a sufficient depth at the bottom of the capillary it was snapped at this level and sealed with epoxy-resin.

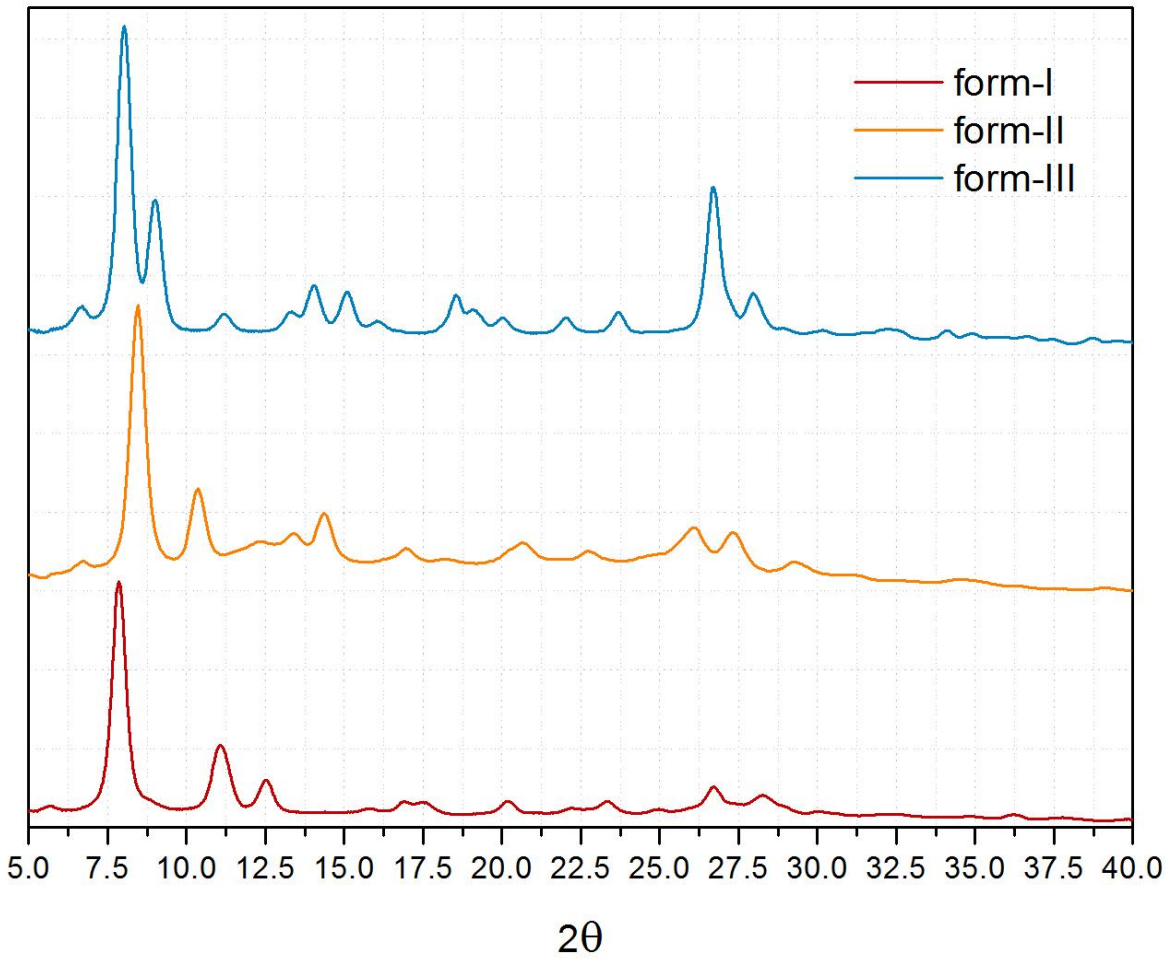

Figure 3.19. Powder diffraction data for the three forms of (16) displaying three distinct crystal structures.

What is immediately apparent from **Figure 3.19** is that not only are the three solid state forms crystalline, but also they exist in three distinct structures, giving three discrete powder diffraction patterns. While this proves that there is indeed structural variation between the three forms, it still does not confirm whether this is the driving force for the differences in opto-electronics, or provide a mechanism by which the differing structures may cause these differences. In order to work towards providing such a mechanism, single-crystal x-ray diffraction experiments needed to be performed.

Powder diffraction was also used to determine the nature of the interaction of **(16)** with ethanol and diethyl ether that also results in a (slower) transformation from red to yellow. It was determined that the yellow solid produced by exposure to these solvents is structurally identical to that produced by vacuum and dry gas flow, confirming that they act to extract water, allowing transformation to **form-II**, and are not forming new solvates.

3.4.4.2 Single crystal x-ray diffraction.

In order to fully structurally describe each form with x-ray diffraction, single crystals first needed to be obtained with structures consistent with each of the three forms of bulk solid.

Red crystals with needle morphology, consistent in appearance with **form-I**, were first to be obtained, due to their stability in the atmosphere, through the method of slow evaporation of an acetonitrile solution while exposed to atmospheric conditions (i.e in the presence of water). Single crystal diffraction and subsequent powder-pattern simulation of these crystals revealed a match with the bulk solid powder pattern, indicating a representative structure.

Blue crystals with needle morphology, consistent in appearance with **form-III**, were obtained from a slow cooled methanol solution, and were again confirmed to be structurally representative of the bulk solid through matching with the powder diffraction pattern.

Four different yellow needle-like crystals consistent in appearance with **form-II** were obtained by various crystallisation methods. Slow cooled ethanol solution, and slow evaporation of acetonitrile solution under inert atmosphere both yielded solvates containing one molecule of their respective solvents per molecule of **(16)**, and gave structurally inconsistent diffraction patterns to that of the **form-II** bulk powder. Solvent layering of diethyl ether onto a dry dichloromethane solution produced yellow solvent-free crystals, though again this structure's diffraction pattern was not found to be representative of the bulk solid powder. None of these crystals displayed vapochromic properties. Structures of these three yellow forms can be found in the supporting information disk.

Slow evaporation of a dilute acetone solution under dry nitrogen yielded a fourth set of yellow crystals. These were revealed to be a second solvent free structure, with a diffraction pattern structurally consistent with that of the bulk solid and thus representative of the structure of the solid powder (see **Figure 3.20** for all comparisons of simulated and measured data).

All the structures obtained crystallised in the monoclinic space group $P2_1/c$, with the acetonitrile solvate being better represented by the non-standard setting of $P2_1/n$.

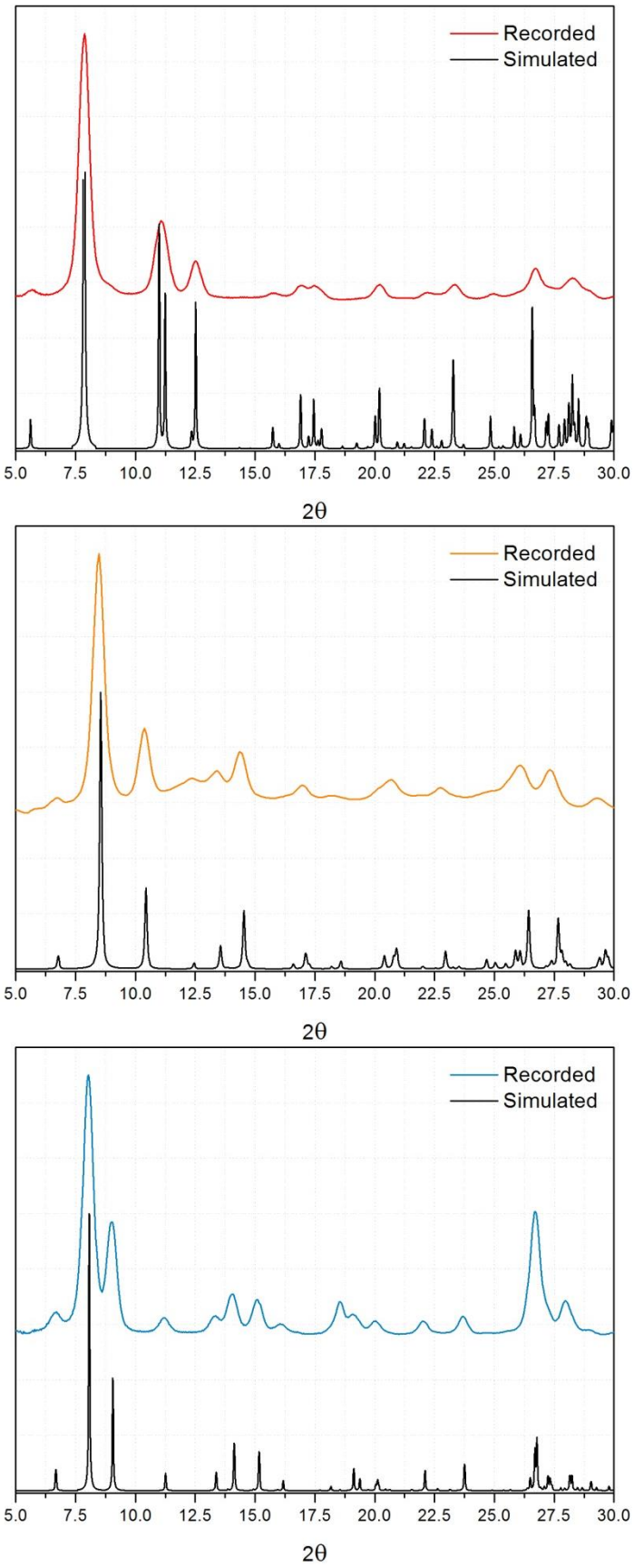

Figure 3.20. Comparison of the recorded powder patterns for the bulk solid and the simulated patterns from the single crystal data. Form-I (top) Form-II (middle) Form-III (bottom).

In the single-crystalline form, the compound is still extremely sensitive to the aforementioned set of property-altering conditions, and mounting samples and performing data collections proved highly challenging. While single-crystal to single-crystal transformations were subsequently observed between **form-I** and **III** by placing crystals of **form-I** in a mixture of acetonitrile and methanol (5:1) for two weeks, any rapid conversion (such as exposure of **form-II** and **III** crystals to air) resulted in immediate fracturing and degradation of the crystals. All attempts at single crystal transformations *in-situ* on the diffractometer to obtain structures of **forms-II** and **III** resulted in crystal fracture, and any conversion to **form-II** at all, from either of the other forms, has not been achieved with retained single-crystallinity.

Structures of the three forms were obtained using synchrotron radiation due to the small size of the crystals obtained, and to reduce experiment duration times in order to preserve the crystal form.

The structure of **form-III** was obtained by injecting a methanol-suspension of the tiny needle crystals into a layer of Fomblin-oil and mounting a single crystal suspended within a droplet of oil onto a micromount. This was then flash frozen to 150K using the Oxford Cryosystems cooling device mounted on the diffractometer, sealing the crystal away from the air.

The structure of the highly sensitive **form-II** was obtained again by injecting an acetone suspension of the crystals into a layer of Fomblin-oil, and mounting in the same way as **form-III**. However, the few seconds between removal of the crystal and oil drop from the oil reservoir and flash cooling on the diffractometer was enough to convert the sample to **form-I** (and lose single crystallinity). This was overcome by freezing the sample in-situ at the microscope using liquid nitrogen, before moving the sample to the diffractometer.

3.4.4.2.1 Crystal structures of the three coloured forms

The structure of **form-I** consists of an asymmetric unit consisting of one neutral molecule of **(16)** and one molecule of water. The platinum centre in **(16)** adopts the expected square planar geometry with the cyanide group *trans*- to the coordinated carbon of the arene ring. The molecule is essentially planar, with the methyl group lying in the plane of the pincer ligand. The square planarity shows the expected minor distortion (N1-Pt1-N2 angle 160.73° (12)) due to the pincer bite angle, with bond parameters in the expected ranges (**Table 3.9**). [21,22,23]

Looking at the extended structure of **form-I** it becomes immediately apparent that planar stacking interactions dominate the packing, with the compound arranged into discrete columns oriented along the c-axis of the crystal (**Figure 3.21**). The molecules within each column also alternate between two rotational orientations along the *c*-axis, resulting in an angle of 33.52(11)° (taken as angle between planes: [C19, Pt1, $C19^{1}$, $Pt1^{1}$] and [$C19^{2}$, $Pt1^{2}$, $C19^{3}$, $Pt1^{3}$] where *1 = (x, y, 1+z), 2 = (x, 1/2-y, 1/2+z), 3 = (x, 1/2-y, -1/2+z)*) between each cyanide group and that of the molecules above and below (**Figure 3.22**).

Form-I

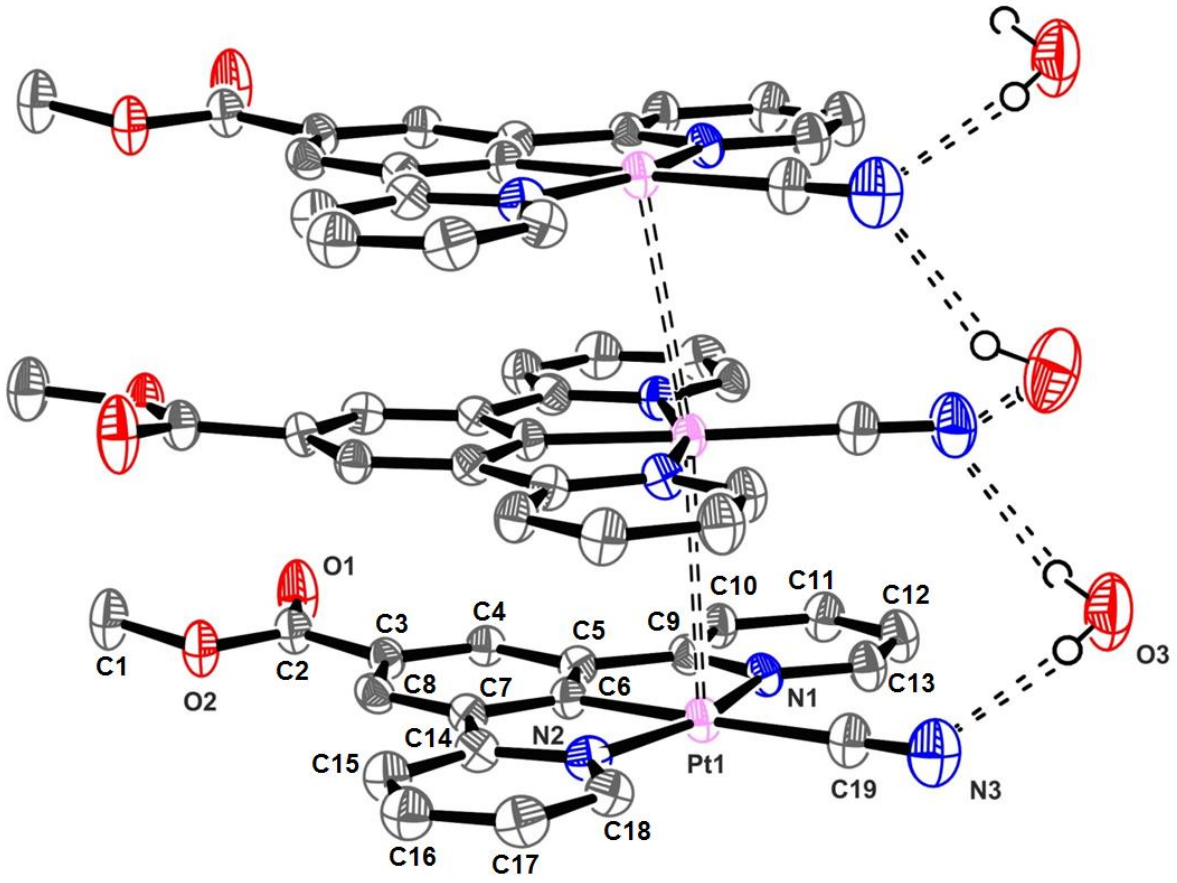

Figure 3.21. Perspective view of the structure of form-I, showing a section of one of the stacks of (16), with platinum interactions and hydrogen bonded water propagating along the c-axis. Non-water H-atoms omitted for clarity.

Table 3.1. Selected bonds for (16) form-I

Bond	Length (Å)
Pt1-N1	2.046(4)
Pt1-N2	2.040(4)
Pt1-C6	1.947(4)
Pt1-C19	2.064(4)
C19-N3	1.149(5)

Significant interaction between platinum centres is evident from this structure, with a Pt-Pt separation of 3.452(3) Å indicating a degree of d_z^2-d_z^2 interaction shown to lead to the formation of new MMLCT states in related compounds.[6,24,25] These platinum interactions result in the formation of continuous linear chains of metal contact that permeate along *c*-axis throughout the crystal. It can

also be seen however, that the metal centres that form this chain of interaction are not in a linear arrangement, showing a slight zigzag in the interaction (Pt-Pt-Pt angle of 154.17(3)°).

It is also clear from **Figure 3.21** and **Figure 3.22** that the water in the structure forms a hydrogen-bonded bridge between the cyanide groups above and below in the stack, with each cyanide acting as a bifurcated acceptor. This results in a columnar hydrogen bonded network of water that exists in a channel extending along the *c*-axis (**Table 3.2**).

Table 3.2. Hydrogen bonding interactions for (16) form-I

Bond	Distance (D..A) (Å)	Distance (H..A) (Å)	Angle (D..H..A) (°)
N3^{1} -H15-O3	2.921 (6)	2.17 (11)	141.71
N3-H14-O3	3.027 (7)	2.27 (7)	172.61

1 = (x, 1/2-y, 1/2+z)

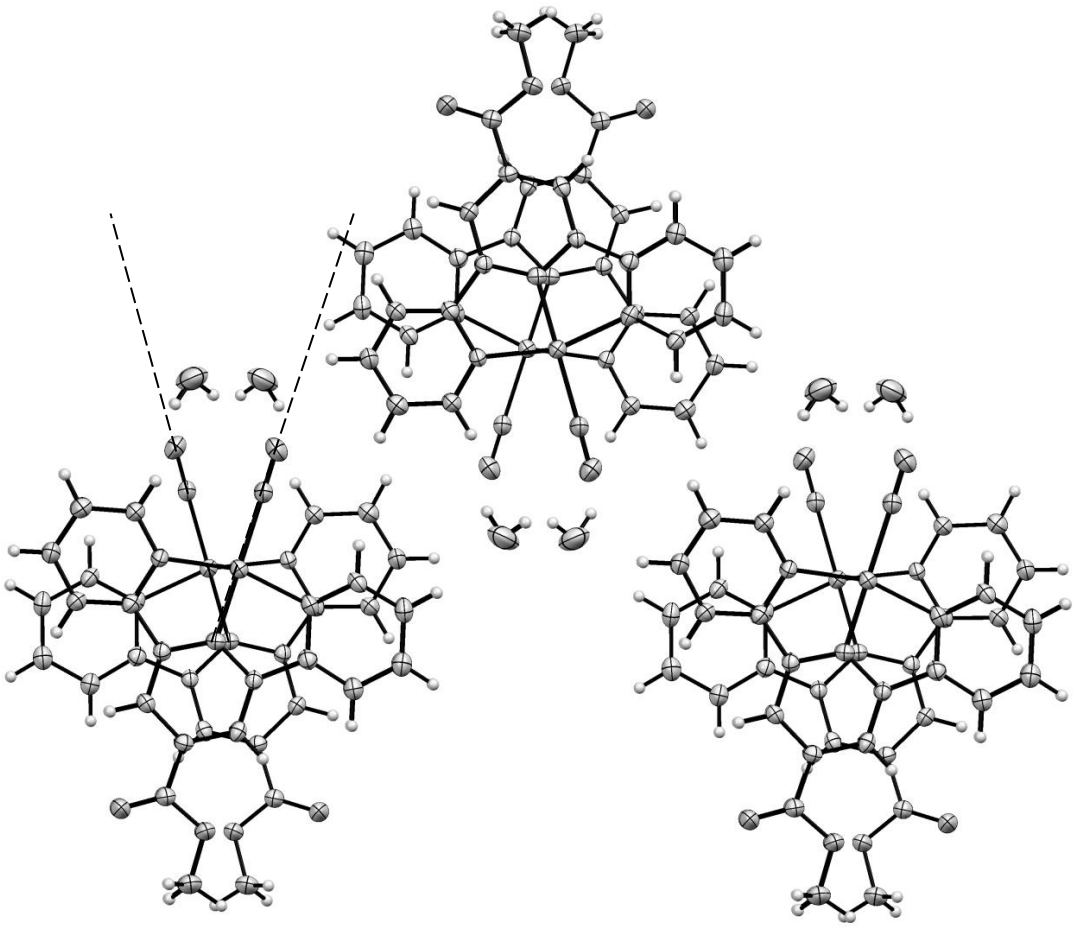

Figure 3.22. View down the c-axis, to highlight the offset of the platinum centres and the columns of water molecules relative to the stacks of (16). Planes [C19, Pt1, C19^{1}, Pt1^{1}] and [C19^{2}, Pt1^{2}, C19^{3}, Pt1^{3}] represented as dashed lines.

Subsequently the presence of one equivalent of water in the bulk solid **form-I** has been confirmed with thermogravimetric analysis. (**Figure 3.23**)

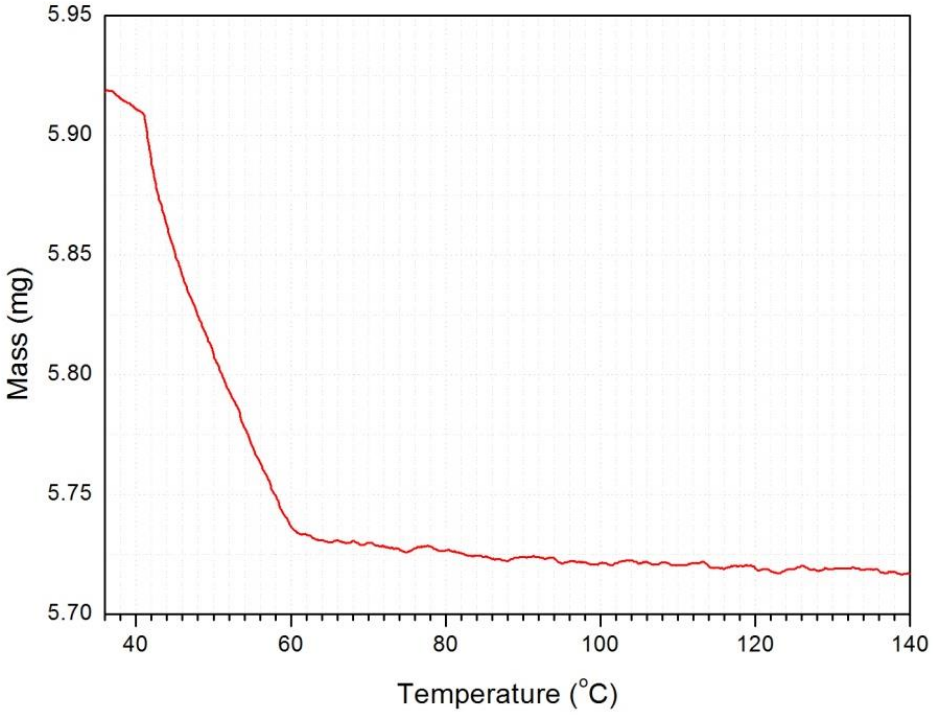

Figure 3.23. Thermogravimetric analysis of (16) Loss by 60 °C corresponds to ~17 g/mol indicating almost the total loss of one equivalent of water per molecule of (16).

Form-II

The structure of **form-II** consists of an asymmetric unit consisting of simply one neutral molecule of **(16)** with internal structure very close to that seen in **form-I**. The platinum centre again adopts the expected square planar geometry with minor distortion (N1-Pt1-N2 angle 160.10° (18)) due to the pincer bite angle, with bond parameters in the expected ranges (**Table 3.3**). [21,22,23]

The most obvious characteristic of the solid-state extended structure of the yellow **form-II** (**Figure 3.24** and **Figure 3.25**) is its similarity to that of **form-I**. It again exists as planar stacks of alternating orientations of **(16)** arranged into columns. The first and most obvious difference between the two is the lack of water in the structure, confirming water loss as a driving force behind the structural rearrangement. A slight planar shift between the alternating molecules within the stacks accompanies this lack of water, enlarging the extent of the staggering seen in the platinum stacking interactions and producing a more pronounced zig-zag. This new Pt-Pt-Pt angle of 142.48(2)° is accompanied by an enlargement of the Pt-Pt separation by 0.21 Å to 3.663(1) Å. This suggests a reduction in dz^2 orbital overlap compared to **form-I.** Apart from this small lateral translation, the structure remains remarkably similar given the notable shift in optical properties, and the torsion of 37.71(15)° (taken as angle between planes: [C19, Pt1, $C19^1$, $Pt1^1$] and [$C19^2$, $Pt1^2$, $C19^3$, $Pt1^3$] where *1 = (x, y, 1+z), 2 = (x, 1/2-y, 1/2+z), 3 = (x, 1/2-y, -1/2+z)*) between alternating molecules is close to that of **form-I**.

Table 3.3. Selected bonds for (16) form-II

Bond	Length (Å)
Pt1-N1	2.018(6)
Pt1-N2	2.025(5)
Pt1-C6	1.917(6)
Pt1-C19	2.055(5)
C19-N3	1.149(5)

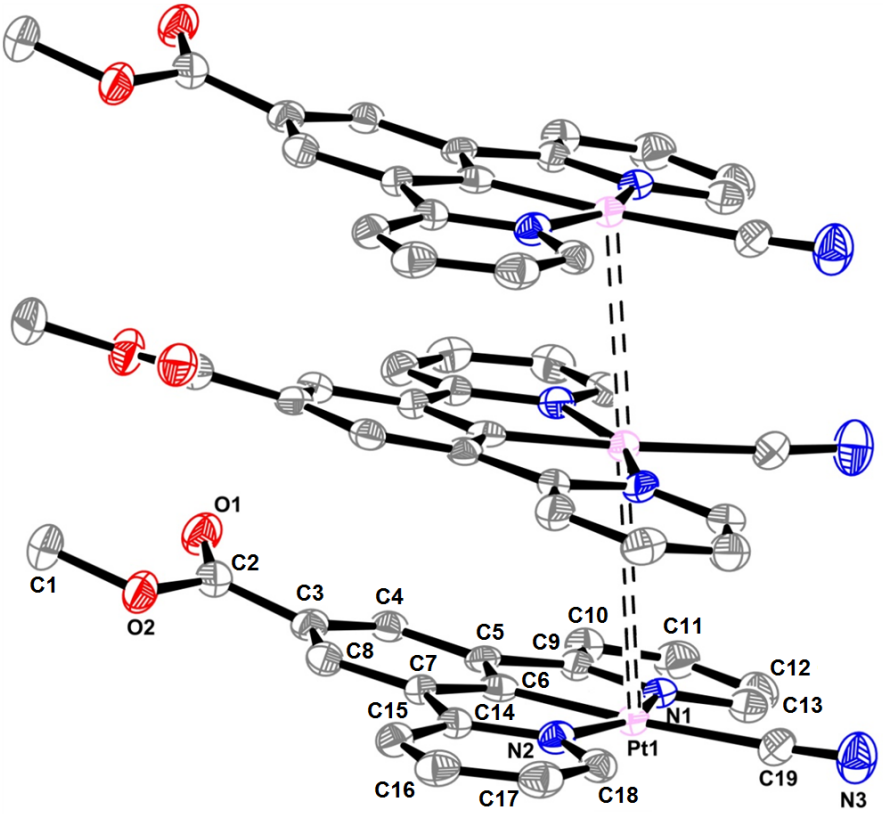

Figure 3.24. Perspective view of the structure of form-II, showing a section of one of the stacks of (16), with highly similar structure for form-I, but with the notable absence of water. H-atoms omitted for clarity.

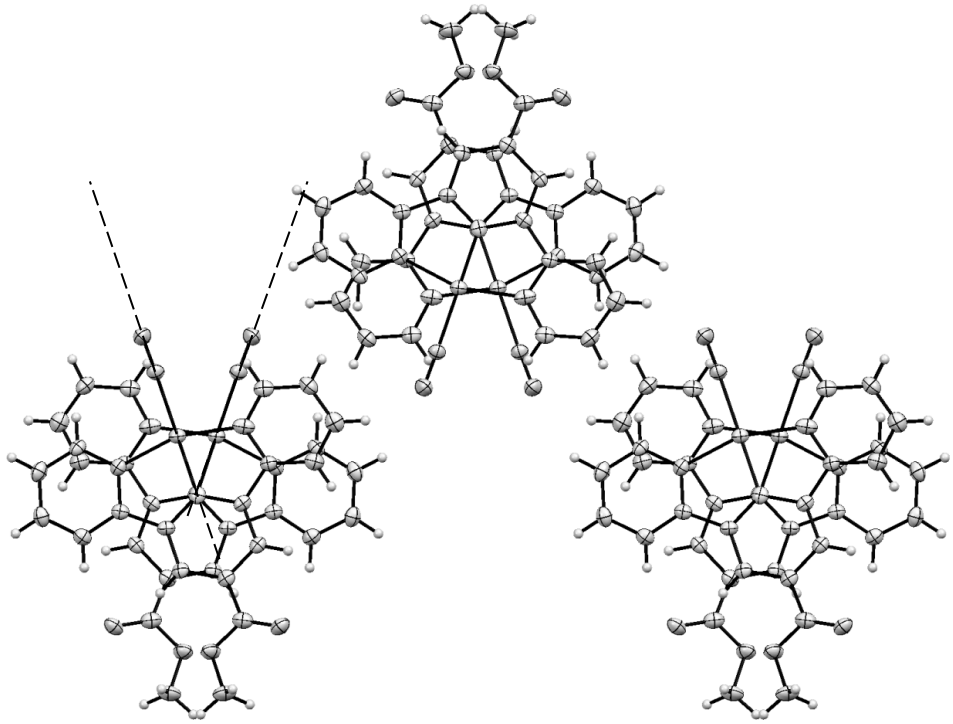

Figure 3.25 View down the c-axis, to highlight the similarity in structure, but also the increased offset of the platinum centres relative to form-I. Planes [C19, Pt1, $C19^{1}$, $Pt1^{1}$] and [$C19^{2}$, $Pt1^{2}$, $C19^{3}$, $Pt1^{3}$] represented as dashed lines.

Form-III

The structure of **form-III** consists of an asymmetric unit consisting of one neutral molecule of **(16)** (again with a very similar internal structure to the two previous forms) and one molecule of methanol. The platinum centre adopts the expected square planar geometry with minor distortion (N1-Pt1-N2 angle 160.37° (12)) due to the pincer bite angle, with bond parameters in the expected ranges (**Table 3.4**). [21,22,23]

The extended structure of **form-III** is once again very similar to that of **form-I** and **II**, with the molecules arranged in a similar stacking arrangement (**Figure 3.26** and **Figure 3.27**). It is clear that for this structure, methanol now fills the role that water plays in **form-I**. Due to the single hydrogen-bond donor nature of methanol, a discrete hydrogen bond (no bridges between adjacent molecules) can be seen (details in **Table 3.5**). The ratio of compound to solvent however, remains 1:1, and hydrogen bonded solvent can be seen to again occupy a channel extending through the entire c-axis of the structure.

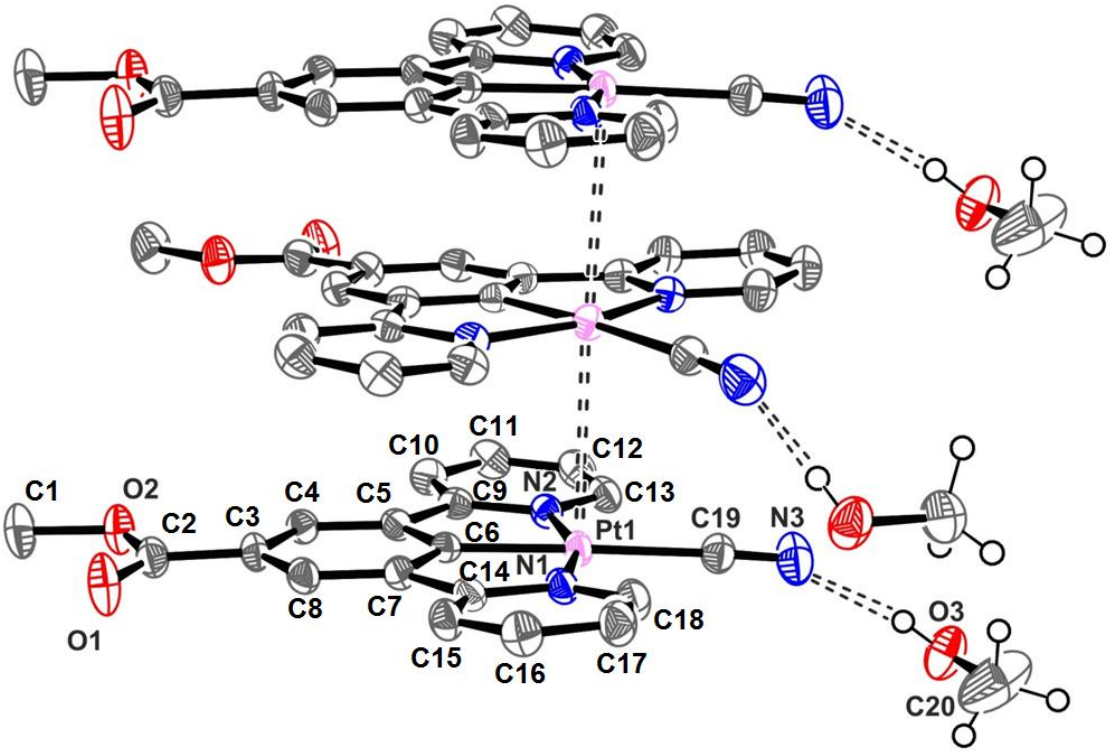

Figure 3.26. Perspective view of the structure of form-III, showing a section of one of the stacks of (16), again with highly similar structure for form-I and II, but with a column of hydrogen bonded methanol following the stacks along the c-axis. (In place of water in form-I). Non-methanol H-atoms have been omitted for clarity.

Table 3.4. Selected bonds for (16) form-III

Bond	Length (Å)
Pt1-N1	2.036(3)
Pt1-N2	2.030(3)
Pt1-C6	1.917(6)
Pt1-C19	2.047(4)
C19-N3	1.139(5)

Table 3.5. Hydrogen bonding interactions for (16) form-III

Bond	Distance (D..A) (Å)	Distance (H..A) (Å)	Angle (D..H..A) (°)
N3 -H17-O3	2.764 (5)	1.95 (5)	173.20

The most pronounced difference between the structure of **form-III** and that of **forms-I** and **II** is the increase in the alternating planar torsion seen relative to neighbouring molecules (52.36(11)°) (taken as angle between planes: [C19, Pt1, $C19^{1}$, $Pt1^{1}$] and [$C19^{2}$, $Pt1^{2}$, $C19^{3}$, $Pt1^{3}$] where *1 = (x, y, 1+z), 2 = (x, 1/2-y, 1/2+z), 3 = (x, 1/2-y, -1/2+z)*), coupled with a planar translation. As a result of this shift, likely driven by the inclusion of the larger methanol molecule between the columns of **(16)**, the chain of platinum interactions that traverses the length of the *c*-axis is now comprised of almost totally aligned platinum centres (Pt-Pt-Pt angle of 178.41(1)°) and with a Pt-Pt distance of 3.3875(6) Å. This is 0.06 Å shorter than **form-I** and 0.27 Å shorter than **form-II**.

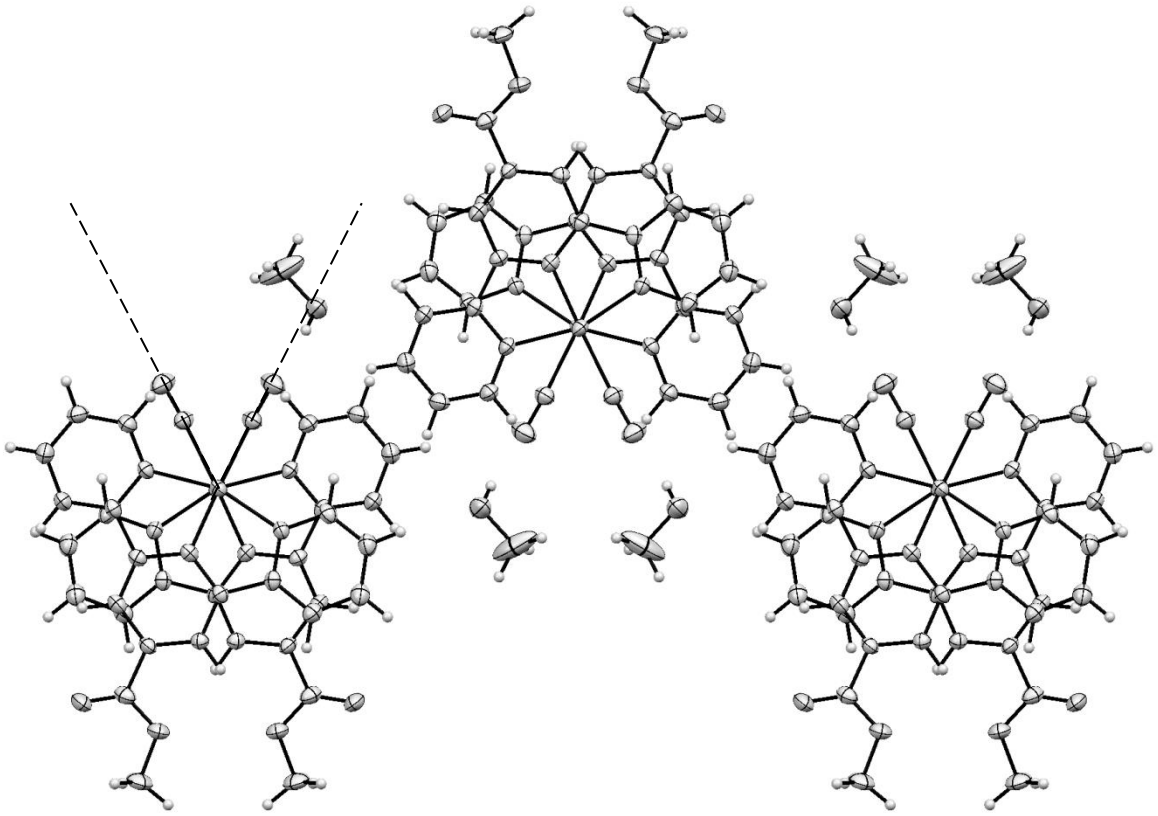

Figure 3.27. View down the c-axis, to again highlight the similarity in structure, but also now the totally eclipsed platinum centres, indicating a high level of d_z^2-d_z^2 overlap. Planes [C19, Pt1, $C19^1$, $Pt1^1$] and [$C19^2$, $Pt1^2$, $C19^3$, $Pt1^3$] represented as dashed lines.

The importance and interactions of the methyl ester group are discussed in **section 3.5.1**.

3.4.4.3 Discussion of structural data

Through observation of the single crystal data, the first conclusion that may be drawn is that the three forms are indeed structurally distinct. The driving force for the structure variation, and therefore the solid state switching observed in the bulk solid appears to be the uptake of either water via atmospheric humidity (**form-I**), or methanol (**form-III**) into the structure in a 1:1 ratio, and the subsequent re-orientation of the molecules of **(16)** to accommodate them efficiently. This appears to be driven by the formation of hydrogen bonding interactions to the cyanide group of the molecule, resulting in the formation of solvent channels that propagate along the c-axis.

Reversion to **form-II** from the other solid forms through exposure to dry gas flow, vacuum, heating or exposure to some solvents is likely to be a response to the removal of absorbed solvent from the solid, and subsequent relaxation of the structure to close the cavity left.

The channels in the structure between the columns of **(16)** contain the solvent, and provide an easy access route for solvent addition, or loss on exposure to elevated temperature or other displacive gases or liquids. This may account for the rapid reversibility observed between forms. The channel size is also likely to be an important factor in the selectivity of the transitions. While a related structure containing ethanol can be grown from ethanol solution (can be found in supporting information), ethanol was not found to enter the pores of the solid structure, and no alcohol except methanol resulted in structural rearrangement. This suggests that methanol is the largest alcohol that can pass in and out of the structure through the pores, and that of the solvents tested, only methanol and water possess small enough size alongside strong hydrogen bond donor properties required for uptake.

This serves well as an explanation for the structural changes observed in the bulk solid of **(16)** as a response to environmental conditions. What this does not do is provide an explanation as to how these three structurally distinct, but largely similar solid forms can exhibit such large variation in optical properties. In order to understand why these three very similar crystal structures can exhibit such shifts in colour and luminescence we need to look more closely at the metal-metal interaction. It is known from literature examples of platinum square planar complexes, that intermolecular interaction of the perpendicular platinum d_z^2 orbitals can sometimes lead to the formation of new higher energy σ*-occupied orbitals.[6,9]
In section **3.4.2.2** it was calculated that due to the lack of destabilising π-donor interactions from the cyanide ligand, the typically high energy d_{xz}/d_{xy}-ligand π*-hybrids were lowered in energy, leading to a high lying d_z^2-orbital relative to the frontier. It was predicted that intermolecular interactions of these orbitals, while the d_z^2 lies so close to the frontier could result in the formation of a σ* orbital rising into the frontier and becoming the new HOMO.

Looking back at the crystal structure data collected for the three forms, a trend can be observed whereby the linearity and closeness of the platinum-platinum interaction (and hence the degree of d_z^2 σ-overlap) is correlated to the red-shift of the measured absorptions (**Figure 3.28**). It would therefore appear that a potential link between the environmental conditions and the colours observed can be drawn based on the crystal structures produced. **Form-II** is the structure that the compound takes in absence of any hydrogen bonding solvent, and has a structure where the Pt-Pt separation is greatest, and the Pt-Pt-Pt angles deviate significantly from linearity. As a result, d_z^2 interactions are likely to be minimal, and we see this coincides with the most blue shifted absorption spectrum. This is consistent with examples of related

compounds whereby longer Pt-Pt distances, along with a more zigzagged Pt-Pt-Pt angle are associated with more blue shifted examples. While the Pt-Pt distance of < 4 Å is suggestive of some limited d_z^2-d_z^2 interaction,[9] It has however also been reported that sufficient metal interaction to induce a red-shift in the absorption spectrum is generally observed in structures with Pt-Pt distances only below 3.5 Å .[26,27]

Upon exposure to atmospheric conditions, the solid rapidly draws moisture into its crystal structure via hydrogen bonding interactions with the cyanide, reverting in structure to **form-I**. The resulting organised structure of hydrogen bonded water contracts the layers of **(16)** into a position where the metals are more aligned, with a shorter Pt-Pt distance. While the overall change to the structure is clearly minimal, the degree of platinum d_z^2 overlap appears to be significantly increased. This coincides with a clear red-shift to the absorption spectrum, which leads to the large colour change observed upon transition. The slightness of the structural change between these two forms goes some way to further explain how the transition can be so fast, as the optical properties are very sensitive to small changes in the metal-metal distances.

Exposure to methanol is seen to have a similar effect on the structure, only this time the effect of including the solvent in the structure is to pull the layers into a position that almost perfectly aligns the metal centres. The d_z^2 overlap for this structure is likely to be maximised, and this increase in interaction coincides with a further red-shift of absorption, leading to the colour change observed.

To summarise, the evidence gained so far seems to suggest that the ability to rapidly switch the solid between three distinct colours, is as a result of the ability to switch between three degrees of intermetallic overlap. This is due to the system having the ability to rapidly re-assemble into three distinct structures according to the conditions it is placed under.

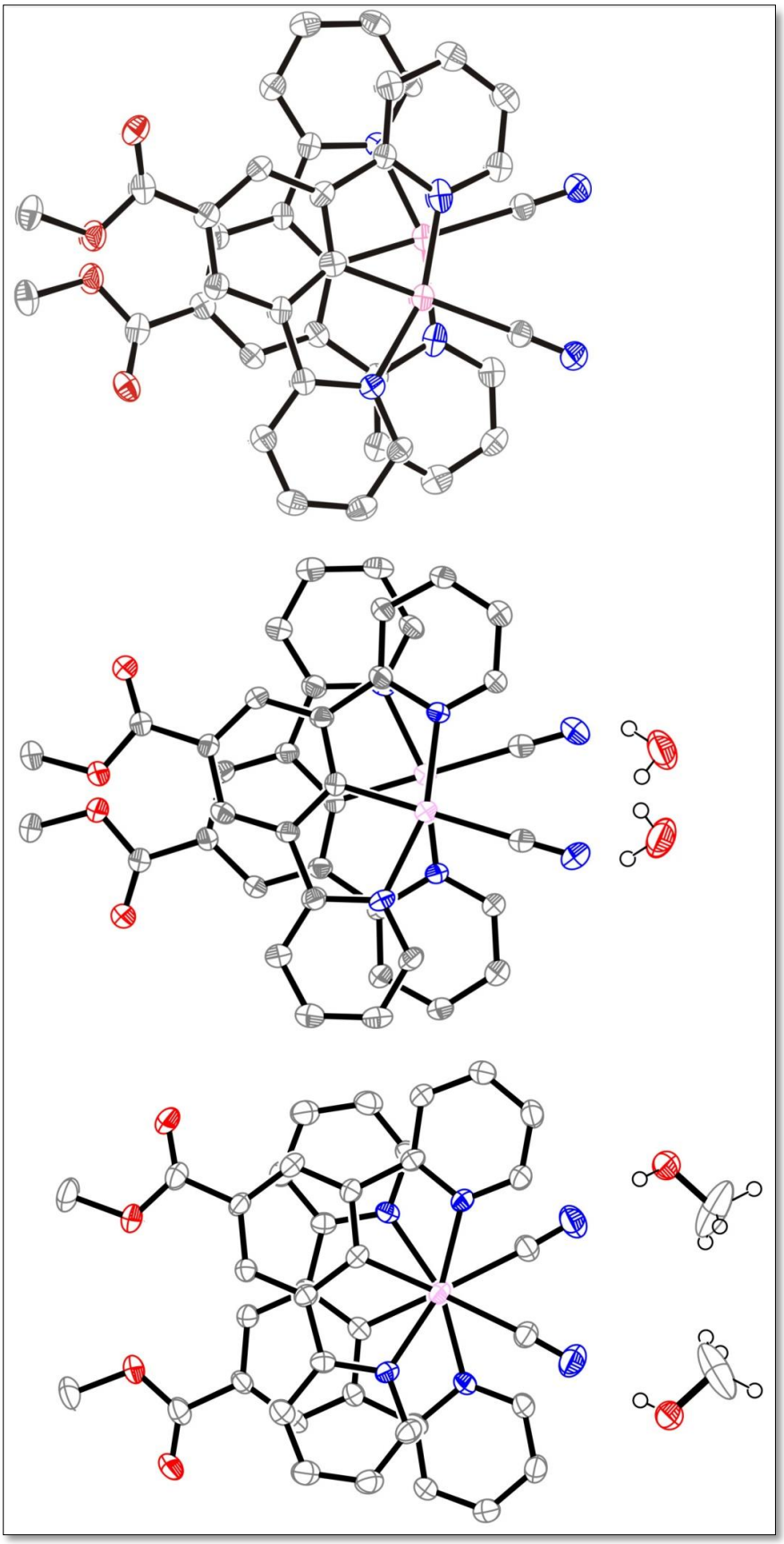

Pt-Pt-Pt (°)	colour
142.48 (2)	yellow
154.17 (3)	red
178.41 (1)	blue

Pt-Pt (Å)	colour
3.663(1)	yellow
3.452 (3)	red
3.3875(6)	blue

Figure 3.28. c-axis view of forms II (top), I (middle) and III (bottom), highlighting the increase in platinum overlap with progression from "bare" to water to methanol solvates.

3.4.4.4 Solid-state calculations

In order to more fully investigate whether the switching between the three degrees of metallic overlap observed crystallographically did in fact lead to the formation of high energy d_z^2-d_z^2 σ*-states and the shifts in optical properties, each crystal structure was investigated using solid-state density-functional theory (DFT) calculations, which were undertaken collaberatively, with calculations being performed by Dr. Jonathan Skelton, at the University of Bath.

In calculating the orbitals for each crystal structure, it was firstly shown that the crystal HOMO of each of the three forms indeed consists entirely of the parallel 1D chains of the Pt d_z^2 orbitals in a σ* arrangement, with the LUMO wavefunction remaining largely delocalised over the ligand π-systems. The solid state lowest energy transition can therefore be assigned as a MMLCT [d_z^2-d_z^2(Pt)→π*(N^C^N)] state.

Looking at **Figure 3.29** and **Figure 3.30** it is clear that while the nature of the crystal HOMO is consistent across the three forms, the degree of σ-interaction between layers clearly increases as the metal centres align. In itself, the presence of the d_z^2 σ*-state as the crystal HOMO confirms that overlap in the solid state causes sufficient splitting for it to form a new, higher energy HOMO. It therefore follows that increasing the degree of interaction will increase the splitting.

The calculations also support this. An energy-level diagram showing the positions of the four highest-energy occupied and lowest-energy unoccupied crystal orbitals can be seen in **Figure 3.31**.

It is evident from this diagram that the HOMO is indeed further displaced to higher energies as a function of the degree of inter-orbital overlap.

This destabilisation of the HOMO in the MMLCT [d_z^2-d_z^2(Pt)→π*(N^C^N)] transitions as a response to the degree of intermetallic overlap offers a definitive explanation for the large shifts to the absorption spectrum measured between the three forms.[2-4,24,28-30]

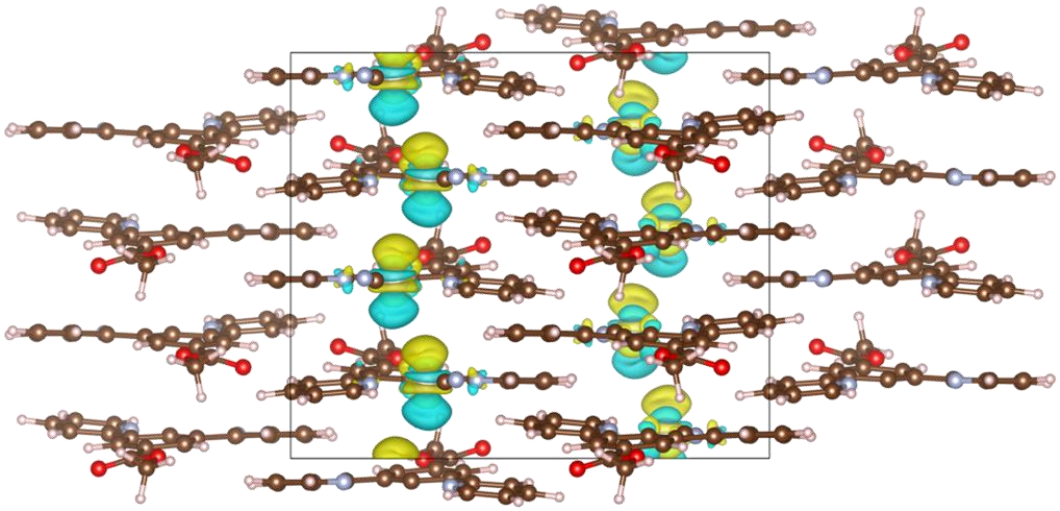

Form-II (Yellow)

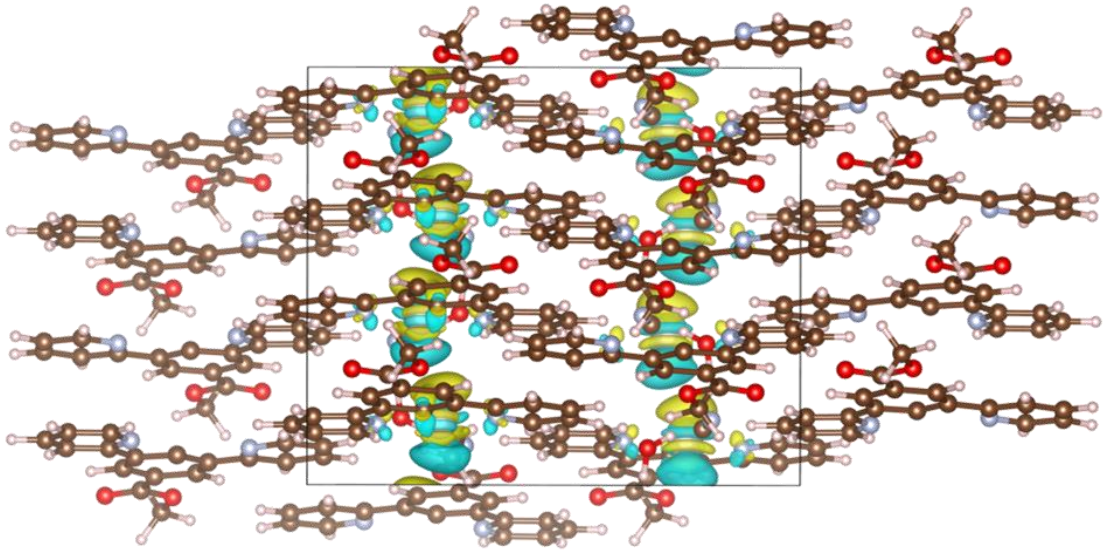

Form-I (Red)

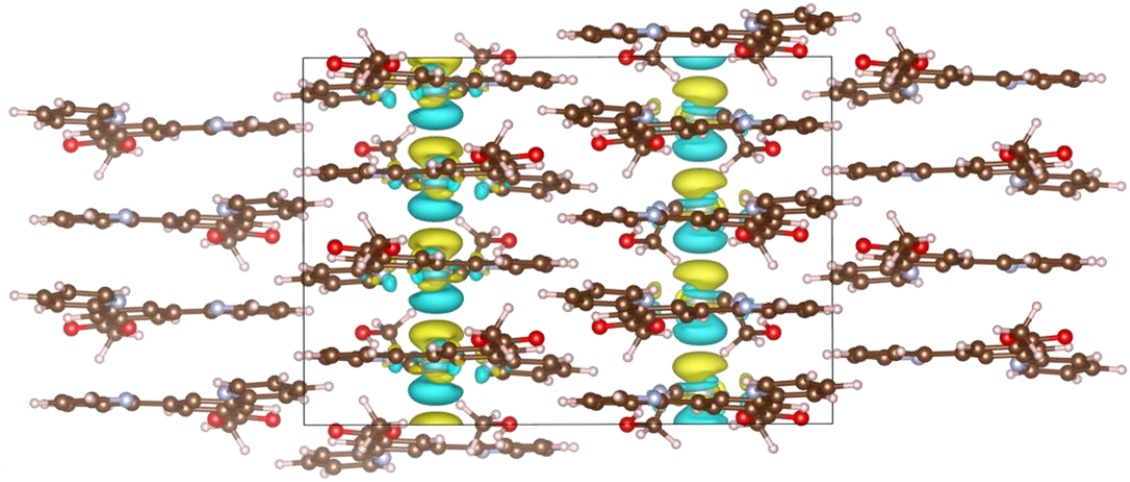

Form-III (Blue)

Figure 3.29. Calculated crystal HOMOs for the three forms, detailing increase in d_z^2 σ*-interaction.

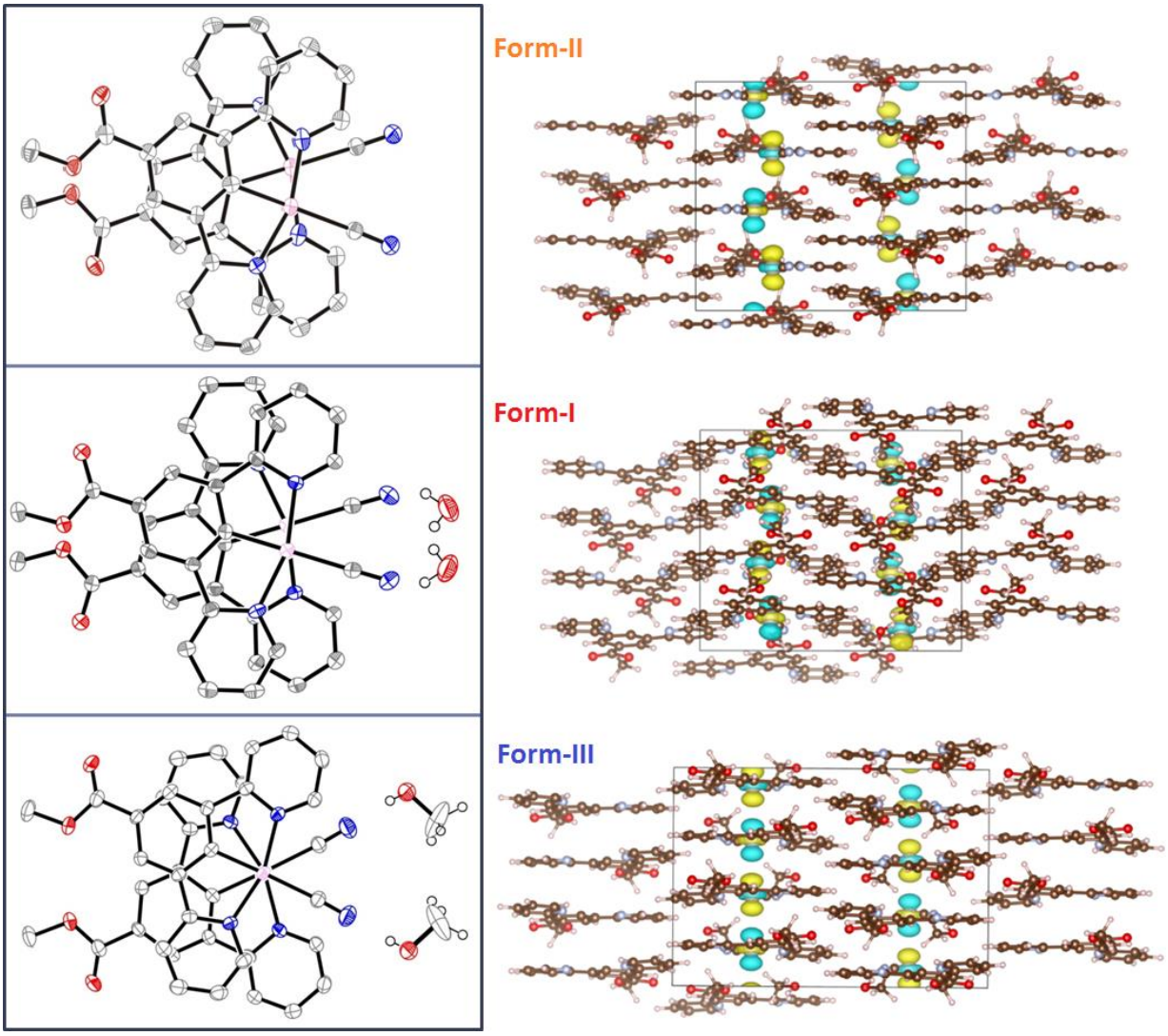

Figure 3.30. C-axis view alongside calculated HOMOs for the crystal structures to highlight how the platinum centres' orientation with respect to each other, affects the degree of intermolecular σ*- overlap in the crystal HOMO.

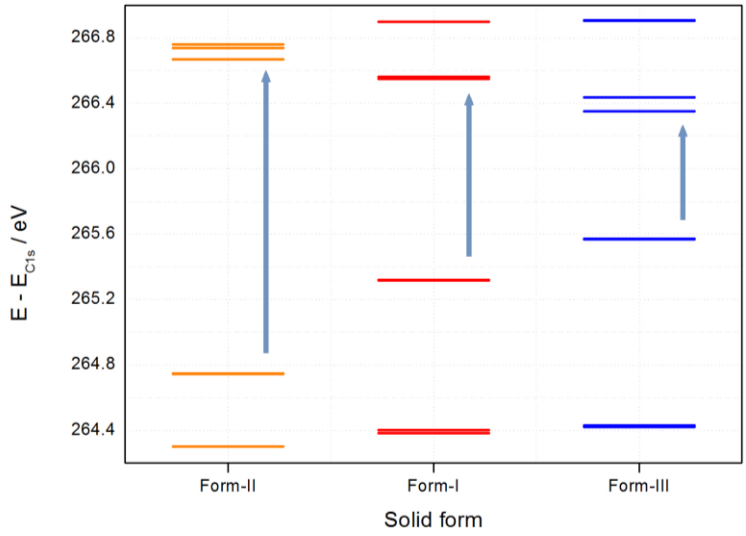

Figure 3.31. Energy level diagram showing the calculated frontier orbitals of each crystal structure. The blue arrow indicates the transition from HOMO-LUMO.

3.5 The role of the functionalisation of the pincer ligand

While vapochromism in related compounds is known, the speed and reversibility at which **(16)** switches in response to specific vapours is unprecedented.[6] The dual role of the cyanide ligand in facilitating this remarkable optical switching of **(16)** has been well established in this chapter. Through crystallographic and computational studies, strong evidence has been provided that the cyanide ligand serves as both a strong field environment for the platinum, allowing for the "exposure" of the d_z^2 orbital to the frontier and providing a suitable orbital structure for intermolecular sensitivity, and also as a hydrogen bonding handle for the rapid uptake of small hydroxyllic solvents, which provides the mechanism for the structural rearrangement.

However, the role (if any) of the methyl ester group of the pincer ligand may have in facilitating these properties is less clear. In order to study how the properties of this group may affect the switching capability of the compound by directing crystal packing, three analogues were synthesised, and their properties studied in order to establish any connection to that of **(16)**.

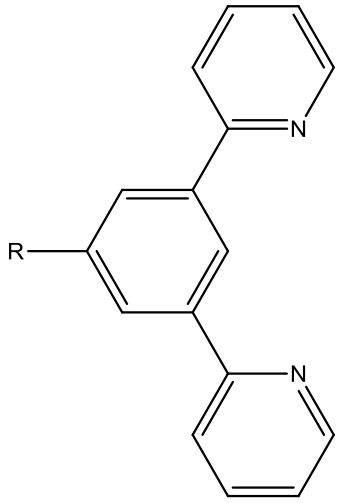

Figure 3.32. Structure of the pincer ligand used with R indicating the site of the methyl ester for (16), and the site of substitution in the subsequent modifications.

3.5.1 Methyl ester interactions in (16)

Initial analysis of the intermolecular interactions of the methyl ester group for the three forms of **(16)** may offer some insight into whether or not its presence mediates the structural rearrangement in some way, and is also a good place to start in deciding which synthetic modifications would be sensible to probe this further.

Form-II

Looking first at the solvent free **form-II**, an analysis of significant intermolecular interactions reveals that a series of C-H donor, weak hydrogen bonds are present in the structure that involve the methyl ester. Highlighted In orange (**Figure 3.33**) are weak C-H hydrogen bonds to oxygen, between the adjacent esters of the molecules above and below in the stack. In blue it can be seen that similar weak hydrogen bonds are also present to the nitrogen of the cyanide groups of the next stack. It would appear that this network of weak interactions may provide some stabilisation to the crystal structure by forming links not only within each stack, but between adjacent stacks. There is also a weak hydrogen bonding interaction between the carbonyl and the pincer of an adjacent molecule, binding the stacks of opposing direction together.

Details of these interactions can be found in **Table 3.6**.

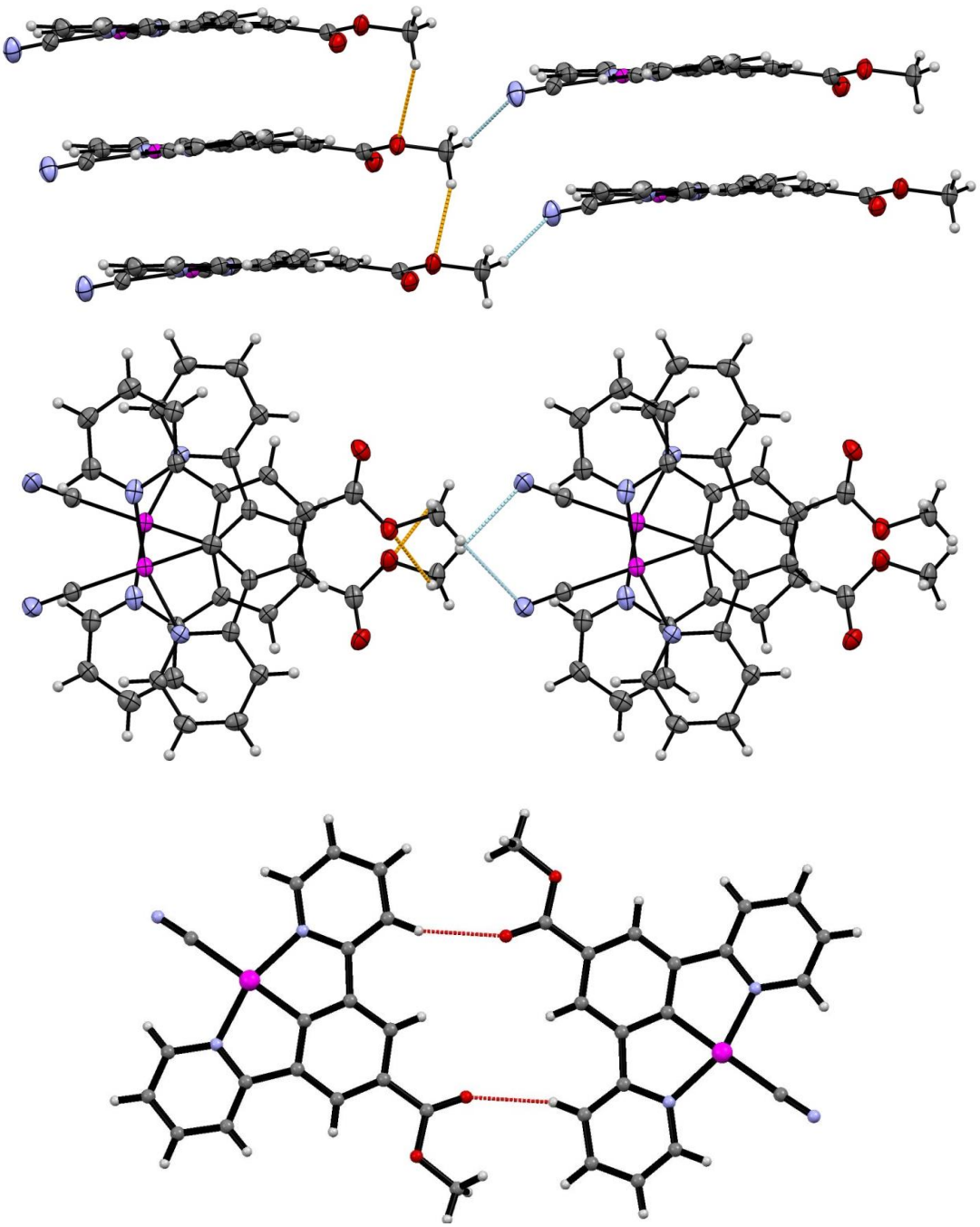

Figure 3.33. The weak hydrogen bonding interactions of form-II viewed along the b-axis (top), and c-axis (middle). Additional interactions between carbonyl and pincer (bottom).

Table 3.6. Weak hydrogen bonding interactions of form-II

Bond	Distance (D..A) (Å)	Distance (H..A) (Å)	Angle (D..H..A) (°)
C1 -H1B-N3[1]	3.524 (9)	2.594	163.37
C10-H10A-O1[2]	3.319 (8)	2.430	159.95
C10-H1A-O2[3]	4.401 (9)	2.723	128.30

1 = (1+x, y, z), 2 = (1-x, 2-y, 1-z), 3 = (x, 1.5-y, -1/2+x)

Form-I

Comparing this to **form-I**, we can see that water molecules have essentially inserted themselves into the weak hydrogen bonds to the cyanides of adjacent stacks (**Figure 3.34**), replacing them with regular strong hydrogen bonds (shown in green) and forming a bridge. The energetic driving force for this interaction is clear, and this may provide some explanation for the affinity of the crystal for water. We can also see that the inter-stack weak hydrogen bonds remain (orange), but this time they are again bridged by the inserted water molecules, possibly helping to stitch the chains together as one unit. The ester based weak hydrogen bonds between the molecules within each stack are no longer present, but looking at the c-axis view it becomes clear that the ester groups are no longer in the correct orientation, and It would appear that the lack of this interaction in maintaining structural integrity is made up for by the new bridging interaction provided by the solvent. The lateral translation of the molecules of **(16)** has also now allowed for a bifurcated weak hydrogen bonding interaction to adjacent pincer ligands via the carbonyl. Details of these interactions can be seen in **Table 3.7**.

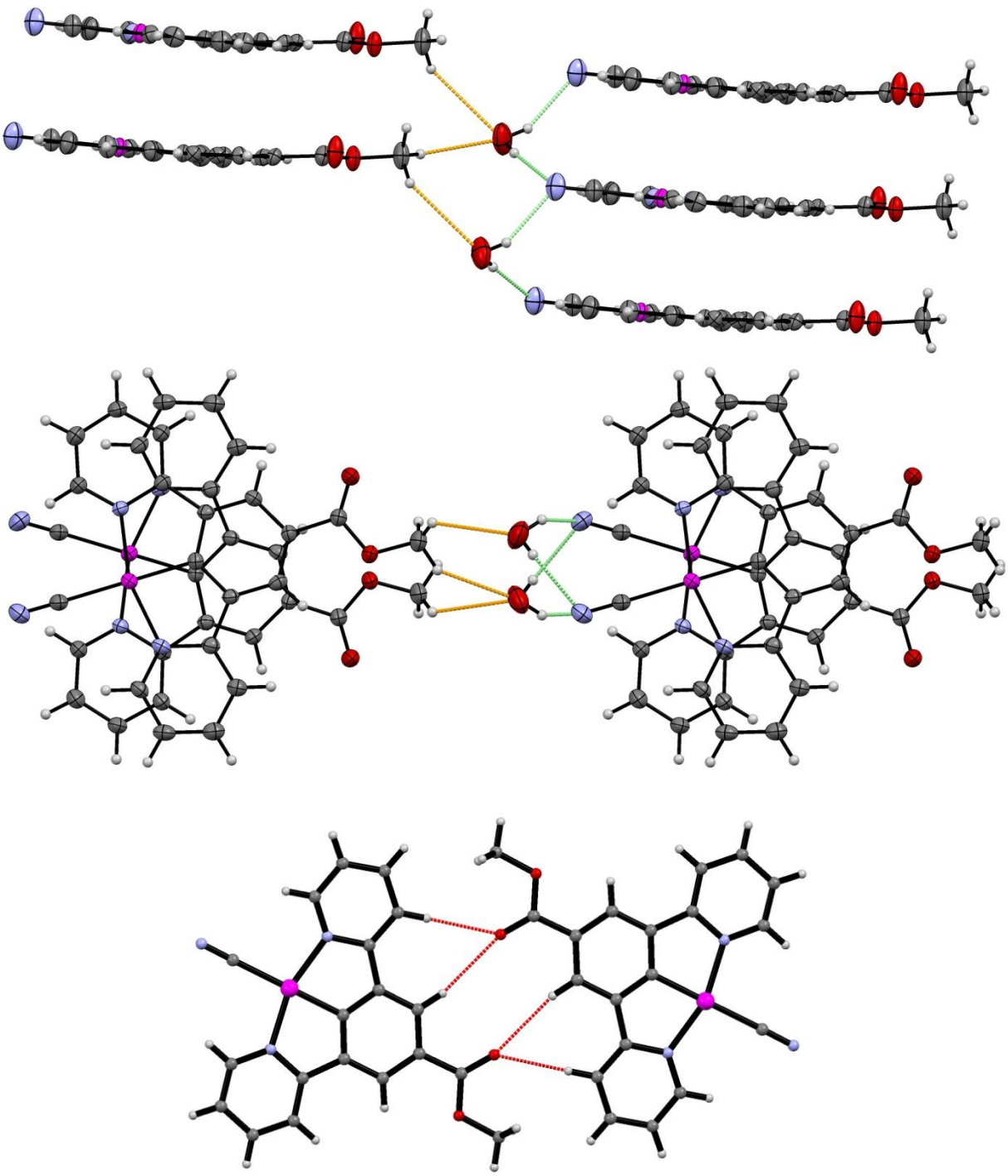

Figure 3.34. The weak hydrogen bonding interactions of form-I viewed along the b-axis (top), and c-axis (middle). Additional interactions between carbonyl and pincer (bottom).

Table 3.7. Weak hydrogen bonding interactions of form-I

Bond	Distance (D..A) (Å)	Distance (H..A) (Å)	Angle (D..H..A) (°)
C15 -H10-O1[1]	3.390 (6)	2.17 (11)	176.37
C8-H5-O1[2]	3.580 (6)	2.650	167.59
C1-H1-O3[3]	3.654 (7)	2.920	132.86
C1-H2-O3[4]	3.392 (7)	2.560	142.93

1 = (2-x, -1/2+y, 2.5-z), 2 = (2-x, 1-y, 2-z), 3 = (1+x, y, z), 4 = (1+x, 1/2-y, 1/2+z)

Form-III

The interactions seen in **form-III** are slightly more complicated (see **Figure 3.35** and **Figure 3.36**). The methanol has again inserted itself into the middle of the interaction between the ester and the cyanide, replacing it with a normal hydrogen bond to the cyanide (green). Again there is a weak C-H---O hydrogen bond (orange) from the ester to the oxygen of the methanol in a bridging fashion, as with the water structure, however, there is also an additional weak interaction from the methyl of the methanol back to the ester, making a small ring of interactions. The interactions between the carbonyl and adjacent pincer are largely the same as for **form-I**. Details of these interactions can be found in **Table 3.8**.

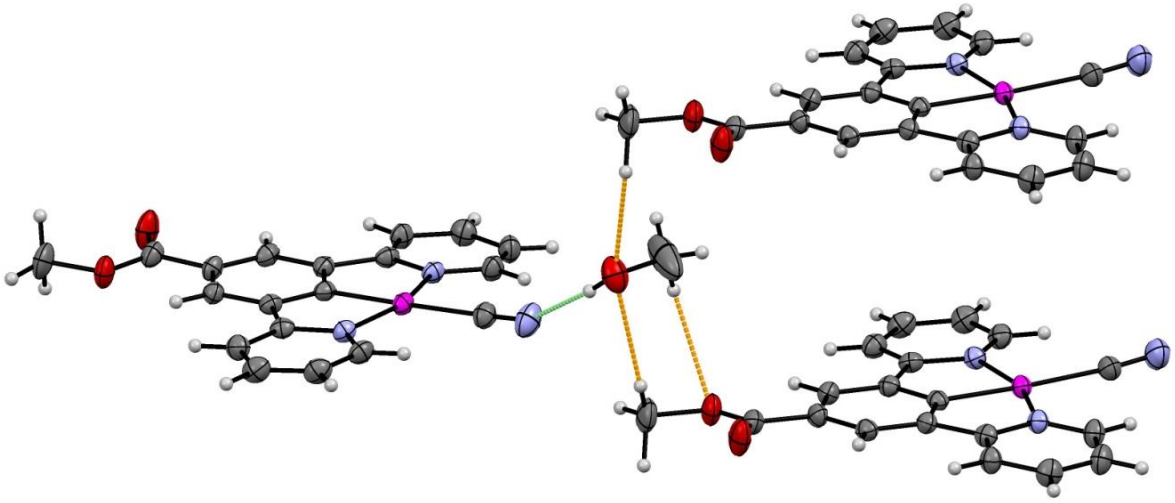

Figure 3.35. A perspective view of the weak hydrogen bonding interactions with uninvolved molecules removed for clarity.

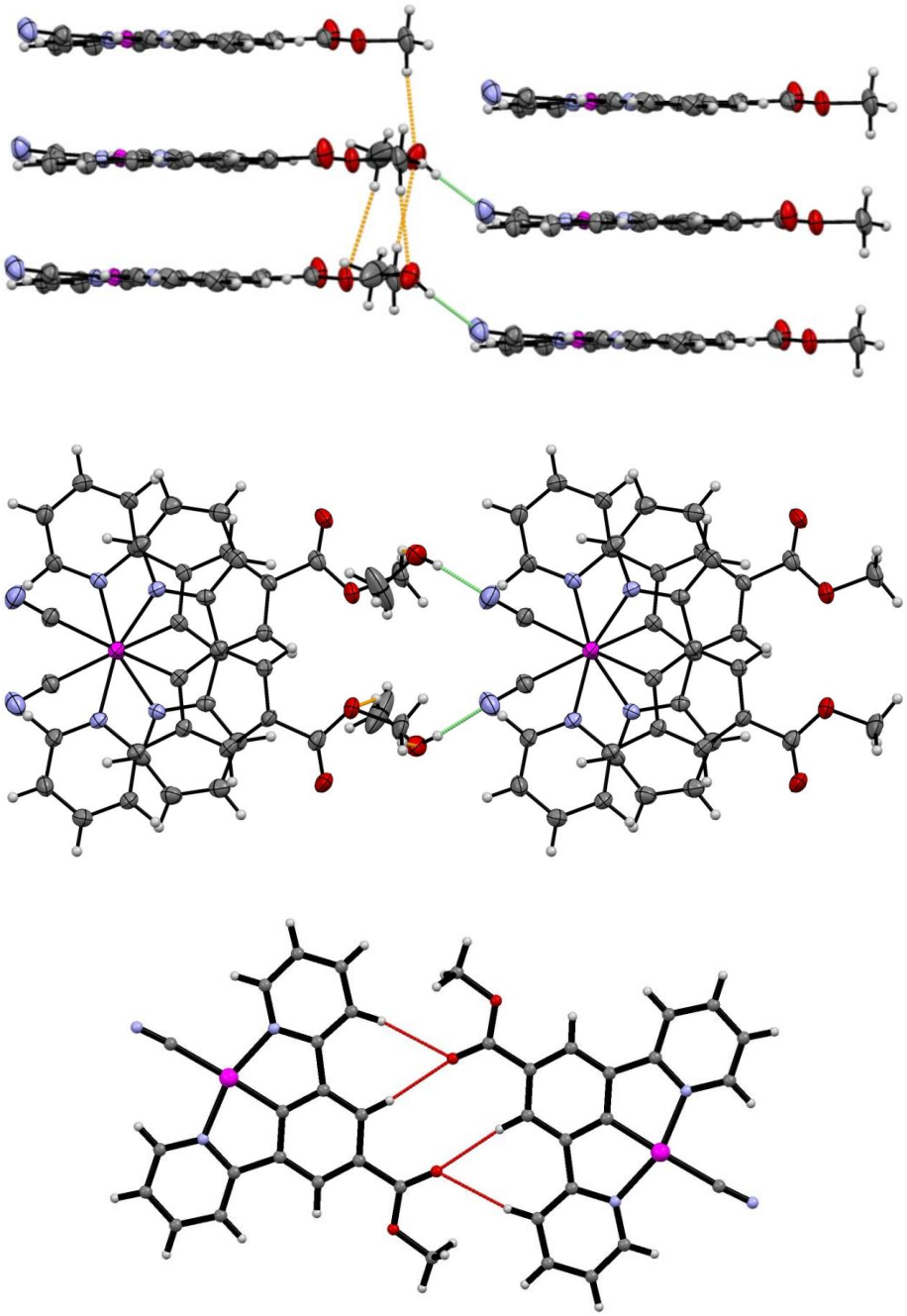

Figure 3.36. The weak hydrogen bonding interactions of form-III viewed along the b-axis (top), c-axis (middle). Additional interactions between carbonyl and pincer (bottom).

Table 3.8 Weak hydrogen bonding interactions of form-III

Bond	Distance (D..A) (Å)	Distance (H..A) (Å)	Angle (D..H..A) (°)
C15 -H10-O1[1]	3.527 (5)	2.624	158.93
C8-H5-O1[1]	3.468 (5)	2.562	159.51
C20-H14-O2[2]	3.659 (7)	2.771	150.92
C1-H3-O3[3]	3.548 (7)	2.646	154.26
C1-H1-O3[4]	3.372 (7)	2.444	139.42

1 = (2-x, 1-y, 1-z), 2 = (-1+x, 1/2-y, -1/2+z), 3 = (1+x, 1/2-y, -1/2+z), 4 = (1+x, 1/2-y, 1/2+z)

Given that interactions of this kind are present in all three coloured forms of **(16)** it seems that they are potentially a significant contributing factor in allowing the structure to transition between forms. Looking at the position of the solvent in **form-I** and **III**, particularly given that no vacant pore exists in **form-II**, it seems that a degree of flexibility is certainly required in the structure (particularly between adjacent stacks) to allow for solvent insertion/removal. It follows that these weak interactions must allow for this in that they maintain inter-stack and intra-stack interactions in the absence of solvent guests bridging *via* the cyanide, but also that the relative weakness of these interactions perhaps offer the structural malleability to allow reorientation in the presence of the stronger solvent interactions.

In order to provide evidence for the importance of these interactions specifically, a series of three analogues were chosen and synthesised and screened for vapochromic/structural rearrangement properties. The choice of analogues was based on making as minor changes as possible, so that isostructural forms could be possible, but to vary these weak interactions in some way (**Figure 3.37**).

- **Cyano[acetyl 3,5-di(2-pyridyl)phenyl]platinum (17)**
- **Cyano[ethyl 3,5-di(2-pyridyl)benzoato]platinum (18)**
- **Cyano[phenyl 3,5-di(2-pyridyl)benzoato]platinum (19)**

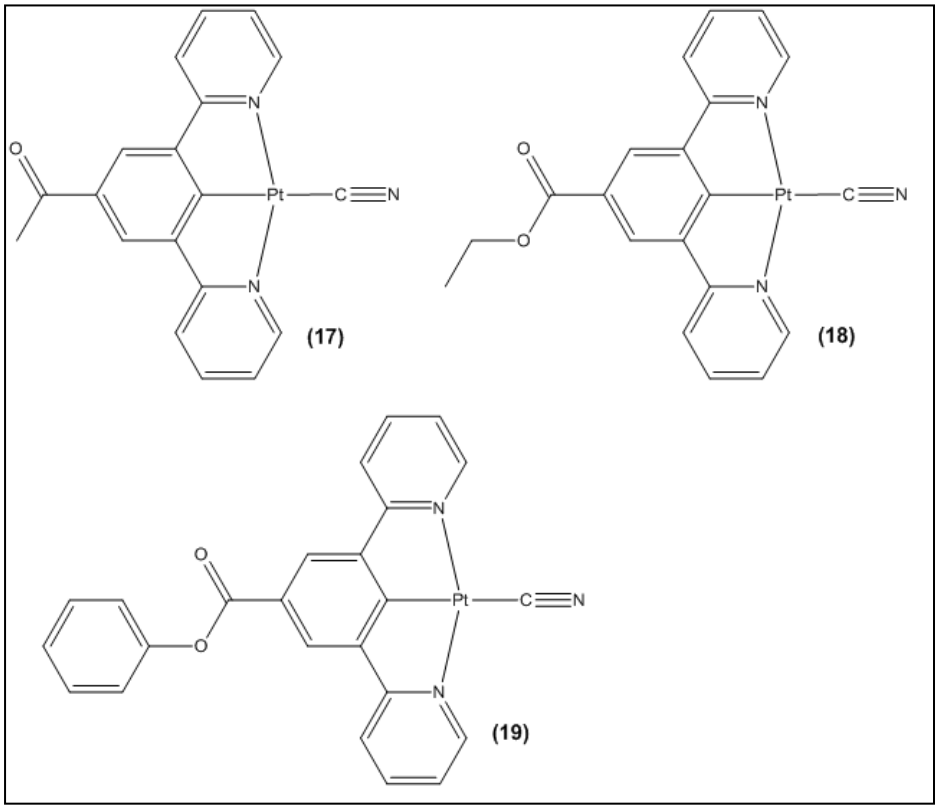

Figure 3.37. The three analogues to (16) synthesised.

3.6 Cyano[acetyl 3,5-di(2-pyridyl)phenyl]platinum (17)

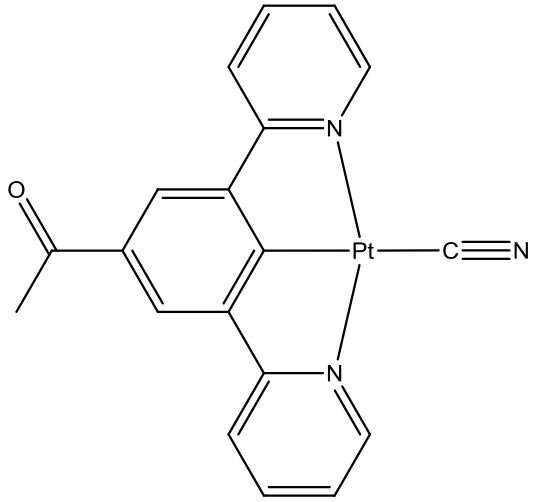

(17) was fully characterised by NMR and solid-state IR spectroscopy, mass spectrometry and x-ray crystallography (See experimental section).

The presence of the acetyl group was clearly indicated by ^{1}H NMR spectroscopy.

The IR spectrum shows a strong, sharp absorption at 2114 cm^{-1}, assignable to the $\nu_{C\equiv N}$ of a cyanide group. This value is consistent with those recorded for a series of related compounds.[12,13] Also seen is a single strong absorption at 1677 cm^{-1} assignable to the $\nu_{C=O}$ of the acetyl group, which is a typical value for an acetophenone derivative. [31,32]

3.6.1 Thermochromic behaviour

(17) displays properties that at first glance appear to be different to that of **(16)**. The compound exists as a green solid (**form-I**), and appears unaffected by the flow of dry gas or the application of solvents. However, upon strong heating (transition beginning at *ca.* 140°C) the compound does display optical switching, from green to yellow (**form-II**) (video available on supplementary information CD). This is irreversible, however, and the compound remains yellow under ambient conditions, unless re-dissolved and precipitated under ambient conditions. Based on assumptions made through comparison with **(16)** it was hypothesised that loss of solvated water from the green form was the driving force for the transition, as seen with the **form-I** to **form-II** transition of **(16)**.

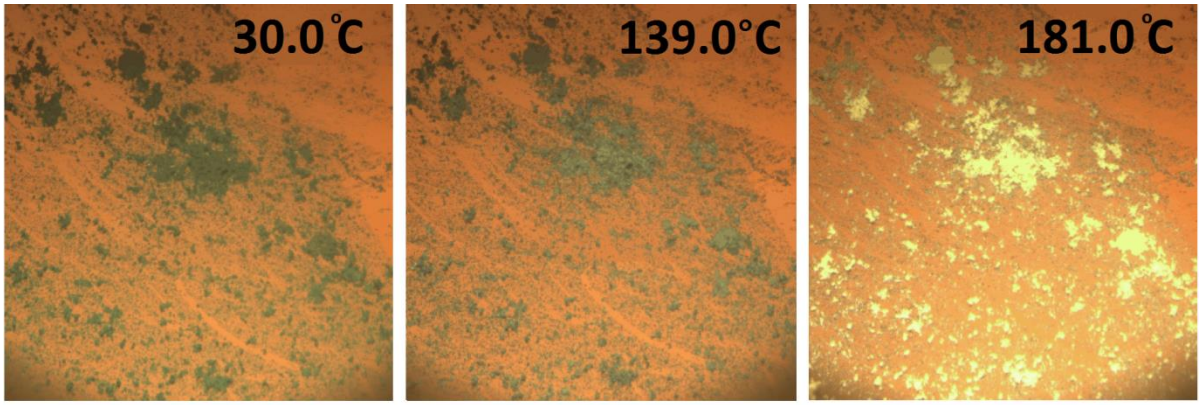

Figure 3.38. Hot-stage microscope images of (17) displaying the colour transformation.

3.6.1.1 Infrared-spectroscopy

In order to determine the nature of the transition, and whether or not it involves the loss of water, IR spectroscopy was first performed in the solid-state for the compound before and after transformation. This could be recorded only because of the irreversibility of the transition. The results of this experiment can be seen in **Figure 3.39**.

The spectra are largely identical, however upon transformation to **form-II**, there is the complete loss of a broad signal at 3405 cm^{-1}. This broad signal is highly characteristic of water as part of a hydrogen bonding network.[33] The only other differences between the two spectra can be seen as small shifts in the peaks assigned to the $\nu_{C\equiv N}$ and $\nu_{C=O}$: to 2108 cm^{-1} and 1670 cm^{-1} respectively. While few specifics can be established from these changes, these two groups are likely to be the ones involved in any hydrogen-bonding interactions with water, so the fact that these are the only two to change is again indicative of water loss.

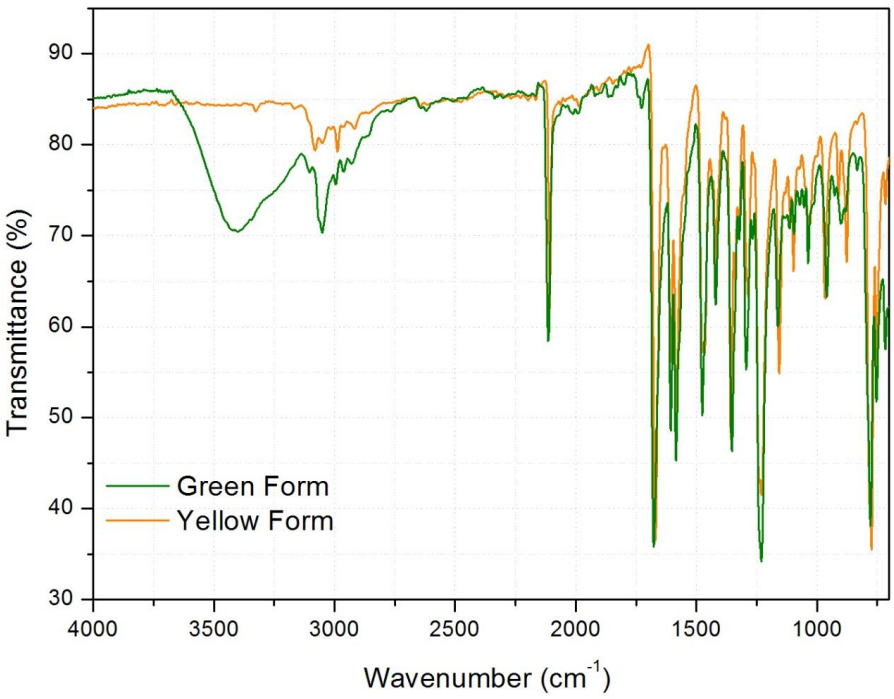

Figure 3.39. Solid-State IR spectroscopy for (17) in both green form-I and yellow form-II.

3.6.1.2 Thermogravimetric analysis

Thermogravimetric analysis was also performed to determine the proportion of water lost during the transition to form-II. The result of this can be seen in **Figure 3.40**, where a two step loss of 3.45% can be seen, which is 17.67 g mol^{-1} or one equivalent of water.

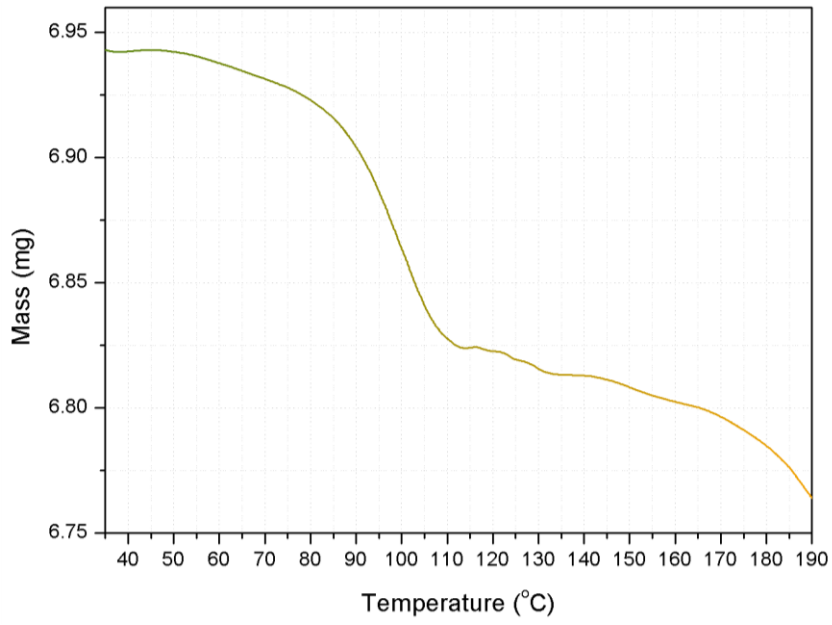

Figure 3.40. Thermogravimetric analysis of (17) showing a two-step loss of 3.45% mass.

3.6.2 Powder x-ray diffraction

In order to establish whether the green to yellow transition was a result of a structural transition, powder diffraction experiments were performed.

First, an experiment was recorded for a sample of the green powder in an open ended capillary. This was then heated using a heat gun until the sample had visibly changed completely to yellow, and another experiment preformed. The result of this experiment can be seen in **Figure 3.41**. While the patterns produced are of low resolution (measured using-in house diffractometer), they serve well as a fingerprinting tool, and it is at first immediately clear that both the forms are crystalline, giving defined diffraction patterns. It is also apparent that the crystal structure has transformed as a result of heating, producing in a markedly different pattern, indicating that a very definite structural transition coincides with the colour change, as with **(16).**

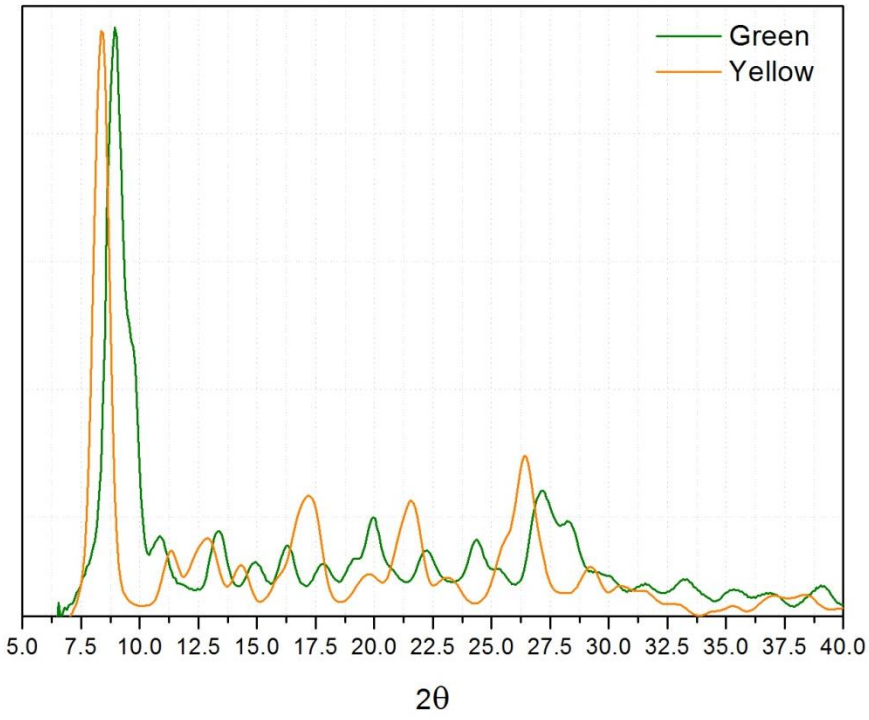

Figure 3.41. X-ray powder diffraction experiment of (17) before heating (form-I) and after heating (form-II).

In order to track the structural changes between the forms, a second capillary of the green powder was prepared (with one open end for water to leave), and a temperature scanned diffraction experiment was performed, whereby experiments were performed from 300K to 390K in 10K intervals. The experiment (seen in **Figure 3.42**) resulted in a phasing-out of the **form-I** pattern with simultaneous phasing-in of the **form-II** pattern, with increasing temperature. This suggests a definite and rapid crystalline switch, with no detectable intermediates. The incomplete conversion can be attributed to lower actual temperatures at the sample position and the restriction of water removal, both due to the powder being enclosed in glass.

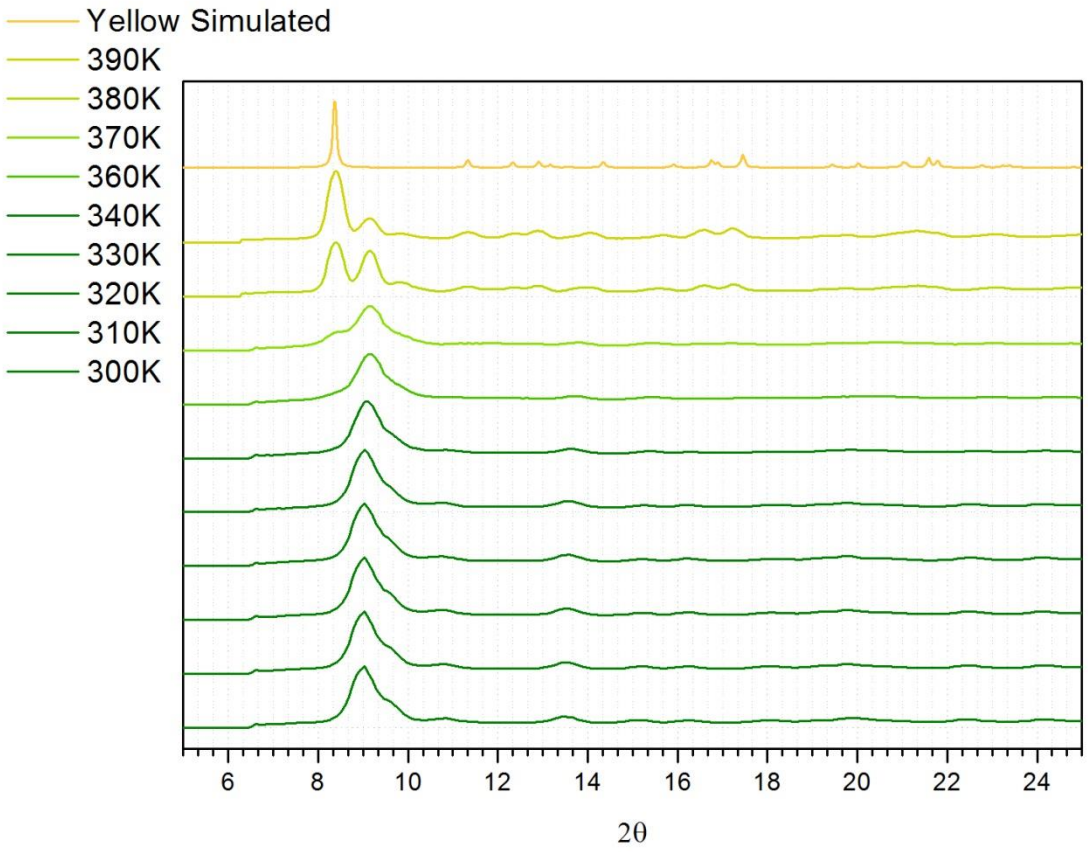

Figure 3.42. Powder diffraction run at increasing cryostat temperature intervals, indicating a crystalline transition between the yellow and green forms at high temperatures.

3.6.3 Single Crystal x-ray diffraction

Single crystal data was next required in order to provide the structure of each of the two crystalline forms, and to determine whether information as to the process of the solvent loss could be gained. Accordingly, crystallisation of the two forms was attempted.

Form-I

Crystals of the green form proved extremely challenging to produce, with the only viable method being slow cooling of a hot methanol/water or acetonitrile/water solution. However even the largest apparent crystals grown were revealed to be bundles of even smaller, extremely thin fibre-like needles (<µm). The bundles of needles/fibres produced highly twinned, almost powder-like diffraction patterns, and the individual fibres were too small to diffract even at a synchrotron source.

It seems that while the green form is certainly ordered, the extremely thin, almost fibrous structures are currently not sufficient for structure determination.

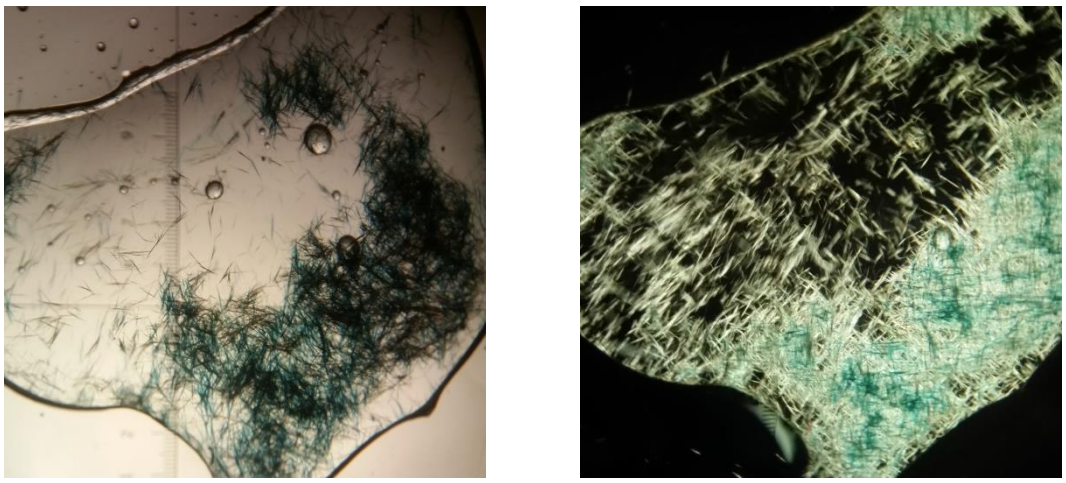

Figure 3.43. Left: Microscope image of green needle/fibre bundles. Right: the same view under crossed polarising filters to demonstrate crystallinity of the fibres.

An alternative green crystal that does not share a diffraction pattern with that of the bulk powder, however, was produced at a size able to be collected although it is of poor quality. While this structure does not accurately represent the structure of the bulk thermochromic powder, it does offer us some insights into the possible structure of the powder. The similar colouration for example suggests there may be a comparable level of intermolecular platinum interaction.

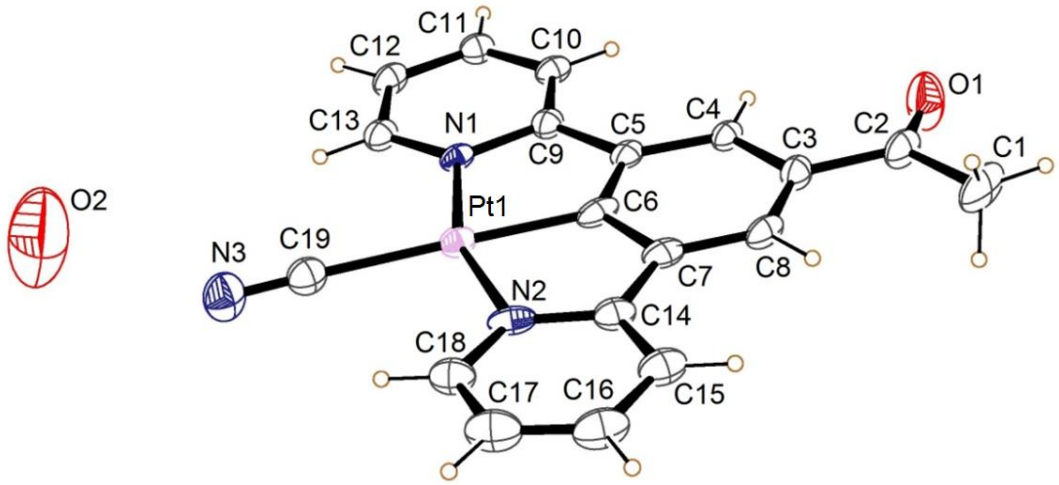

Figure 3.44. The asymmetric unit of (17) as determined by single crystal x-ray diffraction. The crystal was not of sufficient quality to resolve the water hydrogen atoms. Disordered solvent not shown for clarity.

The crystal was obtained by vapour diffusion of *n*-hexane into a water/acetonitrile solution. **(17)** crystallised in the orthorhombic space group I*bam*, with the asymmetric unit consisting of one neutral molecule of **(17)**, one defined molecule of water, and a large quantity of disordered solvent (**Figure 3.44**). The compound adopts the expected geometry, with the cyanide group being situated *trans*- to the coordinated aryl. The molecule is essentially planar, with the acetyl group lying close to the plane of the pincer. The platinum centre adopts the expected square planar geometry with minor distortion (N1-Pt1-N2 angle 159.4° (10)) due to the pincer bite angle, with bond parameters in the expected ranges (**Table 3.9**). [21,22,23]

Table 3.9. Selected bond angles for (17) green crystal

Bond	Length (Å)
Pt1-N1	2.024(18)
Pt1-N2	2.083(22)
Pt1-C6	1.946(28)
Pt1-C19	2.033(31)
C19-N3	1.182(38)

The extended structure of the crystal consists of planar units of **(17)** arranged into columns, with significant levels of platinum-platinum interaction (Pt-Pt-Pt angle of 177.20 (6) °). The molecules also alternate between two planar orientations, separated by a torsion of 47.93° (taken as angle between planes [C19, Pt1, $C19^1$, $Pt1^1$] and [$C19^2$, $Pt1^2$, $C19^3$, $Pt1^3$] where *1 = (x, y, 1+z), 2 = (x, 1/2-y, 1/2+z), 3 = (x, 1/2-y, -1/2+z)*). Each molecule of **(17)** is hydrogen bound to a molecule of water via the cyanide, which are then arranged into a network of water that extends along the c-axis see Table 3.10.

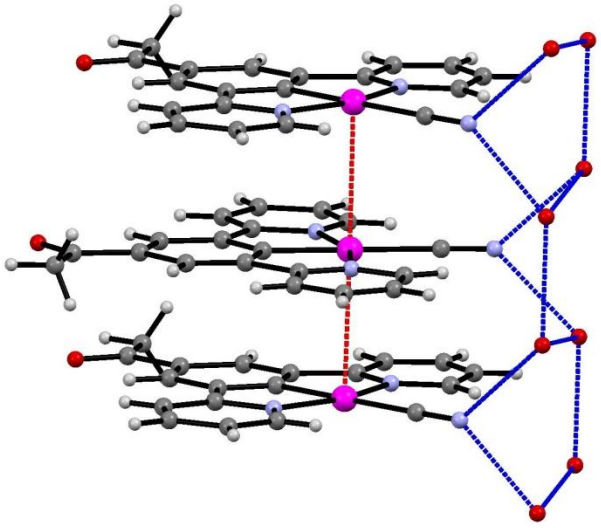

Figure 3.45. The stacks of (17), highlighting the platinum-platinum interactions (red) and hydrogen bonding to the water to the cyanide groups (blue).

Table 3.10. Hydrogen bonding interactions of (17) green crystal

Bond	Distance (D..A) (Å)
O2-N3	2.68 (6)
$O2-O2^1$	3.26 (6)
$O2-O2^2$	2.61 (5)

1 = (x, 1-y, 1/2+z), 2 = (x, y, 2-z)

The structure is also highly porous, with a large void that runs along the c-axis. Not taking into account occupying solvent molecules, the channels take up 35.6% of the total crystal volume. The channel contains disordered solvent that is unable to be resolved due to poor quality diffraction, although it is likely to be a mixture of water and acetonitrile (**Figure 3.46**). The formation of such a large pore is unusual, with packing in this way, and crystallisation in this space group not having been observed in any previous compounds of this type. As can be seen in **Figure 3.45**, the stacks of molecules along the c-axis are not dissimilar from those of **(16)** whereby they are planar, with two

alternating orientations and platinum-platinum interactions, and so in order to understand how a minor change in molecular structure has led to the formation of large pores, intermolecular interactions between these stacks need to be analysed. In **Figure 3.47** the weak C-H donor hydrogen bonding interactions have been highlighted, and it can be seen that unlike **(16)** there are no interactions between the cyanide and the substituted group (acetyl) and the orientation is completely different such that that interaction to this group bridged by solvent is impossible. It appears that the replacement of the ester with an acetyl group has prevented this type of inter-stack interaction. In the absence of this, it can be seen that there are in-plane weak hydrogen bonding interactions from the pincer to the cyanide and carbonyl groups, which in turn leads to a large ring of molecules. These rings then stack up *via* platinum-platinum interactions to create the pores of the structure. Details of these interactions can be seen in **Table 3.11**.

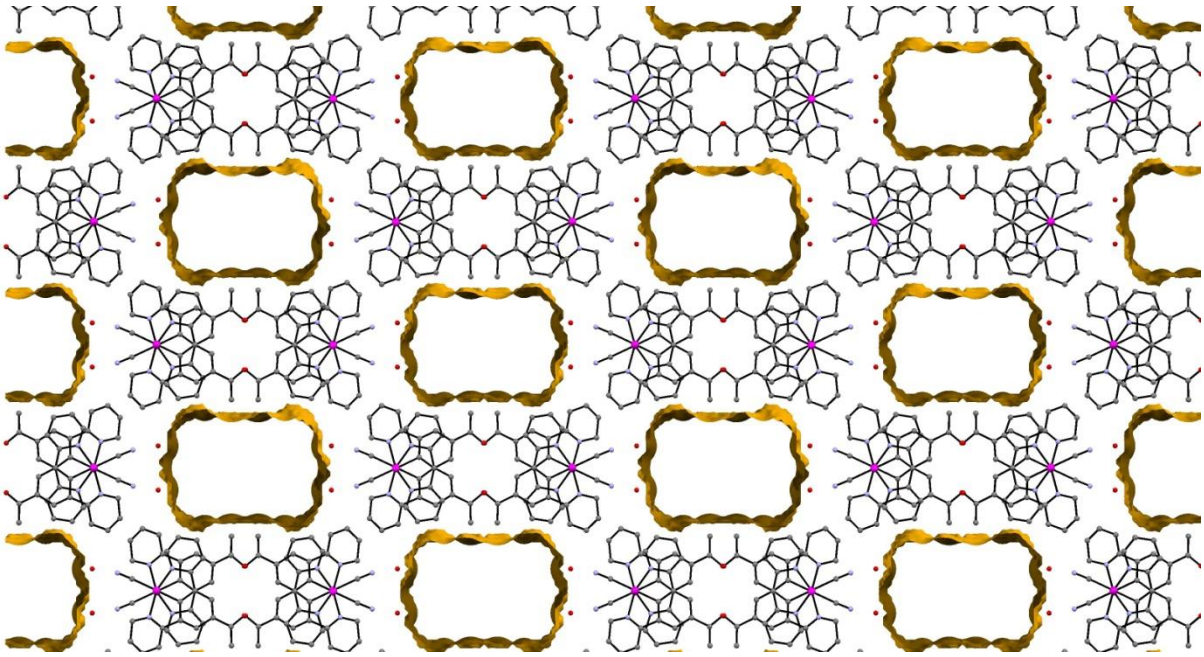

Figure 3.46. C-axis view of the structure with the large pores highlighted. Not pictured is the disordered solvent contained within the pores.

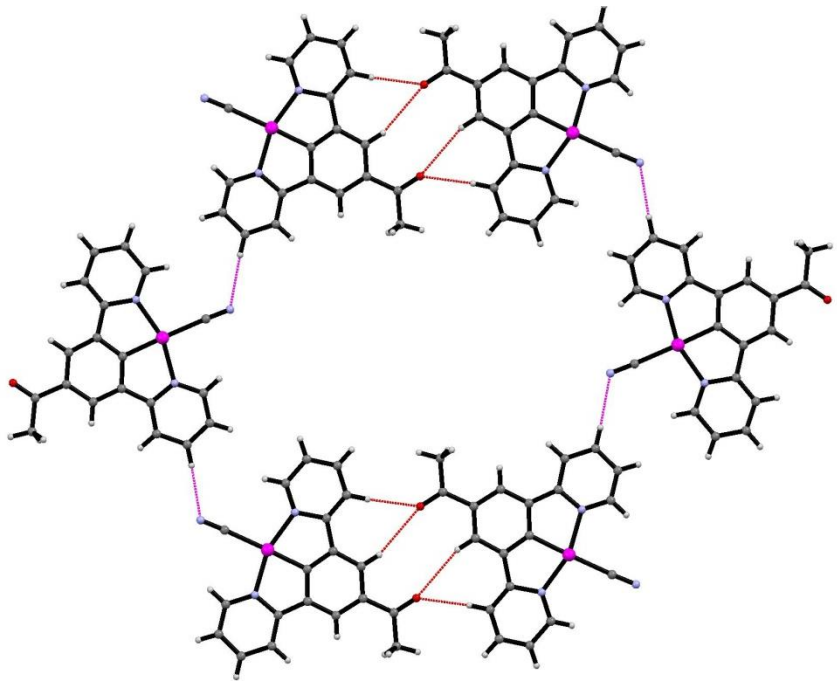

Figure 3.47. Details of the weak hydrogen bonding interactions in the structure.

Table 3.11. Weak hydrogen bonding interactions of (17) green crystal

Bond	Distance (D..A) (Å)	Distance (H..A) (Å)	Angle (D..H..A) (°)
C10 -H10-O1[1]	3.274 (21)	2.345	176.06
C4-H4-O1[1]	3.685 (21)	2.786	162.91
C16-H16-N3[2]	3.352 (23)	2.422	121.76

1 = (1-x, 1-y, z), 2 = (1/2-x, -1/2+y, 1-z)

Form-II (Heated structure)

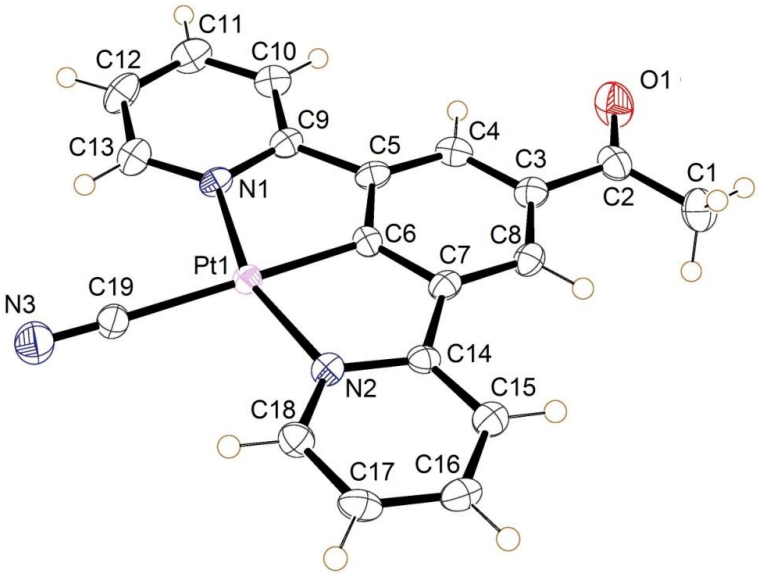

A yellow single crystal form of the compound was also produced, and was crystallised evaporatively from a dry acetonitrile solution. The compound crystallised in the monoclinic space group $P2_1/c$. This form consists of an asymmetric unit consisting of one neutral molecule of **(17)**. The internal structure of the molecule is very similar to that of the previous structure, and again, the platinum centre adopts the expected square planar geometry, with minor distortion (N1-Pt1-N2 angle 159.90° (10)) due to the pincer bite angle, with bond parameters in the expected ranges (**Table 3.12**). [21,22,23]

Table 3.12. Selected bonds for (17) form-II

Bond	Length (Å)
Pt1-N1	2.034(3)
Pt1-N2	2.043(3)
Pt1-C6	1.934(3)
Pt1-C19	2.058(3)
C19-N3	1.148(5)

The yellow crystal structure (**Figure 3.49** and **Figure 3.50**) consists of stacks of end-to end pairs of **(17)**, themselves arranged into a herringbone orientation (two orientations of stacks). Platinum-platinum separation within pairs of 4.813 (1) Å and 5.341 (2) Å between them suggests no interaction is present in this structure. Weak C-H donor hydrogen bonding interactions are present both within each pair, between pairs in the stacks, and between the stacks, which involve either the cyanide or carboxylate groups. Details of these interactions can be found in **Table 3.13**.

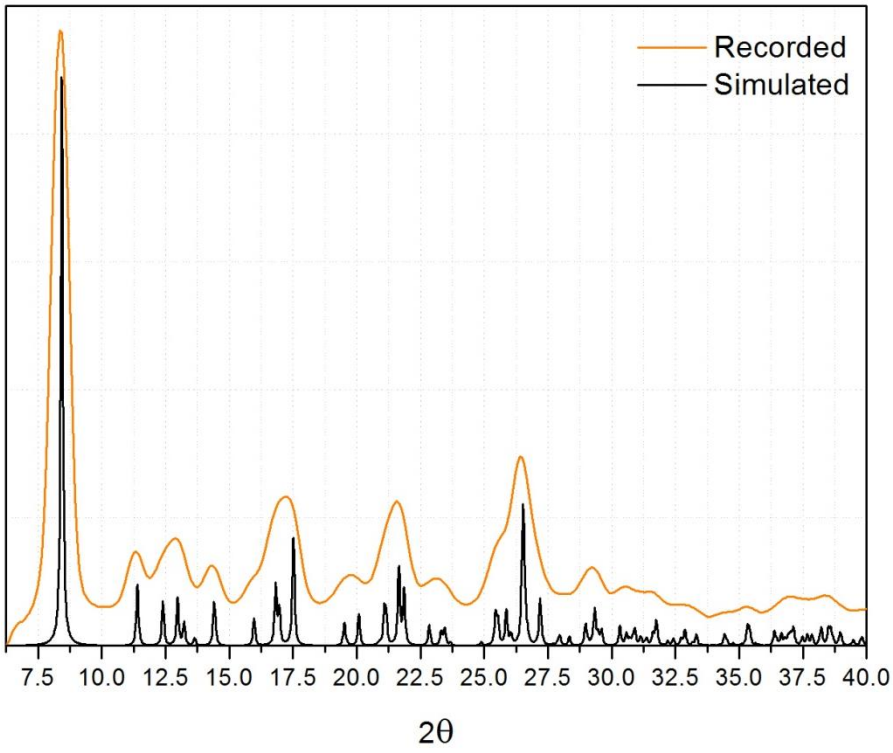

Figure 3.48. Comparison of the recorded powder pattern for (17) after heating (form-II) and the simulated powder pattern from the yellow crystals grown.

As can be seen in **Figure 3.48**, the crystal structure's simulated powder pattern is a good match to that of the heated powder, and as such can be considered a good representation of its structure. The form was revealed to be solvent free, as expected, but is very structurally different to that of **(16)** **form-II**, and it is apparent that the minor change to the pincer group has greatly altered the way the compound packs in the absence of water.

It is clear from the extended structure (**Figure 3.49**) that there are significant differences in arrangement from those of **(16)**, and from the green structure collected. As with the green crystal, there is no interaction between the acetyl group and adjacent cyanides, but it is also non-planar. The absence of this interaction between the cyanide and the substituted group of the pincer could be the important difference that prevents reversible transitions between hydrates/solvates and the dry form for this compound, when compared to **(16)**. It may be the case looking back at **(16)**, that the interaction between the ester and adjacent cyanides stabilises the solvent-free structure in a planar, and similar enough "receptive" configuration that allows for re-insertion of water/other solvents, hence the vapochromic properties (as was seen in **Figure 3.33**). The inter-stack interactions (shown in blue), but more importantly, intra-stack interactions (shown in orange) could not be present for **(17)** with the acetyl functional group.

For **(17)**, we have not determined the structure of the thermochromic green form, however, based on other experimentation and the nature of the alternative green crystals produced, it may be hypothesised that they share similarities. It is likely that the green **form-I** is a planar, platinum stacked structure, due to the heavily shifted green coloration. It has also been shown that water is present in the structure.

Based on this, it may be proposed that due to a lack of the weak intermolecular interactions to adjacent cyanides, provided by the ester group, planar structures facilitating platinum-platinum interactions for this compound are only stable in the presence of water. The transition to a buckled form, unable to re-accept water occurs once water is evacuated, and it may follow that the dissimilarity of this structure to any seen for this class of compounds so far (i.e lack of planarity) may be the cause for this lack of "receptivity".

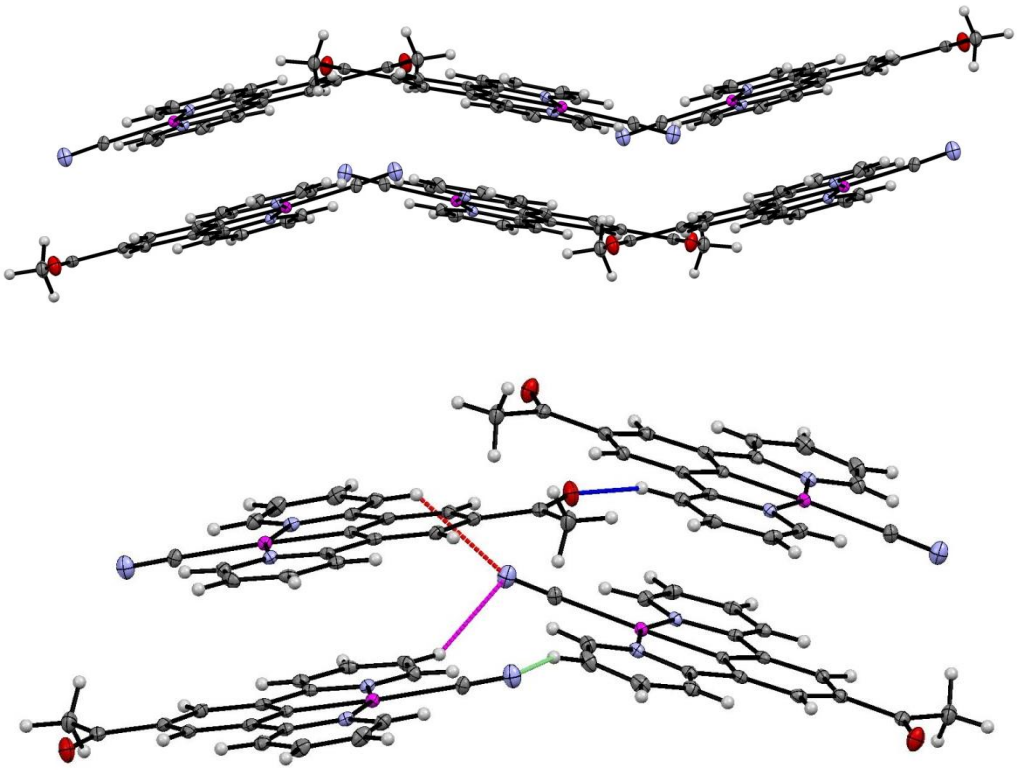

Figure 3.49. Top: herringbone arrangement. Bottom: weak hydrogen bonding interactions between the two orientations of the herringbone structure.

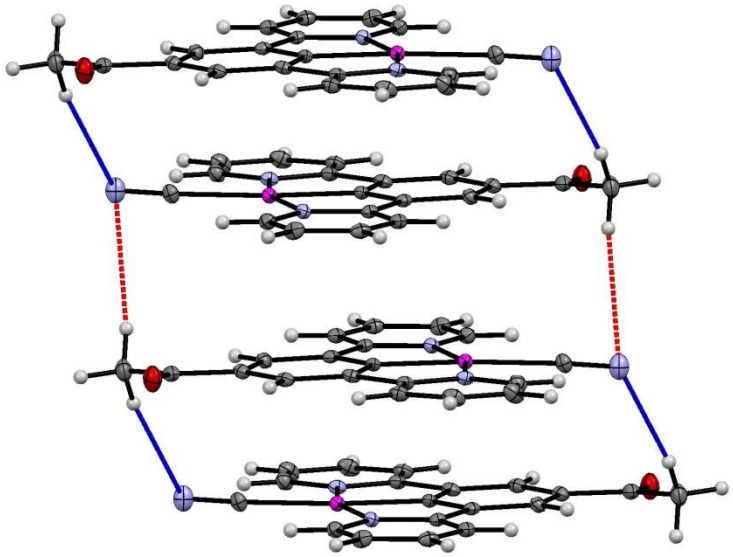

Figure 3.50. Weak hydrogen bonding interactions within and between pairs of molecules.

Table 3.13 Weak hydrogen bonding interactions for (17) form-II

Bond	Distance (D..A) (Å)	Distance (H..A) (Å)	Angle (D..H..A) (°)
C1-H1C-N3[1]	3.736 (6)	2.891	147.42
C1-H1B-N3[2]	3.742 (6)	2.792	170.35
C12-H12-N3[3]	3.315 (5)	2.526	142.80
C15-H15-O1[4]	3.148 (5)	2.447	132.20
C17-H17-N3[5]	3.721 (5)	2.867	153.29
C10-H10-N3[6]	3.460 (5)	2.788	130.08

1 = (-x, -y, 1-z), 2 = (1-x, -y, 1-z), 3 = (x, 1/2-y, 1/2+z), 4 = (x, -1/2-y, -1/2+z)
5 = (x, 1/2-y, -1/2+z), 6 = (1-x, -1/2+y, 1.5-z)

3.7 Cyano[ethyl 3,5-di(2-pyridyl)benzoato]platinum (18)

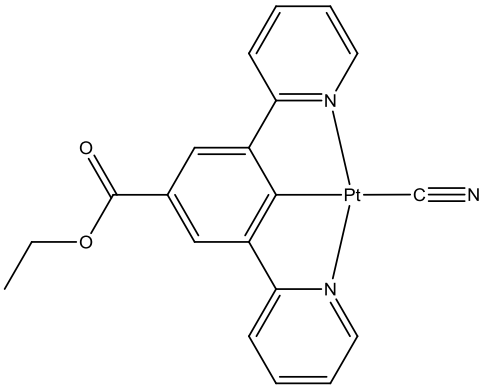

With the hypothesis that the intermolecular interactions provided by an ester are necessary in stabilising the crystal structure to the extent where solvents can exit but also for it to remain in a configuration where they may re-enter the structure, an exploration into producing alternative ester analogues was undertaken. As an obvious way in which this group may be altered in a systematic way is to vary the alkyl component to see if there is a significant impact on these intermolecular interactions and packing, and thus the vapochromic properties.

An ethyl analogue of the pincer ester was synthesised by esterifying 1,3-dibromobenzoic acid, and then performing Stille-coupling [34] as with **(5)**, then performing cyclometallation [17] and salt metathesis steps as with **(16)** to achieve **(18)** (details in **Scheme 3.1** and experimental section).

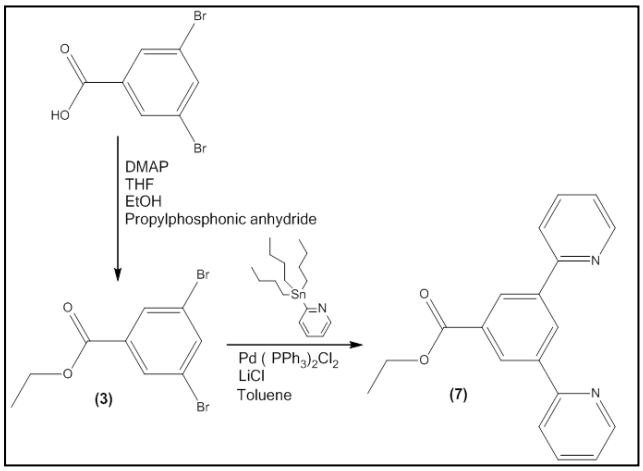

Scheme 3.1. General reaction pathway taken to produce ethyl-ester pincer ligand.

(18) was fully characterised by NMR and solid-state IR spectroscopy, Mass spectrometry and x-ray crystallography (see experimental section). The ethyl signal was clearly visible in ^{1}H NMR spectrum.

The IR spectrum shows a strong, sharp absorption at 2111 cm^{-1} assignable to the $\nu_{C\equiv N}$ of a cyanide group. This value is consistent with those recorded for a series of related compounds.[12,13]

Also seen is a single strong absorption at 1702 cm^{-1} assignable to the $\nu_{C=O}$ of the ester group, which is a typical value for an ethyl benzoate ester.[35]

All spectra corresponded with the structure proposed for **(18).**

3.7.1 Vapochromic behaviour

Like **(16), (18)** displays colour changes through interaction with solvent vapour. However, the interactions are significantly different. The compound when precipitated from methanol under atmospheric conditions appears yellow/orange in colour, however, upon application of solvent vapour (methanol, ethanol or dichloromethane) an extremely rapid transformation to a stable green form can be achieved (video available on supplementary information CD). The compound can be transitioned equally rapidly back to the orange form, through direct application of water. Unlike **(18)** atmospheric water vapour is insufficient to cause this transition, however water vapour produced by bubbling nitrogen through warmed water causes a rapid transition.

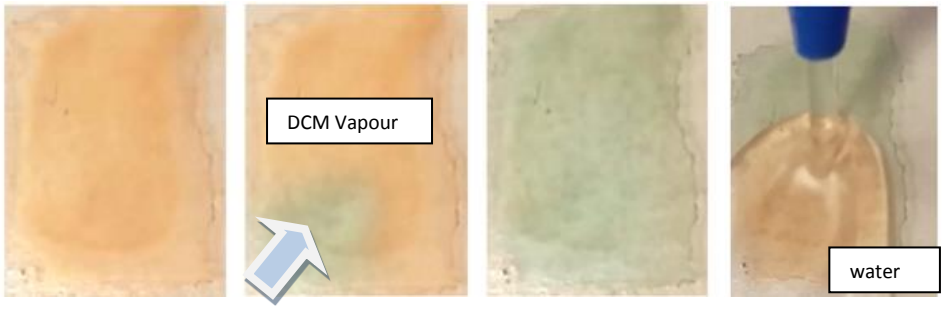

Figure 3.51. Photographs showing the solvent interactions of (18). Top: application of dichloromethane vapour to a drop cast sample on a glass slide. Bottom: application of water to the same sample to return it to the orange form.

The reversibility of this transition is also different to **(16)**. For **(18)**, some thin film samples, the transition to green became slower/less complete with repeated transitions, and unless re-precipitated the sample eventually became permanently orange. Investigation into why this may be, led to the realisation that the substance has a high affinity for crystallisation with dichloromethane, and it is proposed that this non vapochromic solvate may be a more stable configuration, resulting in eventual transformation to this form. In response to this, the solid was dissolved in acetone and repeatedly dried rapidly under heat and vacuum to try and remove residual crystallised dichloromethane from the reaction conditions. The solid was then dissolved in hot isopropanol, and precipitated as green solid. This solid transitions between green and orange more reversibly.

The nature of these transitions was investigated in the same manner as for **(16)**, with the additional advantage of having a detailed description and understanding of the highly similar **(16)** prior to doing so. It would perhaps, for instance, be a reasonable assumption that the rapid switching between

coloured forms is again due to a structural rearrangement facilitating varying degrees of inter-metallic overlap. It may also be hypothesised that due to the orange form being produced upon exposure to water, that a form structurally similar to that of **(16)** **form-I** could plausibly be produced, with the water hydrogen bonding to the cyanide ligands.

The green form however is not as easily explainable. The compound does not initially appear to uptake any solvent into the structure, given that multiple solvents result in the same visual response, including the non-hydrogen bonding solvent dichloromethane. It was therefore proposed that the green form is perhaps analogous to the solvent-free **form-II**, and the solvent vapour acts to displace the bound water molecules. However, transition to the green form was not producible with heat, vacuum, or dry gas flow, and so it would appear that the workings of the vapochromic response may be complex.

3.7.1.1 Absorption spectroscopy of the two forms

UV-visible absorption spectroscopy was also performed on the two forms of **(18)** in the solid state on thin films. As can be seen in **Figure 3.52**, upon application of solvent vapour, a completely new absorption at 600 nm appears, indicating a new lower energy transition. This suggests that as with **(16)**, a change in solvent occupation may be inducing a structural change leading to an increase in platinum dz^2 interaction.

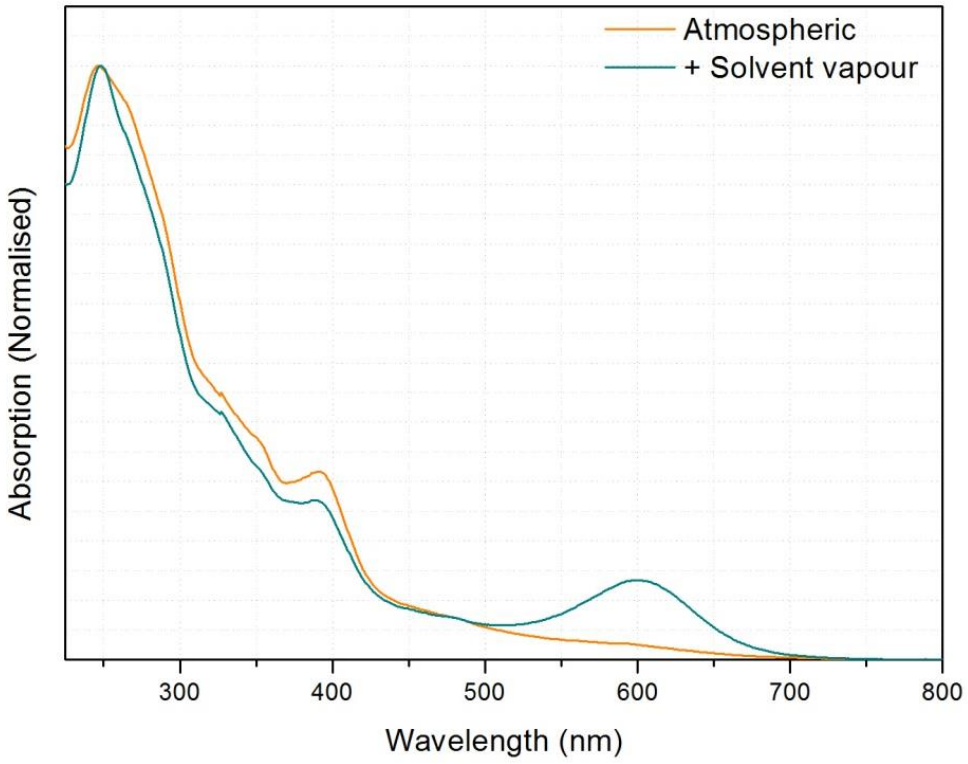

Figure 3.52. UV-Visible spectrum of (18) before and after solvent vapour application.

3.7.2 Powder x-ray diffraction

Powder diffraction studies were performed on the yellow and green forms of **(18)**. However it became immediately apparent that both forms lacked long range order. This was an unexpected result, but upon repeating the experiments it appeared that the two forms were indeed amorphous. This makes studying the structural transitions between the two forms exceedingly difficult, and as such, the cause for the colour changes for this compound can only be based on speculation.

It would appear that the green form is again, likely to involve platinum stacking in some way, however due to the lack of order, it may be that the amorphous solid arranges in pairs where there is platinum interaction. It also appears that water is responsible for the transition to the orange form, and due to the range of solvents eliciting the same response in returning to green, it is likely that the solvents are displacing water from the structure somehow. It is possible that the water is interacting to break-up pairs of molecules with overlapping platinum centres to produce the orange hue, and by changing the ester, sensitivity to different water displacing solvents has been achieved which reverts the structure back to overlapped pairs.

3.7.3 Single crystal x-ray diffraction

The production of single crystal forms of **(18)** were attempted, no forms with vapochromic properties could be produced. Only non solvent-sensitive yellow crystals were obtained, from slow evaporation of dichloromethane solution, and crystals were revealed to be a dichloromethane solvate (**Figure 3.53**). It is possible that the ethyl ester possesses the correct interactions to allow for vapochromic structures, but that they are weakened to the extent that no long range order can be achieved, and so only amorphous powders with the required structure can be produced.

The compound crystallised in the triclinic space group P-1. The structure of this form consists of an asymmetric unit consisting of two neutral molecules of **(18)**, and one of dichloromethane. The internal structure is largely similar to that of **(16)**, with the ester groups lying close to the plane of the pincer ligand. The platinum centres adopt the expected square planar geometry with minor distortion (N1-Pt1-N2 angle 160.3° (2) and N4-Pt2-N5 angle 159.7 (2)°) due to the pincer bite angle. Bond parameters are within expected range (**Table 3.14**).[21,22,23] The extended structure is close to planar, however Pt-Pt separation of 4.6139 (5) Å suggests no interaction. Weak C-H donor hydrogen-bonding to the dichloromethane, cyanide and carboxylate groups is also present in the structure. Details of these interactions can be seen in **Table 3.15**.

Table 3.14. Selected bonds for (18)

Bond	Length (Å)	Bond	Length (Å)
Pt1-N1	2.023 (5)	Pt2-N4	2.051 (6)
Pt1-N2	2.050 (7)	Pt2-N5	2.054 (6)
Pt1-C7	1.943 (6)	Pt2-C27	1.938 (7)
Pt1-C20	2.089 (7)	Pt2-C40	2.078 (7)
C20-N3	1.120 (10)	C40-N6	1.129 (9)

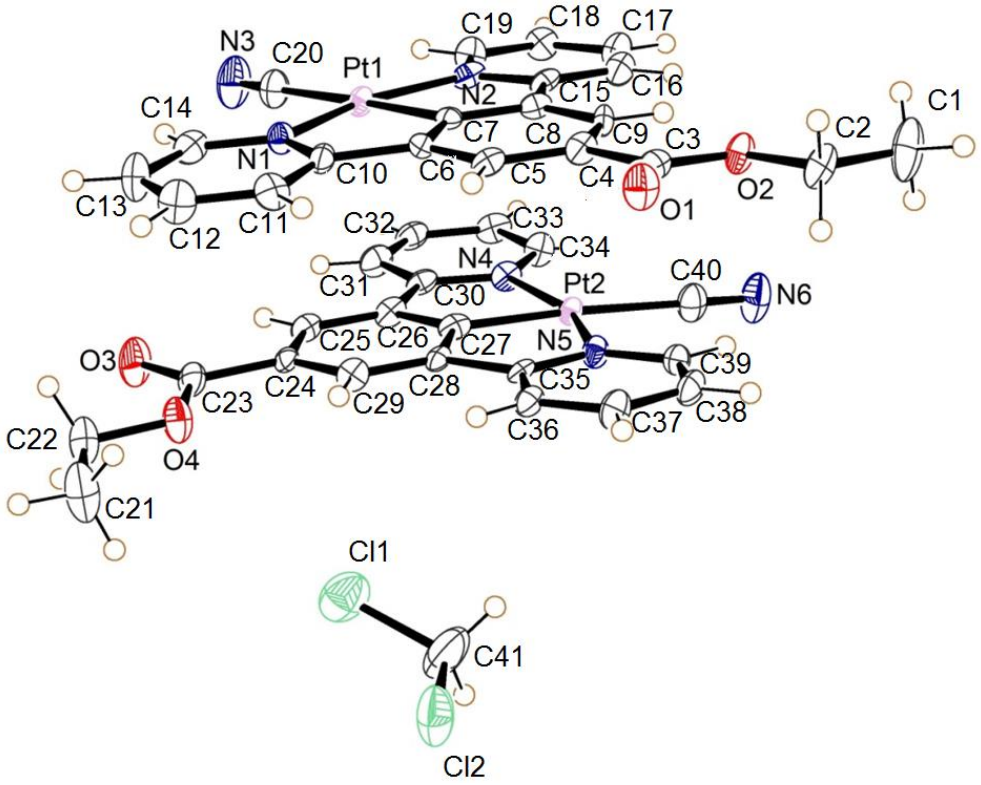

Figure 3.53. Dichloromethane solvate of (18).

Table 3.15. Weak hydrogen bonding interactions for (18)

Bond	Distance (D..A) (Å)	Distance (H..A) (Å)	Angle (D..H..A) (°)
C31-H23-Cl2[1]	3.759 (8)	2.840	170.16
C13-H10-Cl2[2]	3.469 (9)	2.820	127.87
C12-H9-Cl2[2]	3.532 (8)	2.939	122.93
C38-H29-N6[3]	3.546 (10)	2.777	140.80
C21-H17-N3[4]	3.486 (11)	2.730	136.15
C18-H14-N6[5]	3.450 (12)	2.590	153.93
C13-H10-03[4]	3.2215 (09)	2.471	137.90
C33-H25-N6[5]	3.557 (10)	2.867	131.84
C32-H24-O1[6]	3.574 (9)	2.651	172.03

1= (x, 1+y, z), 2 = (1-x, 1-y, -z), 3 = (1-x, 1-y, 1-z), 4 = (1-x, 2-y, -z), 5 = (1-x, 2-y, 1-z), 6 = (1+x, 1+y, z)

3.8 Cyano[phenyl 3,5-di(2-pyridyl)benzoato]platinum (19)

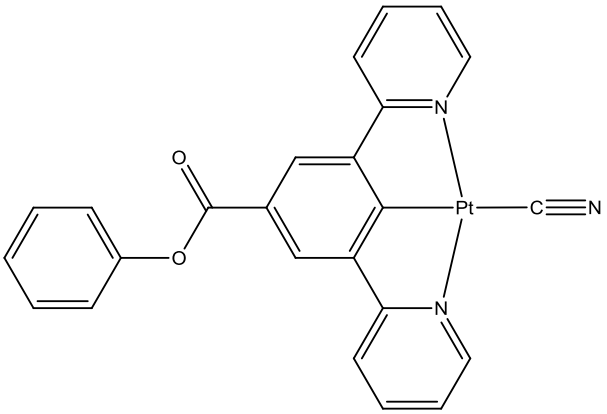

Given that the ethyl ester analogue retained vapochromic properties, but lacked long range order in its solid structure, an inherently more ordered alternative ester analogue was attempted that was likely to have more robust intermolecular interactions. A phenyl analogue was chosen for this task, as its rigidity along with the possibility of π-stacking interactions, hopefully allowing a more ordered vapochromic structure to form. The pincer ligand ester was synthesised by esterifying 1,3-dibromobenzoic acid, and then performing the Stille-coupling, cyclometallation and salt metathesis steps as before (**Scheme 3.2**).

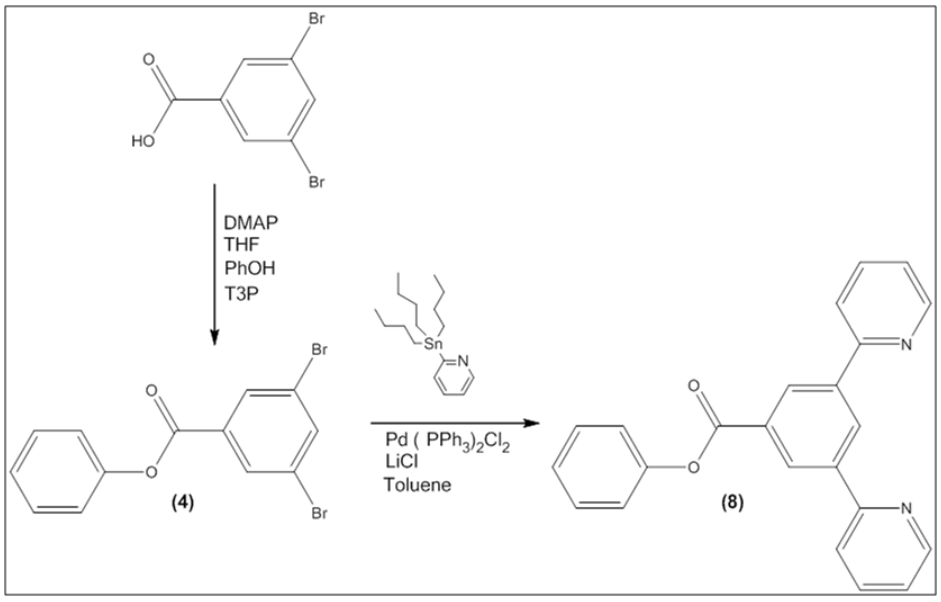

Scheme 3.2 General reaction pathway taken to produce phenyl-ester pincer ligand.

(19) was fully characterised by NMR and solid-state IR spectroscopy, mass spectrometry and by x-ray crystallography (see experimental section). The presence of the phenyl group was clearly indicated by ^{1}H NMR spectroscopy.

The IR spectrum shows a strong, sharp absorption at 2116 cm^{-1}, assignable to the $\nu_{C\equiv N}$ of a cyanide group. This value is consistent with those recorded for a series of related compounds.[12,13] This value is consistent with those recorded for a series of related compounds.[36,37] Also seen is a single strong absorption at 1725cm^{-1} assignable to the $\nu_{C=O}$ of the ester group, which is a typical value for a benzoate ester.[38]

All spectra corresponded with the structure proposed for **(19).**

3.8.1 Vapochromic behaviour

(19) again displays vapochromic behaviour. The compound may be precipitated from dichloromethane/methanol or dichloromethane/tetrahydrofuran solution as a purple film, which is extremely sensitive to gentle vapour flow (air squeezed from solvent wash bottle with straw removed) of a variety of polar solvents: methanol, dichloromethane, ethanol, acetone, isopropanol (in order of decreasing sensitivity). Each solvent appears to elicit the same response, whereby the compound transforms to a cherry red colour. However, upon direct application of liquid methanol or dichloromethane, the film appears to dry with a greenish colour. This greenish film is still sensitive to the same solvent conditions, and will still turn the same cherry red colour.

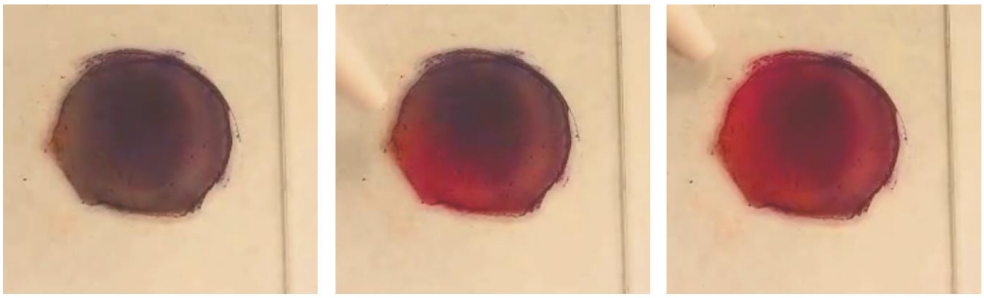

Figure 3.54. Vapochromic properties of a drop-cast thin film (from methanol/dcm solution) (ca. 2cm in diameter) of (19) is responding to a gently flow of methanol vapour.

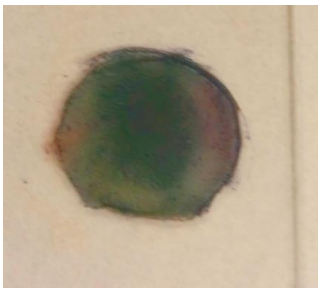

Figure 3.55. The same film of (19) after washing with methanol, and drying.

3.8.2 X-ray powder diffraction

Powder diffraction experiments were performed to determine whether the transformations for this compound display long range order/crystallinity. A capillary was prepared of the freshly precipitated powder first, and an experiment run. The same capillary was then filled with a small amount of methanol, turning the powder red, and the experiment repeated. It was determined that unlike **(18)** the powders were indeed crystalline, although the diffraction data was poor, and very little could be determined regarding the nature of the transitions. It did appear that there was some change to the diffraction, but resolution was so low that this cannot be confirmed (**Figure 3.56**).

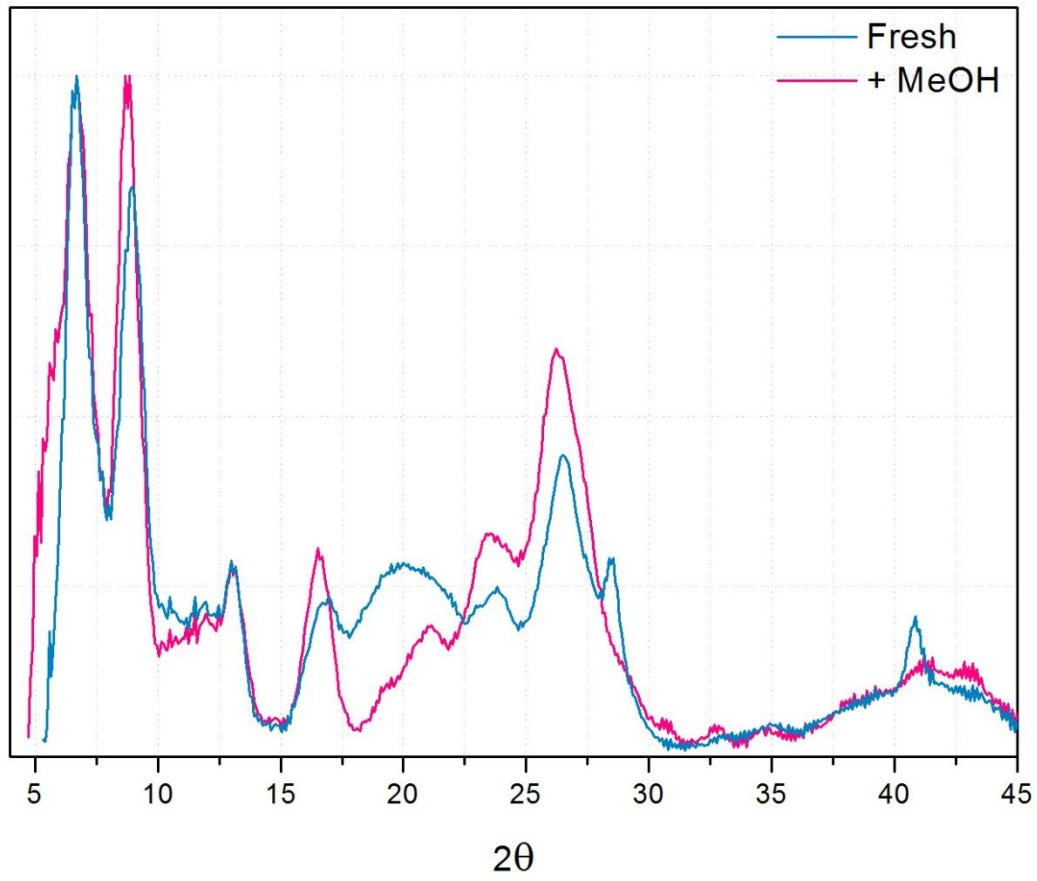

Figure 3.56. Powder diffraction of (19) before and after methanol exposure.

3.8.3 Single crystal x-ray diffraction

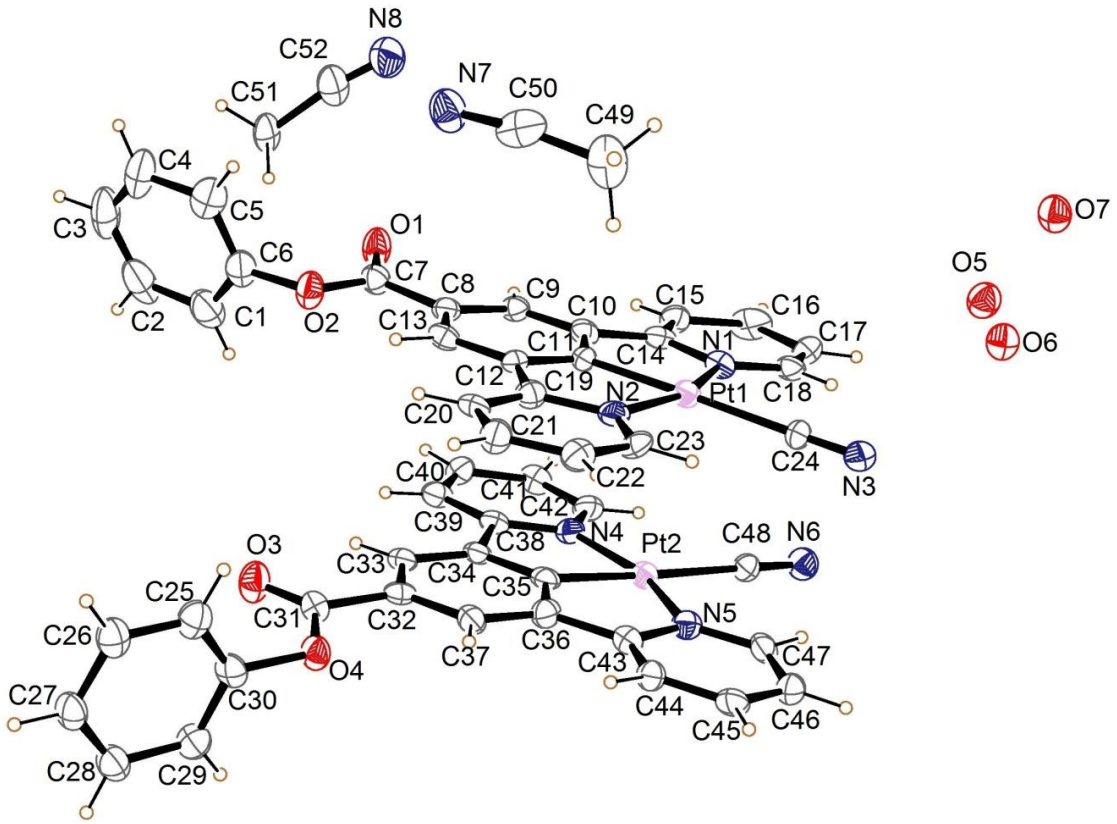

Figure 3.57. Asymmetric unit of the crystal structure obtained for (19).

Attempts were made to crystallise **(19)** in forms representative of the vapochromic films. The first single crystals of **(19)** were obtained as green needle plates by vapour diffusion of diethyl-ether into an acetonitrile/water solution, and crystallised in the monoclinic space group $P2_1/n$. The crystals appear green to the naked eye, but were revealed to display dichroism under turning polarising filters, where the larger crystals could be seen to transform between blue and yellow (**Figure 3.58**). The crystals were extremely air sensitive, changing to red immediately upon direct air exposure, and after a few minutes under Fomblin oil.

The structure of this form consists of an asymmetric unit consisting of two neutral molecules of **(19)**, two of acetonitrile and three of water. The internal structure is broadly the same as the other compounds in this chapter, with the exception that the phenyl ring of each ester now lies closer to perpendicular to the plane of the pincer (angle of phenyl plane to plane [N1 Pt1 C19 N2 C10 C12 C14 C11] = 70.95° and angle of phenyl plane to plane [C38 C43 N5 Pt2 N4 C34 C35 C36] = 83.09°). The platinum centres adopt the expected square planar geometry with minor distortion (N1-Pt1-N2 angle 160.5° (6) and N4-Pt2-N5 angle 160.5 (6)) due to the pincer bite angle, with bond parameters in the expected ranges (**Table 3.16**). [21,22,23]

Table 3.16. Selected bonds for (19)

Bond	Length (Å)	Bond	Length (Å)
Pt1-N1	2.06 (1)	Pt2-N4	2.03 (2)
Pt1-N2	2.03 (2)	Pt2-N5	2.03 (2)
Pt1-C11	1.97 (2)	Pt2-C35	1.93 (2)
Pt1-C24	1.12 (2)	Pt2-C48	2.05 (2)
C24-N3	1.120 (10)	C48-N6	1.17 (3)

Upon structure solution it was revealed that the structure is highly porous and contains large amounts of solvent. Solvent occupies channels of void space that make up 21.8% of the unit cell volume. These channels in the structure can be divided into two types. There is a cavity formed by four ester phenyl rings at the back of the molecules, coming together to form a box like channel (**void 1**), which takes up 8.8% of the unit cell volume, and there is the channel more akin to that of **(16)** whereby the cyanide groups point into void space (**void 2**), which takes up 13.0 %. In this structure **void 1** is filled with acetonitrile, which appears to be held in place only by weak C-H---N and C-H---O interactions (**Figure 3.59**). **Void 2** is far more complicated, and extends in 2-dimensions through the crystal, almost in a grid structure. This void is filled with three water molecules and one acetonitrile molecule per asymmetric unit. The acetonitrile again is only involved in weak carbon donor H-bonds (**Figure 3.63**). The water, however, forms a complicated network of strong hydrogen bonds, with three water molecules bound to each cyanide, and each of the waters bound to each other in a network of water that extends through two dimensions in the crystal (see **Figure 3.60**, **Figure 3.61**, **Figure 3.62**). Details of the hydrogen bonding interactions can be found in **Table 3.17** and **Table 3.18**. The structure is generally planar, with the molecules of **(19)** arranged in stacks, with two planar orientations of stacks. There are significant platinum-platinum interactions within each stack, with Pt-Pt-Pt angle of 174.18 (4) °, and platinum-platinum separations of 3.2550 (11) Å within the ASU and 3.3470 (11) Å between them. This angle indicates that the d_z^2 interaction lies between that of **(16)** form-I and form-III, being closer to that of form-III. Given the green colour of this crystal, this is to be expected. The structure as a whole is of a different form to that of **(16)** as all the stacks are pointing away from a point (this creates void 2). But a network of weak hydrogen bonding interactions is seen with the occupying solvent in this void, along with between stacks, "stitching" the molecules in each plane together (**Figure 3.59**).

Table 3.17 Hydrogen bonding interactions for (19)

Bond	Distance (D..A) (Å)
N3 O6	3. 02 (2)
N3 O7[1]	3.05 (2)
N3 O5[2]	3.06 (2)
O7[1] O6[1]	2.84 (2)
O6[1] O5[1]	2.77 (2)
N6 O5[1]	2.75 (3)

1 = (1+x, y, z), 2 = (1/2+x, 1/2-y, 1/2+z)

Table 3.18 Weak hydrogen bonding interactions for (19)

Bond	Distance (D..A) (Å)	Distance (H..A) (Å)	Angle (D..H..A) (°)
C51 H36 O1	3.36 (2)	2.622	134.30
C51 H34 N8[1]	3.69 (4)	2.784	157.66
C27 H18 N8[2]	3.65 (4)	2.967	131.38
C26 H17 N8[2]	3.79 (4)	2.969	146.21
C40 H24 N8[3]	3.49 (4)	2.564	172.76
C49 H32 N6[4]	3.45 (3)	2.539	158.04
C49 H33 O6[5]	3.28 (3)	2.421	148.17
C49 H31 O7[6]	3.37 (4)	2.744	161.38
C41 H25 N7[7]	3.48 (3)	2.740	134.74
C21 H13 N7[3]	3.51 (3)	2.852	153.17
C25 H16 N7[3]	3.55 (4)	2.826	134.74

1 = (1-x, -y, -z), 2 = (2+x, y, 1+z), 3 = (1+x, y, z), 4 = (-1+x, y, 1+z), 5 = (-1/2+x, 1/2-y, 1/2+z), 6 = (1/2+x, 1/2-y, 1/2+z), 7 = (1+x, y, -1+z)

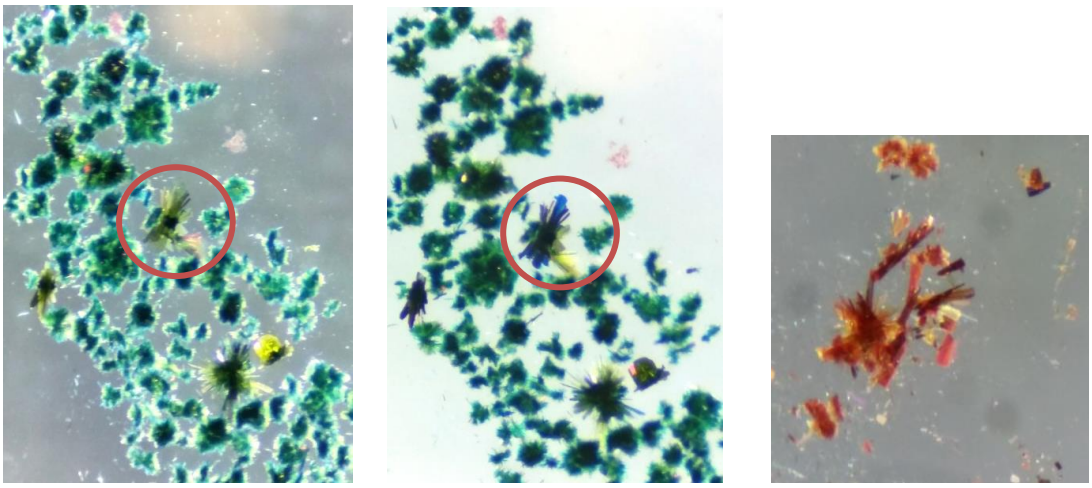

Figure 3.58. Left/middle: Dichroism seen in crystals of (19) under two orientations of polarising filter. Within the circle in both photographs is the same cluster of crystals. Right: The same crystals after exposure to air.

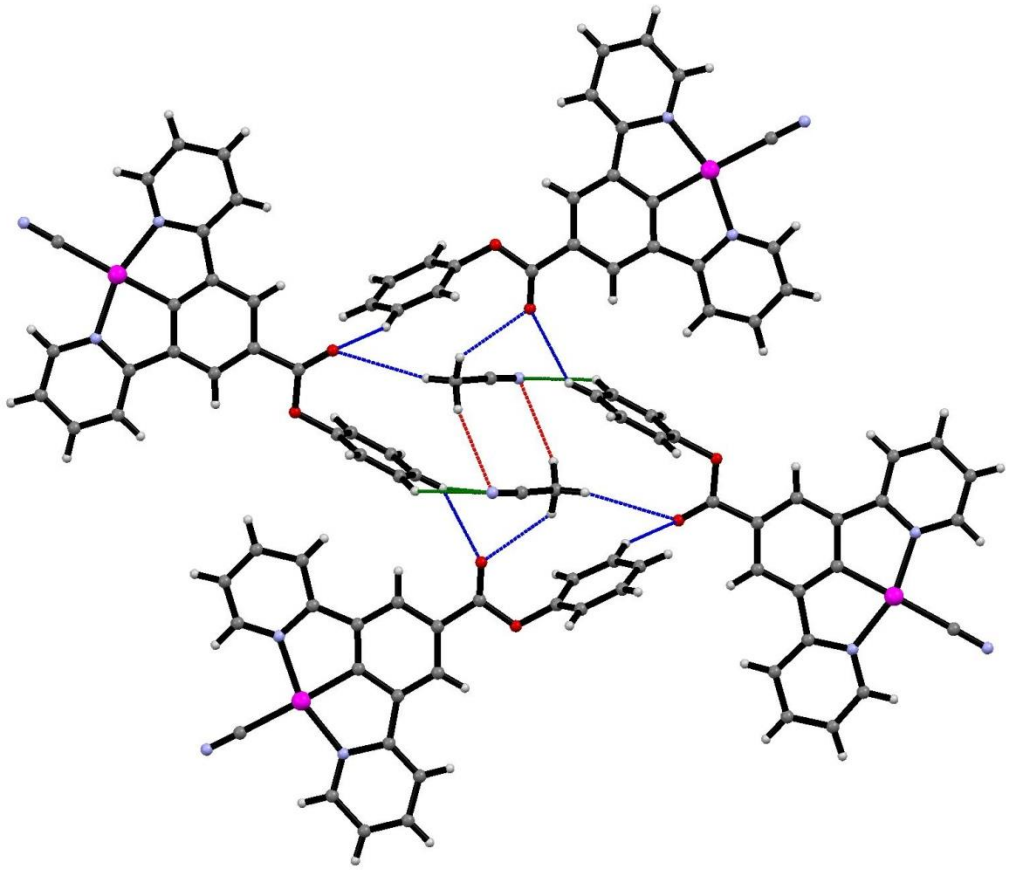

Figure 3.59. The complex network of weak hydrogen bonding interactions between adjacent molecule stacks. Red: inter-solvent. Green: acetonitrile as acceptor. Blue: Ester as acceptor.

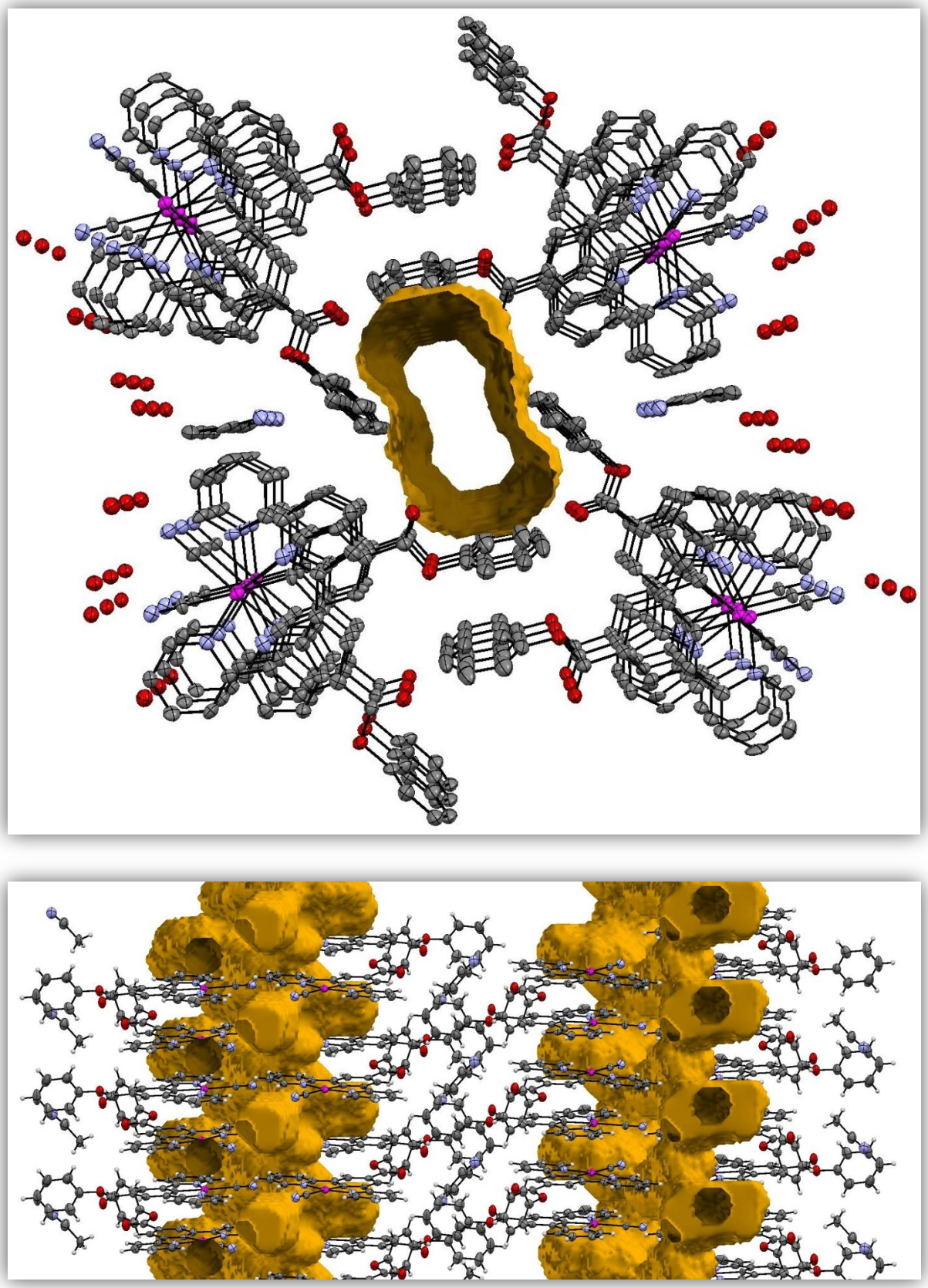

Figure 3.60. Calculated void space for the structure once occupying solvent molecules have been removed. Top: Void 1. Bottom: Void 2.

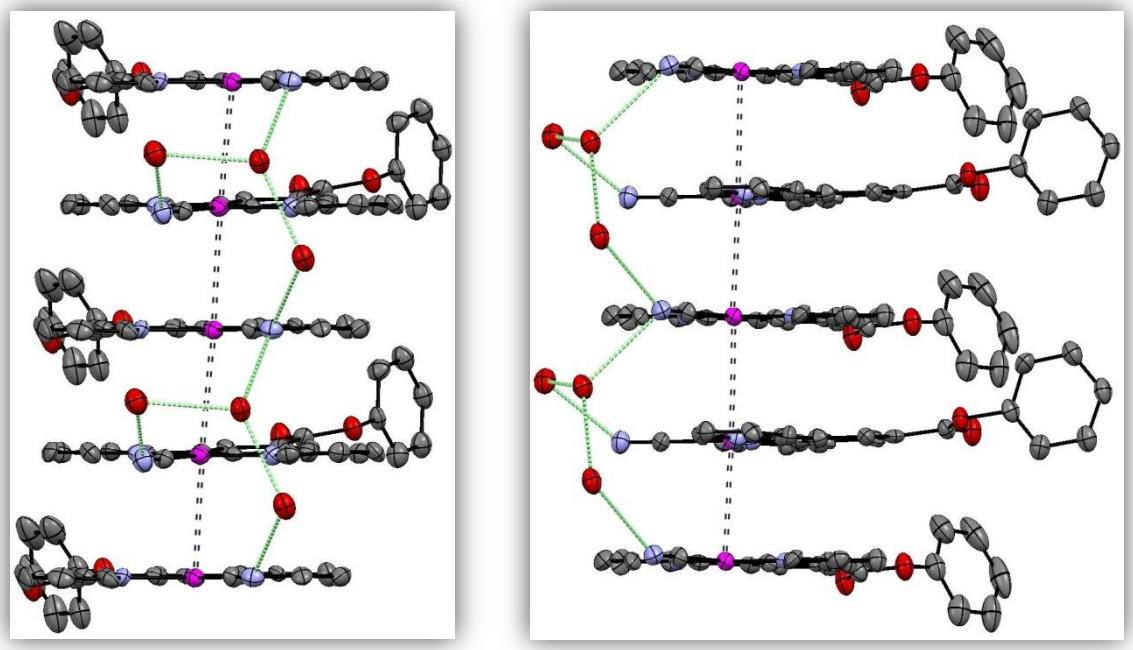

Figure 3.61. front (left) and side-on (right) view of the structure of the crystal, highlighting the platinum - platinum interactions, and hydrogen bound network of water present.

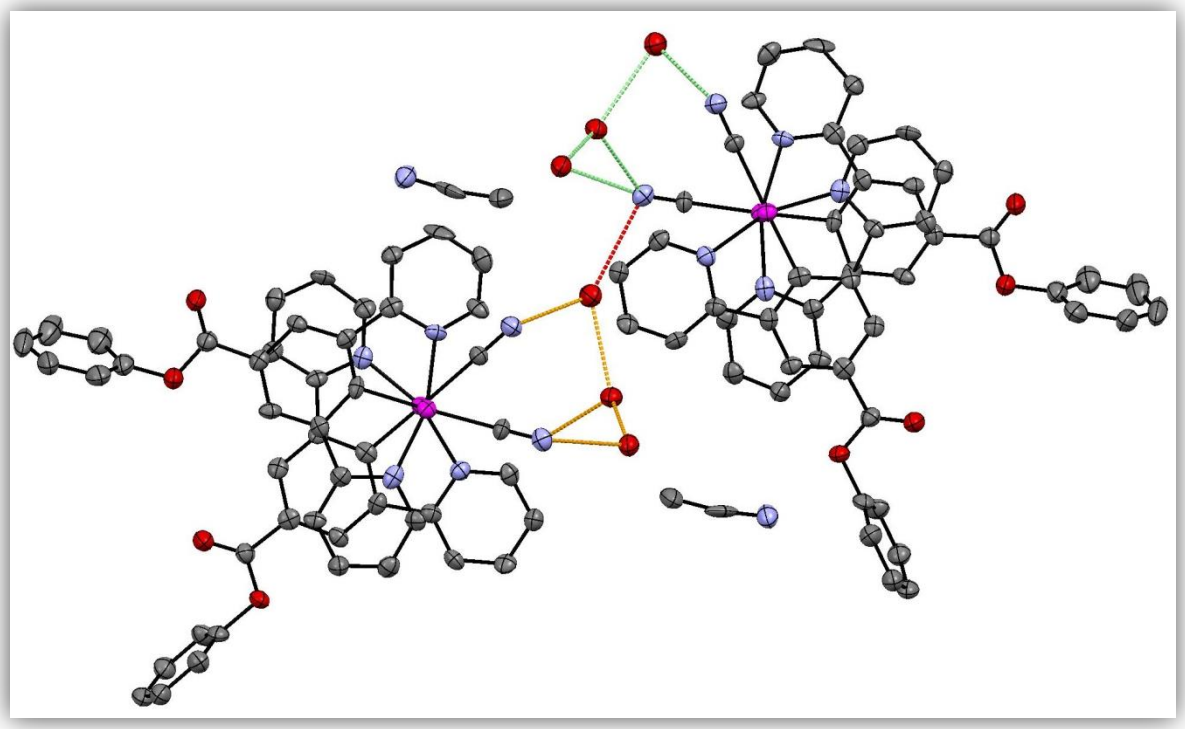

Figure 3.62. a-axis view of a section of the crystal, detailing how the two planar orientations of stacks are arranged with respect to each other, and how they are stitched together by a hydrogen bonded network of water in Pore 2. The orange and green contacts show the individual stacks' water interactions (as seen in Figure 3.61), and the red contact shows the hydrogen bond that links them.

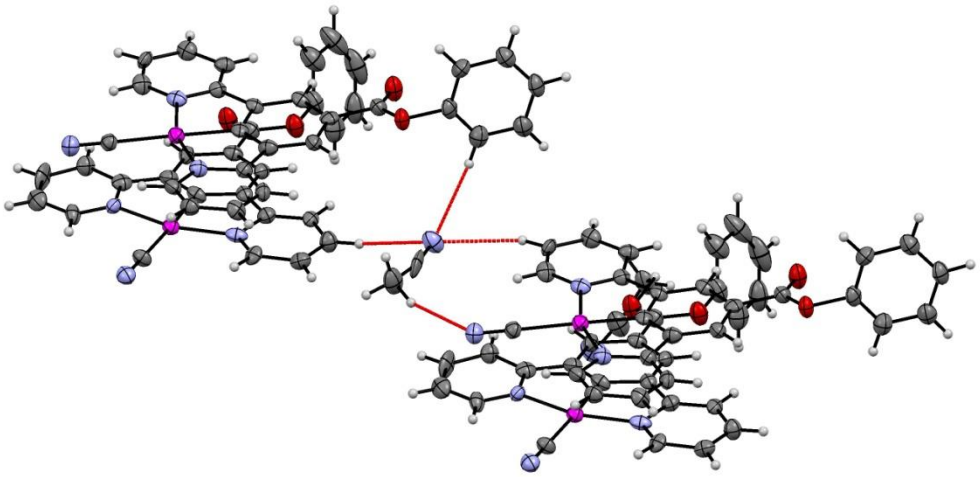

Figure 3.63. The weak hydrogen bonding interactions of the acetonitrile occupying Pore 2.

Given how porous the crystal is, and the extent to which the structure contains hydrogen bonding solvents, it is likely that by changing the solvent environment that the structure is exposed to, exchange of solvents in and out of this cavity may provide a variety of structures, as the variation in interactions could shift the planar stacking of the compound to a degree. This structure is unlikely to represent the films produced due to the inclusion of acetonitrile, however it offers a plausible mechanism for the confusing divergence in responses between solvent vapours and liquids, if the structures show some resemblance.

For this structure there are two channels that may contain solvent. It has been shown in **(16)** that hydrogen bound water existing in a channel such as that seen in this structure (**void 1**) can be displaced easily with certain solvents. It is therefore possible that this is also the case for this compound, and that by applying methanol vapour for example, the water is being momentarily replaced with methanol (transition to red), and then returning from the atmosphere (return to purple). The second channel however (**void 2**) has no analogue in **(16)**. What we can say about it, however, is that it does form interactions with occupying solvents (in this case acetonitrile). It is possible therefore that in our purple films, this void space is occupied by some other solvent. Perhaps, methanol, water, dichloromethane, or the rings are differently positioned and no solvent occupies this space. The other channel is likely to contain water as before (given that atmospheric exposure is all that is needed to return to this form), but by applying a liquid solvent, perhaps a transition to a form containing only methanol in **void 2** is produced, which shifts the structure somewhat, so that upon return to atmospheric exposure, and the return to a water filled void 1, it returns to a green version of the hydrate, perhaps not dissimilar to the acetonitrile solvate we have crystallised.

3.9 Summary of results and conclusions

The work in this chapter set out to establish whether by incorporating a small strong field ligand into the fourth coordination site of the platinum pincer backbone, intermetallic d_z^2 -d_z^2 interactions could be used as a potential mechanism for controlling the optical properties.

Three new vapochromic compounds and one thermochromic compound have resulted from this study, and significant evidence has been presented that the cyanide ligand serves not only as a hydrogen bonding site for solvent uptake, but as a facilitator for the colour changing interactions by allowing the stabilisation of the HOMOs with which it shares π-interaction, allowing for a prominent non-bonding d_z^2 orbital relative to the frontier.

The systems studied have shown a proportional response in the absorption and emission spectra (in the form of a red-shift) to the degree of intermetallic d_z^2 - d_z^2 overlap, facilitated by crystal structure changes upon absorption/desorption of solvent vapours, and these findings have been confirmed using solid state TD-DFT calculations.

Many vapochromic compounds based on the interaction of platinum centres are known to the literature, with Magnus' green salt being the first discovered, and many following. [6] None, however, have been demonstrated to show such a rapid transition and sensitive response as the compounds of this chapter. While at this stage due to time limitations only **(16)** is fully structurally understood, the work of this chapter offers an exciting new route to extremely rapidly responsive vapochromic materials.

Alongside the cyanide ligand, the importance of the substituted group of the pincer phenyl has also been investigated. It has been established that the weak intermolecular interactions provided by an ester group appear to be key in allowing for rapid, and reversible transitions for these compounds, and one aspect of future work that should be undertaken in this research is to create further analogues with various potential intermolecular interactions, in order to fully understand how to direct the crystallisation to achieve a desired set of properties.

Industrial applications of such a protocol for designing rapidly responsive vapochromic materials would be many, with platinum vapochromic compounds as practical chemosensor devices currently considered a promising prospect that has yet to be implemented successfully. [6]

One such attempt at device manufacture has been to immobilise a vapochromic material into a polymer substrate in order to create "smart coatings" for chemical sensing application.[39]

A subsequent trial of **(16)** embedded into a porous polymer matrix has already been attempted, with preliminary results showing a vastly superior response time (<1 second) to solvent vapour in comparison to other known systems. Microscope images of the polymer are shown in **Figure 3.64** where microcrystals of **(16)** can be seen to be fairly evenly distributed. Videos of the polymer transitions can be found in the supporting information, whereby multiple transitions between red and yellow can be seen at high magnification using dry argon, and a transition to blue can be seen as methanol vapour is applied (focal depth changes from methanol vapour due to high magnification).

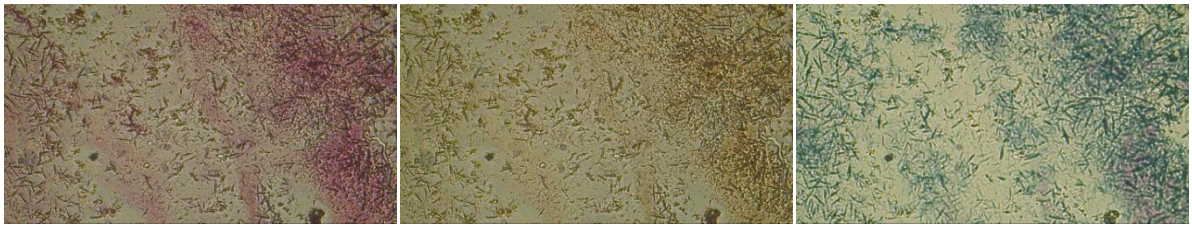

Figure 3.64. Microscope images of crystals of (16) embedded in a polymer, under atmospheric conditions (left), dry argon (middle) and methanol vapour (right).

3.10. References

(1) Sharpe, A. G. *The chemistry of cyano complexes of the transition metals*; London: Academic Press, **1976**.
(2) Connick, W. B.; Henling, L. M.; Marsh, R. E.; Gray, H. B. *Inorg. Chem.* **1996**, *35*, 6261.
(3) Chen, Y.; Lu, W.; Che, C.-M. *Organometallics* **2012**, *32*, 350.
(4) Rossi, E.; Colombo, A.; Dragonetti, C.; Roberto, D.; Demartin, F.; Cocchi, M.; Brulatti, P.; Fattori, V.; Williams, J. A. G. *Chemical Communications* **2012**, *48*, 3182.
(5) Ma, B.; Li, J.; Djurovich, P. I.; Yousufuddin, M.; Bau, R.; Thompson, M. E. *Journal of the American Chemical Society* **2005**, *127*, 28.
(6) Kobayashi, A.; Kato, M. *European Journal of Inorganic Chemistry* **2014**, *2014*, 4469.
(7) Chen, Y.; Li, K.; Lu, W.; Chui, S. S.-Y.; Ma, C.-W.; Che, C.-M. *Angewandte Chemie International Edition* **2009**, *48*, 9909.
(8) Williams, J. A. G. *Top Curr Chem* **2007**, *281*, 205.
(9) Connick, W. B., Schaefer, W.P, Marsh, R.E, Gray, H.B *Inorg. Chem.* **1997**, *36*, 913.
(10) Farley, S. J.; Rochester, D. L.; Thompson, A. L.; Howard, J. A. K.; Williams, J. A. G. *Inorganic Chemistry* **2005**, *44*, 9690.
(11) Williams, J. A. G.; Develay, S.; Rochester, D. L.; Murphy, L. *Coordination Chemistry Reviews* **2008**, *252*, 2596.
(12) Lemus-Santana, A. A., Rodríguez-Hernández, J., delCastillo, L.F, Basterrechea, M., Reguera, E. *Journal of Solid State Chemistry* **2009**, *182*, 757.
(13) Kayano, T.; Takayasu, S.; Sato, K.; Shinozaki, K. *Chemistry – A European Journal* **2014**, *20*, 16583.
(14) Bio-Rad; Bio-Rad/Sadtler IR Data Collection: Philadelphia, p FTIR.
(15) Sigma-aldrich **2011**.
(16) Porterfield, W. W. *Inorganic Chemistry: A Unified Approach*; 2nd ed.; Academic Press Inc., **1993**.
(17) Williams, J. A. G., Beeby, A., Davies, E.S., Weinstein, J.A., Wilson, C. *Inorg. Chem.* **2003**, *42*, 8609.
(18) Tessler, N.; Medvedev, V.; Kazes, M.; Kan, S.; Banin, U. *Science* **2002**, *295*, 1506.
(19) Konstantatos, G.; Huang, C.; Levina, L.; Lu, Z.; Sargent, E. H. *Advanced Functional Materials* **2005**, *15*, 1865.
(20) Shen, H.; Zheng, Y.; Wang, H.; Xu, W.; Qian, L.; Yang, Y.; Titov, A.; Hyvonen, J.; Li, L. S. *Nanotechnology* **2013**, *24*, 475603.
(21) Khan, M. S., Al-Suti, M.K, Al-Mandhary, M.R.A, Ahrens, B, Bjernemose, J.K, Mahon, M.F, Male, L, Raithby, P.R, Friend, R.H, Kohler, A, Wilson, J.S. *Dalton Trans.* **2002**, 65.
(22) Berenguer, J. R., Lalinde, E, Torroba, J. *Inorg. Chem.* **2007**, *46*, 9919.
(23) Chen, Y.; Li, K.; Lu, W.; Chui, S. S.-Y.; Ma, C.-W.; Che, C.-M. *Angewandte Chemie International Edition* **2009**, *48*, 9909.
(24) Choi, S. J.; Kuwabara, J.; Nishimura, Y.; Arai, T.; Kanbara, T. *Chem. Lett.* **2012**, *41*, 65.
(25) Lu, W.; Chan, M. C. W.; Zhu, N.; Che, C.-M.; Li, C.; Hui, Z. *J. Am. Chem. Soc.* **2004**, *126*, 7639.
(26) Zhang, X.; Wang, J.-Y.; Ni, J.; Zhang, L.-Y.; Chen, Z.-N. *Inorganic Chemistry* **2012**, *51*, 5569.
(27) Miskowski, V. M.; Houlding, V. H. *Inorg. Chem.* **1991**, *30*, 4446.
(28) Wadas, T. J.; Wang, Q. M.; Kim, Y.-J.; Flaschenreim, C.; Blanton, T. N.; Eisenberg, R. *J. Am. Chem. Soc.* **2004**, *126*, 16841.
(29) Zhang, X.; Wang, J.-Y.; Ni, J.; Zhang, L.-Y.; Chen, Z.-N. *Inorg. Chem.* **2012**, *51*, 5569.
(30) Ni, J.; Zhang, X.; Wu, Y.-H.; Zhang, L.-Y.; Chen, Z.-N. *Chem. Eur. J.* **2011**, *17*, 1171.
(31) Inc., C. S. In *NIST Chemistry WebBook*; PERKIN-ELMER CORP.: **2009**.
(32) SDBS, Spectral database for organic compounds.
(33) Mizuse, K. *Spectroscopic Investigations of Hydrogen Bond Network Structures in Water Clusters*; Springer Science & Business Media, **2013**.

(34) Stille, J. K. *Angewandte Chemie International Edition* **1986**, *25*, 508.
(35) SDBS, Spectral database for organic compounds.
(36) Devi, L. S., Al-Suti, M.K, Zhang, N, Teat, S.J, Male, L, Sparkes, H.A, Raithby, P.R, Khan, M.S, Kohler, A. *Macromolecules* **2009**, *42*, 1131.
(37) Khan, M. S., Al-Suti, M.K, Al-Mandhary, M.R.A, Ahrens, B, Bjernemose, J.K, Mahon, M.F, Male, L, Raithby, P.R, Friend, R.H, Kohler, A, Wilson, J.S *Dalton Trans.* **2002**, 65.
(38) SDBS, Spectral database for organic compounds.
(39) Kumpfer, J. R.; Taylor, S. D.; Connick, W. B.; Rowan, S. J. *Journal of Materials Chemistry* **2012**, *22*, 14196.

Chapter 4: Mechanochromism in a platinum N^C^N pincer compound

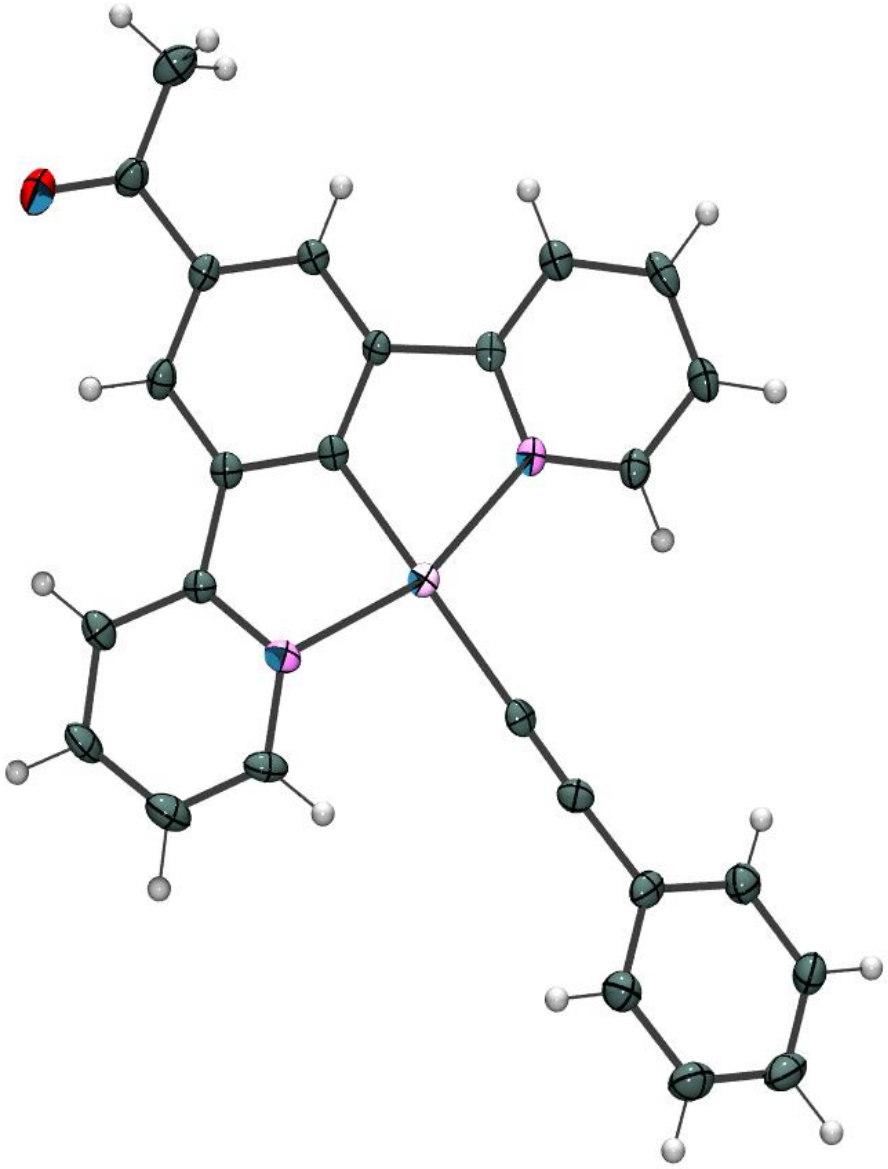

Abstract

In the previous chapter, a set of new platinum pincer complexes were studied that exhibited switchable optical properties caused by structural changes upon exposure to either solvents or heat.

The work in this chapter presents an investigation into an optical switching response to two new stimuli - mechanical grinding, and hydrostatic pressure.

Upon the serendipitous discovery of luminescence red-shifting, in response to mechanical grinding of a new platinum pincer complex **(20)**, a full investigation into the mechanochromic properties of **(20)** in the solid state was undertaken.

Initially an attempt to rationalise the ability of **(20)** to transition from yellow/green luminescence to deep red upon gentle abrasion was made. It has been subsequently determined that the nature of the emission transitions from monomeric, in a crystalline state, to cooperative (excimeric), upon disruption of crystallinity and amorphisation as a response to shear forces. This has also been shown to mimic the behaviour of **(20)** in concentrated solution, where excimer emission has been detected.

Due to the sensitivity of **(20)** to intermolecular interaction, studies into the behaviour of the compound under hydrostatic pressure were also undertaken.

By performing spectroscopic experiments at high-pressures, through the use of a diamond anvil cell, it has been shown that the absorption spectrum of **(20)** strongly red-shifts with applied pressure.

An attempt was also made to study this structurally, with high-pressure crystallographic experiments. However, a transition to a triclinic cell at low pressures meant that the restricted data inherent to DAC experiments made higher pressure structures unattainable. This problem was overcome using the computational simulation software GASP. This had previously been used to determine flexibility in framework materials, but its application to molecular materials proved extremely useful in determining the behaviour of **(20)** at higher pressures.

In combination with TD-DFT calculations, an explanation for this material's red-shifting absorption spectrum has been produced, whereby an increase in overlap between molecule HOMOs via the pincer phenyl ring has been shown to destabilise the HOCO (the HOMO equivalent in the crystal) independent of the LUCO (the LUMO equivalent in the crystal).

4. Mechanochromism in a platinum N^C^N pincer compound

4.1 Introduction

4.1.1 Mechanochromism

Mechanochromism refers to the transformation of the colour or emissive frequency of a substance as a response to some form of mechanical stimuli. This usually refers to either mechanical grinding or milling, known as tribochromism, or through exposure to high pressures, known as piezochromism.[1]

The work presented in this chapter involves the study of the effects of mechanical stimuli on the optical properties of a platinum N^C^N pincer complex. The platinum pincer complex chosen for this study was selected because of the serendipitous discovery of significant luminescent tribochromic effects while purifying the compound after synthesis. While this response in similar compounds is known in the literature,[2,3,4] it presented an opportunity to study another facet of the relationship between structure and optical properties in this class of compounds (platinum N^C^N pincer compounds). The presence of this response for the compound in question indicates sensitivity of the optoelectronics to intermolecular interactions, and it was decided that this would make it a suitable candidate for further study of mechanical forces on these properties.

4.2 Phenylethynyl[acetyl 3,5-di(2-pyridyl)phenyl]platinum (20)

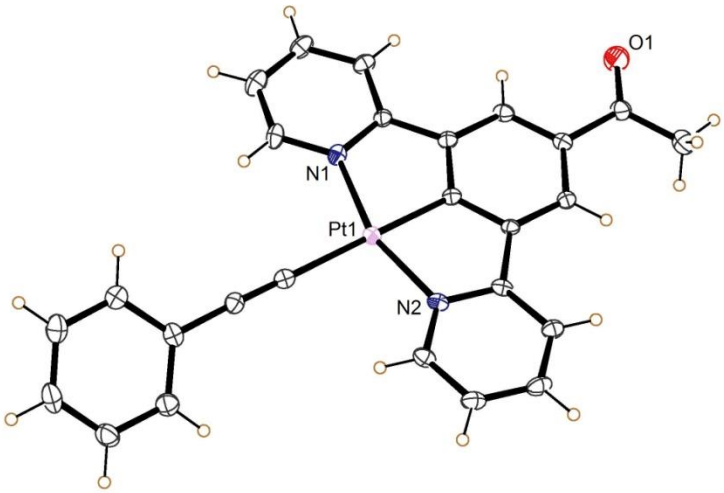

(20) is very similar to **(13)** described in **Chapter 2**, with the difference being in the substitution of the pincer ligand. The methyl ester group has been replaced by an acetyl group, but the platinum substitution remains a phenylacetylene group.

4.2.1 Compound synthesis

(20) was synthesised using the same methods developed in the work of **Chapter 2** and **3** (see **Scheme 4.1**). Pincer ligand **(6)**, which incorporates an acetyl group in place of the methyl ester, is the same as used in **Chapter 3** to produce **(17)** and was synthesised using the same methods. Likewise the same cyclometallation reaction was performed to produce a platinum (II) pincer chloride **(10)**. This was then used as starting material for the final product, achieved *via* salt metathesis with phenylacetylene, using the same protocol developed in **Chapter 2** to produce **(13)**.

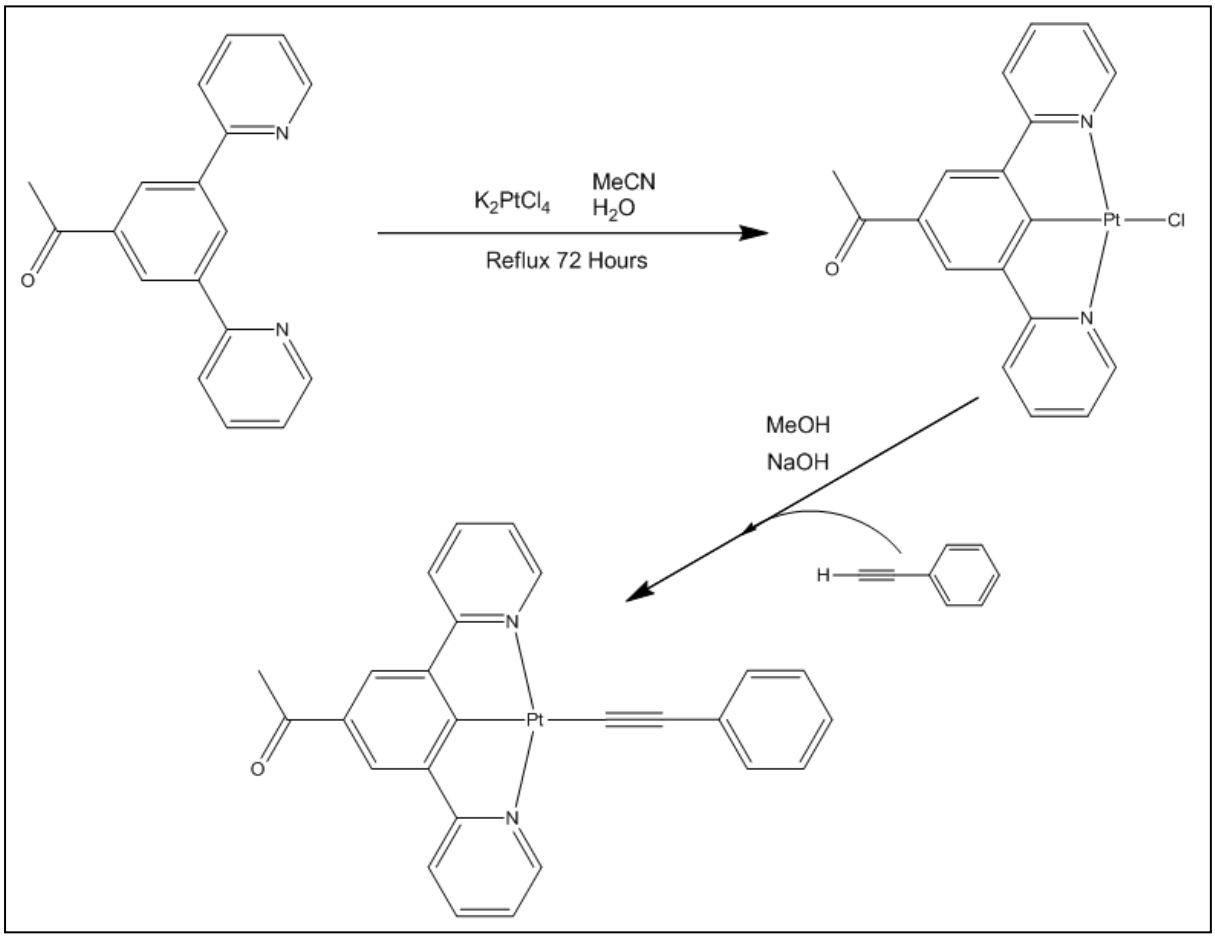

Scheme 4.1. Synthetic pathway to product (20)

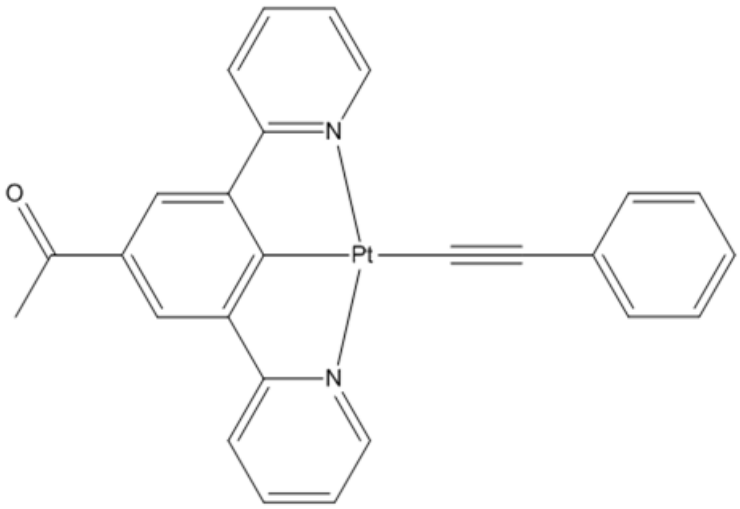

(20) was fully characterised by NMR and solid-state IR spectroscopy, Mass spectrometry and X-Ray crystallography. (See experimental section)

The IR spectrum shows a strong, sharp absorption at 2084 cm^{-1}, assignable to the $\nu_{C\equiv C}$ of a σ-alkynyl group. This value is consistent with those recorded for a series of related compounds.[5,6] Also seen is a single strong absorption at 1658 cm^{-1} assignable to the $\nu_{C=O}$ of the acetyl group, which is a typical value for an acetophenone derivative.[7]

^{1}H NMR, and $^{13}C\{^{1}H\}$ NMR spectra of **(20)** were obtained on the product dissolved in deuterated chloroform. The correct assignment of hydrogen atoms was supported with the use of a 2-dimensional HCOSY experiment, with signals for the acetyl group and pendant phenyl clearly observed.

All spectra corresponded with the structure proposed for **(20)**

4.3 Luminescence tribochromism

While purifying **(20)** it was discovered that it exhibited luminescent tribochromic properties. By gently running a spatula over the compound, the solid powder was observed to irreversibly shift its luminescent emission from yellow/green to a deep-red with no apparent loss in intensity, essentially allowing any relatively hard object to be used to write in the powder (photography can be seen in **Figure 4.1**). Relative to the luminescent effect, the effect on the colour of the compound was seen to be relatively minor, with significant force being require to elicit any shift in colour- which even then involves only a slight change to a more orange colour.

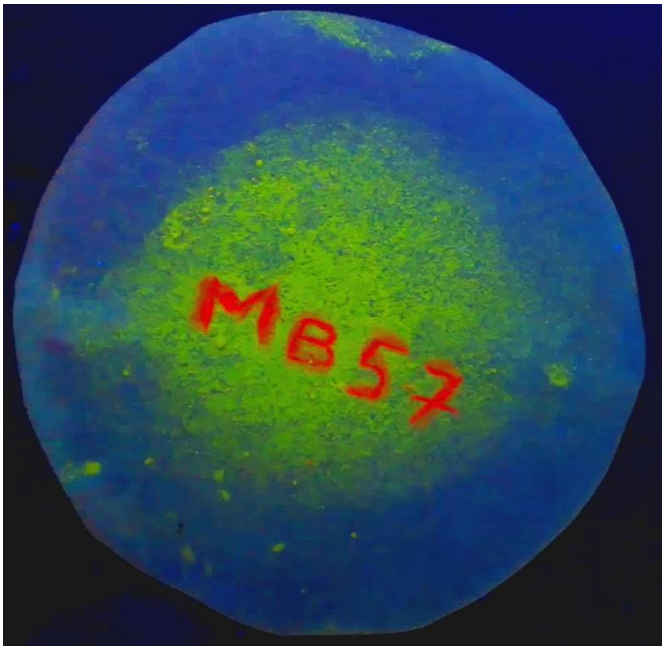

Figure 4.1. Luminescent emission from a powder film of (20) ca. 5x5cm collected on a filter paper. The compound's initial label "MB57" can be seen written in the powder using only gentle pressure from a metal spatula.

This divergence of the absorption and emission properties seemed to suggest that the compound's response to grinding was exhibiting effects on the emissive energy without having any effect on the frontier orbital energies (as this would result in a change in absorption energy). The most typical way in which this divergence can be produced is through excimer emission.[8] Excimer emission was previously described in **Chapter 2**, albeit in the solution state. The same principle applies to the solid state, whereby molecules are excited as monomers, but then emit cooperatively with an adjacent molecule. This results in a broad, featureless, and red shifted emission band in comparison to monomeric emission, along with an unchanged absorption spectrum. It was hypothesised that this could be the case for **(20)**, in that grinding of the solid could result in increased intermolecular contact, defects, or π-stacking that would allow for excimer emission. Similar compounds have been demonstrated to display this property in the literature,[4] whereby mechanical grinding produced powders with highly red-shifted emission spectra that were assigned to solid state excimer emission. A notable example is the closely related complex Pt(5dpb)Cl synthesised by Abe *et al.* [2] which was found to produce strongly red-shifted emission once the solid crystalline powder was ground. This was subsequently attributed to excimer emission in response to amorphisation of the powder. This property in related compounds has also been demonstrated to have application in highly efficient near-IR OLED fabrication. [2,9,10] As such the nature of these properties observed in this compound were to be further investigated, along with a subsequent study into further physical manipulations of the compound.

4.4 Spectroscopy of powders and solutions

Upon grinding of the freshly precipitated yellow/green emitting powder, the observed colour under ambient light changes little. This can be clearly seen in **Figure 4.2**. Upon more aggressive grinding in a pestle and mortar with significant pressure applied, the powder can be made to turn orange. For the purpose of these experiments, however, gentle grinding until the luminescence had changed to red was applied on solid state samples.

4.4.1 UV-Visible absorption spectroscopy

In order to determine whether excimer emission is indeed responsible, UV-visible spectroscopy was performed on **(20)** in both solution and on thin powder films.

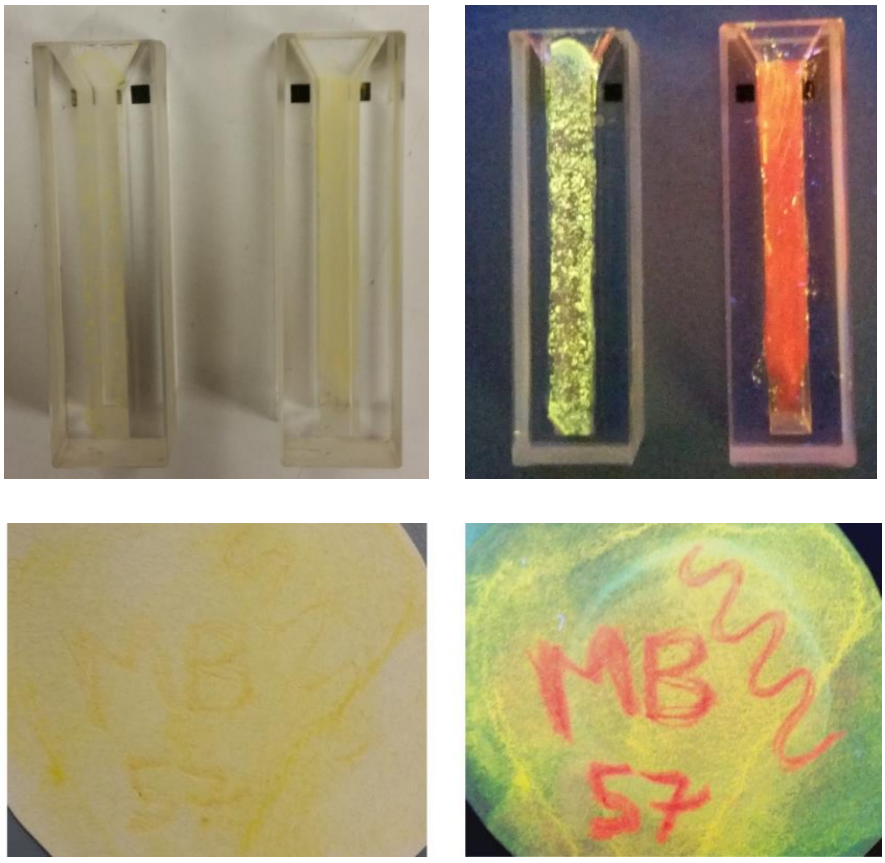

Figure 4.2. Comparison between the freshly precipitated powder, and the ground powder under ambient lighting (left) and under UV-lighting (right). The top images show thin film samples deposited on quartz cuvettes, used to record the solid state spectroscopy. The bottom images show a powder film collected on filter paper, and "written on" with a metal spatula.

Spectra were first recorded for the compound at various concentrations of dichloromethane solution, to see if any evidence of aggregation or association in the ground-state could be detected. Detection of such species would point to a cause other than excimeric behaviour and perhaps suggest aggregation effects.

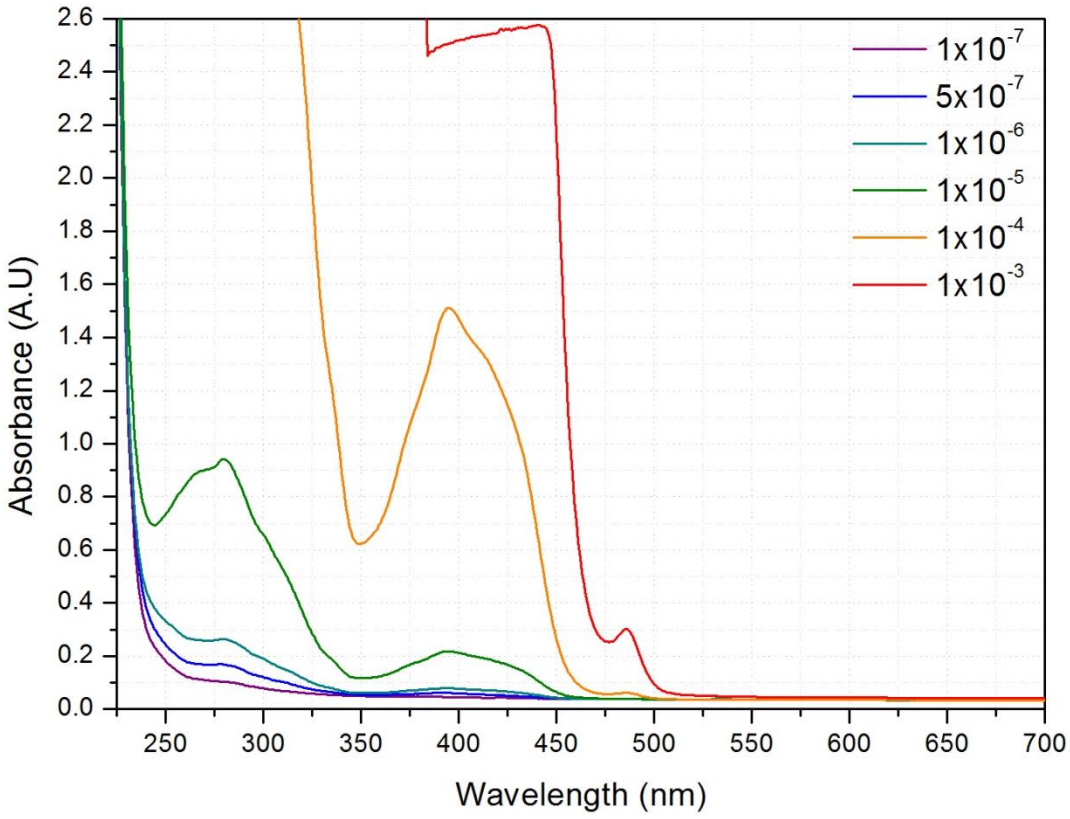

Figure 4.3. UV-Visible absorption spectra for (20) in increasing concentrations (mol dm^{-3}) in dichloromethane.

- Lowest energy main peak λ_{max} = 395nm.

The results of the solution state experiment can be seen in **Figure 4.3**. It is readily apparent that no change to the profile of absorption, or peak λ_{max} positions can be detected with increasing concentration (the strange peak shape of the 1x10 mol dm^{-3} solution is an artefact due to reaching the limit of the spectrometer detector sensitivity at high concentrations). The lowest energy main peak is positioned with λ_{max} = 395nm, and can be attributed to the typical standard $^{1}\pi$-π^* state with some MLCT character, as described in **Chapters 1** and **2**. The higher energy peak stands at λ_{max} = 279nm. The appearance of the extremely weak peak at λ_{max} = 485.5 nm, visible only in concentrations > $1x10^{-4}$ mol dm^{-3}, can be attributed to direct excitation of $^{3}\pi$-π^* states facilitated by the platinum's high spin-orbit effect.[11] This result points towards a lack of ground-state aggregation, at least in solution, supporting excimeric emission as a possible mechanism.

The next step was to produce UV-visible absorption spectra for the solid powder in its fresh and mechanically ground states. This was done by precipitation of a thin film onto the face of two quartz cuvettes, and grinding the solid of one of the films in-situ until the luminescence appeared red (**Figure 4.2**: top).

The results of this experiment can be seen in **Figure 4.4**. It is again clear from this experiment, that very little difference can be seen between the two films in terms of peak positions, and differences in intensity can be attributed to differences in film uniformity and thickness. The spectra also bear a close resemblance to that of the solution state, further hinting that the absorption is not significantly affected by intermolecular interaction. In order for ground state aggregation in the solid to be a potential explanation for the properties seen, a red-shift would be seen in the absorption spectrum of the ground film. This is evidently not seen.

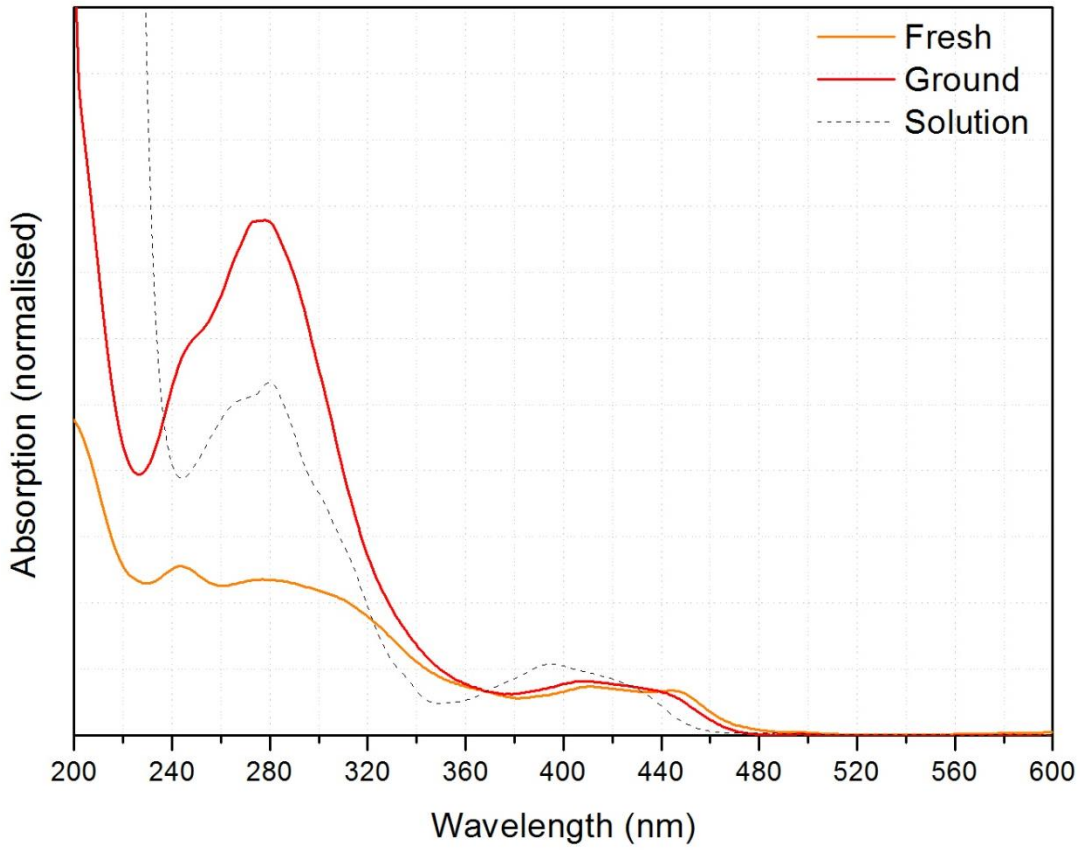

Figure 4.4. Solid-state emission spectra of the fresh (yellow/green emitting) film (orange line) and the ground (red emitting) film (red line). Also present is an overlay of the solution state spectrum (dashed line). Absorbance has been normalised for ease of comparison.

4.4.2 Emission spectroscopy

From the absorption spectroscopy data, it is clear that there is no increase in aggregation or intermolecular association of the ground state molecules facilitated by the grinding process. This is strongly supportive of the excimer hypothesis.

Emission spectroscopy was then carried out on the compound in order to obtain information about the nature of the emissive states.

Spectroscopy was first recorded in the solution state to see if any evidence of excimer formation can be detected at high concentration. A series of concentrations of **(20)** in degassed dichloromethane were produced, and all irradiated at 352nm. The results of this can be seen in **Figure 4.5**.

It is clear from this graph that **(20)** exhibits excimer emission in solution in concentrations exceeding $1x10^{-4}$ mol dm^{-3} with the formation of a broad structureless peak at λ_{max} = 688 nm. Also notable is the small red-shift of the main emissive peak and loss of some vibrational structure seen in concentrations above $1x10^{-7}$ from λ_{max} = 485.5 nm to λ_{max} = 502 nm. This is simply an inner-filter artefact from the emerging 0-0 direct triplet absorption, which combined with normalisation of the graphs leads to a false drifting of the maxima.

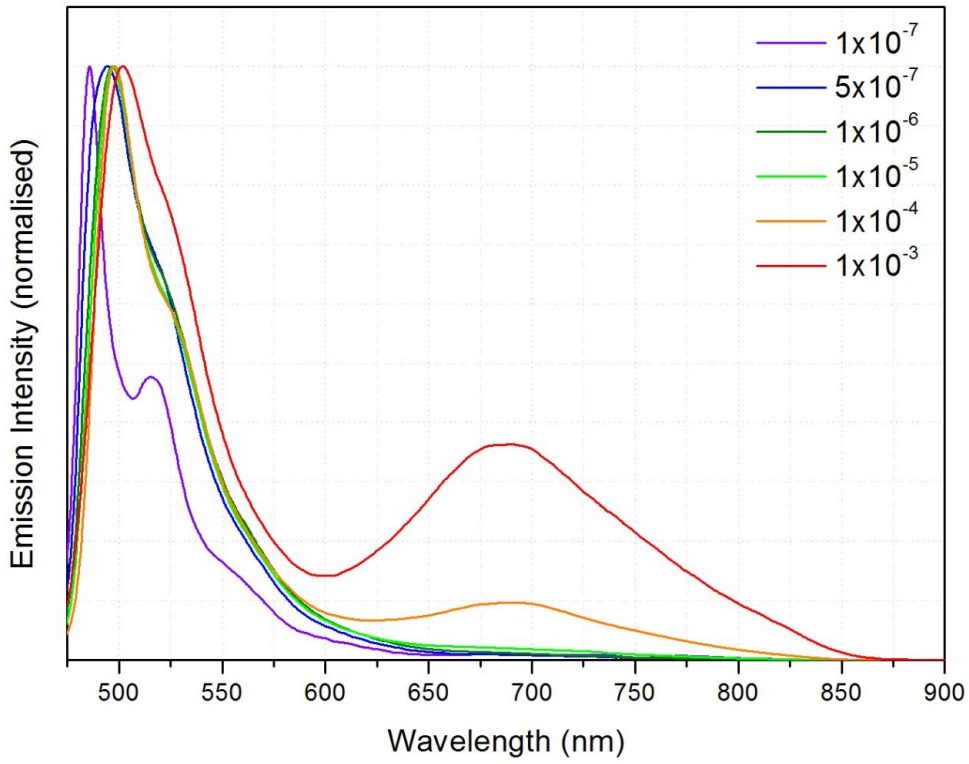

Figure 4.5. Normalised emission spectra for a series of dichloromethane solutions (concentrations in mol dm^{-3}) of (20).

To compare the solution-state excimer behaviour to the observed solid-state properties, emission spectra were recorded for a powder sample before and after mechanical grinding. This also served to quantify the degree to which the luminescence red-shifts for the compound. In **Figure 4.6** the two resulting spectra have been superimposed along with the $1x10^{-3}$ mol dm^{-3} solution which features both monomer and excimer peaks (dashed line). It is clear from this graph that the extent of the red shift is significant. The sample before grinding (**Orange line**) is seen to have a fairly sharp, slightly structured emission close to that of the solution state monomer, with λ_{max} at 511nm. The same powder sample, after having mechanical pressure applied to it within the cuvette gives us the **Blue line**, with its λ_{max} now at 678nm and its broad featureless profile extending into the near-IR frequencies. The small residual signal at 511nm is due to incomplete grinding of the entire sample.

As stated, the solution state monomer emission is very similar in profile and energy to that of the un-ground powder, but in addition, the broad and featureless excimer emission of the solution conforms well to the spectrum of the ground powder. It would appear therefore that in the un-ground powder the emission is likely to originate from monomer units, and that intermolecular interactions play only a minor role, leading only to a small red-shift. Once ground, the emission appears to share its properties with the solution state excimeric emission, and this, along with the proportionately unchanged absorption spectra, provides evidence that the emission shift in the ground powder may indeed be as a result of solid state excimer emission.

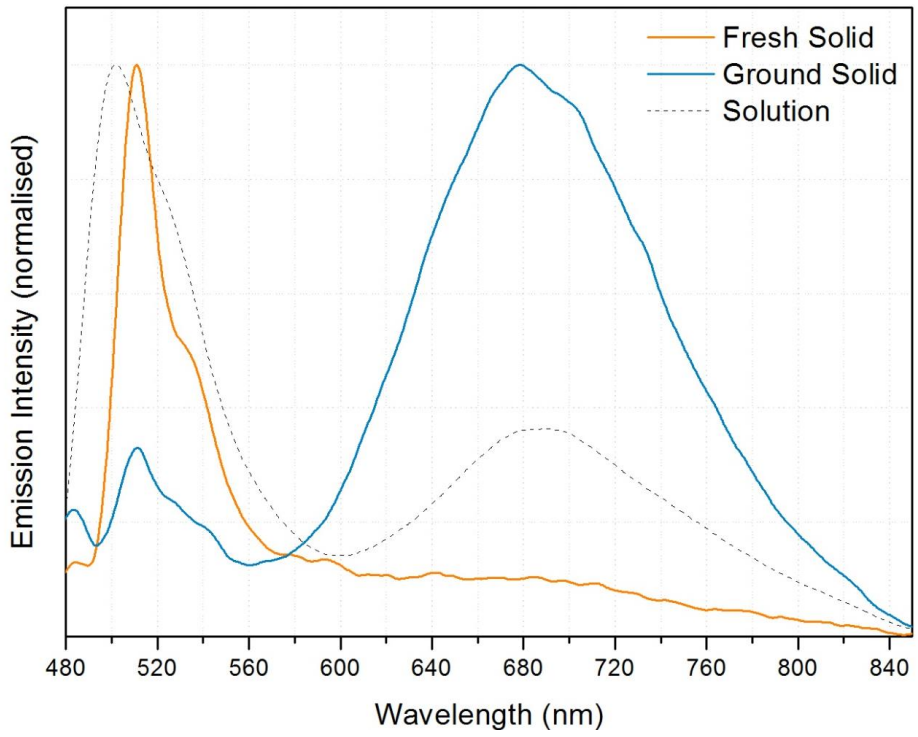

Figure 4.6. Solid state emission spectrum of a powder sample of (20) before (orange) and after (blue) mechanical grinding, measured within a quartz cuvette. Also overlaid is the emission from a $1x10^{-3}$ mol dm^{-3} solution (dashed).

4.5 Powder diffraction

In order to further understand the changes to the optical properties seen, powder diffraction experiments were run. In previous literature examples, in order to elicit red-shifted emission from the solid, disruption of the crystallinity to produce an amorphous solid was required.[2,3]

To determine whether this was the case for **(20)**, x-ray diffraction experiments were recorded for capillaries of the fresh, and ground powders.

It was determined that while the green/yellow fluorescing powder produced a very well defined diffraction pattern (which can be seen in **Figure 4.7**), upon grinding the powder indeed became amorphous, losing all diffraction. By grinding more gently in order to attempt to observe a second crystalline form, a powder with a bulk orange emission was produced that simply produced a combined lower quality diffraction pattern matching the green/yellow fluorescing powder alongside noise from amorphous material.

Due to this result, it can be said with some confidence that the colour change observed upon grinding is a product of amorphisation of the compound, and destruction of its crystalline order, further explaining the irreversibility of the process until recrystallisation. This also suggests strongly that the observed effect is due to shear forces. This loss of crystallinity appears to result in the formation of excimeric emission from the bulk solid, perhaps as a result of increased π-stacking.

4.6 Single crystal x-ray diffraction

While the luminescence effect appears to be due to a transition to amorphous solid, it does show that the compound's optical properties are sensitive to intermolecular interaction and structural orientation, with ordered structures possessing vastly different emission profiles to amorphous solids, perhaps due to a change in the nature of the intermolecular interactions.

With this in mind, it was hypothesised that manipulation of the crystalline environment with a softer and more controllable stimulus may yield additional optical property transitions that may be studied in more detail. It was decided to study the compound under variable hydrostatic pressure, to see if any new optical-property shift could be produced that, unlike the excimer-luminescence phenomenon, could be studied structurally and that would perhaps be reversible. To follow this route, firstly single crystal data was required for the yellow coloured, green/yellow emitting solid that was measured to have a crystalline structure using powder diffraction. An attempt was therefore made to produce crystals that structurally represent the yellow, un-ground sample.

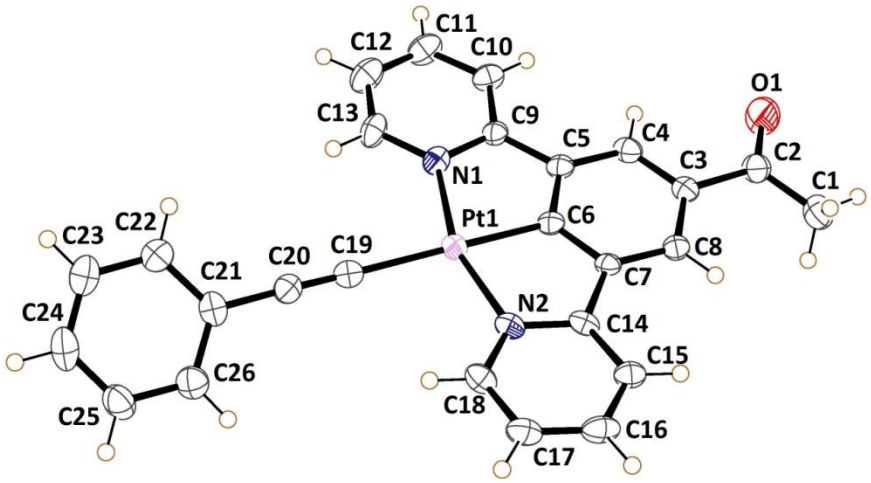

Yellow crystals with needle morphology, consistent in appearance with the yellow un-ground powder, and exhibiting a yellow/green luminescence (see **Figure 4.8**), were obtained through the method of slow evaporation of an acetone or dichloromethane solution. The first crystals measured, produced simulated powder patterns in accordance with that of the un-ground powder. Upon subsequent x-ray data collections from several different crystallisations, however, it was revealed that a second similar polymorph, also yellow, existed for **(20)** which did not represent the bulk powder. Both polymorphs crystallised in the space group $P2_1/n$. The polymorph consistent with the powder will be referred to as "**polymorph 1**" and the second structure "**polymorph 2**".

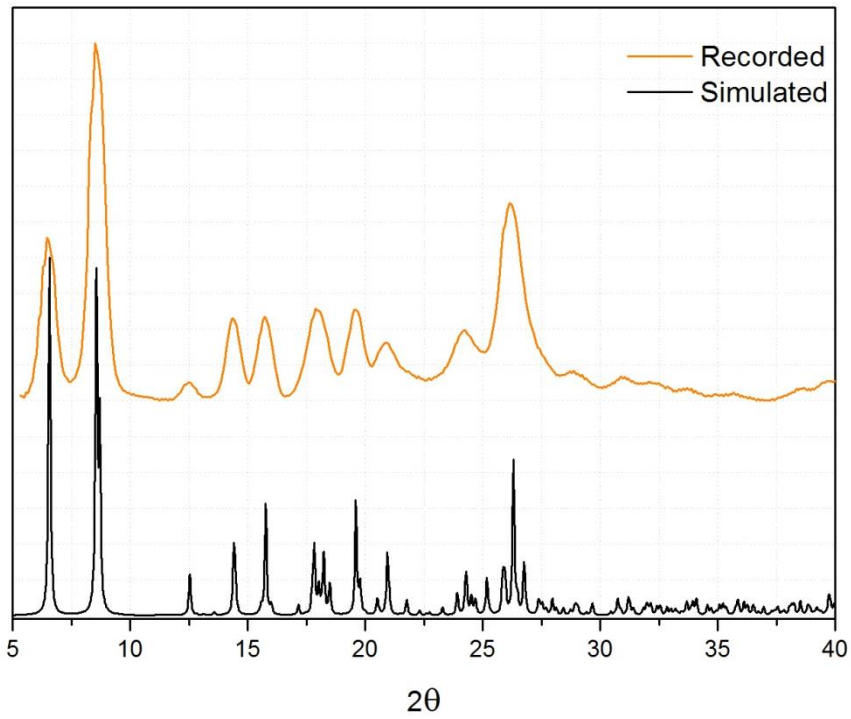

Figure 4.7. Comparison of the recorded powder patterns for the bulk un-ground solid and the simulated pattern of polymorph 1 from the single crystal data.

4.6.1 Polymorph 1

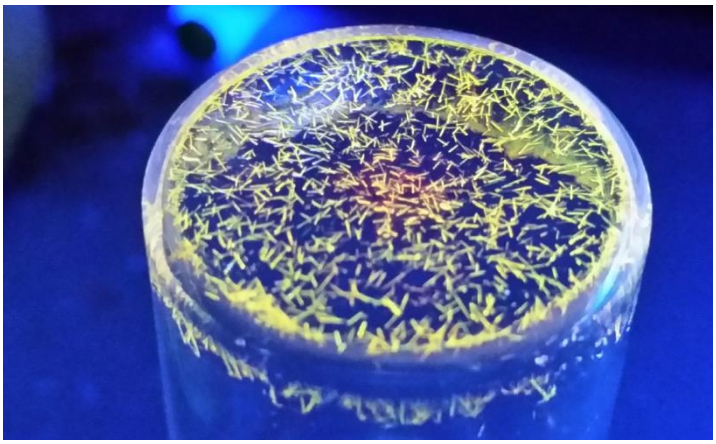

Figure 4.8. Yellow/green fluorescence from crystals of polymorph 1 under UV lamp. Grown from acetone solution.

(20) polymorph 1 crystallised as relatively large needles obtained by slow evaporation of concentrated dichloromethane or acetone solution. **Polymorph 1** crystallises in the monoclinic space group $P2_1/n$, with the asymmetric unit consisting of one neutral molecule of **(20)**. The acetylide group is almost planar with the pincer (C20-Pt1-C6 angle of 179.17 (15) °), and the average plane of the phenyl ring is twisted by 33.02 (12) ° from the average plane of [Pt1, C5, C6, C7, C9, C14, N1 and N2]. The Platinum centre adopts the expected square planar geometry with minor distortion (N1-Pt1-N2 angle 159.82 (16) °) due to the pincer bite angle, with bond parameters in the expected ranges. The C≡C bond distance, 1.174 (7) Å is also typical (**Table 4.1**).[12,13,14]

Table 4.1. Selected bonds and angles for (20) polymorph 1

Bond	Length (Å)
Pt1-N1	2.031 (4)
Pt1-N2	2.036 (4)
Pt1-C6	1.931 (5)
Pt1-C19	2.077 (5)
C19-C20	1.174 (7)

Bonds	Angle (°)
Pt1-C19-C20	178.4 (4)
C19-C20-21	177.8 (5)

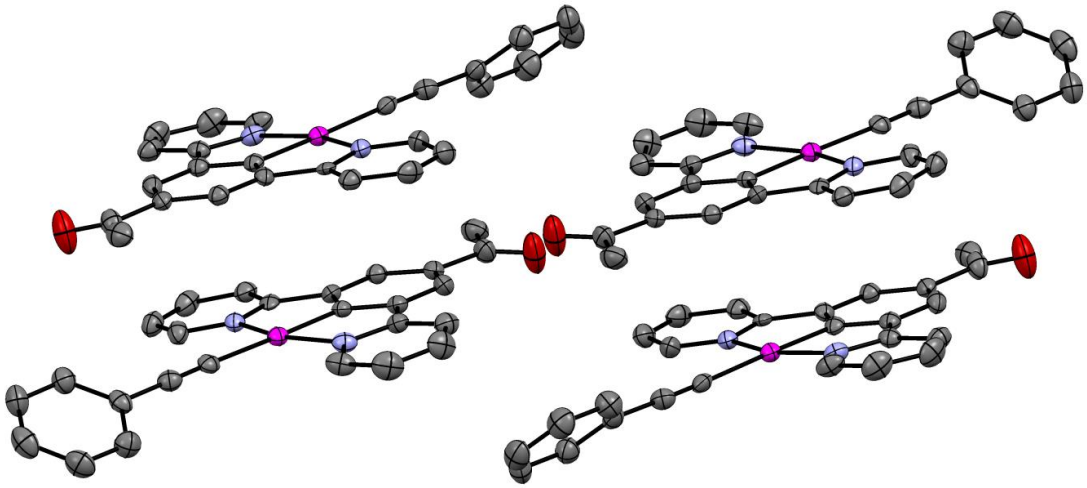

Figure 4.9. Extended structure of Polymorph 1, displaying end-to-end structure and planarity of the pincer units. Hydrogen atoms removed for clarity.

It can be seen from the extended crystal structure of **Polymorph 1** that the molecules arrange into end-to end pairs, which lie in a planar configuration with respect to each other (**Figure 4.9**). The twisted pendant phenyl ring appears to be stabilised by a weak C-H---O hydrogen bonding interaction between then phenyl and the carbonyl of the adjacent molecule (**Figure 4.10**). While the extended structure is planar, the platinum-platinum distance of 5.3688 (3) Å within each pair suggests no intermetallic interaction. The intermolecular interactions in the structure centre around weak C-H---O hydrogen bonds to the carbonyl group, details of which can be found in **Table 4.2**.

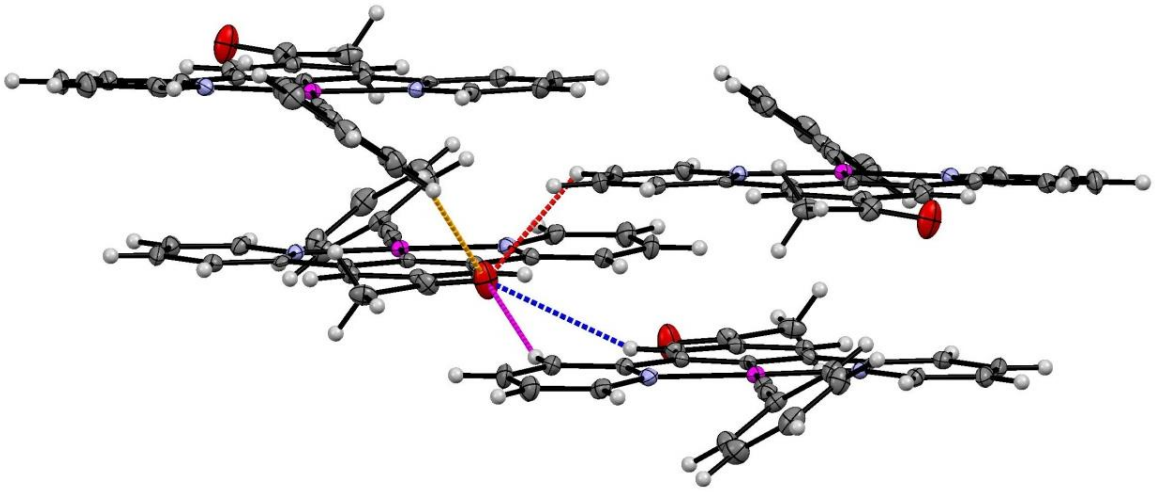

Figure 4.10. C-H---O Weak hydrogen bonding interactions present in Polymorph 1 centred around the carbonyl group. Symmetry equivalent interactions not shown for clarity.

Table 4.2. Weak hydrogen bonding interactions for (20) polymorph 1

Bond	Distance (D..A) (Å)	Distance (H..A) (Å)	Angle (D..H..A) (°)
C26[1]-H18[1]-O1	4.026 (8)	3.143	159.27
C17[2]-H12[2]-O1	3.142 (7)	2.656	121.67
C4[3]-H4[3]-O1	3.827 (7)	3.020	146.05
C10[3]-H16[3]-O1	3.200 (7)	2.358	150.28

1 = (1/2-x, -1/2+y, 1/2-z), 2 = (1/2+x, 1/2-y, 1/2+z), 3 = (1-x, 1-y, 1-z)

4.6.2 Polymorph 2

(20) polymorph 2 crystallised as large yellow blocks obtained by slow evaporation of concentrated dichloromethane or acetone solution. **Polymorph 2** also crystallises in the monoclinic space group $P2_1/n$, with the asymmetric unit consisting of one neutral molecule of **(20)**. The acetylide group deviates slightly more from planar with the pincer (C20-Pt1-C6 angle of 176.5 (3) °), and the average plane of the phenyl ring is more twisted, now by 53.8 (2)° from the average plane of [Pt1, C5, C6, C7, C9, C14, N1 and N2]. The platinum centre adopts the same expected square planar geometry with minor distortion (N1-Pt1-N2 angle 159.8 (3) °) due to the pincer bite angle, with bond parameters in the expected ranges. The C≡C bond distance, 1.220 (10) Å is also typical (**Table 4.3**).[12,13,14]

Table 4.3. Selected bonds and angles for (20) polymorph 2

Bond	Length (Å)
Pt1-N1	2.033 (7)
Pt1-N2	2.032 (8)
Pt1-C6	1.923 (8)
Pt1-C19	2.042 (9)
C19-C20	1.220 (10)

Bonds	Angle (°)
Pt1-C19-C20	175.5 (8)
C19-C20-21	179.0 (10)

The extended structure of **Polymorph 2** shares many similarities with **Polymorph 1** in that it consists of planar "couplets" of end to end pairs with a twisted pendant phenyl interacting with adjacent carbonyls.

However, for **Polymorph 2**, there are two planar orientations of the pairs, rotated almost 90° in plane from each other, leading to a zig-zag structure instead of a linear one seen in **Polymorph 1** (see **Figure 4.13** for further details), and the pairs of molecules are no longer coplanar, with the structure having a herringbone configuration (**Figure 4.12**). The pendant phenyl is also more twisted from the plane of the pincer at 53.8 (2) °. Again, the platinum-platinum separation of 5.1394 (7) Å suggests no interaction.

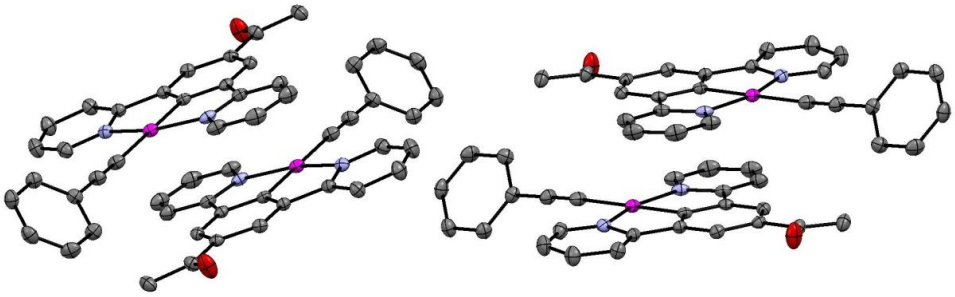

Figure 4.11. Extended structure of Polymorph 2, displaying end-to-end structure and the herringbone arrangement of pairs with two orientations.

Intermolecular interactions of **Polymorph 2** are essentially the same as for **Polymorph 1**, where weak C-H donor hydrogen bonding interactions to the carbonyl make up the majority of the contacts (**Table 4.4**)

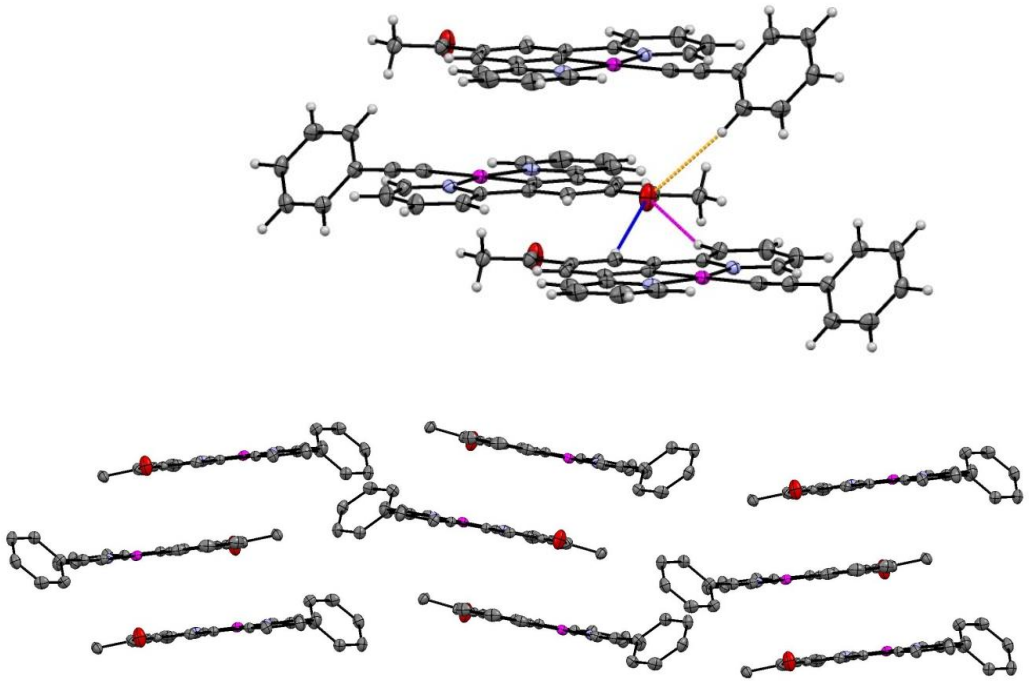

Figure 4.12. Top: C-H---O Weak hydrogen bonding interactions present in Polymorph 2 (symmetry equivalent interactions not shown for clarity). Bottom: Extended structure of Polymorph 2, showing the herringbone structure.

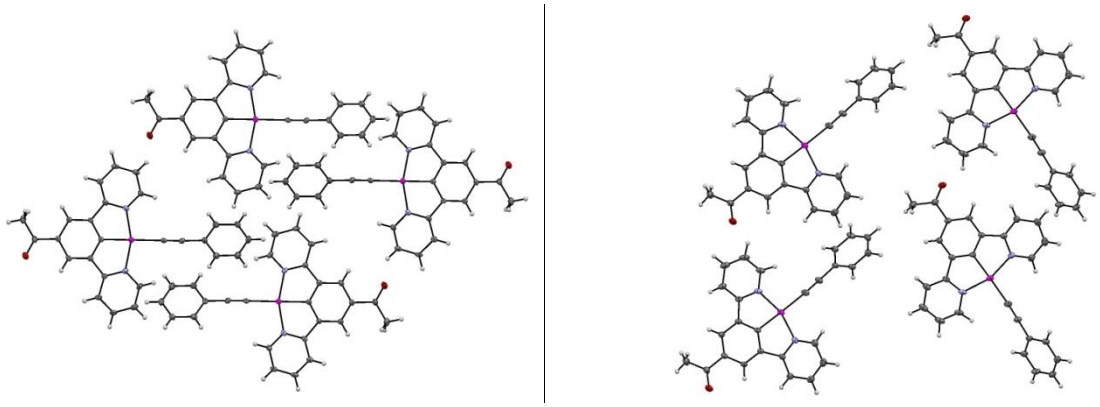

Figure 4.13. Comparison of the extended structures of polymorph 1 (left) and Polymorph 2 (right) showing the "linear" and "zig-zag" arrangements. Only one molecule of each pair pictured for clarity.

Table 4.4 Weak hydrogen bonding interactions for (20) polymorph 2

Bond	Distance (D..A) (Å)	Distance (H..A) (Å)	Angle (D..H..A) (°)
$C26^{1}$-$H26^{1}$-O1	3.756 (12)	2.835	171.10
$C10^{2}$-$H10^{2}$-O1	3.413 (11)	2.532	158.24
$C4^{2}$-$H4^{2}$-O1	3.653 (10)	2.827	148.60

1 =(1-x, -y, 2-z), 2 = (2-x, -y,3 -z)

4.7 Studying compounds at high-pressures

In order to study compounds at high pressures spectroscopically, a diamond anvil cell (DAC) is typically used. A DAC consists of two high quality conical diamonds, each cut with a flat surface or "culet" at the narrow end, mounted into tungsten carbide brackets set into steel plates. The plates are joined by screws to create a vice that may be tightened to move the diamond culets towards each other. The diamonds are positioned on either side of a thin (*c.a.* 0.2 mm) foil gasket (steel or tungsten) with a small hole drilled through it, creating a small cavity between the culets (**Figure 4.14**). In order to induce pressure on a sample, it is placed in this cavity along with a liquid pressure medium to ensure and evenly distributed pressure on the sample, and the tightening screws are used to apply pressure between the two diamonds. Pressure between the diamonds is often measured by monitoring the fluorescent emission of a small ruby placed alongside the sample.[15]

Due to the high transparency of diamond to a broad spectrum of electromagnetic radiation, the sample may be probed with a variety of spectroscopic techniques, allowing for solids to be studied in depth to pressures as high as 300 GPa in large cells.[16,17]

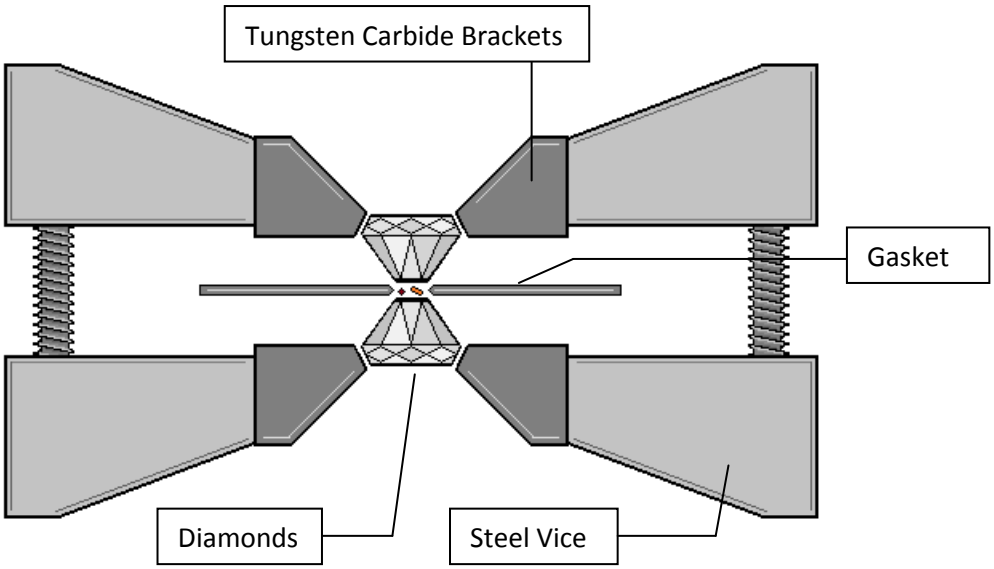

Figure 4.14. Schematic of the workings of a diamond anvil cell [18]

4.8 High pressure studies of (20)

4.8.1 High pressure UV visible spectroscopy

In order to investigate the effect of hydrostatic pressure on the optical properties of the crystalline sample of **(20)**, absorption spectroscopy was carried out on the compound in a crystalline form, under a steadily increasing hydrostatic pressure.

4.8.1.1 Experiment set-up

In order to perform this experiment, a diamond anvil cell was used to contain a single crystalline sample of **(20)** in a pressure medium of Fomblin-oil, which was then mounted on a goniometer-head for accurate alignment. Due to time restrictions in using the equipment, only **Polymorph 1** was measured spectroscopically, as this structure is representative of the bulk powder for which we see the shear optical effects. A ruby was also leaded into the cell, and its fluorescent emission was used as a way to determine the sample pressure. See **Figure 4.15** for details.

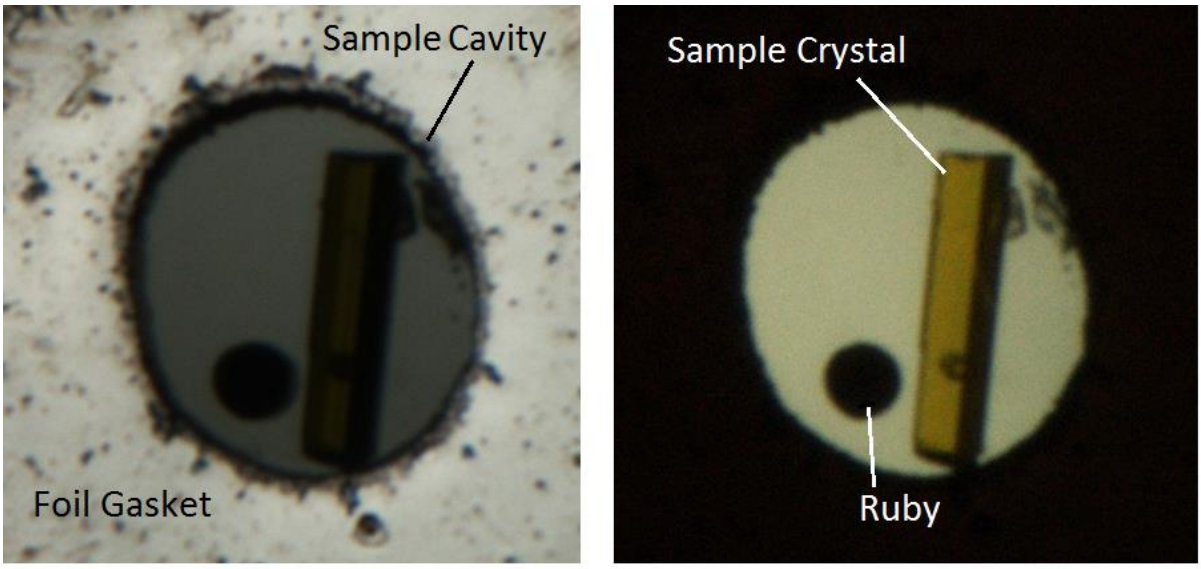

Figure 4.15. Surface-lit (left) microscope photograph of the crystal sample (ca. 50 µM length) within the diamond anvil cell, highlighting the gasket and sample cavity. Back-lit (right) photograph highlighting the sample crystal and the ruby.

Spectra were then collected at various pressure intervals using a microspectrophotometer *via* transmission of a 50 µm diameter probe beam through the single crystal within the anvil-cell after careful alignment (see **Figure 4.16** for experimental set-up).

Spectra were collected at room temperature using mirrored lenses (Bruker) mounted in an off-axis geometry with a deuterium halogen light source (Ocean Optics). Absorption was monitored over the 300-750 nm wavelength range using a Shamrock 303 imaging spectrograph (Andor).

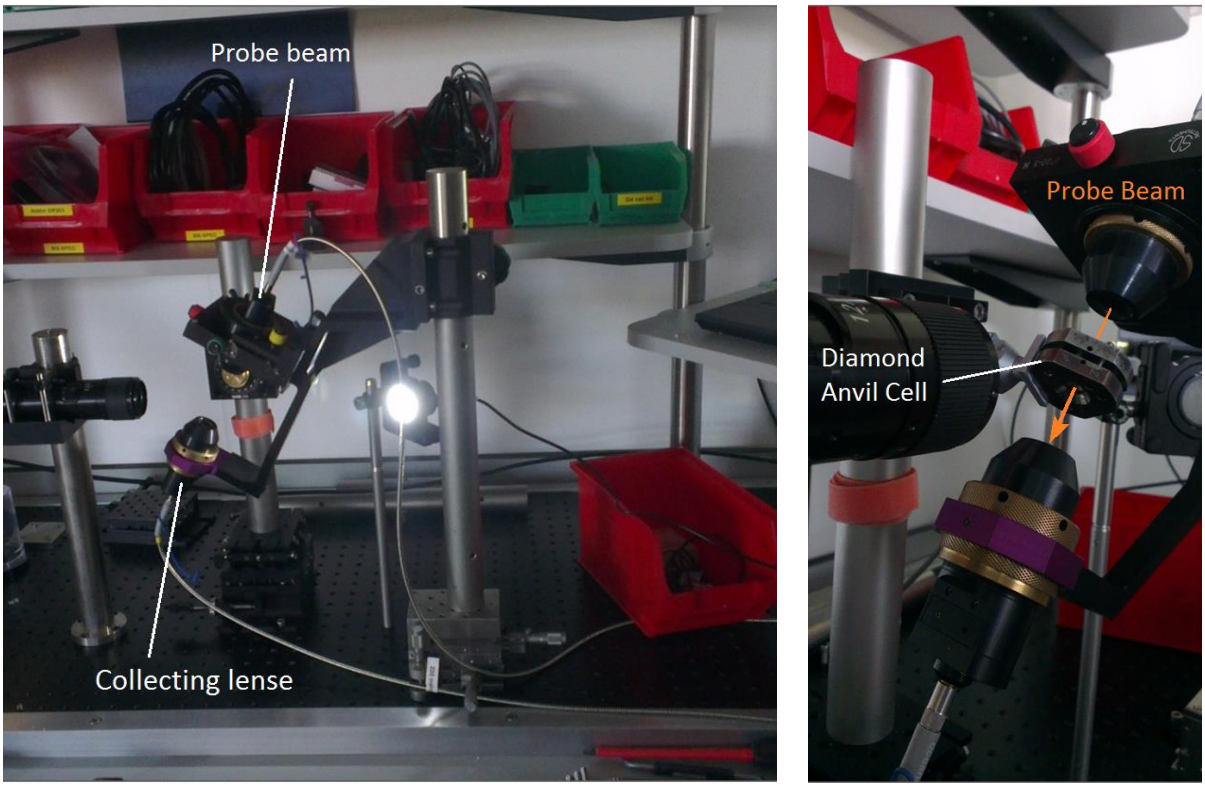

Figure 4.16. The high-pressure spectroscopy experimental set up used.

4.8.1.2 Results and discussion

UV visible spectra were recorded on the crystal of **(20) Polymorph 1** at regular intervals between 0 and 10 GPa. In **Figure 4.17** microscope photographs of the single crystal at each pressure interval can be seen, and even before seeing any spectroscopy data it is possible to see a clear colour change from the standard yellow, all the way to a deep red at 10 Gpa. This is clearly reflected in the spectroscopy (**Figure 4.18**) where a significant red-shift to the lowest energy absorption is observed following the increase in pressure on the crystal. This red shift appears to result from the broadening of the absorption peak, moving the λ_{max} from around 500nm to almost 600nm with the tail of the absorption spreading as far as 700nm.

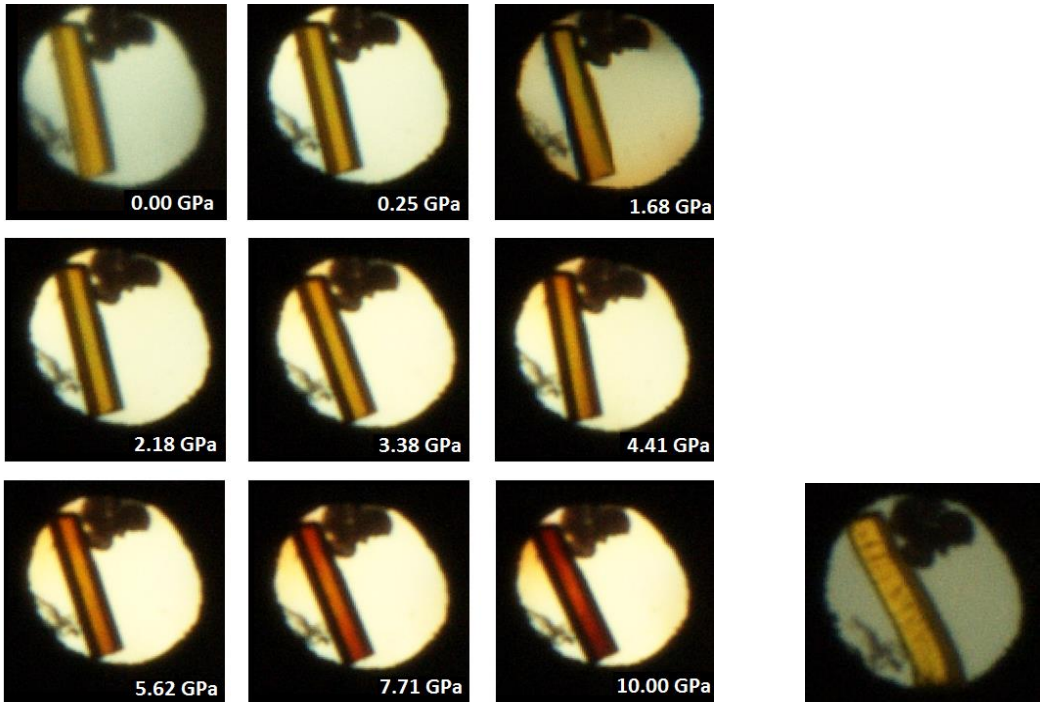

Figure 4.17. Microscope photographs of the single crystal of (20) at each of the pressure intervals, displaying the clear colour transition with increasing pressure. Offset is the crystal returned to atmospheric pressure.

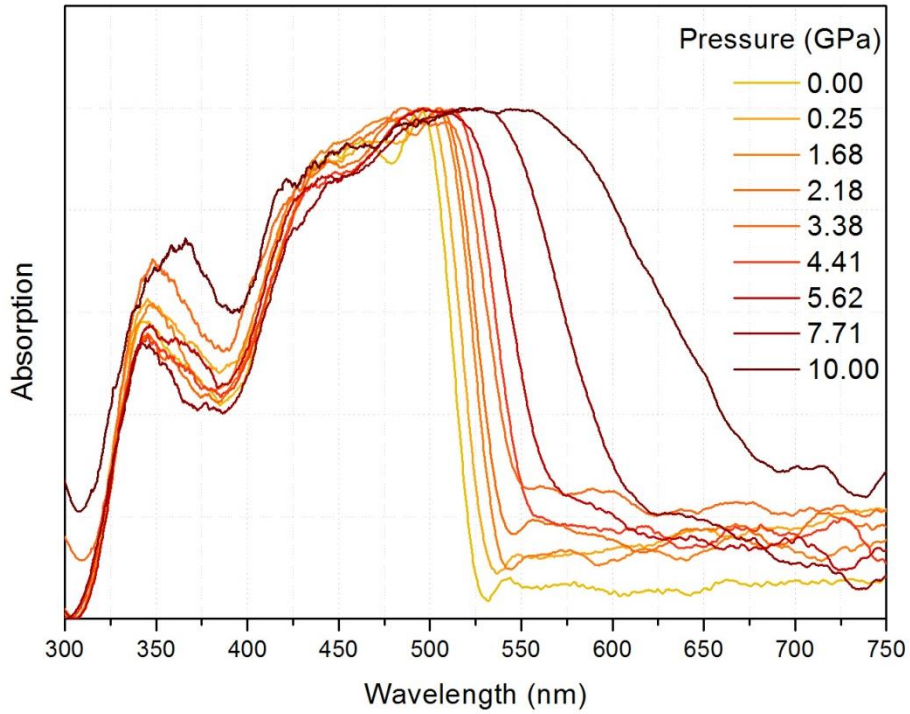

Figure 4.18. UV-Visible spectra of a single crystal of (20) Polymorph 1 at various pressure intervals.

While the single crystallinity appears to have been lost (potentially due to the depressurisation being too rapid) the crystal returned to its original colour upon release of the pressure, confirming that this effect differs from the irreversible shear effect observed through grinding.

Before an attempt to structurally characterise **(20)** under a high-pressure environment was made, ways in which a crystalline change, and likely a change in intermolecular interactions, could lead to a change in absorption energy for this compound were hypothesised.

While it is possible that pressurising the structure could lead to a lateral sliding that may result in increase platinum-platinum interactions, it is however unlikely to involve d_z^2 interactions such as those seen in **Chapter 3**. This prediction was based on the work of **Chapter 2** whereby the phenylacetylene ligand has been shown to provide significant π* donor interactions to the occupied d-orbital containing HOMOs with lobes in the correct plane for interaction with the π-system (d_{xz} and d_{xy}). If this is the case for **(20)**, the d_z^2 orbital is likely to be a significant way from the frontier. It was, therefore, hypothesised that increasing π-π interactions, perhaps resulting in an increase in π-destabilisation experienced by either the d_{xz} or d_{xy} orbitals with pressure, is the likely driving force behind the shifting. It was predicted this increase could be a result of either direct intermolecular interaction, or through a change in pendant phenyl torsion affecting the π-system.

4.8.2 High pressure X-ray crystallography

In order to attempt to explain the colour change seen in the crystals under pressure, single crystal x-ray diffraction experiments were performed. Experiments were performed on both **Polymorph 1** and **2**, to see if the structures behave differently under pressure. The experimental set up was broadly the same as that of the high-pressure uv-vis experiments performed (**4.6.1**), whereby a diamond anvil cell was used to place the sample under non-ambient pressure, and then x-ray diffraction was performed through the cell's aperture.

When performing crystallographic experiments at high-pressures however, there are several considerations need to be taken into account that are not a concern for spectroscopic experiments.

Firstly, when performing crystallographic experiments through a diamond anvil cell, the angle at which x-ray data can be received by the detector is severely restricted by the aperture of the cell. Combined with the additional loss of intensity, achieving sufficient data completeness is often problematic, particularly on low symmetry crystals where data completeness sufficient for structural solution is often unachievable. This may be partially mitigated by careful sample mounting, and using by synchrotron radiation enabling shorter wavelengths not available on lab sources, and higher intensities to be used. Short wavelengths compress the diffraction pattern and reduce the extent of the data lost. Even so, large parts of the diffraction pattern will be obscured.

Also to be taken into consideration are diffraction artefacts such as rings from the gasket, and ruby and diamond diffraction spots.

All of these issues need to be resolved in order to produce useful data, and this is done in the data processing stage. The shadowed parts of the pattern may be masked from the data during processing, and standard data-processing software is sufficient to index the correct spots for the sample. In order to bypass the solution stage of the process for data with low completeness, an ambient structure model is usually fitted to the data and refined to give the best possible representation of the high-pressure structure.

4.8.2.1 Polymorph 1

Unfortunately, in this experiment, crystals of **Polymorph 1** were unable to withstand the high pressure environment while maintaining crystallinity. Visibly, no defects were seen in the crystals under increasing pressure, however upon performing diffraction experiments it became apparent that the single-crystallinity of the structure suffered greatly. Even obtaining unit cells proved difficult, and were therefore considered to be unreliable.

4.8.2.2 Polymorph 2

Polymorph 2 seemed to withstand the pressure better than **Polymorph 1** potentially due to its lack of planarity preventing crystal shearing. **Polymorph 2** also underwent a reversible transition from the ambient yellow colouration to a deep red at the lower pressure of 5.041 GPa, which was accompanied by a unit cell change at each pressure interval detailed in **Table 4.5**.

It can be seen that the majority of the compression of the cell is observed in the **a** and **b** axes, along with a consistent increase of β-angle, and a distortion of the monoclinic cell towards triclinic at pressures >1.671 GPa.

Table 4.5. Unit cells for polymorph 2 under increased pressure.

Pressure	Unit Cell Dimensions					
(Gpa)	a	b	c	α	β	γ
0.000	6.9648 (3)	26.3983 (11)	11.2123 (5)	90	100.844 (2)	90
1.671	6.6043 (10)	25.3614 (16)	11.0792 (6)	90	101.851 (6)	90
3.283	6.252 (18)	24.78 (2)	11.035 (8)	89.27 (3)	102.77 (8)	85.88 (8)
5.041	6.185 (15)	24.22 (2)	11.086 (8)	87.86 (4)	104.61 (8)	84.20 (12)

The transition from a monoclinic cell to a low-symmetry triclinic cell proved troublesome regarding data completeness and structural solution, with data lost to shadowing from the DAC. The structure in the first pressure interval, owing to the cell remaining monoclinic, has been solved however.

Pressure 1: 1.671 GPa

The structure at 1.671 GPa was able to be solved due to its retention of monoclinic symmetry. In **Figure 4.19** a comparison is made between the structure of **Polymorph 2** at atmospheric pressure (Blue) and at 1.671 GPa. It can be seen that the compression, while seen in all axes, is primarily seen in the b-axis. As a result, the outer pair of molecules in the structure can be seen to move laterally towards the central pair, which remain relatively unaffected. Other than this, there appears to be very little deformation to the structure, and very little distortion within each molecule excepting a minor change of the acetylide angles (**Table 4.6**).

Table 4.6. Selected bonds and angles for (20) polymorph 2 at 1.671 GPa

Bond (0.000 GPa)	Length (Å)
Pt1-N1	2.042 (2)
Pt1-N2	2.034 (3)
Pt1-C6	1.933 (3)
Pt1-C19	2.059 (3)
C19-C20	1.200 (4)

Bonds (0.000 GPa)	Angle (°)
Pt1-C19-C20	174.7 (3)
C19-C20-C21	179.1 (4)

Bond (1.671 GPa)	Length (Å)
Pt1-N1	2.040 (5)
Pt1-N2	2.048 (5)
Pt1-C6	1.920 (5)
Pt1-C19	2.036 (15)
C19-C20	1.212 (19)

Bonds (1.671 GPa)	Angle (°)
Pt1-C19-C0	172 (2)
C19-C20-C21	178 (2)

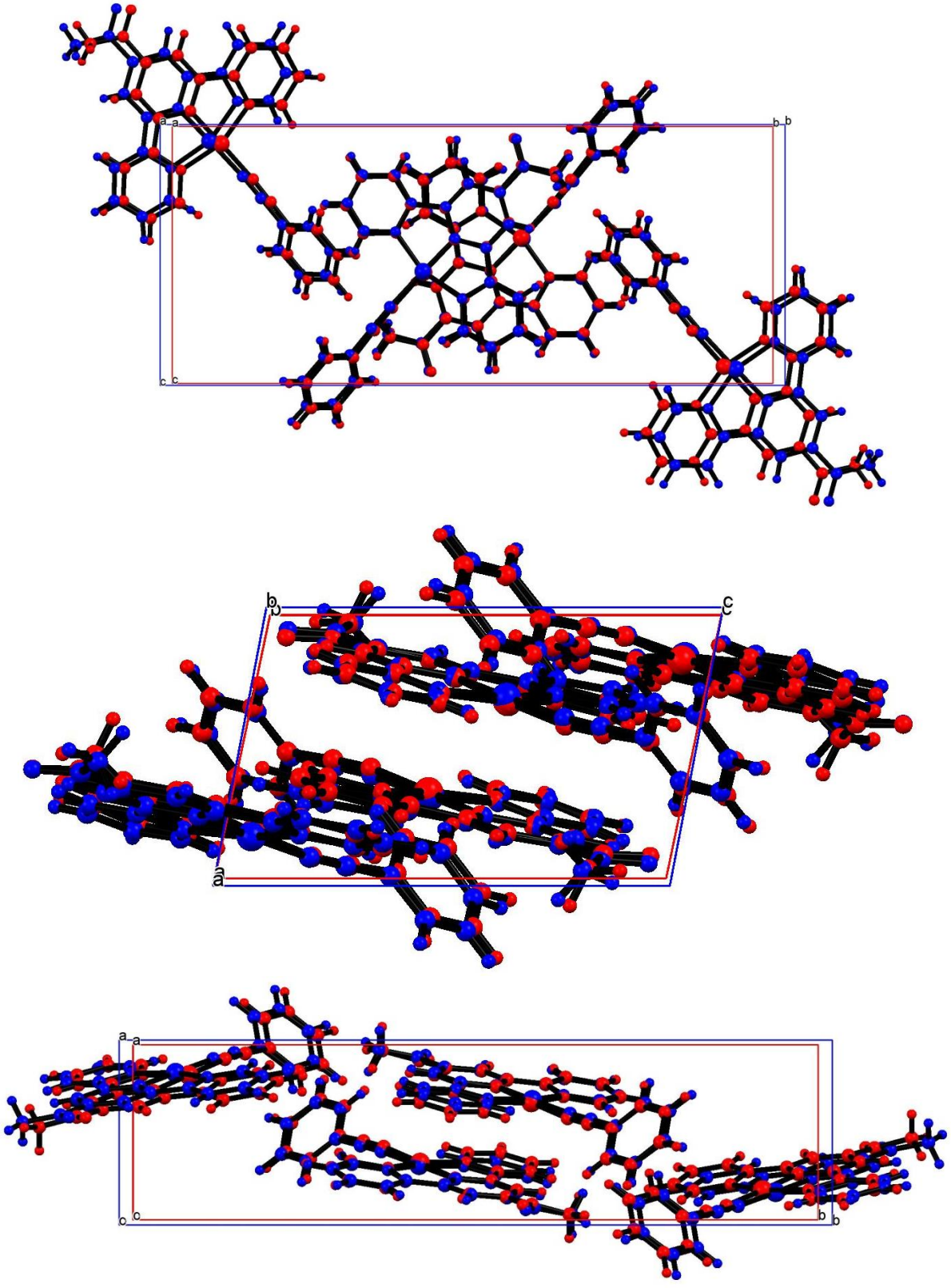

Figure 4.19. Comparison of polymorph 2. at 1.671 GPa (red) with that of the atmospheric structure (blue), viewed along a-axis (top), b-axis (middle) and c-axis (bottom).

4.8.2.3 Simulation

Due to the loss of symmetry experienced with both polymorphs, and the resulting lack of structural solution, alternative methods at elucidating the behaviour of the compound under pressure were looked into.

A collaboration with Dr Stephen Wells, at the University of Bath, was established, in which software previously used to study the “flexibility-window” framework materials, such as zeolites and perovskites, under pressure, was to be adapted for use in molecular crystals. The software is known as "Geometric Analysis of Structural Polyhedra" or GASP.[19]

The simulations were conducted by inputting the atomic coordinated of the atmospheric-pressure structure at room temperature, and then "compressing" the structure by inputting the experimentally determined unit-cell parameters at each pressure interval. In order to establish whether this approach is reliable in replicating the crystal structures rendered unattainable by low symmetry, combined with pattern shrouding from the DAC, a comparison of the simulated structure for the solved pressure interval of **Polymorph 2** at 1.671 GPa, with that obtained experimentally, was performed.

The structure generated proved to be a good replication of the experimental structure, with only slight differences (**Figure 4.20**). This may indicate that higher pressure structures simulated using this technique, may be of some merit in determining the cause for the colour change observed.

Due to the unreliable unit cells, and poor data achieved for **Polymorph 1**, GASP simulations generated heavily distorted and improbable structures. This either calls into question the validity of the unit cells obtained from the increasingly poor data, or confirms that the structure is unable to retain order at high pressures. Whichever is true, further solid state analysis of this polymorph is impractical.

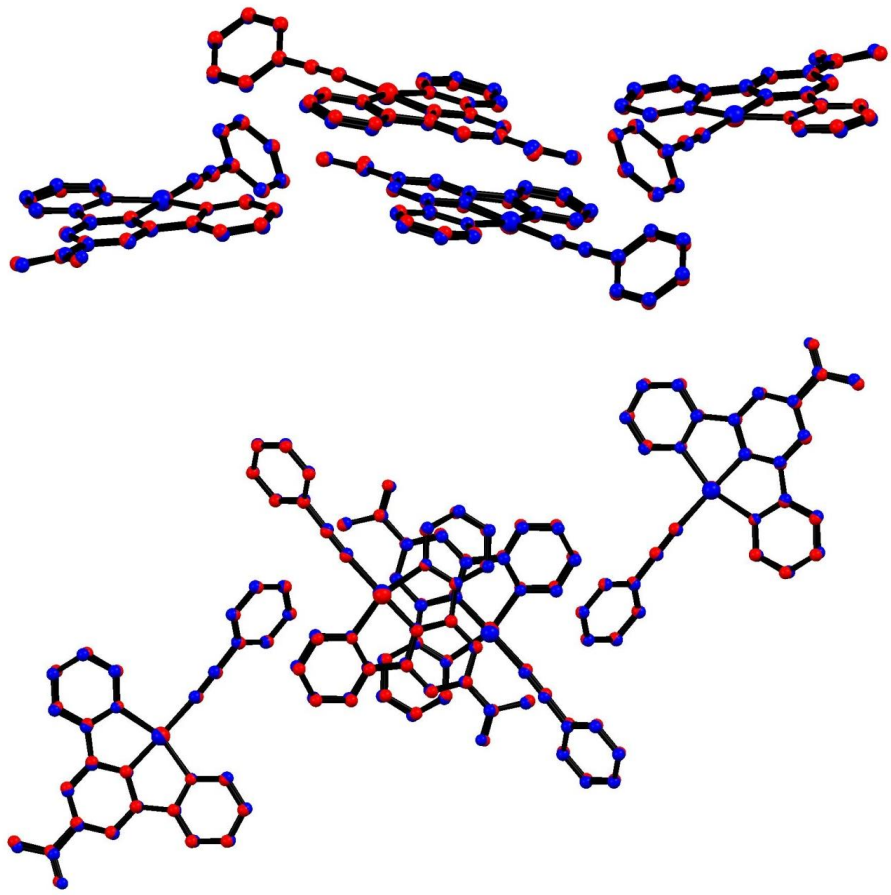

Figure 4.20. Structural overlay of the experimentally determined solution (blue) and the structure simulated using GASP (red).

In **Figure 4.21** the comparison of the simulated structures for each pressure interval can be seen (**polymorph 2**). The way the simulations predict the structure to behave seem reasonable, with the experimentally determined trend between the atmospheric and 1.671 GPa structures continuing. The trend with increasing pressure follows that the two molecules at each end of the unit cell compress towards each other, and this is accompanied by a twisting of the two inner molecules in such a way as to move the phenyl pendants towards one another. The deviation between the orientation of the central pair, and the two outer molecules means the two orientations are no longer symmetry equivalents for the triclinic structures, and in **Table 4.7**, their internal parameters are reported separately. The pairs with the orientation shown in the centre of the cell in **Figure 4.21** will be referred to as **Pair 1**, and the outer molecules form **Pair 2**.

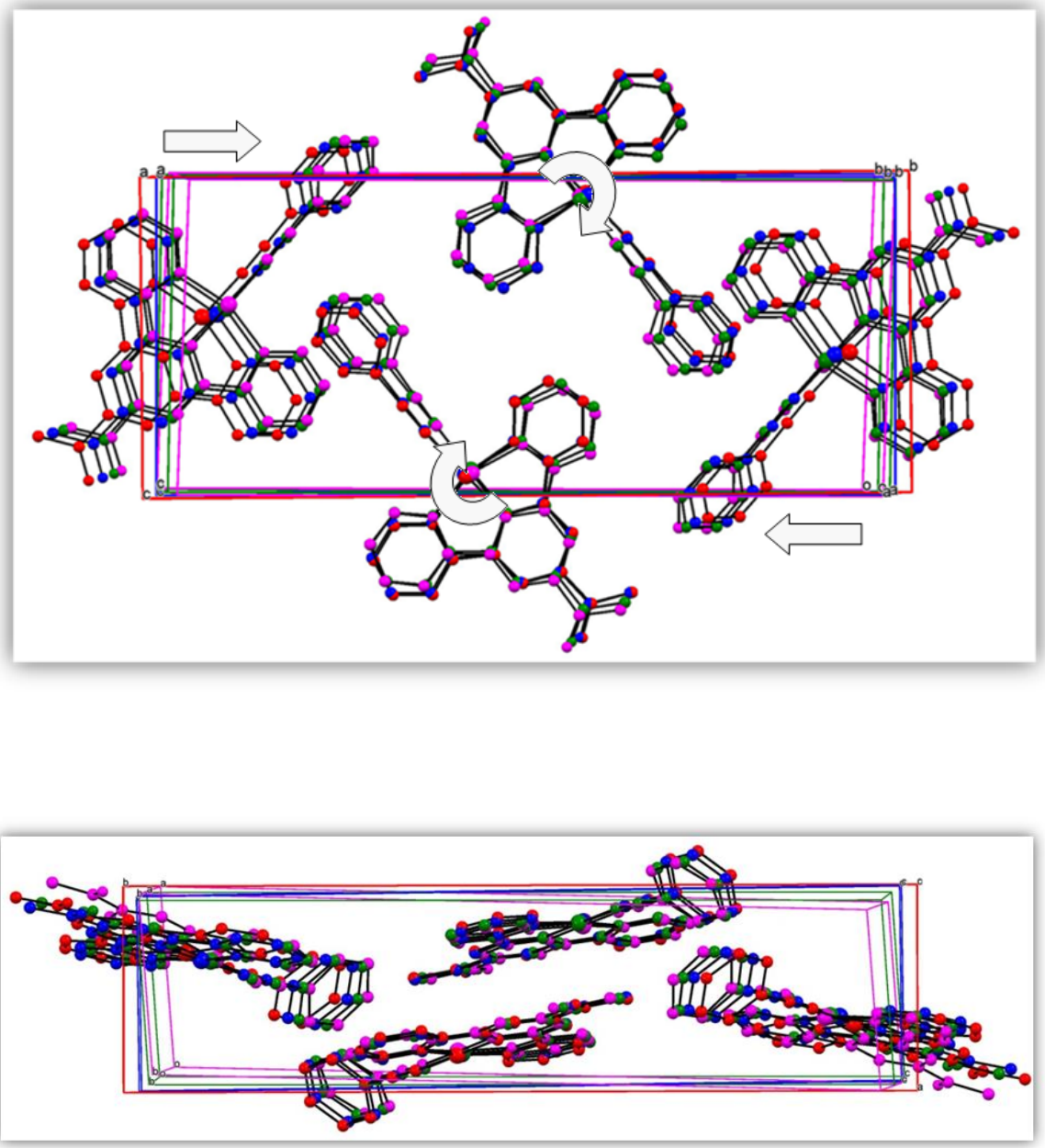

Figure 4.21. "Top-down" and "side-on" views of polymorph 2 simulated structure at each pressure interval (GPa). Red: 0.00, Blue: 1.671, Green: 3.283, Magenta: 5.041.

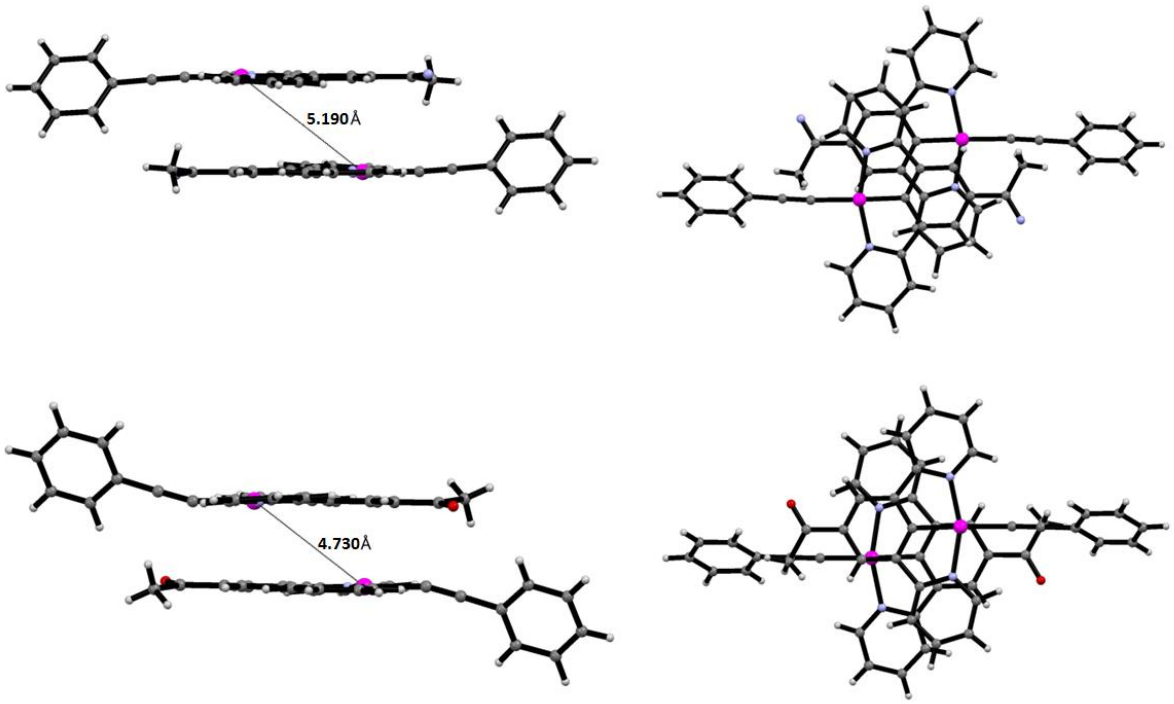

Figure 4.22. Comparison of the intermolecular interactions between the atmospheric structure (top) and the simulated structure at 5.041 GPa (bottom) in Pair 2.

Table 4.7. Internal parameters for pair 1 and pair 2 at pressure intervals

Parameter (Pair 1)	0.000 Gpa	1.671 Gpa	3.283 Gpa	5.041 Gpa
C20-Pt1-C6 angle (°)	176.38 (10)	175.62	176.71	177.10
Phenyl Torsion (°)	53.65 (9)	54.26	50.14	46.95
Pt-Pt distance (Å)	5.1895 (3)	5.035	4.936	4.884

Parameter (Pair 2)	0.000 Gpa	1.671 Gpa	3.283 Gpa	5.041 Gpa
C20-Pt1-C6 angle (°)	176.38 (10)	175.62	175.31	173.27
Phenyl Torsion (°)	53.65 (9)	54.26	56.44	61.72
Pt-Pt distance (Å)	5.1895 (3)	5.035	4.980	4.730

Looking at **Figure 4.22** it can be seen that the platinum-platinum distance is shortened significantly for the high-pressure structure, particularly for the molecules in **Pair 2**. However, despite this there is still a significant displacement between them. This suggests that direct intermetallic interaction is unlikely to be the route cause for the colour changes present.

As stated in **4.6.1.1**, dz^2-dz^2 interactions are unlikely to be the driving force for spectral shifts in **(20)**, however it remains a possibility that a shift in the planar stacking of the pincer ligands may be cause a significant perturbation to the frontier orbital energies through π-π interactions of the ligands. In order to fully understand how these relatively subtle changes to the structure can result in large shifts to the optical properties, solid state DFT calculations were performed.

4.8.3 Solid state calculations: Explaining the colour change

While crystallographic analysis of the compound in the solid state has proven to be highly challenging, application of the GASP program in conjunction with high-pressure crystallography has allowed the structural effect of pressure on the more robust **Polymorph 2** of **(20)** to be elucidated. The solid-state model obtained through combining these techniques, however, offers no evidence as to the electronic mechanism behind the progressive red-shifting of the absorption spectrum. In order to probe this, periodic electronic-structure calculations were undertaken collaboratively, as in the work of **Chapter 3**, with calculations being performed by Dr. Jonathan Skelton.

The structures obtained from GASP at pressures of 0.000, 1.671, 3.283 and 5.041 GPa were used as input to periodic density-functional theory (DFT) calculations carried out using the VASP code.[20] Details of the methodology used can be found in the experimental section. The frontier orbitals of the crystallographic (ambient) and GASP structures (under pressure) were visualised, in order to better understand the changes occurring under pressure. HOMO-LUMO gaps and a simulated absorption spectrum for each pressure interval were also obtained.

The first thing to note is that the calculation results are in qualitative agreement with the spectroscopic data, with the simulated absorption spectrum showing a clear red-shift in the lowest energy part of the absorption spectrum with increasing pressure. As can be expected for calculations of this type, which represent a low-level approximation to full time dependant DFT (TD-DFT), the absorption energies are significantly overestimated, leading to a blue shift with respect to the experimental spectra. Proportionally, however, there is good agreement. This is further supported by the orbital calculations with a consistent reduction in the HOMO-LUMO gap with increasing pressure being predicted.

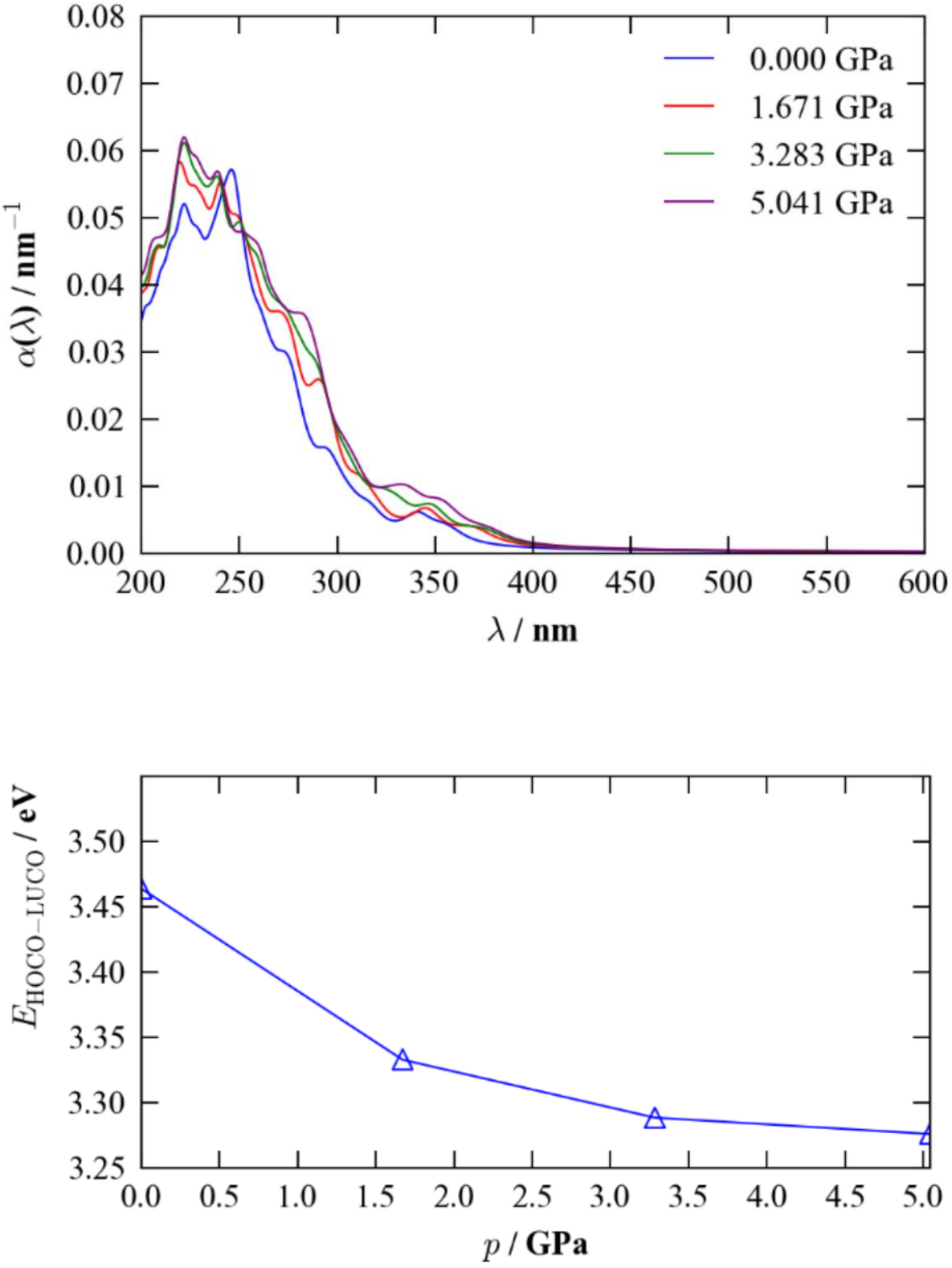

Figure 4.23. Top: Simulated absorption spectrum. Bottom: Calculated HOMO-LUMO gap (k-point 1 (Γ)).

The mechanism by which this red-shift occurs was analysed based on the orbital densities of the frontier orbitals at the four pressures.

As with other systems in this thesis, the crystal LUMO (lowest-unoccupied crystal orbital; LUCO) again appears to be relatively unaffected by the changes in pressure. The form of the orbital remains consistent under pressure, remaining predominantly on the pincer ligand.

The nature of the change to the HOCO under pressure is thus what might offer an explanation for the optical properties. At ambient pressure, the HOCO appears to mirror that of the single molecule HOMO. Consistent with the other systems studied in this thesis, it is comprised of the π* interaction between the occupied d_{xz} orbital of platinum and its surrounding π-donor ligand environment i.e. the phenylacetylene and a small component from the pincer phenyl ring.

As can be seen in **Figure 4.22**, the main displacement that occurs between molecules with increasing pressure is a lateral translation between pairs "pincer first" towards each other, bringing the platinum centres towards each other, and further superimposing the two pincer ligands.

As was discussed in **Section 4.6.2.1**, the intermetallic distances are still too large for any direct contact to result, however, from the calculations can be seen that the metals are involved in the change in optical properties, albeit indirectly.

Looking at **Figure 4.24**, it can be seen that upon increasing pressure, and inducing a translation of the molecules, there is an increased interaction between the phenyl ring of each adjacent pincer in the pairs. Because these orbitals are involved in π* interactions with the platinum d_{xz} orbitals as part of the HOCO, increasing these out of phase interactions serves to destabilise the HOCO.

In short, the HOCO transitions from being simply the discrete HOMOs of the individual molecules, to consisting of the out of phase combination of the HOMOs of each pair, "bridged" in an interaction between the phenyl pincer π-systems. The combined orbital of these linked pairs is then sensitive to the interaction along this bridge, and thus by pressurising the crystals and shortening this distance, a greater interaction is produced, destabilising the orbital and hence reducing the HOCO-LUCO gap.

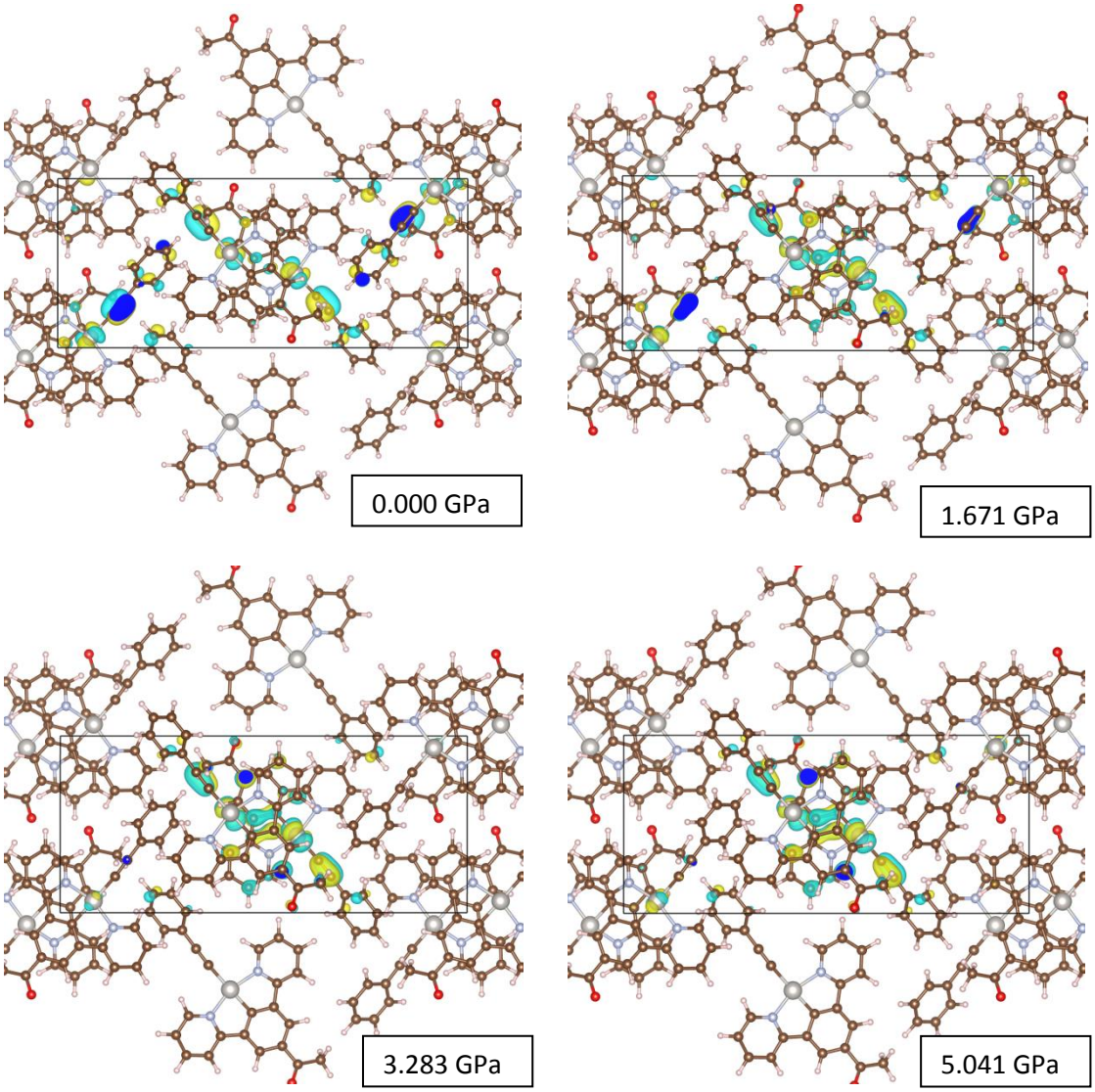

Figure 4.24. Calculated HOCOs for (20) Polymorph 2 at each pressure interval, showing increasing interaction of the platinum orbitals via the phenyl rings of the pincers.

4.9 Summary of results and conclusions

The work in this chapter presents detailed investigations into the serendipitous discovery of mechanochromic properties in a platinum pincer system. It has been established that the compound is sensitive to both shear forces (irreversibly) and hydrostatic pressure (reversibly), both eliciting a different response to the optical properties.

The ability of **(20)** to transition from yellow/green luminescence to deep red upon gentle abrasion has been thoroughly investigated. It has been determined that the nature of the emission transitions from monomeric, in a crystalline state, to cooperative (excimeric), upon disruption of crystallinity and amorphisation. This has been shown to mimic behaviour in concentrated solution, where excimer peaks have been detected, and also provides satisfactory explanation for the divergence of absorption and emission properties seen.

Subsequent studies into the behaviour of the compound under hydrostatic pressure were also undertaken. It has been shown that both polymorphs of the compound exhibit strong red-shift in their absorption as a response to increased pressure, and this was further investigated crystallographically.

Potentially due to planar shearing, **Polymorph 1** retains very little single crystallinity upon application of pressure, and this combined with the limitations to data quality imposed through use of diamond anvil cells, meant that no structural data at pressure could be acquired. This may however offer further insight into this polymorph's sensitivity to shear forces in inducing amorphous material with excimeric luminescence.

Polymorph 2 however, was able to be studied to some degree, although a transition to a triclinic cell again meant that the restricted data inherent to DAC experiments meant higher pressure structures were unattainable. This problem was overcome using the software GASP. This had previously been used to determine flexibility in framework materials, but its application to molecular materials proved extremely useful.

In combination with TD-DFT calculations, an explanation for this material's red-shifting absorption spectrum has been arrived at, whereby an increase in overlap between molecule HOMOs *via* the pincer phenyl ring has been shown to destabilise the HOCO.

4.10 References

(1) Bamfield, P. *Chromic Phenomena : Technological Applications of Colour Chemistry* 2nd ed.; Royal Society of Chemistry, **2010**.
(2) Abe, T.; Itakura, T.; Ikeda, N.; Shinozaki, K. *Dalton Transactions* **2008**, *2009*, 711.
(3) Zhang, X.; Wang, J.-Y.; Ni, J.; Zhang, L.-Y.; Chen, Z.-N. *Inorganic Chemistry* **2012**, *51*, 5569.
(4) Lin, W.-J.; Naziruddin, A. R.; Chen, Y.-H.; Sun, B.-J.; Chang, A. H. H.; Wang, W.-J.; Hwang, W.-S. *Chemistry – An Asian Journal* **2015**, *10*, 728.
(5) Devi, L. S., Al-Suti, M.K, Zhang, N, Teat, S.J, Male, L, Sparkes, H.A, Raithby, P.R, Khan, M.S, Kohler, A. *Macromolecules* **2009**, *42*, 1131.
(6) Khan, M. S., Al-Suti, M.K, Al-Mandhary, M.R.A, Ahrens, B, Bjernemose, J.K, Mahon, M.F, Male, L, Raithby, P.R, Friend, R.H, Kohler, A, Wilson, J.S *Dalton Trans.* **2002**, 65.
(7) Inc., C. S. In *NIST Chemistry WebBook*; PERKIN-ELMER CORP.: **2009**.
(8) Birks, J. B. *Rep. Prog. Phys.* **1975**, *38*, 903.
(9) Cocchi, M.; Virgili, D.; Fattori, V.; Williams, J. A. G.; Kalinowski, J. *Appl. Phys. Lett.* **2007**, *90*, 023506.
(10) Ku, H.-Y.; Tong, B.; Chi, Y.; Kao, H.-C.; C-C., Y.; Chang, C.-H.; Lee, G.-H. *Dalton Transactions* **2015**, *44*, 8552.
(11) Williams, J. A. G., Beeby, A., Davies, E.S., Weinstein, J.A., Wilson, C. *Inorg. Chem.* **2003**, *42*, 8609.
(12) Khan, M. S., Al-Suti, M.K, Al-Mandhary, M.R.A, Ahrens, B, Bjernemose, J.K, Mahon, M.F, Male, L, Raithby, P.R, Friend, R.H, Kohler, A, Wilson, J.S. *Dalton Trans.* **2002**, 65.
(13) Berenguer, J. R., Lalinde, E, Torroba, J. *Inorg. Chem.* **2007**, *46*, 9919.
(14) Chen, Y.; Li, K.; Lu, W.; Chui, S. S.-Y.; Ma, C.-W.; Che, C.-M. *Angewandte Chemie International Edition* **2009**, *48*, 9909.
(15) Millar, D. I. A. *Energetic Materials at Extreme Conditions*; Springer Science & Business Media, **2011**.
(16) Mao, H. K.; Wu, Y.; Chen, L. C.; Shu, J. F.; Jephcoat, A. P. *Journal of Geophysical Research: Solid Earth* **1990**, *95*.
(17) Jayaraman, A. *Reviews of Modern Physics* **1983**, *55*.
(18) Tobias1984 Wikimedia Commons, **2012**.
(19) Wells, S. A.; Sartbaeva, A. *Materials* **2012**, *5*, 415.
(20) Kresse, G.; Hafner, J. *Phys. Rev. B* **1993**, *47*, 558.

Chapter 5: Electrochromism in a platinum N^C^N pincer compound

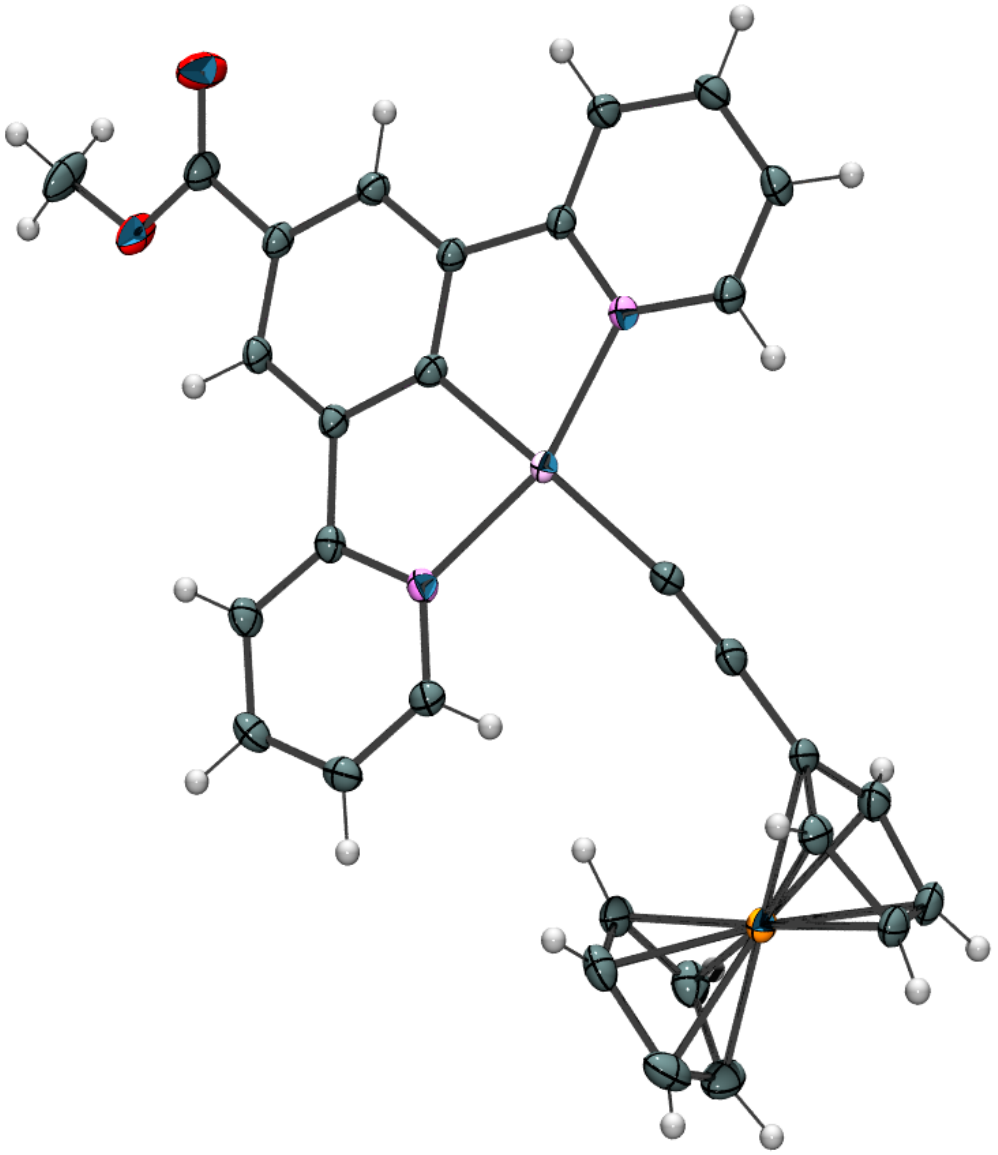

Abstract

It was established in the work of **Chapter 2** that by using acetylide ligands as a "bridge" to the platinum centre of a pincer complex, good electronic communication through the delocalised π-system could be achieved, resulting in the energies of the platinum HOMOs being sensitive to the nature of the ligand.

This led to the hypothesis that if the nature of an adjoining ligand could be influenced through the application of an external stimulus, this might result in a switchable system with a visual response.

Following this strategy it was decided that the stable and electrochemically active ferrocene moiety would be incorporated into a platinum pincer complex using an acetylide bridge, with the aim to create a mixed metal complex with optical properties that are switchable as a function of voltage.

This synthetic strategy has proven successful, with the mixed metal complex **(21)** being synthesised and fully characterised. DFT calculations suggest the HOMO consists of both the platinum d_{xz} and the iron $d_{x^2-y^2}$ orbitals, bridged by an out of phase π-interaction with the acetylene, and this indicates that the original hypothesis was sensible.

Electrochemical experiments have been performed in solid and solution phases to determine whether manipulation of the ferrocene containing HOMO, through redox processes, influences the optical properties.

It has subsequently been shown that in the solution state, through the use of ionic liquids, a stable reversible redox process is achievable, although absorption in the visible spectrum remains unchanged by this process.

Through application of solid crystalline films of **(21)** onto ITO sheets, however, a stable redox process resulting in a reversible transition between two absorption spectra has been achieved.

5. Electrochromism in a platinum N^C^N pincer compound

5.1 Introduction

In **Chapter 2**, the nature of the frontier orbitals for N^C^N pincer compounds of platinum (II) were investigated, and it was determined that by manipulating the influence that the fourth coordinating ligand has on the occupied metal d-orbitals *via* π-interaction, the HOMOs of the compound can be altered. Moving forward with this knowledge, ways in which this property can be directly affected *in situ* were proposed, with the aim of introducing external switchability to the compound, possibly leading to a direct, reversible, optical response to a certain stimulus. This method of introducing a switching mechanism to the compound's chromophore, unlike the techniques used for **Chapter 3** does not in theory rely on solid state aggregation effects to implement the response, allowing for potential solution state device fabrication/processing, or simply a lower reliance on crystallinity in a solid component. So while switchability has been successfully introduced to the compounds in **Chapter 3**, this mechanism may offer a more stable and potentially easier to process system.

In order to introduce switchability to the metal orbitals, a suitable ligand with a switchable motif needed to be decided upon and synthesised. The decision making centred around two criteria:

- Ability for said ligand to link a π-system to the d-orbitals of the platinum with good overlap
- Inherent switchability of the ligand, in such a way as to alter the π-interactions, in response to a stimulus that is convenient or useful.

Regarding the first point, it was decided that some kind of acetylide would be a good choice in providing a bridge of any ligand π-system to the metal centre in a way that provides good overlap, as this has already been demonstrated in **Chapter 2**, along with a synthetic protocol already having been established during that work.

The second point, therefore, was essentially to decide upon a fragment that can be linked via π-interactions to an acetylide, but which also possesses an inherent switchability of its electrical properties from a stimulus that is easy/useful to study. Ferrocene was chosen to fulfil this role, owing to its extremely well understood electrochemical switching, and its aromaticity potentially allowing for a good π-system interaction from the electrochemically active iron centre to the platinum centre. This could then allow for an electrically controlled switching of the optical properties of an N^C^N platinum (II) compound.

Examples of platinum-ethynylferrocene complexes are known to the literature, and it is often the case that limited electronic communication exists between the platinum and iron centres.[1-3]

The circumstances under which communication between these metal centres is likely to arise is discussed by Long *et al.*[4] It is stated that the communication is typically mediated by the extent to which the bridging ligand orbitals overlap with the orbitals from the metals i.e. communication is achieved when there is conjugation of the metals through the bridging ligands. It is also stated that the frontier orbitals the (predominantly the HOMO and HOMO-1) are the most important in deciding whether conjugation between the metal centres is present.

From the work of **Chapter 2** it was established that the HOMOs of platinum acetylides as part of a pincer ligand complex typically originate from π-interaction between the entire R-acetylene fragment and the occupied platinum d-orbitals. If this holds true when R = ferrocene, then communication between the iron and platinum centres is likely to exist. It has also been shown that the HOMO of ethynylferrocene fragments is typically based on the d_{xy} or $d_{x^2-y^2}$ of the iron centre in combination with the acetylene orbitals, and so communication to the platinum seems plausible.[1]

Electrochromic materials are relatively well studied and well known.[5] The work in this chapter is not a study of new electrochromic materials with aims to improve current technology, it is an investigation into the possibility of manipulation of the platinum pincer chromophore via an acetylide bridge. The attempted inclusion of an inherently switchable fragment into the HOMO orbitals via acetylide bridge may then allow an external force to manipulate the optical properties of the molecule.

5.1.1 Ferrocene

Ferrocene is a complex of two cyclopentadienyl rings, and one iron (II) centre in a "sandwich" arrangement, known as a metallocene. Unlike many organic complexes of iron, ferrocene is a highly stable unit and is unaffected by air or moisture. This is due to the way in which the rings are bound to the metal, whereby each carbon of the stable aromatic anions is bound equally to the iron through π-interaction (ie. a 6 electron interaction with an η^5 hapticity). This allows the d^6 iron centre to obtain a noble gas configuration of valence 18 electrons.[6]

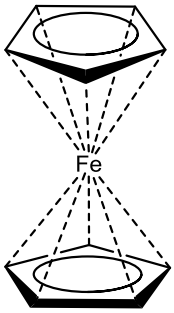

Figure 5.1. Ferrocene.

5.1.1.1 Electrochemical properties

Ferrocene is one of the most studied, and best understood electrochemically active compounds, and was instrumental in the development of the first blood glucose biosensor system for the management of diabetes, acting as an extremely stable and reliable electron transfer medium between glucose and the electrode.[7] Ferrocene undergoes a reversible one-electron oxidation at relatively low potentials (*ca.* 0.5V relative to SCE)[8] to a stable ion known as ferrocenium. This redox chemistry can be achieved in both aqueous and non-aqueous media, making ferrocene a robust electrochemical group for inclusion into other systems.

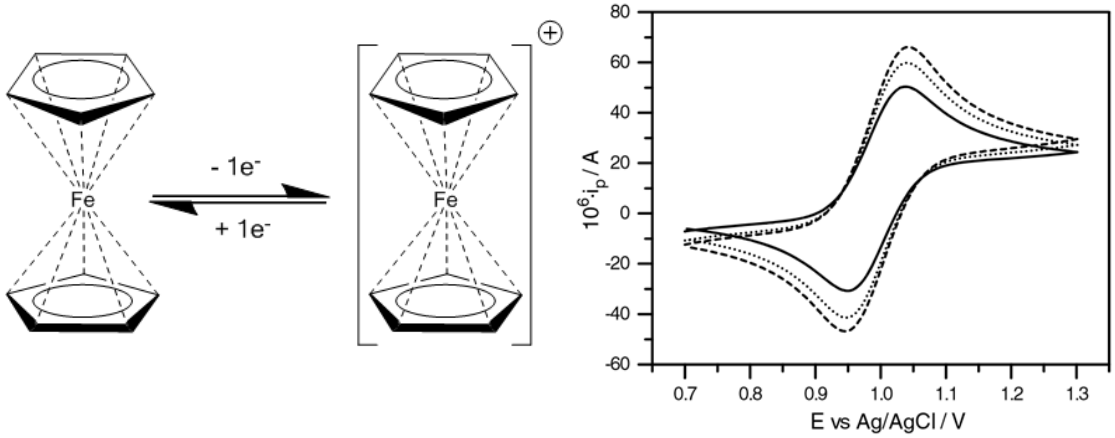

Figure 5.2. Left: Ferrocene-Ferrocenium redox couple. Right: Cyclic voltammograms of ferrocene (0.002 mol dm^{-3}) in MeCN (0.1 mol dm^{-3} NBu_4PF_6) (Pt electrode) at different scan rates 0.05 V/s (solid), 0.08 V/s (dotted) and 0.10 V/s (dashed).

5.1.1.2 Chemistry of ferrocene

Due to the stability of the molecule, and the inert nature of the iron centre, the chemistry of ferrocene is essentially equivalent to that of simple aromatics, where the cyclopentadienyl rings can be functionalised in much the same way as benzene, including sulfonation with H_2SO_4, and acylation via the Friedel-Crafts method.

For the chemistry of ferrocene reported in this chapter, the most useful reaction of ferrocene is metalation with lithium (**Figure 5.3**).

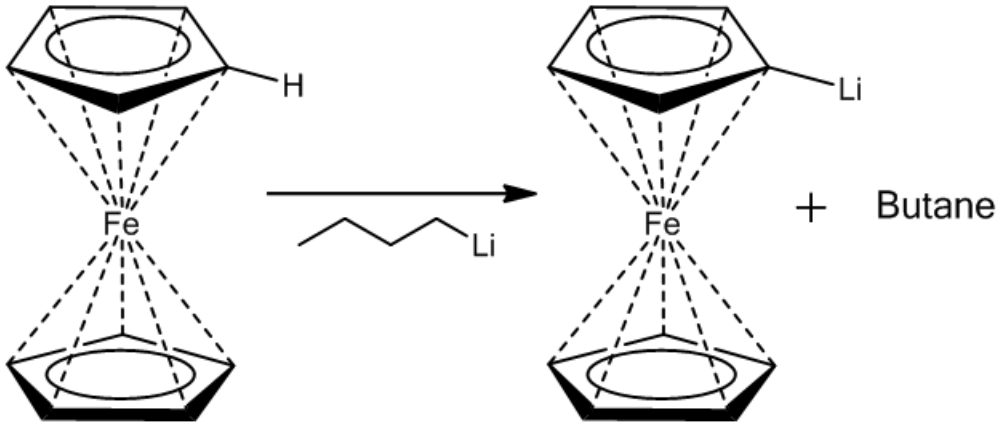

Figure 5.3 General reaction mechanism for ferrocene and butyllithium.

The reaction with butyllithium allows for functionalisation of a cyclopentadienyl ring, and with subsequent treatment with more butyllithium, and a base such as TMEDA, both rings can be functionalised. The lithiated forms of ferrocene are (as with all organolithium compounds) highly reactive species, and so by further introduction of various reagents *in-situ*, the rings can be made to incorporate a variety of functional groups.

It was decided that a mono-substituted ethynylferrocene complex of the platinum N^C^N moiety would be attempted first, and following this a 1,1'-disubstitued ethynylferrocene would be synthesised and a Pt-Fc-Pt dimer would then be attempted.

5.1.2 Predictions of how this will potentially affect the chromophore of the platinum compound

Based on the electronic orbital information obtained during the work in **Chapter 2**, It was hypothesised that the LUMO of an ethynylferrocene complex of the platinum N^C^N fragment would remain situated on the pincer and be largely unaffected by the substitution. Similarly, the HOMO was hypothesised to be composed of the interaction of the d_{xz} or d_{xy} orbital in its out of phase π-interaction with the acetylide (depending on the orientation of the ferrocene), as has been seen in the aromatic acetylides already synthesised. However, it was not clear whether or not the iron centre orbitals would be included in the HOMO, and based on previous literature examples (mentioned in **section 5.1**), good communication between the two metal centres is rare.

If this was to be the case, however, then in theory, it might be possible to use the oxidation of this iron centre to affect the energy across the extent of this delocalised orbital, and hence allowing for electrochemically controlled switching of the HOMO-LUMO gap. In order to first assess whether this was a sensible initiative, preliminary gas-phase DFT calculation were performed to test whether theoretically, electronic communication could exist between the iron and platinum centres *via* the conjugated bridge of an ethynylcyclopentadienyl group (details of the methods used can be found in the supporting information).

As can be seen in **Figure 5.4** the Frontier orbitals align with the predictions about their character made based on theoretical work (ligand field theory) and experimental data obtained during the work of **Chapter 2**.

The minimum energy position for the ferrocene (the plane of the connected cp-ring) was calculated as twisted away from the plane of the pincer by 32.26°. The LUMO remains based on the platinum pincer fragment pyridine π*-orbitals (74%), although some pincer phenyl (13%) and platinum contribution (9%) is also present.

The HOMO is calculated to again be made up of the of the platinum d_{xz}-orbital in an out of phase π-interaction with that of the acetylide bridge (19%), but significantly this orbital extends through the π-system to include that of the cyclopentadienyl, allowing for a very large contribution (54%) from the non-bonding $d_{x^2-y^2}$ orbital of the iron centre. Essentially, calculations predict that the HOMO of this system is shared between the platinum and the iron centre through a conjugated π-system bridge.

Based on the criteria for intermetallic communication set out by Long *et al.* [4] (discussed in **section 5.1)** it would appear that hypothetically there should be good communication between the metal centres in this complex. Following on from this, it may then be possible to manipulate the HOMO-LUMO gap *via* electrochemical manipulation of the iron centre.

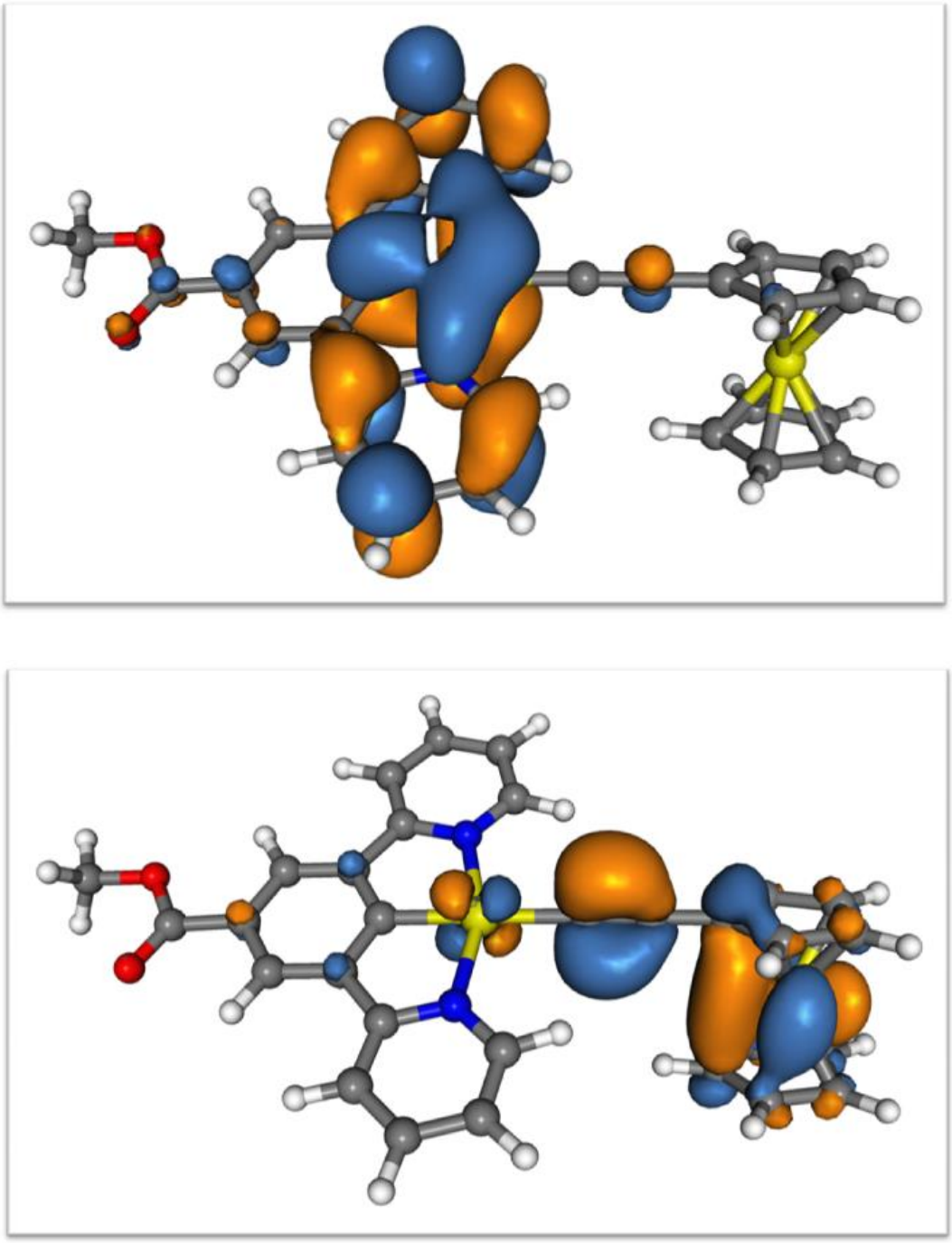

Figure 5.4. Predicted HOMO (bottom) and LUMO (top) of an ethynylferrocene compound of the platinum (II) N^C^N pincer unit in the gas phase energy minimised configuration.

5.2 Objectives and strategy

The aim for this chapter's work, was to attempt to synthesise complexes that link the electrochemically active iron centre of ferrocene to that of a platinum centre of an N^C^N cyclometallated compound by bridging one or more of the aromatic cp rings via an acetylide bridge. In doing so, the aim was to reversibly manipulate the HOMO-LUMO gap and thus the optical properties of resulting compounds by electrochemical switching of the attached ferrocene.

It was hoped that as the occupied platinum d-orbitals that the HOMOs contain are calculated to be linked to the ferrocene through π-interactions, oxidising and reducing the ferrocene electrochemically could be used as an electrically controllable switching mechanism for the energy of the HOMO and hence the optical properties of the compound.

Given the free rotation around the iron centre, a dimeric version of the compound could also offer some interesting intramolecular Pt-Pt interaction along with the electrochemical properties. Synthesis of this compound, however, proved highly challenging. It was therefore decided that given time constraints, focusing on the monomer only was the best course of action. Some of the synthetic intermediates to this have been included.

5.3 Synthetic procedure

5.3.1 Functionalised ferrocene

In order to functionalise the ferrocene, literature procedures were used (see **Scheme 5.1** and **Scheme 5.2**).[9,10] The first step of this process was to use butyllithium to metallate the ferrocene. Subsequently, iodine could be added to create the iodo- substituted compound. The mono and 1,1' bis-substituted compounds can both be achieved using this method, and through changes in stoichiometry, and the addition of TMEDA the bis-product can be favoured. Both products are produced in each reaction, however, and need to be separated using column chromatography once iodated.

Once separated, a simple Sonogashira reaction can be used to take each compound through to the trimethylsilylacetylide product. The final compounds were characterised by ^{1}H NMR and solid-state IR spectroscopy, with all spectra being consistent with those reported in the literature. The *bis*-product was further characterised with x-ray crystallography (**Figure 5.5**), although it crystallised as a polymorph not reported in the literature.[11]

Metalation and iodation

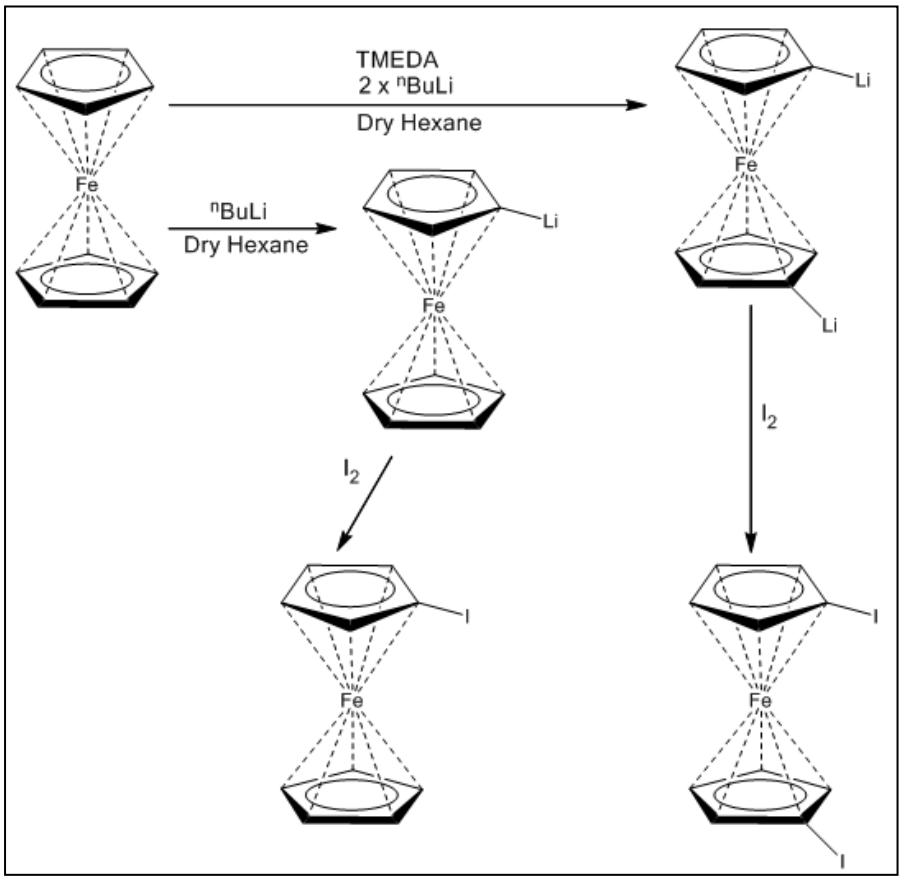

Scheme 5.1. Reaction pathway for the mono- and bis- lithiation and subsequent iodation of ferrocene. [9]

Sonogashira reaction

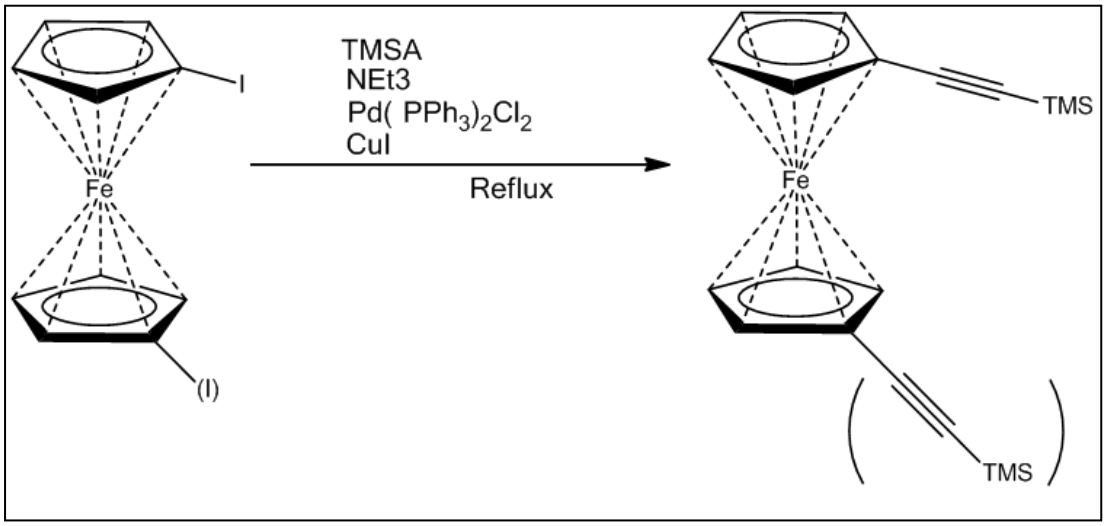

Scheme 5.2. Sonogashira reaction conditions used to produce the trimethylsilylethynyl- products. [10]

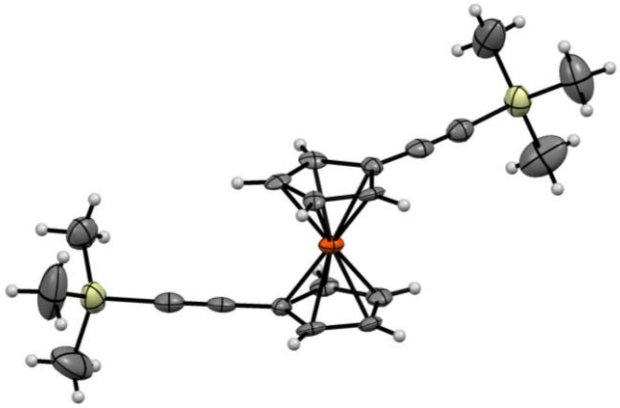

Figure 5.5. Structure of 1,1' bis-trimethylsilylethynylferrocene obtained as additional characterisation using x-ray crystallography.

5.3.2 Compound synthesis

The Platinum pincer fragment was synthesised as the chloride **(9)** and the same procedure found in **Chapter 2** was used. The reaction of the ferrocene fragment with the platinum pincer was performed using the same method as with the polyaromatic acetylides in **Chapter 2**. Unfortunately the final 1,1' bis-substituted dimer product could not be produced. The reaction carried out in the same way as for the mono product led to insoluble residues that were impossible to characterise, leading to the hypothesis that some form of polymerisation was occurring. Many variations of the reaction were attempted, though none proved successful. The mono-substituted product however proved very successful, and could be obtained in good yield.

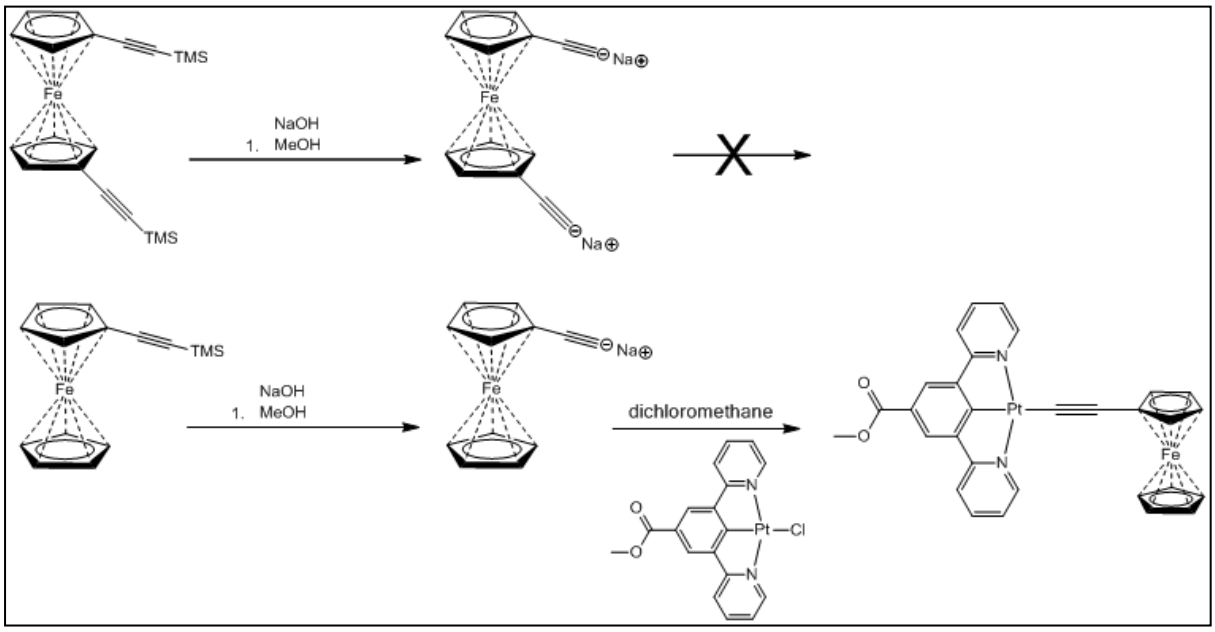

Scheme 5.3. Reaction scheme leading to the final product (21).

5.4 Platinum[methyl 3,5-di(2-pyridyl)benzoate]Ethynylferrocene (21)

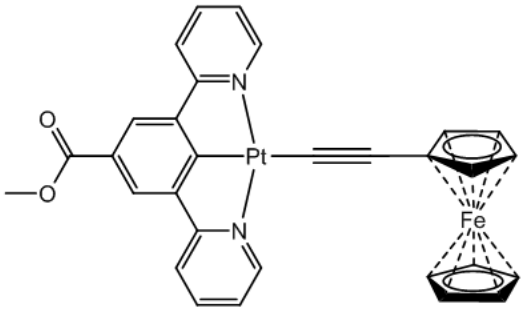

(21) was fully characterised by NMR and solid-state IR spectroscopy, Mass spectrometry, and X-Ray crystallography. (See experimental section)

The IR spectrum shows a strong, sharp absorption at 2088 cm^{-1}, assignable to the $\nu_{C\equiv C}$ of a σ-alkynyl group. This value is consistent with those recorded for a series of related compounds.[12,13] Also seen is a single strong absorption at 1698 cm^{-1} assignable to the $\nu_{C=O}$ of the ester group, which is a typical value for a methyl benzoate ester.[14,15]

^{1}H NMR, and $^{13}C\{^{1}H\}$ NMR experiments of **(21)** were run on the product in deuterated dichloromethane. The correct assignment of hydrogen atoms was supported with the use of a 2-dimensional HCOSY experiment. The ^{1}H NMR clearly indicated the presence of the substituted ferrocene in the structure.

All spectra corresponded with the structure proposed for **(21)**.

5.4.1 Crystallography

Two crystalline polymorphs of the complex were produced. As solid state electrochemical methods were planned for this compound, it was important to understand the solid state structure of the compound in detail, including any porosity/possible ion diffusion. When precipitated somewhat rapidly from dichloromethane, a film of tiny crystalline yellow/orange needle-like structures can be produced on surfaces. If the crystallisation process is slowed down significantly large discrete red prismatic crystals can be produced instead from the same solvent. Given the variation in colour and physical form between these two solid forms, it was proposed that they are likely to be structurally distinct (see **Figure 5.6**). The structure of the large red prisms (**Polymorph 1**) was easily collected using an in-house diffractometer, the structure of which can be seen in **Figure 5.9**. However, the crystalline film also offers a convenient physical form for electrochemical measurements and so the nature of this film also needed to be determined. Due to the tiny size of the individual crystallites, this structure was recorded using synchrotron radiation (**Polymorph 2**).

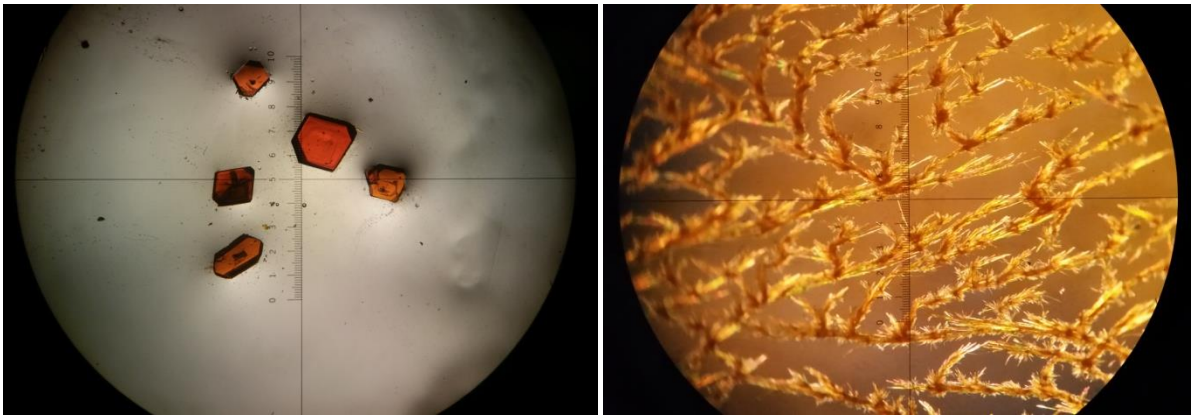

Figure 5.6. Left: red prisms of (21) Polymorph 1. Right: yellow needles of (21) Polymorph 2.

5.4.1.1 Polymorph 1

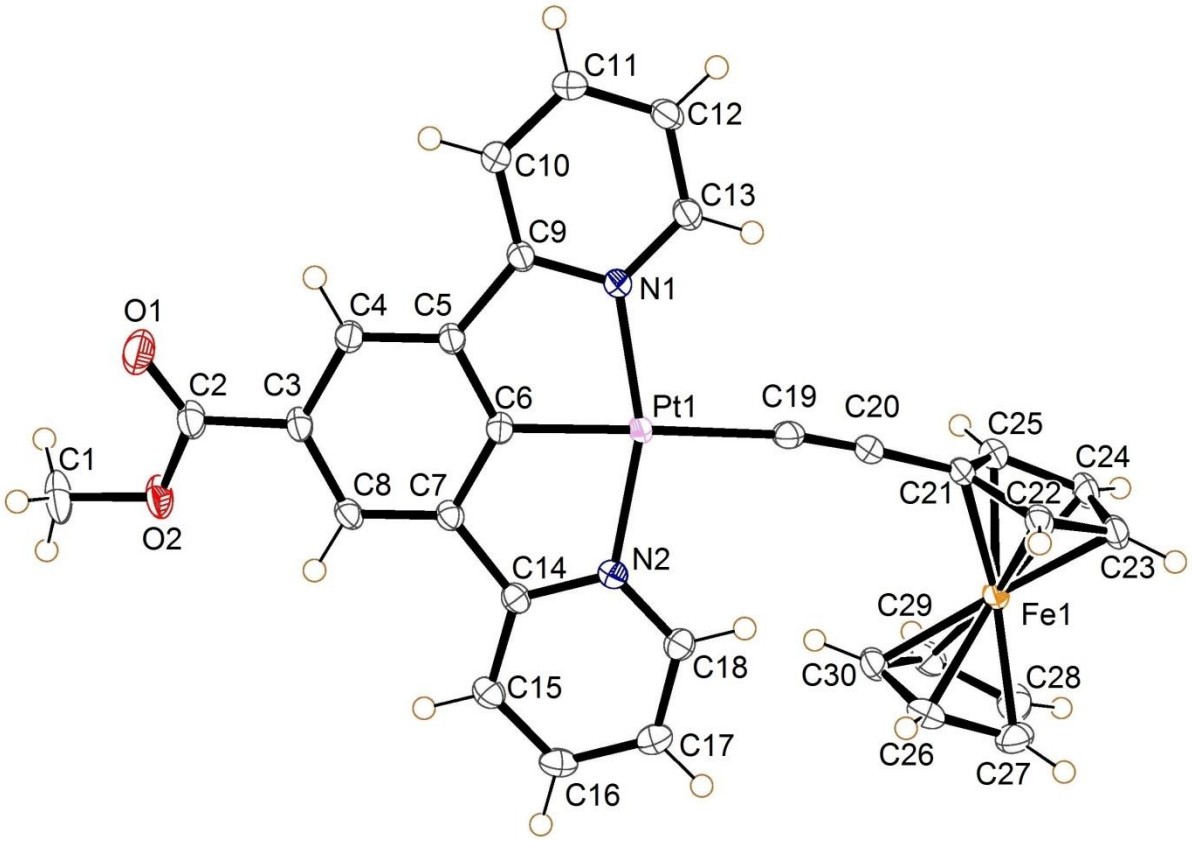

Figure 5.7. The asymmetric unit of (21) polymorph 1.

Polymorph 1 of **(21)** crystallised as large red prisms (seen in **Figure 5.6**) obtained slow evaporation of concentrated dichloromethane solution. **Polymorph 1** crystallises in the monoclinic space group $P2_1/c$, with the asymmetric unit consisting of one neutral molecule of **(21)**.

The acetylide group is slightly bent out of the plane of the pincer (C20-Pt1-C6 angle of 171.52 (7) °). The ferrocene unit lies almost perpendicular to the plane of the pincer (differing from the calculated minimum position of 32.26°) with the average plane of the connecting cyclopentadienyl ring being twisted by 78.23 (6) ° from the average plane of [Pt1, C5, C6, C7, C9, C14, N1 and N2]. The platinum centre adopts the expected square planar geometry with minor distortion (N1-Pt1-N2 angle 160.13 (7) °) due to the pincer bite angle, with bond parameters in the expected ranges. The C≡C bond distance, 1.197 (3) Å is also typical (**Table 5.1**).[16,17,18]

Table 5.1. Selected bonds and angles for (21) polymorph 1

Bond	Length (Å)
Pt1-N2	2.039 (2)
Pt1-N1	2.034 (2)
Pt1-C6	1.933 (2)
Pt1-C19	2.060 (2)
C19-C20	1.197 (3)

Bond	Angle (°)
Pt1-C19-C20	168.3 (2)
C19-C20-C21	176.7 (3)

The twisting away from the ideal torsion of the ferrocene along with a large bend in the acetylene group seems to be a result of packing efficiency along with weak C-H---O weak hydrogen bonding interactions to the carboxylate of adjacent molecules. This also has the effect of twisting the ester out of the plane by 17.36 (39) ° (torsion C4, C3, C2, O1). Interactions are summarised in **Figure 5.8** and **Table 5.2**.

The extended packing of Polymorph 1 is relatively featureless, with a non-porous structure and a slight herringbone planarity. See **Figure 5.9** for details.

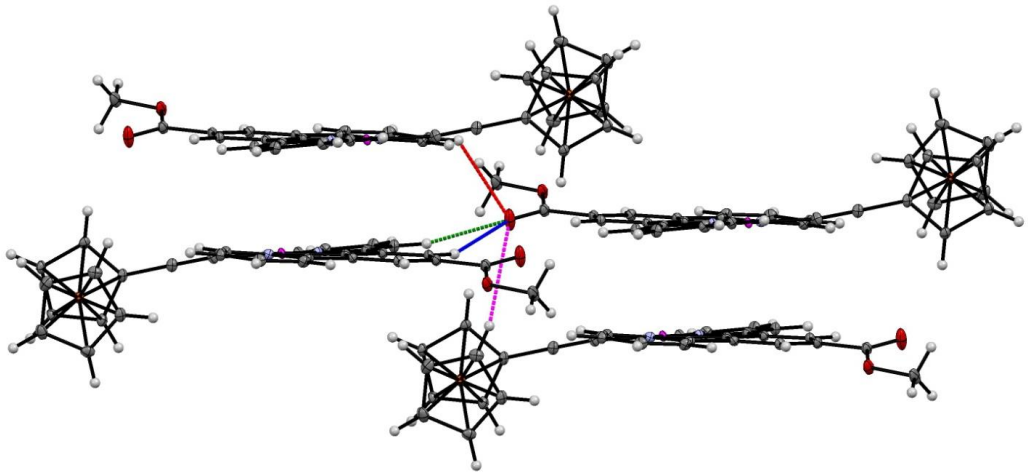

Figure 5.8. Intermolecular interactions of Polymorph 1. Symmetry equivalent interactions not shown for clarity.

Table 5.2 Weak hydrogen bonding interactions for (21) polymorph 1

Bond	Distance (D..A) (Å)	Distance (H..A) (Å)	Angle (D..H..A) (°)
$C4^{1}$-$H4^{1}$-O1	3.586 (3)	2.706	158.06
$C10^{1}$-$H6^{1}$-O1	3.394 (3)	2.479	167.93
$C17^{2}$-$H12^{2}$-O1	3.734 (3)	3.044	132.38
$C26^{3}$-$H21^{3}$-O1	3.974 (4)	3.112	155.96
1 = (-x, -1-y, -z), 2 = (x, -1+y, z), 3 = (-x,-y,-z)			

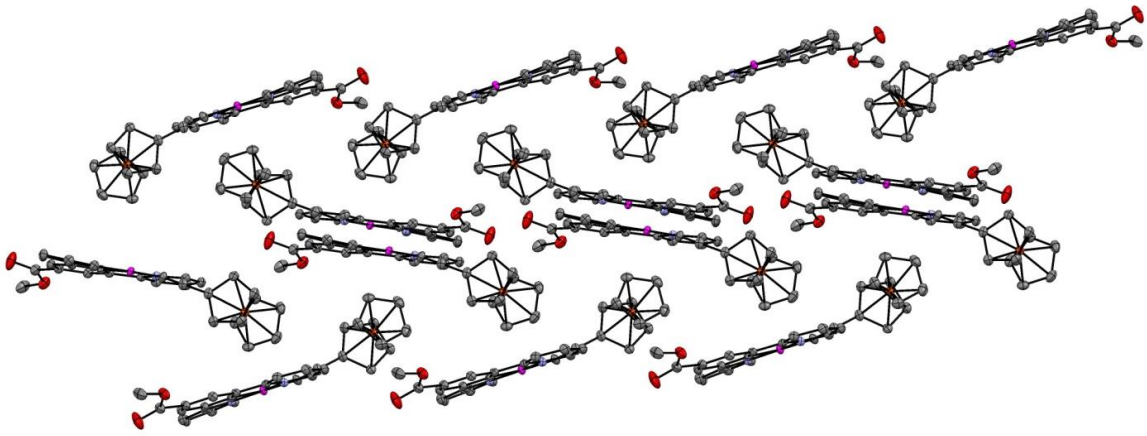

Figure 5.9. Extended packing of Polymorph 1

5.4.1.2 Polymorph 2

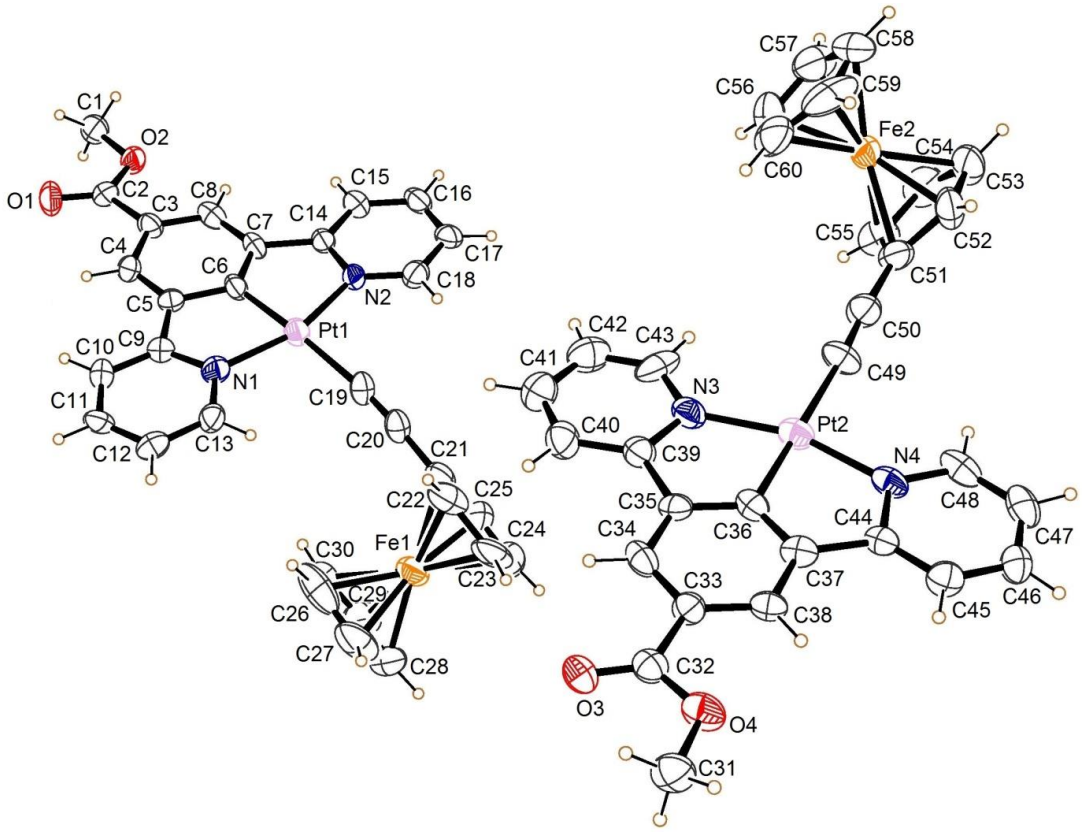

Figure 5.10. The asymmetric unit of (21) polymorph 2.

Polymorph 2 (**Figure 5.10**) of **(21)** crystallised in thin films of very small yellow/orange needles (seen in **Figure 5.6**) obtained by rapid evaporation of concentrated dichloromethane solution. **Polymorph 2** crystallises in the triclinic space group *P-1*, with the asymmetric unit consisting of two neutral molecules of **(21)**. Once again, the acetylide group is slightly bent out of the plane of the pincer for both molecules (C20-Pt1-C6 angle of 172.83 (43) ° and C50 Pt2 C36 angle of 175.97 (46) °). For this polymorph the ferrocene units lie twisted from the plane of the pincer (and differ from the calculated minimum position of 32.26°), with the average plane of the connecting cyclopentadienyl ring being twisted (less so than **Polymorph 1**) at an angle of 59.6 (4) ° from the average plane of [Pt1, C5, C6, C7, C9, C14, N1 and N2] and 49.8 (6) ° from the average plane of [Pt2, C35, C36, C37, C39, C44, N3 and N4].

The platinum centres adopt the expected square planar geometry with minor distortion (N1-Pt1-N2 angle 159.5° (4) and N3-Pt2-N4 angle 159.8 (5)) due to the pincer bite angle, with bond parameters in the expected ranges. The C≡C bond distances of 1.195 (19) and 1.181 (18) Å are also typical (**Table 5.1**).[16,17,18]

Table 5.3. Selected bonds and angles for (21) polymorph 2

Bond	Length (Å)
Pt1-N1	2.022 (11)
Pt1-N2	2.047 (10)
Pt1-C6	1.903 (12)
Pt1-C19	2.065 (16)
C19-C20	1.195 (19)

Bonds	Angle (°)
Pt1-C19-C20	172 (1)
C19-C20-C21	176 (2)

Bond	Length (Å)
Pt2-N3	2.007 (12)
Pt2-N4	2.020 (11)
Pt2-C36	1.915 (13)
Pt2-C49	2.059 (14)
C49-C50	1.181 (18)

Bonds	Angle (°)
Pt2-C49-C50	173 (1)
C49-C50-C51	175 (2)

Unlike **Polymorph 1**, the extended structure of this crystal exhibits general planarity of the molecules (see **Figure 5.11**). Intermolecular interaction between the planar units consist of weak C-H donor hydrogen bonding interactions to the oxygen atoms of the methyl ester (**Figure 5.12**). Details of these interactions can be found in **Table 5.4**.

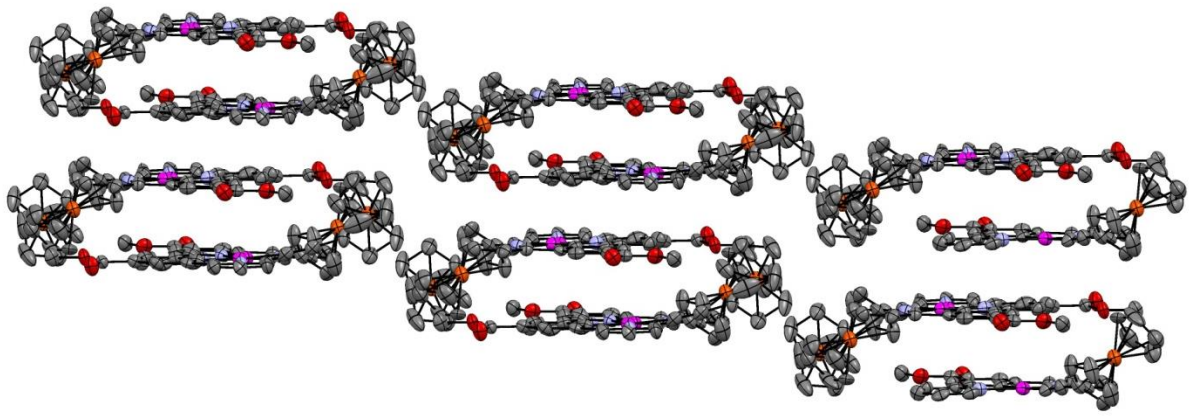

Figure 5.11. Extended structure of Polymorph 2 showing the general planarity of the molecules.

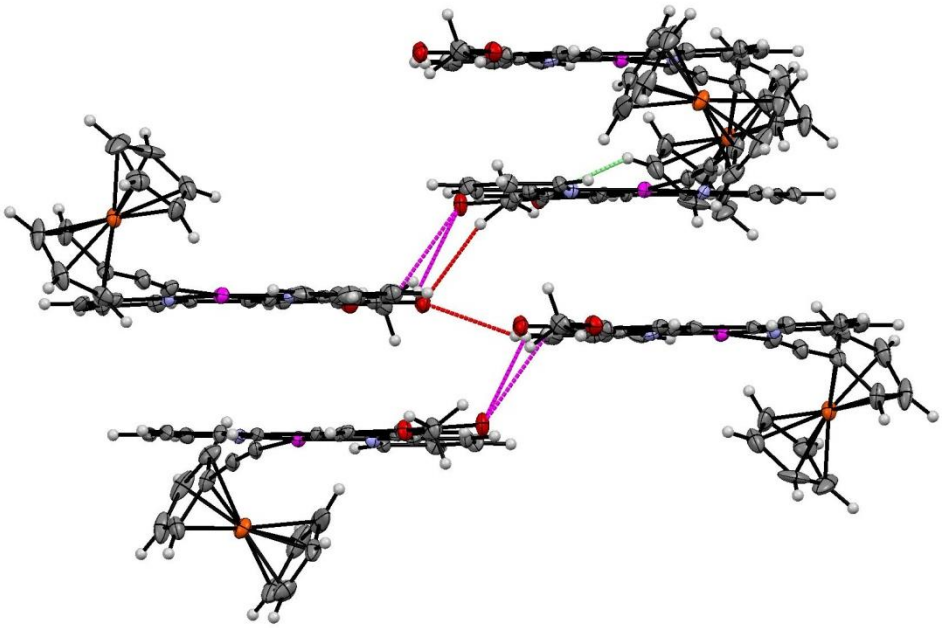

Figure 5.12. Weak hydrogen bonding interactions of Polymorph 2. Interactions with O1 shown in magenta, O2 in red and O3 in green.

Table 5.4. Weak hydrogen bonding interactions for (21) Polymorph 2

Bond	Distance (D..A) (Å)	Distance (H..A) (Å)	Angle (D..H..A) (°)
C1-H3 O3[1]	3.50 (2)	2.629	150.87
C10-H6-O1[2]	3.48 (2)	2.631	151.88
C4-H4-O1[2]	3.61 (2)	2.760	152.66
C46-H37-O3[3]	3.50 (2)	2.609	159.93
C38 H34-O1[4]	3.58 (2)	2.924	126.76
C45-H36-O1[4]	3.64 (2)	2.959	130.65
C60-H60-O2[5]	3.84 (2)	3.035	146.36

1 = (1-x, 1-y, 2-z),2 = (2-x, -y, 2-z), 3 = (1-x, 2-y, 2-z), 4 = (1-x, 1-y, 2-z), 5 = (-1+x, 1+y, z)

5.5 Optical properties

5.5.1 Absorption spectroscopy

The absorption spectrum of the compound is, as expected, similar to that of the polyaromatic acetylide compounds of **Chapter 2**. Given the calculated nature of the HOMO consisting of significant out of phase π-interactions with the ethynylferrocene fragment and the platinum d_{xz} the red-shift to the absorption relative to **(9)** is as expected. The low energy peak at 388nm with a shoulder peak at 480nm can be assigned as π-π* transitions between occupied combinations of the metal d-orbitals and the ethynylferrocene π-system, and vacant pincer ligand orbitals.

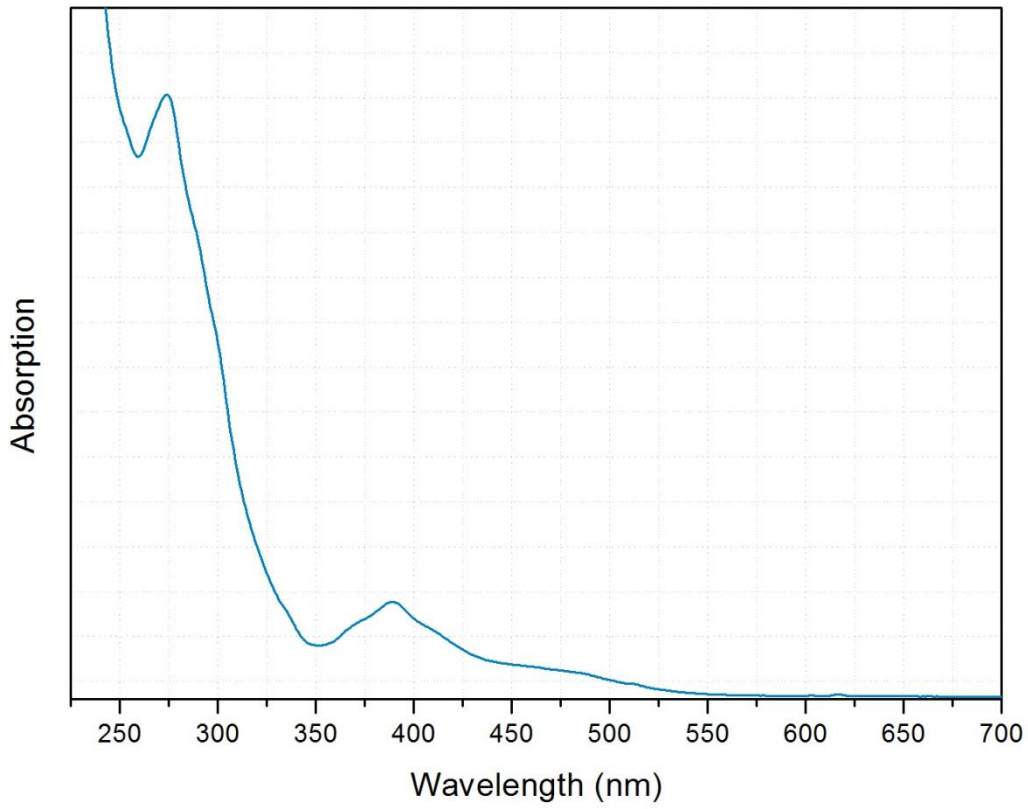

Figure 5.13. Absorption spectrum of a $1x10^{-5}$ mol dm^{-3} dichloromethane solution of (21). Peaks at 274, 388 and 480nm.

5.5.2 Emission spectroscopy

The emission spectrum of **(21)** can be seen in **Figure 5.14**. It is clear from this spectrum that the emission is not dissimilar to that of many other compounds synthesised in this body of research with a highly structured peak at 481nm, resembling that of **(9)**. This led to the assignment of the emissive state as ^{3}LC origin. However upon performing concentration scales, it becomes apparent that there is some form of quenching of the emission intensity with increasing concentration past $1x10^{-5}$ $moldm^{-3}$ with no excimeric emission resulting. This appears to be simply a result of the primary inner filter effect as opposed to any kind of aggregation, possibly in combination with concentration quenching (although ES lifetime measurements would be required to be certain). Evidence for this is provided by closer analysis of the compound's absorption spectrum, whereby increasing concentration firstly does not lead to a shift in energy or any new absorptions with increasing concentration, as evidenced by the straight Beer-Lambert plot at both the excitation frequency and emission λ_{max} frequency (**Figure 5.15**), this rules out any ground state aggregation. Secondly, the absorbance in **Figure 5.15** shows a steep rise at the excitation wavelength, and at the concentrations where emissive intensity starts to decline, absorbance has exceeded 0.5 AU. This level of absorbance (>0.1) is likely to be affecting the emission intensity.[19,20]

The secondary inner filter effect also appears to be a contributing factor due to the asymmetry of emissive quenching, and absorption spectrum overlap.

At concentrations at or above $5x10^{-5}$ mol dm^{-3} the lowest energy shoulder/tail of the absorption (centred at around 480nm) becomes a significant feature of the spectrum, and so a self absorption of the emissive frequencies at high concentration is likely in a cell with a path length of this size (1cm). The disproportionate reduction in the highest energy peak is particularly apparent in comparing the spectra of $1x10^{-5}$ and $1x10^{-4}$ where the highest energy peak is significantly reduced in the more concentrated solution, the second peaks are comparable, and the lowest is in fact slightly higher in intensity for the concentrated solution. This non-uniform reduction in intensity mirrors the shape of the absorption band seen in **Figure 5.15** providing more evidence for self absorption.[21,22]

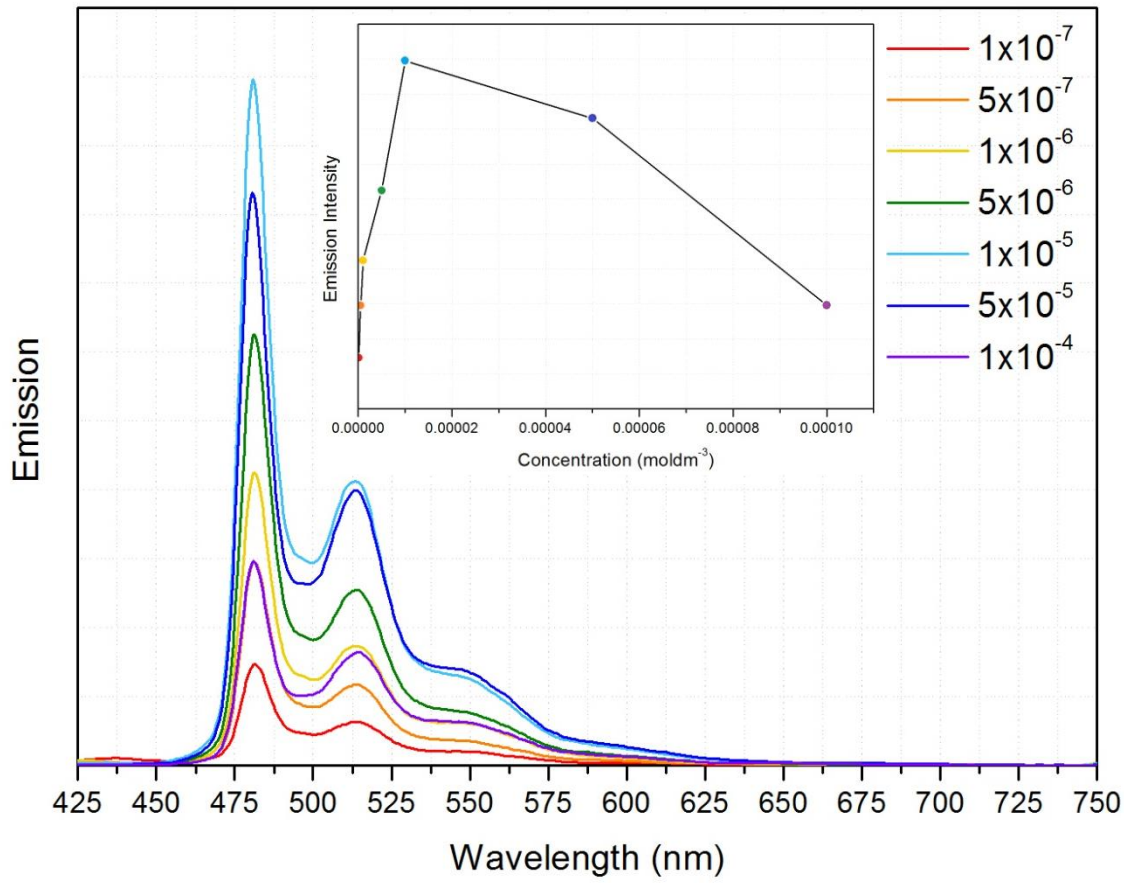

Figure 5.14. Emission spectrum of (21) under 388nm excitation, with variable concentrations demonstrating internal absorption effects past $1x10^{-5}$ mol dm^{-3}.

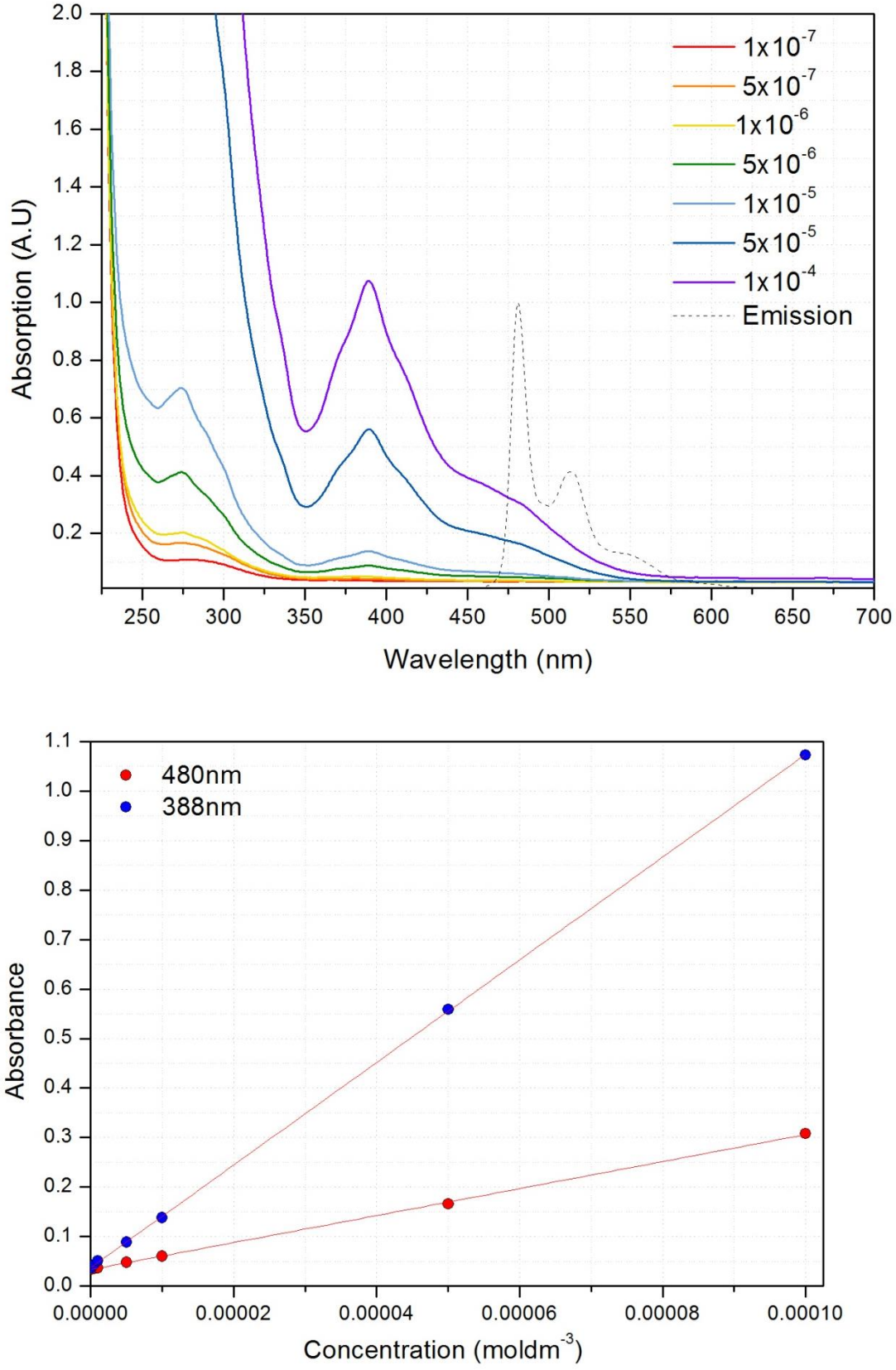

Figure 5.15. Top: Absorption spectra of (21) in dichloromethane solution at incremental concentrations, along with an overlay of the emission spectrum (arbitrary intensity). Bottom: Beer-Lambert plot for the absorbance at 480 (emission max) and 388nm (excitation frequency), with linear fit indicating a lack of intermolecular interactions.

5.5.2.1 Quantum yield

As stated in **Chapter 2**, measuring accurate quantum yields with the equipment available proved challenging, however approximations were made by comparison of emission maxima through concentration scales with the previously determined chloride starting material **(9)** as a standard (φ_{lum} = 0.56 in degassed dichloromethane).[23]

The quantum yield was calculated by plotting the integrated emission intensity at a series of concentrations in degassed dichloromethane (concentrations ranged from $1x10^{-7}$ to $1x10^{-5}$ to avoid the inherent self-quenching) vs. absorbance measured at the probe frequency (for the same set of solutions). The gradients of this linear plot was then used to calculate the approximate quantum yields using, **Equation 5.1** whereby a comparison is made to the corresponding plot created for the chloride standard.

$$\varphi_x = \varphi_{st} \left(\frac{Gradient_x}{Gradient_{st}} \right) \left(\frac{\eta_x^2}{\eta_{st}^2} \right)$$

Equation 5.1. Formula used for calculating quantum yields, where ϕ_x and ϕ_x = the quantum yields of the compound and standard respectively, and η_x and η_{st} = the refractive index of the solvents.

Through this method the approximate quantum yield in degassed dichloromethane was determined to be $\varphi_{lum} \approx 0.33$.

5.6 Electrochemistry

Electrochemistry experiments were performed on the compound collaboratively with Dr Elena Madrid, and Professor Frank Marken, at the University of Bath.

5.6.1 Solution state electrochemistry

In order to study whether electrochemical redox processes were a plausible switching mechanism for **(21)**, cyclic voltammetry was first performed in solution to attempt to determine how the compound behaves under potential control, but also whether the compound is stable under this relatively harsh manipulation.

Literature examples of cyclic voltammograms of similar compound in solution exist, and it is generally the case that the redox is irreversible due to permanent reactions occurring during redox processes. Due to this it was considered unlikely that any reversible switching process would be feasible in solution. With this in mind, solution state cyclic voltammetry was performed simply to establish the redox behaviour of **(21)**, before moving on to investigations in alternative states.[23,24]

5.6.1.1 Cyclic voltammetry in solution

Cyclic voltammetry was performed using a μAutolab type III potentiostat (Ecochemie, NL) controlled by GPEs software. A three electrode system was used in a standard all-glass electrochemical cell. The working electrode chosen was glassy carbon (3 mm diameter), with platinum wire as the counter electrode and saturated calomel electrode (SCE, Radiometer, Copenhagen) as the reference.

The solution state experiment was performed on a $1x10^{-3}$ mol dm^{-3} dichloromethane solution of **(21)** with 0.1 molar tetrabutylammonium hexafluorophosphate (NBu_4PF_6) used as an inert supporting electrolyte. Prior to any experiment, argon was used to purge the solution of oxygen, and an argon atmosphere was maintained while the cyclic voltammograms were recorded.

A scan rate of 20 mV s^{-1} was used.

The surface of the working electrode was prepared by polishing with alumina slurry (0.1 μm particle size) using a polishing mat. The electrode surface was subsequently rinsed thoroughly with water to remove all traces of the polishing material, and the electrode was allowed to air dry. To ensure the cleanness of the working electrode a "blank" was carried out over the 0.1 mol dm^{-3} NBu_4PF_6 in dichloromethane.

An initial cyclic voltammogram was also recorded using a platinum microelectrode, which makes diffusion effects negligible (hence the shape of the graph differing from traditional CV). The result of this experiment can be seen in **Figure 5.16**. The first oxidation peaks can be assigned due its double I_{p1} (current peak) to a two electron process involving the oxidation of the Pt(II) to the Pt(IV) species. It was seen, however, that as with literature examples of platinum pincer compounds, the compound decomposed during this oxidation.

Looking at the voltammetric response in **Figure 5.17** , the first oxidation peak can be seen to occur at E=0.35V. This can be assigned as oxidation of the platinum centre. The shoulder at E_{ox} = 0.45 V may correspond to an intermediate oxidation state of Pt(III). [25]

Due to the irreversibility of these processes the return wave for these oxidations is poorly defined.

The oxidation at E= 0.68 V can be assigned to the ethynylferrocene unit, and has a reversible reduction peak at E = 0.58 V.

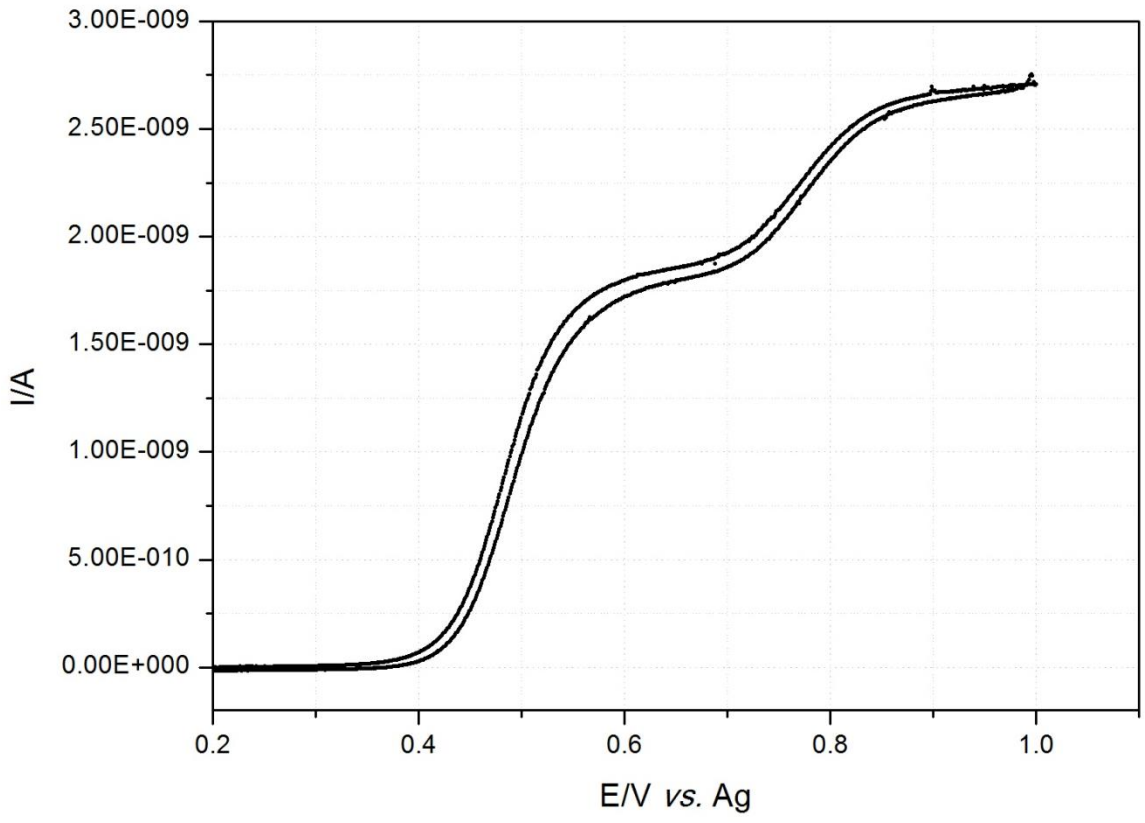

Figure 5.16. Cyclic voltammogram of 1mmol dm^{-3} (21) in 0.1M NBu_4PF_6 dichloromethane solution using 25µm Platinum microelectrode as a working, platinum wire as counter and silver wire as a reference electrode.

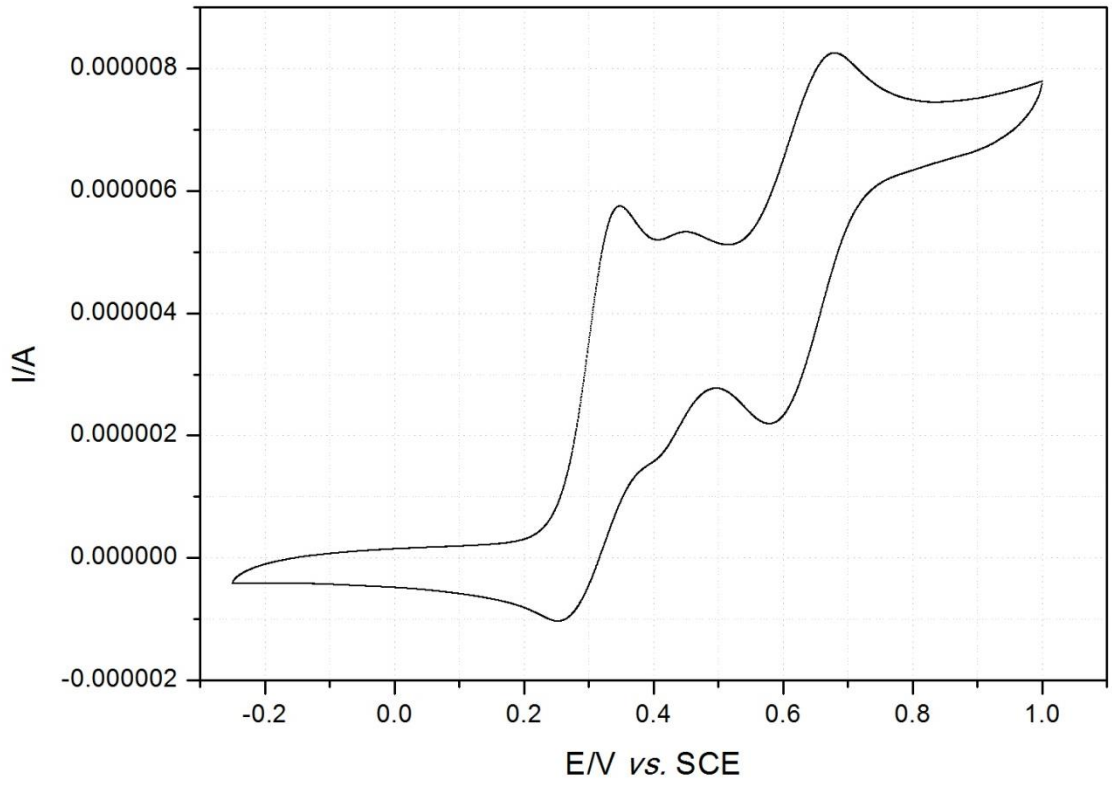

Figure 5.17. Cyclic voltammogram of 1mmol dm^{-3} dichloromethane solution of (21) using 0.1 mol dm^{-3} NBu_4PF_6 as a background electrolyte. Working electrode is a glassy carbon. Scan rate 20mVs^{-1}.

5.6.2 Solid state electrochemistry

Due to the anticipated instability of this compound under simple solution state redox processes, if a stable electrochemical switching of the optical properties was to be achieved, solid state experiments needed to be performed.

Electrochemical experiments were initially performed using crystals of **Polymorph 1**.

In order to establish the behaviour of the solid crystals under redox processes, whether solid state processes would prove to be more reversible, and identify anion transport properties, cyclic voltammetry was again conducted (using the same potentiostat as with solution experiments). A three electrode system was used in a standard all-glass electrochemical cell with a 5mm diameter basal plane pyrolytic graphite working electrode, a platinum wire as counter, and a saturated calomel reference electrode.

All measurements were carried out in aqueous solution, and electrolytes which were purged under argon for at least 15 minutes prior to measurements. An argon blanket was maintained above the solutions throughout all measurements

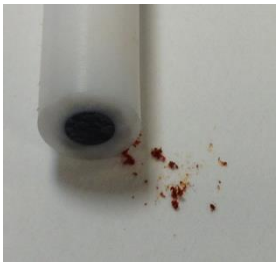

Figure 5.18. Preparation of crystals of (21) Polymorph 1 & pyrolytic graphite electrode.

The working electrode was prepared by rubbing a fragmented crystal of **(21) Polymorph 1** into the freshly sanded surface using techniques described by Marken *et al*. (**Figure 5.18**). [26]

In order to study anion transport processes (insertion/expulsion coupled with redox processes) and structural changes, cyclic voltammetry was performed for a range of anions. The first experiment was conducted using 0.1 mol dm^{-3} $NaNO_3$. As can be seen from **Figure 5.19**, redox processes of the crystals using this background electrolyte solution are unstable, given the sharp decline in current measured with each additional cycle. The nature of the processes also appear to change suggesting significant degradation. The voltammetric response for 0.1 mol dm^{-3} Na_2SO_4 can be seen to show very similar features suggesting that these two anions are unsuitable for use in this system.

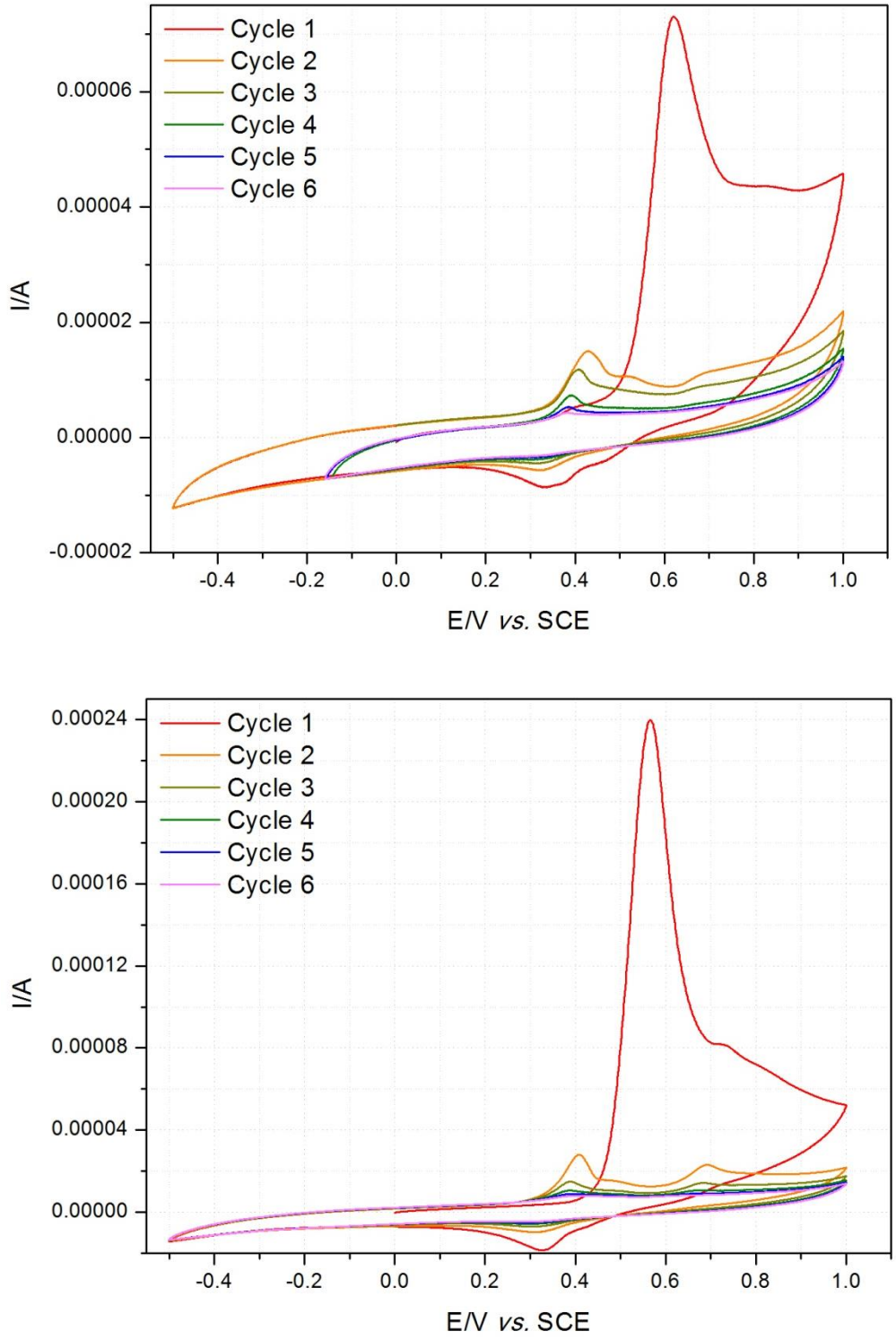

Figure 5.19. Cyclic voltammograms (scan rate 20mVs^{-1}) for oxidation and reduction of (21) as solid crystalline Polymorph 1.

Top: 0.1 mol dm^{-3} $NaNO_3$

Bottom: 0.1 mol dm^{-3} Na_2SO_4

Different behaviour was however observed with ClO_4^- and BF_4^-. Looking at **Figure 5.20** it can be seen that for these anions, after an initial change in the response after the first cycle, a stable state is observed. Two independent oxidation processes can be clearly seen for these systems, and the position of these peaks is seen to vary with the electrolyte used. This initial shift is potentially due to a rearrangement in response to anion transfer to the crystal.

Interestingly for the experiment performed on PF_6^-, the oxidation peaks appear to merge together, and the current increase with each additional cycle. A possible explanation for this is the fragmentation of the crystals with ion transfer through the solid, revealing a higher surface area with each cycle.

Due to its stability, the reversible system based on the perchlorate anions was chosen for further investigation and for spectroelectrochemical measurements. First, however, an attempt to identify the redox species was made.

In order to establish whether either of the two peaks can be attributed to oxidation of the platinum pincer moiety, the experiment was repeated using the chloride substituted analogue **(9)**. In **Figure 5.21** it can be seen that the oxidation occurs at (E_{ox} = 0.7 V), and unlike **(21)** decays upon cycling. Subsequently the peak observed at E_{ox} = 0.55 V for **(21)** may be assigned as the oxidation of the platinum from oxidation state Pt(II) to Pt(IV).

The lower energy oxidation process (E_{ox} = 0.3 V) can be attributed to a $1e^-$ redox transfer from the ferrocene moiety based on its redox potential.[8]

Moving on from this, spectroelectrochemical experiments were set up to attempt to record any changes to the optical spectrum facilitated by these redox processes.

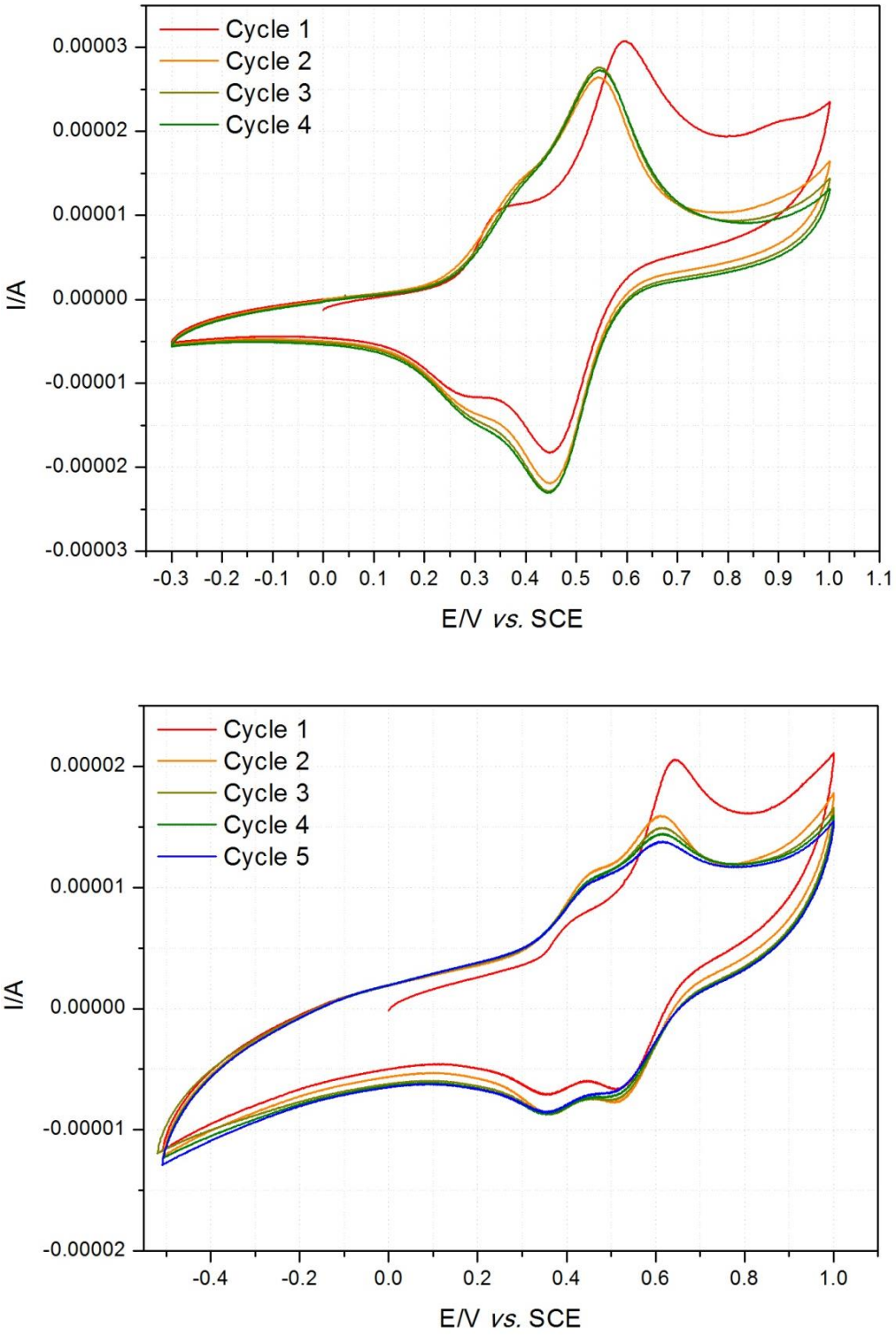

Figure 5.20. Cyclic voltammograms (scan rate 20mVs^{-1}) for oxidation and reduction of (21) as solid crystalline Polymorph 1.

Top: 0.1 mol dm^{-3} $NaClO_4$

Bottom: 0.1 mol dm^{-3} $NaBF_4$

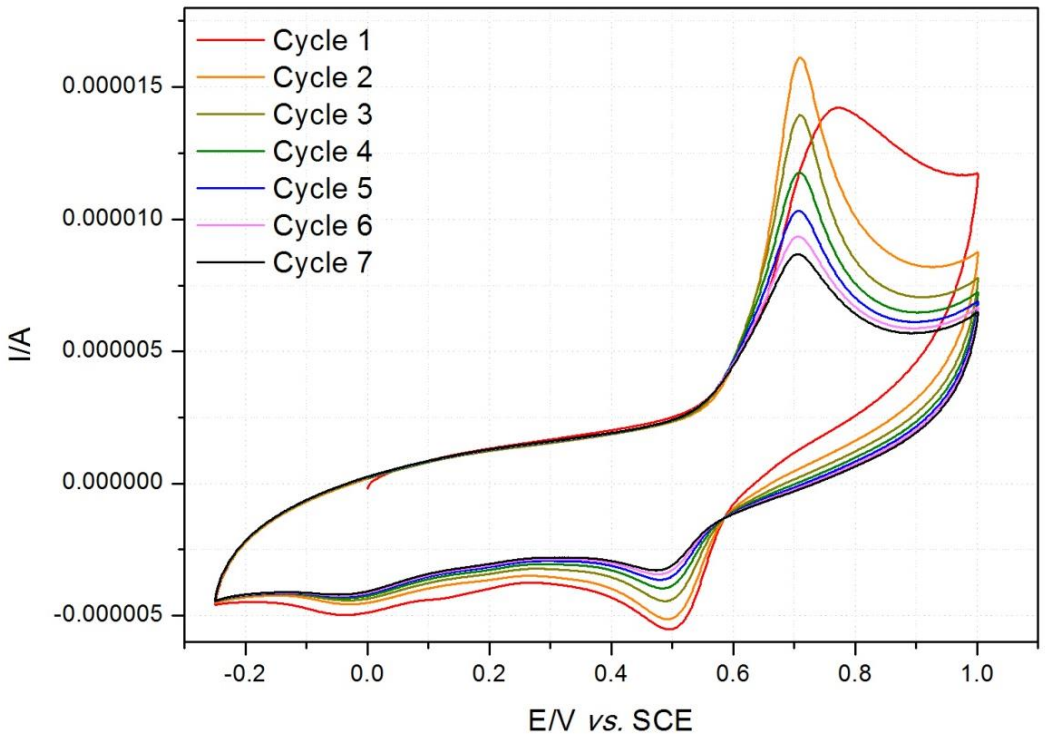

Figure 5.21. Cyclic voltammograms (scan rate 20mVs^{-1}) for oxidation and reduction of (9) as a crystalline solid in 0.1 mol dm^{-3} $NaClO_4$

5.6.2.1 Spectroelectrochemistry

In order to determine whether the compound exhibits changes in optical properties as a response to the reversible oxidation and reduction in the solid state, *in-situ* cyclic voltammetry needed to be performed on a solid sample of the compound while performing UV-visible spectroscopic measurements; this is known as spectroelectrochemistry.

In order for this to be done in the solid state using equipment available, a suitable sample environment needed to be devised whereby a transmission based spectroscopic experiment could be performed on a solid, within an electrolytic cell. The way this was constructed was to use the transparent electrically-conductive material indium tin oxide (ITO) as a substrate for sample deposition, and to use this as the working electrode. The Indium tin oxide (ITO) used was modified with ITO nanoparticles (diameter ca. 20 nm, dispersion in water, Nanophase Technologies Corp. USA) in order to increase the surface of contact with the crystals of **(21)**. This was prepared as described by Marken *et al*. [27]

The ITO electrode was then cut to fit inside a spectrochemical cuvette, and placed with a platinum wire counter electrode, and a silver wire reference. Black tape was then used to restrict the light path to only the area of interest.

The sample was prepared on the ITO working electrode by drop casting a concentrated dichloromethane solution of **(21)**, creating a thin microcrystalline orange/yellow film, consistent in appearance with **Polymorph 2**. The ITO electrodes were then positioned perpendicular to the tape opening of the electrochemical cell.

Due to the required use of transmitted light for the absorption spectroscopy, thin films of **(21)** were a requirement. In order to get good contact with the electrode surface, drop casting was used to crystallise microcrystalline films on the electrode surface (the previously used technique of rubbing pre-crystallised solid into the surface is unsuitable due to the hardness of the ITO resulting in poor adhesion of crystals to the surface). It was noticed upon formation of these films that they differed in appearance significantly from the large prismatic red blocks (**Polymorph 1**) from which the initial crystal structure was obtained. It was this observation that led to an investigation into the nature of the films, and the eventual determination of **Polymorph 2**. In addition to being convenient in its formation of thin but crystalline films, **Polymorph 2** also contains other features that may lend itself to the application of solid state electrochemical experiments.

The planarity of the structure, combined with the fact that the ferrocene groups of **Polymorph 2** are oriented towards a central point, may allow for the possibility of better ion transfer through the crystal. While no formal pore/channel can be seen down the centre of this point, two voids do exist on the outside of two of the ferrocenes, potentially allowing some flexibility in this structure and possible ion migration through the structure under solid state film electrochemical experiments.

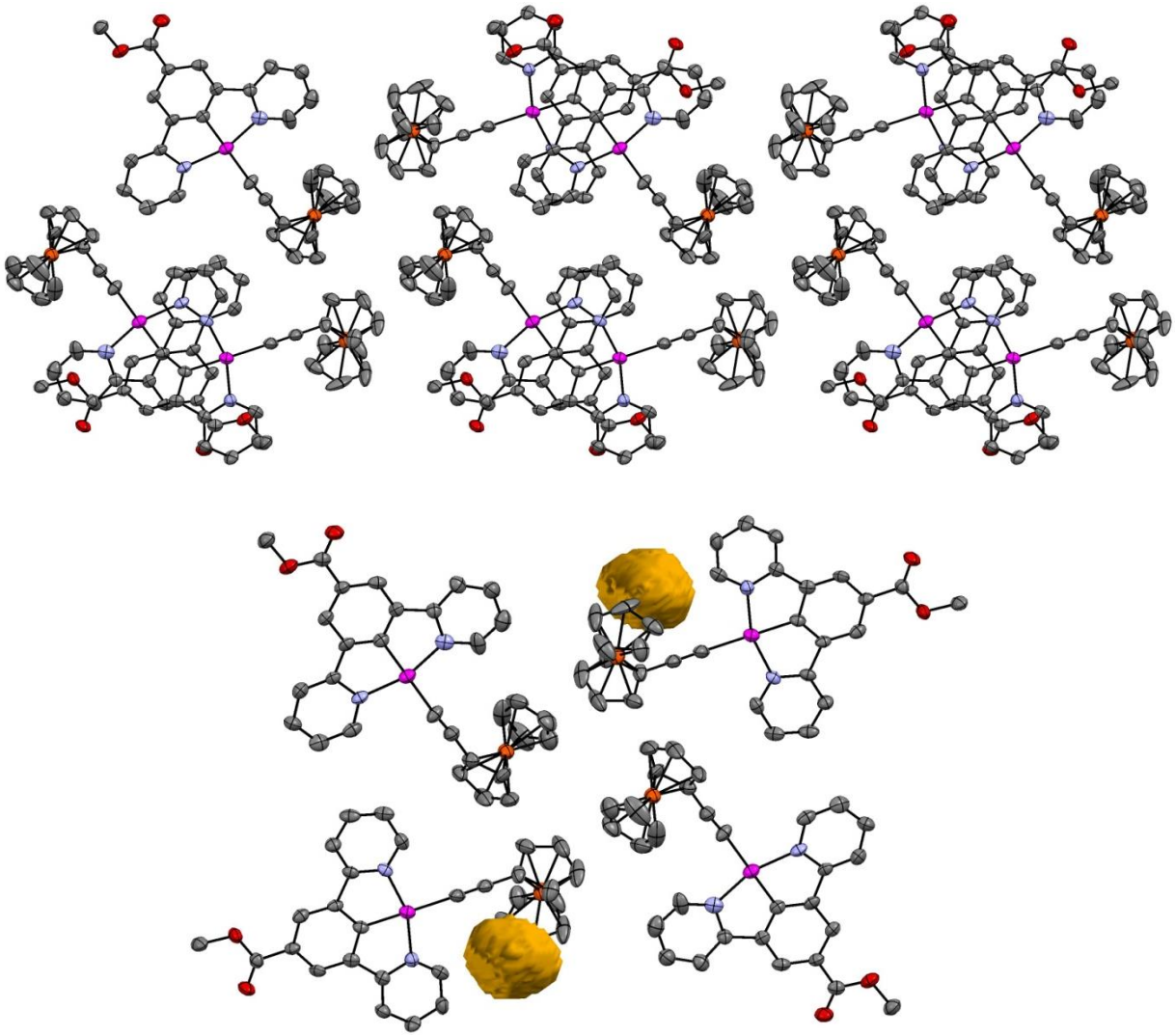

Figure 5.22. Top: Extended structure of Polymorph 2 showing a c-axis view of extended structure, and highlighting the arrangement of ferrocene groups towards a central point. Bottom: Top: Yellow shapes are calculated void spaces in the structure.

Cyclic voltammetry was first performed on this solid film using a 0.1 mol dm^{-3} $NaClO_4$ electrolyte to compare the redox behaviour of the ITO to the pyrolytic graphite electrode, and to ensure that the solid form achieved by drop casting (**Polymorph 2**) remains stable during the redox processes, as with **Polymorph 1**.

The redox activity of this form in thin films on ITO was revealed to show similar behaviour in the cyclic voltammogram to the previous solid-state measurements, confirming that this method provides a suitable sample environment for spectroelectrochemical measurements.

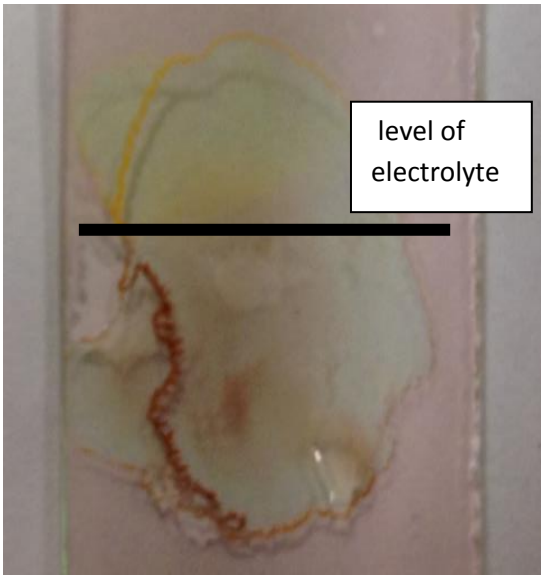

Figure 5.23. Drop-cast film of (21) on ITO, after redox processes. Below the level of the electrolyte, an irreversible transition can be observed from yellow to red.

The UV-visible spectroscopy measurements were subsequently carried out on this sample using a Varian Cary 50 UV/Vis Spectrophotometer, controlled using Cary WinUV software. As can be seen from **Figure 5.23**. The solid film showed an initial irreversible change to its absorption spectrum, coinciding with the initial change in CV observed. This clear red shift occurs completely through the film to the point of contact with the ITO (suggesting complete transformation of the film, and possibly ion migration through the solid film). This initial change is potentially a result of a structural rearrangement of some form to accommodate counter ions. After this initial change, a stable reversible system is set up whereby a notable change to the absorption spectrum as a function of voltage is measured. The transition was also reversible, with the spectrum returning to its original form upon returning to negative potentials.

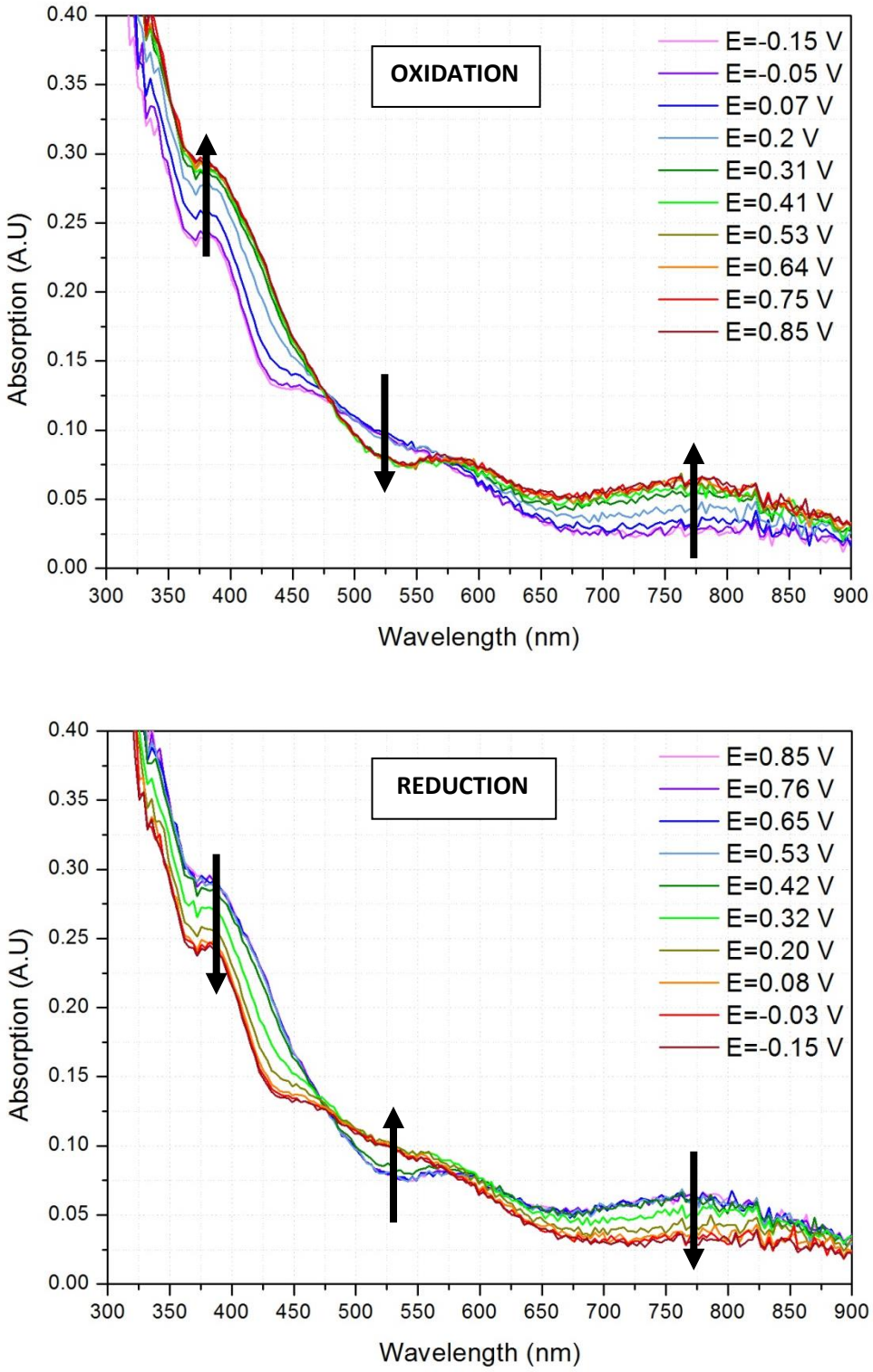

Figure 5.24. Spectroelectrochemistry. Cyclic voltammograms (scan rate 20 mVs^{-1}) for the oxidation and back-reduction of (21) deposited onto ITO working electrode using in 0.1M $NaClO_4$ as a background electrolyte.

Top: Oxidation scan showing significant increase in absorption between 650 and 900 nm.

Bottom: Reduction scan showing complete reversal to initial absorption spectrum

5.6.3 Ionic liquid

Due to the difficulty in producing a reversible system in solution, and in studying the behaviour of the compound in the solid state, a middle ground was attempted in which the compound was dissolved into an ionic liquid as an electrolyte. This bulky, liquid-salt removes the need for solvent, while still allowing for fluid ion transfer, potentially stabilising the redox process and allowing for reliable reversible and stable redox in a solution environment.

The ionic liquid chosen was trihexyl(tetradecyl)phosphonium tris(pentafluoroethyl)trifluorophosphate $[P_{14,666}][TPTP]$ (**Figure 5.25**), and a 0.02 mol dm^{-3} solution of **(21)** was produced by stirring over two days.

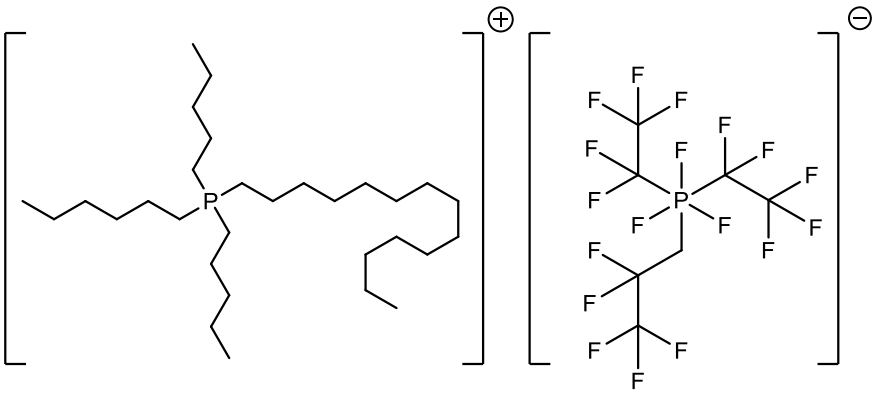

Figure 5.25. trihexyl(tetradecyl)phosphonium tris(pentafluoroethyl)trifluorophosphate [P14,666][TPTP].

An initial cyclic voltammetry experiment performed on this solution can be seen in **Figure 5.26**. It can be seen that unlike previous solution state experiments, a reversible redox process is observed.

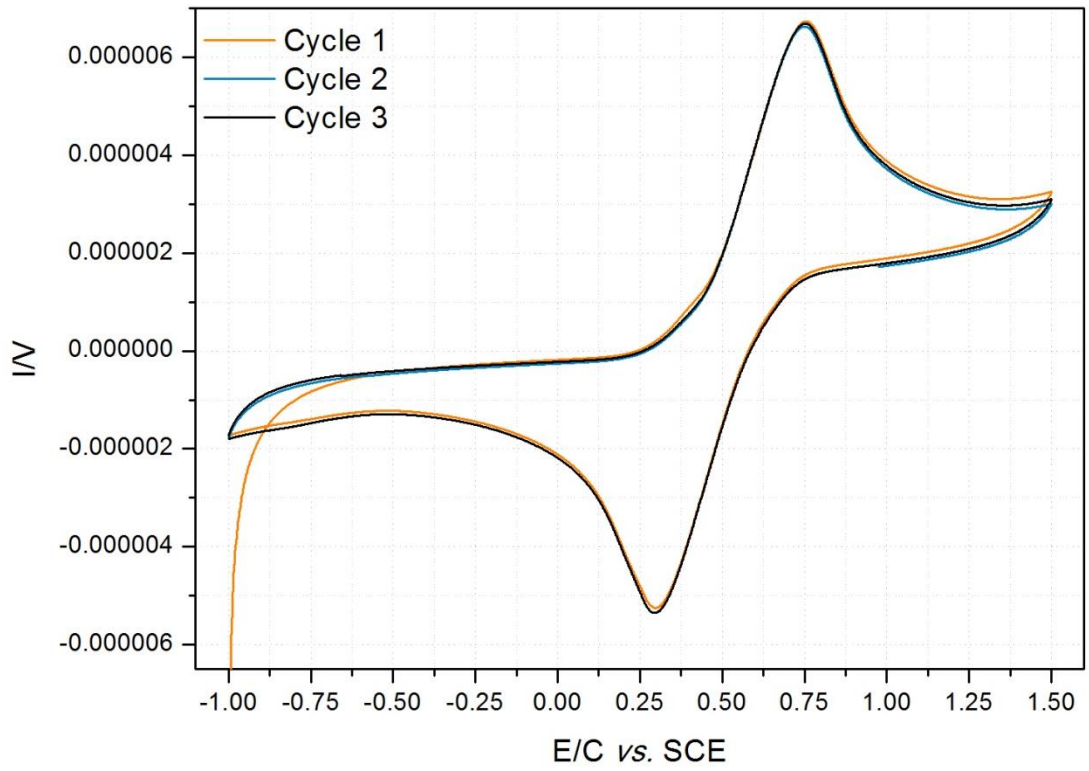

Figure 5.26. Cyclic voltammograms for 0.025 moldm^{-3} solution of (21) in [P14,666][TPTP] at a glassy carbon electrode. Scan rate 20 mVs^{-1}

5.6.3.1 Spectroelectrochemistry

Spectroelectrochemical experiments subsequently conducted using an optically transparent thin layer electrochemical (OTTLE) cell (Omni-cell from Specac) (**Figure 5.27**). The OTTLE cell used allows a volume of 1 mL of liquid sample in between two CaF_2 windows. Platinum mesh is used as the working electrode, and platinum wire and silver wire as the counter, and pseudo-reference electrodes respectively.

Figure 5.27. Electrochemical cell used.

Spectroelectrochemistry experiments were carried out using the spectrometer/potentiostat described previously (**Figure 5.28**).

An initial absorption spectrum was recorded for a $1x10^{-3}$ mol dm^{-3} solution of **(21)** in $[P_{14,666}][TPTP]$, within the OTTLE cell before any potential control, and it can be seen to show an absorption profile consistent to that recorded in dichloromethane solution (**Figure 5.15**) with absorption bands at 230 and 260 nm, and a lower energy absorption at 375 nm. Chronoamperometry at E= 1.2 V was then applied to oxidize the compound, and absorption spectra were recorded until no further changes could be observed (1800 s). A small change to the absorption profile can be seen for the solution in the oxidised state, whereby the absorption at 260 nm shows a slight increase in intensity, and the apparent loss of the peak at 230. However the spectrum appears to change very little towards the low energy regions. A reduction potential (E=0.25 V) was then applied for a further 1800s, and another spectrum recorded. A complete reversal to the original profile can be seen, suggesting a return to the initial species present.

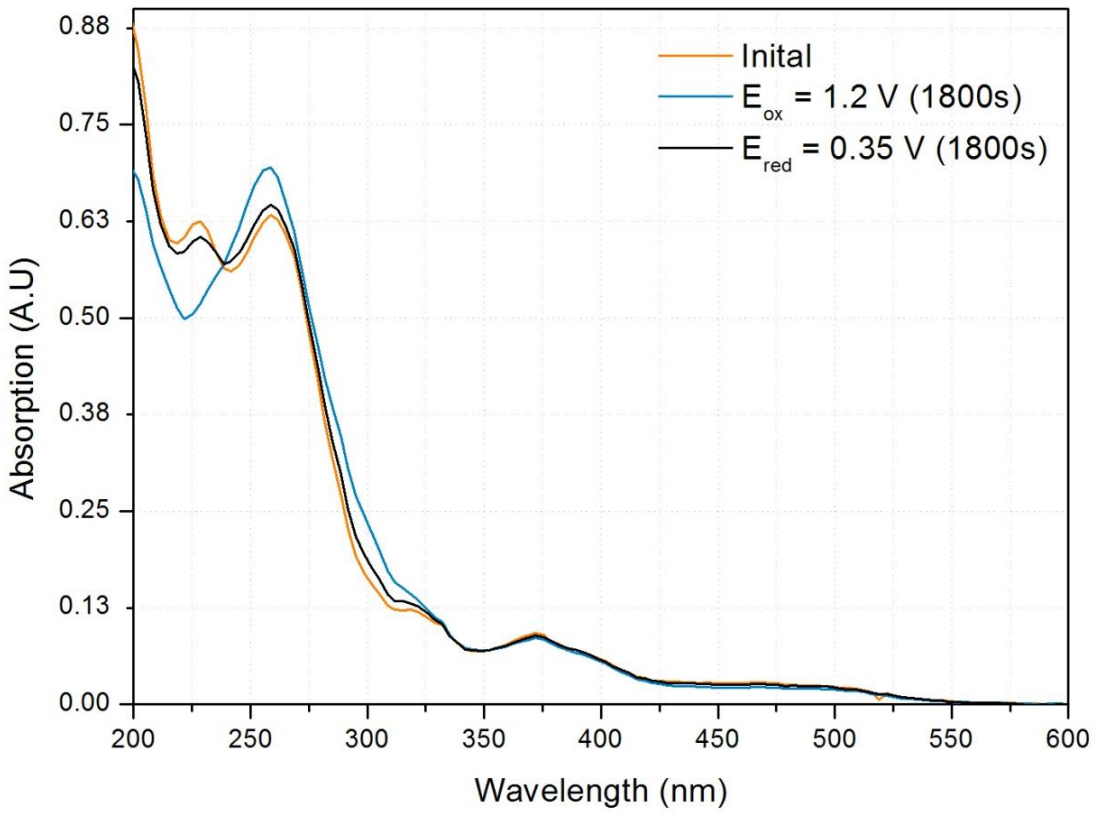

Figure 5.28. The UV/VIS spectral changes accompanying the oxidation/reduction of (21). Conditions: $1x10^{-3}$ mol dm^{-3} solution in [P14,666][TPTP]; OTTLE spectroelectrochemical cell.

5.7 Summary of results and conclusions

The aim of this chapter was to determine whether a molecule with inherently switchable properties could be incorporated into the HOMO of the platinum pincer fragment, and then used as an active site through which to influence the optical properties.

The method taken was to incorporate the well studied electrochemically switchable molecule ferrocene into the HOMO of the molecule, and to use voltage as a stimulus to try and change energy of the orbitals through redox processes, and thus switch the colour.

It was established in the work of **Chapter 2** that the acetylide ligand provided a synthetically convenient bridge through which a ligand could be connected to the platinum d-orbitals through both xz and xy planes, and that the resulting HOMOs were sensitive to the nature of this ligand. Subsequently this approach was taken in attempting to incorporate ferrocene into the HOMO and the unit was successfully synthetically incorporated in this way.

This approach has proven successful, with DFT calculations suggesting the HOMO consists of both the platinum d_{xz} and the iron $d_{x^2-y^2}$ orbitals, bridged by an out of phase π-interaction with the acetylene bridge, while the LUMO remains relatively unchanged.

Electrochemical experiments were then performed to determine whether manipulation of the now ferrocene containing HOMO, through redox processes, could be used as a way of switching the overall optical properties of the compound.

It has subsequently been shown that in the solid state, and through the use of ionic liquids, a stable reversible redox process is possible to achieve for such compounds. Through application of solid crystalline films of **(21)** onto ITO sheets, it has also been shown that it is possible to control the colour using voltage as a stimulus.

Further work to be undertaken in this line of research has many possibilities. While colour switching has been achieved through this method, the degree to which the optical properties have been shown to switch, and the degree of control is limited. Incorporation of alternative switchable fragments into the compound via the acetylide bridge is one approach that should be investigated. Through this method, sensitivities to a variety of stimuli could be envisaged, such as the use of azobenzenes for light sensitivity, or amines for pH sensitivity. Overall this approach shows significant potential in the design of molecular sensors and switches.

5.8 References

(1) Vives, G.; Carella, A.; Sistach, S.; Launay, J.-P.; Rapenne, G. *New Journal of Chemistry* **2006**, *30*, 1429.
(2) Osella, D.; Gambino, O.; Nervi, C.; Ravera, M.; Russo, M. V.; Infante, G. *Inorganica Chinica Acta* **1994**, *225*, 35.
(3) Osella, D.; Gobetto, R.; Nervi, C.; Ravera, M.; D'Amato, R.; Russo, M. V. *Inorganic Chemistry Communications 1* **1998**, 239.
(4) Long, N. J.; Martin, A. J.; Vilar, R.; White, A. J. P.; Williams, D. J.; Younus, M. *Organometallics* **1999**, *18*, 4261.
(5) Mortimer, R. J. *Annual Review of Materials Research* **2011**, *41*, 241.
(6) Roberts, J. D.; Caserio, M. C.; Marjorie, C.; Benjamin inc.: Menlo Park, CA., **1977**.
(7) Clarke, S. F.; Foster, J. R. *British Journal of Biomedical Research* **2012**, *69*, 83.
(8) Gross, M.; Jordan, J. *Pure & Appl. Chem.* **1984**, *56*.
(9) Roemer, M.; Nijhuis, C. A. *Dalton Transactions* **2014**, *43*, 11815.
(10) Sonogashira, K.; Tohda, Y.; Hagihara, N. *Tetrahedron Letters* **1975**, *16*, 4467.
(11) Bruce, M. I.; Jevric, M.; Skelton, B. W.; White, A. H.; Zaitseva, N. N. *Journal of Organometallic Chemistry*, *695*, 1906.
(12) Devi, L. S., Al-Suti, M.K, Zhang, N, Teat, S.J, Male, L, Sparkes, H.A, Raithby, P.R, Khan, M.S, Kohler, A. *Macromolecules* **2009**, *42*, 1131.
(13) Khan, M. S., Al-Suti, M.K, Al-Mandhary, M.R.A, Ahrens, B, Bjernemose, J.K, Mahon, M.F, Male, L, Raithby, P.R, Friend, R.H, Kohler, A, Wilson, J.S *Dalton Trans.* **2002**, 65.
(14) Bio-Rad; Bio-Rad/Sadtler IR Data Collection: Philadelphia, p FTIR.
(15) Sigma-aldrich **2011**.
(16) Khan, M. S., Al-Suti, M.K, Al-Mandhary, M.R.A, Ahrens, B, Bjernemose, J.K, Mahon, M.F, Male, L, Raithby, P.R, Friend, R.H, Kohler, A, Wilson, J.S. *Dalton Trans.* **2002**, 65.
(17) Berenguer, J. R., Lalinde, E, Torroba, J. *Inorg. Chem.* **2007**, *46*, 9919.
(18) Chen, Y.; Li, K.; Lu, W.; Chui, S. S.-Y.; Ma, C.-W.; Che, C.-M. *Angewandte Chemie International Edition* **2009**, *48*, 9909.
(19) Xia, C.; Cao, L.; Liu, W.; Su, G.; Gao, R.; Qu, H.; Shi, L.; He, G. *CrystEngComm* **2014**, *16*, 7469.
(20) Omary, M. A.; Patterson, H. H. *Electronic Spectroscopy: Luminescence Theory*; Academic Press: London, **2000**.
(21) Fonin, A. V.; Sulatskaya, A. I.; Kuznetsova, I. M.; Turoverov, K. K. *PLOS ONE* **2014**, *9*.
(22) Henderson, G. *Journal of Chemical Education* **1977**, *54*, 57.
(23) Williams, J. A. G., Beeby, A., Davies, E.S., Weinstein, J.A., Wilson, C. *Inorg. Chem.* **2003**, *42*, 8609.
(24) Rossi, E.; Colombo, A.; Dragonetti, C.; Roberto, D.; Ugo, R.; Valore, A.; Falciola, L.; Brulatti, P.; Cocchi, M.; Williams, J. A. G. *Journal of Materials Chemistry* **2012**, *22*, 10650.
(25) Ojha, R.; Nafady, A.; Shiddiky, M. J. A.; Mason, D.; Boas, J. F.; Torriero, A. J.; Bond, A. M.; Deacon, G. B.; Junk, P. C. *ChemElectroChem* **2015**.
(26) Babu, K. F.; Kulandainathan, M. A.; Katsounaros, I.; Rassaei, L.; Burrows, A. D.; Raithby, P. R.; Marken, F. *Electrochemistry Communications* **2010**, *12*, 632.
(27) Collins, A. M.; Blanchard, G. J.; Marken, F. *Electroanalysis* **2012**, *24*, 246.

6. Conclusions and future work

6.1 Conclusions

The overall goal of the research presented in this thesis was to take the inherently brightly coloured and luminescent platinum N^C^N pincer moiety and to investigate various ways in which its opto-electronic properties could be manipulated. Gaining some control over the system's colour, and/or luminescent emission, could then allow for the design of visible responses to applied stimuli, paving the way for the development of highly selective molecular sensors.

In order to undertake this study it was first necessary to fully understand and explain the mechanism by which this class of compounds exhibits colour through absorption and emission processes. This was undertaken in the work of **Chapter 2**. The approach was taken to develop a new series of systematically varying platinum pincer complexes, containing polyaromatic fragments bridged by acetylide units at the fourth coordination site of the platinum. Previous studies in the literature indicated that for platinum N^C^N pincers, low energy (visible) absorptions were likely to exist between HOMOs -consisting of occupied non σ-bound metal d-orbitals in an out of phase π-interaction with the fourth coordinating ligand, and LUMOs based primarily on the pincer ligand, in a π-π* metal/ligand to ligand charge transfer.[1-8]

It was hypothesised that by systematically altering the degree of π-interaction experienced by these occupied metal d-orbitals, the energies of the HOMOs could be altered, while leaving the LUMOs unaffected - creating colour change. In order to ensure adequate orbital interaction between the ligand substituent and these orbitals, an acetylide "bridge" was employed. The acetylide unit was chosen for its sp hybridisation, allowing for electronic communication from the ligand to the metal through both xy and xz planes, and acting as a linear linker that would result in neutral complexes overall.

Through spectroscopic and computational analysis, the work of this chapter confirmed this hypothesis, and it was established that control over the HOMO energies (with d-orbital components with the correct symmetry (d_{xz} and d_{xy})) could be imparted through the acetylide linker, with an increase in π-donation resulting in a destabilisation of the HOMO while leaving the LUMO unaffected.

As a result of the knowledge gained in this work, two potential strategies were devised to produce materials with switchable, or externally controllable optical properties. The first of these was investigated in the work of **Chapter 3**.

So far it had been established that by increasing the degree of π-donation to the platinum d_{xz} and d_{xy} orbitals, the energy of the two HOMOs could be raised. It was therefore a reasonable prediction that by reducing this parameter, their energies could also be made to fall. The HOMO-2 of many related systems (including those of **Chapter 2**) consists of the completely unbound platinum d_z^2 orbital, and it is a well known phenomenon in square planar platinum complexes that intermolecular d_z^2- d_z^2 interaction can lead to the formation of new lower energy excited states. In an attempt to produce a compound highly sensitive to intermolecular interaction (particularly in the solid state), the incorporation of the small, and strong-field, cyanide ligand was decided upon.

Due to cyanide's very low π-donor properties, it was hoped that the d_{xz} and d_{xy} orbitals would be stabilised, resulting in the d_z^2 orbital lying close to the frontier. If this was to be the case, any intermetallic interaction through overlap with this orbital would likely result in the creation of new MMLCT states that are highly sensitive to the degree of interaction.

The first compound of this type, **(16)**, developed in **Chapter 3** exhibited just these properties. The compound exists in three distinctly coloured forms- red yellow and blue, and was shown to be able to switch between these forms with unprecedented speed, through exposure to either water or methanol vapour. In order to investigate the mechanism behind this rapid switching, solid state techniques were employed, and through spectroscopic, crystallographic, and computational study, a complete understanding of this material was obtained.

It was shown that by exposure to either water or methanol vapour, the solvent permeated the crystal structure, hydrogen bonding to the cyanide group. The resulting slight planar shift between the molecules was shown to be the route cause for the optical shifts. The three coloured forms all possess linear chains of metal contact running along a crystal axis, with each form exhibiting different degrees of platinum d_z^2 overlap. The degree of red-shift in the lowest energy absorption was shown to correlate with the degree of platinum overlap, and was assigned to a new MMLCT state. Further studies into pincer ligand substitutions also lead to the production of two further vapochromic compounds exhibiting different colours and sensitivities, along with an irreversible thermochromic material.

The work of **Chapter 4** involved studies following the serendipitous discovery of mechanical sensitivity in another platinum pincer system. It was discovered that upon application of shear forces to the compound in the solid-state a large red-shift in its luminescent emission (green/yellow to deep-red/near IR) can be observed, while showing almost no change to the absorption spectrum. This made it possible to write on solid films of the compound with a hard object, visible under UV

light. Through crystallographic and both solid and solution state spectroscopic analysis it was determined that this property was a result of amorphisation of the microcrystalline powder producing excimeric emission.

Having established that the compound was sensitive to intermolecular interactions, it was decided that the compound should be studied using hydrostatic pressure. The compound was shown to exhibit a reversible red-shift or absorption (yellow to red) as a function of pressure, and with spectroscopic, crystallographic, and computational analysis it was established that interactions between pincer phenyls resulted in destabilisation of the LUMO (d_{xz} orbital + ligand π-system).

The work of **Chapter 5** explored the second strategy for introducing controlled visual responses to applied stimuli. From **Chapter 2** it was determined that by using an acetylide as a bridge, π-interactions from various ligands could be transmitted to the HOMOs of the platinum pincer, and manipulate their energies. It was hypothesised that rather than simply altering this ligand synthetically to influence this property, if a ligand with inherent switchability could be included into the π-system, then by switching this ligand's π-interactions would lead to switchable optical properties in the resulting platinum pincer complex. The ligand chosen for this role was ferrocene, with the intention of creating a platinum pincer complex with an optical response to applied voltage. It was hoped that by linking the π-system of a ferrocene's cyclopentadienyl ring to the platinum centre via an acetylide, that electrochemical manipulation of the ferrocene could impart changes on the HOMOs.

Following spectrochemical and electrochemical study, it was determined that for thin crystalline films of **(21)** on an indium tin oxide electrode, a reversible switching between two absorption spectra as a function of voltage is possible. It was also shown that through the use of ionic liquids (or liquid salts), previously unstable solution state electrochemistry for platinum pincers can be accessed.

Overall the original objective of this research has been achieved. By gaining a thorough understanding of the opto-electronic properties of platinum pincer complexes, two controllable routes to imparting externally switchable optical properties have been established.

6.2 Future work

It has been shown in this thesis that the two routes of synthetic modifications to this class of compound are both viable in directing the design of highly specific molecular sensors to a variety of properties. Future work in this line of research seems likely to be fruitful in producing useful materials.

Firstly, investigation into alternative ligands to ferrocene in eliciting a change to π-donor properties looks to be a promising route for further research. For example, linking inherently light-switchable fragments such as azobenzenes or norbornadiene, could allow for production of light switching compounds with a visible response (i.e. using the platinum pincer as a reporting group) allowing for possible applications in data storage. Many other groups with various sensitivities could also be included as a way of producing a visible or luminescent reporting mechanism for a variety of stimuli.

Secondly, the inter-molecular approach has proven highly successful in producing vapour/chemosensors with excellent selectivity and response time. Two paths of further work should be taken for this approach. The first is regarding processing. **(16)** has already drawn interest for several potential applications, however difficulties in processing the microcrystalline films used in the analysis of **Chapter 3** has proven to be a sticking point. Subsequent investigations into processing this material into a more usable format are ongoing, and immobilising the material into a solvent permeable polymer matrix is showing excellent potential in processing the complex into a functional "smart-coating" or vapochromic paint. Further research into this area is likely to continue.

Investigation into new materials should also be undertaken to try and further change the sensitivities, and responses. It has been shown through the work of **Chapter 3** that the ester group plays a useful role in maintaining dry-forms of this class of compound in a planar "solvent receptive" state. Future work should therefore be directed towards producing a further changes to the ester group, and detailed investigation into the nature of these intermolecular interactions and their effect on the overall vapochromic response.

6.3 References

(1) Williams, J. A. G., Beeby, A., Davies, E.S., Weinstein, J.A., Wilson, C. *Inorg. Chem.* **2003**, *42*, 8609.

(2) Williams, J. A. G.; Develay, S.; Rochester, D. L.; Murphy, L. *Coordination Chemistry Reviews* **2008**, *252*, 2596.

(3) William A. Tarran; Gemma R. Freeman; Lisa Murphy; Adam M. Benham; Ritu Kataky; Williams, J. A. G. *Inorg. Chem.* **2014**, *53*, 5738.

(4) Yam, V. W.-W.; Chan, K. H.-Y.; Wong, K. M.-C.; Zhu, N. *Chemistry – A European Journal* **2005**, *11*, 4535.

(5) Williams, J. A. G. *Chemical Society Reviews* **2009**, *38*, 1783.

(6) Nisic, F.; Colombo, A.; Dragonetti, C.; Roberto, D.; Valore, A.; Malicka, J. M.; Cocchi, M.; Freeman, G. R.; Williams, J. A. G. *Journal of Materials Chemistry C* **2014**, *2*, 1791.

(7) Rochester, D. L.; Develay, S.; Zalis, S.; Williams, J. A. G. *Dalton Transactions* **2009**, 1728.

(8) Sotoyama, W.; Satoh, T.; Sato, H.; Matsuura, A.; Sawatari, N. *The Journal of Physical Chemistry A* **2005**, *109*, 9760.

7. Experimental

7.1 Instrumentation

7.1.1 Nuclear magnetic resonance spectroscopy

^{1}H NMR and ^{13}C NMR spectra were recorded on either a Bruker Avance 400 MHz or 500 MHz instrument. Chemical shifts (expressed in parts per million) are referenced to residual solvent peaks. Coupling constant, *J* is given in Hertz.

7.1.2 Infrared spectroscopy

Infrared spectra were recorded on a PerkinElmer Spectrum One spectrometer as neat solids.

7.1.3 Mass spectrometry

Mass spectra were acquired using a micro TOF electrospray Time-of-Flight (ESI-TOF) mass spectrometer (Bruker Daltonik GmbH).

7.1.4 UV-Visible spectroscopy

UV-visible spectra were obtained a PerkinElmer, Lambda 650 UV/VIS Spectrometer (solution state).

Solid state UV-visible spectroscopy was recorded using a microspectrophotometer with a 50 µm diameter probe beam. Spectra were collected using mirrored lenses (Bruker) mounted in an off-axis geometry with a deuterium halogen light as the light source (Ocean Optics). Absorption was monitored over the 200-750 nm wavelength range using a Shamrock 303 imaging spectrograph (Andor). Time resolved measurements, were recorded every 200 ms for the duration of the experiment. Thermogravimetric analyses (TGA) were recorded on a PerkinElmer TGA4000 thermogravimetric analyser.

7.1.5 Photoluminescence spectroscopy

Photoluminescence spectroscopy was performed using a PerkinElmer LS55 luminescence spectrometer.

7.1.6 Thermogravimetric analysis

Thermogravimetric analysis was performed using a PerkinElmer TGA4000 thermogravimetric analyser.

7.1.7 X-ray crystallography

Single crystal x-ray diffraction experiments were performed using multiple instruments:

- **University of Bath**
  - Oxford Diffraction Gemini A Ultra diffractometer equipped with an Oxford Cryosystems Cryojet XL 2.
  - Agilent technologies SuperNova S2CCD diffractometer equipped with 700 series Oxford Cryosystems cryostream.
  - Agilent technologies Xcalibur S2CCD diffractometer, equipped with an Oxford Cryosystems Cryostream Plus.

- **Station 11.3.1, Advanced Light Source, Lawrence Berkeley National Laboratory, CA, USA.**
  - Bruker APEX II CCD diffractometer equipped with a 700 series Oxford Cryosystems cryostream.

Powder diffraction for fingerprinting was performed using the Gemini and SuperNova instruments, with Copper Kα radiation, and with glass capillary sample environments.

7.1.8 High-pressure measurements

High pressure studies were performed using a Merill-Basset diamond anvil cell, using boehler-almax diamonds with 600 μm culets.[1] Laser cut tungsten or steel (200 μm thickness) was used as a gasket material. Gasket holes were drilled using an Oxford Lasers laser mill to 200 μm diameter.

Cells were loaded with ruby powder as a pressure calibrant, with calibration performed using the ruby fluorescence method.[2] 4:1 methanol-ethanol mix, or Fomblin oil, was used as a hydrostatic medium.

The purity of the bulk samples for the new complexes were primarily assessed by a combination of powder X-ray diffraction and mass spectroscopic techniques.

7.2 Synthesis

All synthetic procedures performed in the absence of air and moisture were performed using standard Schlenk techniques under an atmosphere of dry nitrogen or argon. All solvents involved in air and moisture sensitive procedures were dried prior to use using either an automated solvent purification system, or through distillation over an appropriate drying agent, and stored on molecular sieves. Solvents were subsequently degassed using freeze-pump-thaw techniques. All chemicals were purchased from a commercial source and used without further purification unless stated.

*** = new compound**

† = intermediate

7.2.1 1-trimethylsilylethynylnaphthalene (1) †

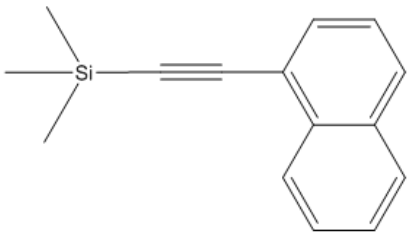

Adapted Sonogashira cross-coupling reaction.[3]

To a solution of 1-bromonaphthalene (2.18ml, 15.5mmol) in dry degassed triethylamine (40ml), $PdCl_2(PPh_3)_2$ (200mg), CuI (100mg), and trimethylsilylacetylene (1.79g, 2.6ml, 18.27 mmol) were added, and the mixture was degassed once more. The suspension was then heated at reflux for 48 hours, and then quenched with water, leaving a black slurry.

All volatiles were then removed under vacuum, and the organics were extracted with n-hexane (30ml), and filtered through celite.

Volatiles were removed from the resulting solution, and the product purified by recrystallisation by dissolving in a minimum quantity of hot diethyl ether, and leaving to chill overnight in the freezer.

Yield: 2.85g, 82%.

^{1}H NMR (400 MHz, $CDCl_3$) δ_H: 8.34 (d, $^3J_{H-H}$=8.3 Hz, 1H), 7.83 (t, $^3J_{H-H}$=7.7 Hz, 2H), 7.71 (d, $^3J_{H-H}$=7.1 Hz, 1H), 7.59 (d, $^3J_{H-H}$= 7.5 Hz, 1H), 7.52 (t, $^3J_{H-H}$= 7.4 Hz, 1H), 7.41 (t, $^3J_{H-H}$= 7.5 Hz, 1H), 0.35 (s, 9H, TMS)

NMR analysis consistent with literature.

7.2.2 9-trimethylsilylethynylanthracene (2) †

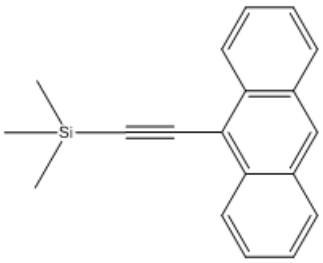

Adapted Sonogashira cross-coupling reaction.[3]

To a solution of 9-bromoanthracene (4g, 15.5mmol) in dry degassed triethylamine (40ml), $PdCl_2(PPh_3)_2$ (200mg), CuI (100mg), and trimethylsilylacetylene (1.79g, 2.6ml, 18.27 mmol) were added, and the mixture was degassed once more. The suspension was then heated at reflux for 48 hours, and then quenched with water, leaving a black slurry.

All volatiles were then removed under vacuum, and the organics were extracted with n-hexane (30ml), and filtered through celite. Volatiles were removed from the resulting solution, and the product purified by recrystallisation by dissolving in a minimum quantity of hot diethyl ether, and leaving to chill overnight in the freezer.

Yield: 2.89g, 68%.

^{1}H NMR (400 MHz, $CDCl_3$) δ_H: 8.55 (d, $^3J_{H\text{-}H}$=8.7 Hz, 2H), 8.42 (s, 1H), 7.99 (d, $^3J_{H\text{-}H}$=8.5 Hz, 2H), 7.58 (t, $^3J_{H\text{-}H}$=7.1 Hz, 2H), 7.50 (t, $^3J_{H\text{-}H}$=7.5 Hz, 2H), 0.42 (s, 9H, TMS)

NMR data consistent with literature.

7.2.3 Ethyl 3,5-dibromobenzoate (3) †

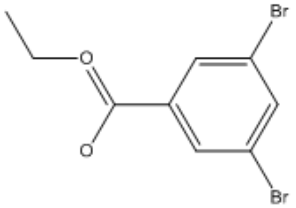

Synthesised by collaborator. Procedure adapted from a literature procedure.

NMR data consistent with literature.

7.2.4 Phenyl 3,5-dibromobenzoate (4) †

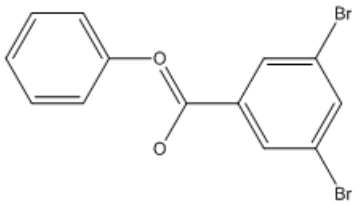

Synthesised by collaborator. Procedure adapted from a literature procedure.

NMR data consistent with literature.

7.2.5 Methyl 3,5-di(2-pyridyl)benzoate (5) †

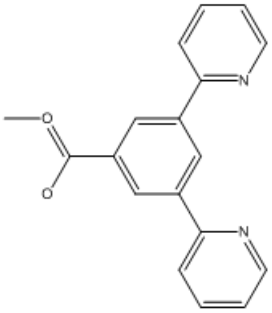

Procedure adapted from a literature procedure.[4]

Stille-Coupling performed: Methyl-3,5-dibromobenzoate (2g, 6.8mmols), 2-tri-n-butylstannylpyridine (tech. 80%) (6ml, 15mmols), bis(triphenylphosphine)palladium dichloride (300mg, 0.43mmol) and LiCl (2.8g, 65.4mmol) were added to dry degassed toluene (30ml) and the mixture was freeze-pump-thaw degassed for five cycles. The mixture was then heated at reflux (120°C) for 24 h under inert atmosphere.

The reaction was allowed to cool to room temperature before a saturated aqueous solution of KF was added to quench the reaction. The resulting slurry was filtered over diatomaceous earth, washed with toluene (10ml) and the eluent retained, and dried under vacuum. To the resulting residue, DCM (150ml) was added, and the solution purified two times in a separating funnel with 100ml of 5% aqueous $NaHCO_3$ solution, retaining the DCM solution each time. The solution was then dried with anhydrous $MgSO_4$, filtered, and the solvent removed under reduced pressure.

The resulting mixture was then purified in a column of silica with gradient elution of hexane, to (1:4) (hexane:Et_2O) resulting in pure product as a fluffy white powder in good yield.

Yield: 1.56g, 79%.

^{1}H NMR (400 MHz, $CDCl_3$) δ_H: 8.98 (t, $^4J_{H\text{-}H}$= 1.8 Hz, 1H, *para-Ph*), 8.80 (d, $^3J_{H\text{-}H}$= 4.8 Hz, 2H, *ortho-Py*), 8.77 (d, $^4J_{H\text{-}H}$= 1.8 Hz, 2H, *ortho-Ph*), 7.97 (d, $^3J_{H\text{-}H}$= 8.0 Hz, 2H, *meta-Py*), 7.86 (td, $^3J_{H\text{-}H}$= 7.7 Hz, $^4J_{H\text{-}H}$= 1.8 Hz, 2H, *para-Py*), 7.36 (dd, $^3J_{H\text{-}H}$ = 4.8 Hz, $^4J_{H\text{-}H}$= 1.1 Hz, 1H, *meta-Py*), 7.34 (dd, $^3J_{H\text{-}H}$ = 4.8 Hz, $^4J_{H\text{-}H}$= 1.1 Hz, 1H, *meta-Py*), 4.04 (s, 3H, COOCH_3)

NMR data consistent with literature.

7.2.6 Acetyl-3,5-di(2-pyridyl)benzene (6) †

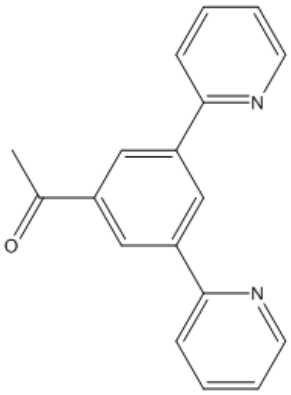

Procedure adapted from a literature procedure.[4]

Stille-Coupling performed as with **(5)**, substituting methyl-3,5-dibromobenzoate with acetyl-3,5-dibromobenzene.

Yield: 1.54g, 83%.

^{1}H NMR (400 MHz, $CDCl_3$) δ_H: 8.89 (s, 1H, *para-Ph*), 8.75 (d, $^3J_{H\text{-}H}$= 4.6 Hz, 2H, *ortho-Py*), 8.66 (s, 2H, *ortho-Ph*), 7.91 (d, $^3J_{H\text{-}H}$= 7.7 Hz, 2H, *meta-Py*), 7.81 (t, $^3J_{H\text{-}H}$= 7.6 Hz, 2H, *para-Py*), 7.30 (t, $^3J_{H\text{-}H}$ = 7.3 Hz, 2H, *meta-Py*), 2.77 (s, 3H, COCH_3)

NMR data consistent with literature.

7.2.7 Ethyl 3,5-di(2-pyridyl)benzoate (7)* †

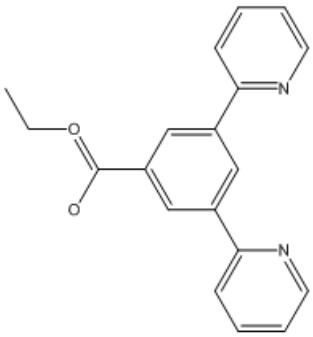

Stille-Coupling performed as with **(5)**, substituting methyl-3,5-dibromobenzoate with ethyl-3,5-dibromobenzene **(3)**.

Yield: 551mg, 71% (from 775mg **(3)**)

^{1}H NMR (500 MHz, $CDCl_3$) δ_H: 8.93 (s, 1H, *para-Ph*), 8.77 (d, $^{3}J_{H\text{-}H}$= 4.7 Hz, 2H, *ortho-Py*), 8.73 (s, 2H, *ortho-Ph*), 7.93 (d, $^{3}J_{H\text{-}H}$= 7.9 Hz, 2H, *meta-Py*), 7.83 (t, $^{3}J_{H\text{-}H}$= 7.7 Hz, 2H, *para-Py*), 7.32 (t, $^{3}J_{H\text{-}H}$ = 6.1 Hz, 2H, *meta-Py*), 4.48 (q, $^{3}J_{H\text{-}H}$ = 7.1 Hz, 2H, $CO_2CH_2CH_3$), 1.48 (t, $^{3}J_{H\text{-}H}$ = 7.1 Hz, 3H, $CO_2CH_2CH_3$)

IR (cm^{-1}): ν(C=O) 1710

Mass Spectrometry (positive loop injection): Measured (MeOH) *m/z* – 327.1138, Calculated for $[C_{19}O_2N_2H_{16}][Na]^+$ – 327.110947. Correct isotope pattern.

Crystallography: CIF file available in supporting information.

7.2.8 Phenyl 3,5-di(2-pyridyl)benzoate (8)* †

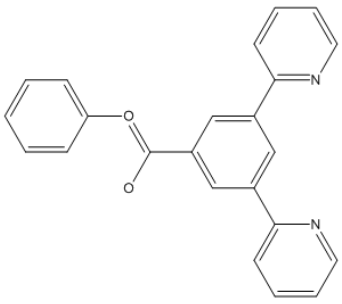

Stille-Coupling performed as with **(5)**, substituting methyl-3,5-dibromobenzoate with phenyl-3,5-dibromobenzene **(4)**.

Yield: 2.31g, 78% (from 3g **(4)**)

^{1}H NMR (500 MHz, $CDCl_3$) δ_H: 9.02 (t, $^4J_{H\text{-}H}$= 1.7 Hz 1H, *para-Ph*), 8.90 (d, $^4J_{H\text{-}H}$= 1.7 Hz, 2H, *ortho-Ph*), 8.78 (d, $^3J_{H\text{-}H}$= 4.2 Hz, 2H, *ortho-Py*), 7.95 (d, $^3J_{H\text{-}H}$= 8.0 Hz, 2H, *meta-Py*), 7.84 (td, $^3J_{H\text{-}H}$= 7.7 Hz, $^4J_{H\text{-}H}$= 1.7 Hz, 2H, *para-Py*), 7.48 (t, $^3J_{H\text{-}H}$ = 7.9 Hz, 2H, *meta-Py*), 7.31 (m, 5H, *pendant-Ph*)

IR (cm^{-1}): ν(C=O) 1733

Mass Spectrometry (positive loop injection): Measured (MeOH) *m/z* – 375.1133, Calculated for $[C_{23}O_2N_2H_{16}][Na]^+$ – 375.110399. Correct isotope pattern.

Crystallography: CIF file available in supporting information.

7.2.9 Chloro[methyl 3,5-di(2-pyridyl)benzoato]platinum (9) †

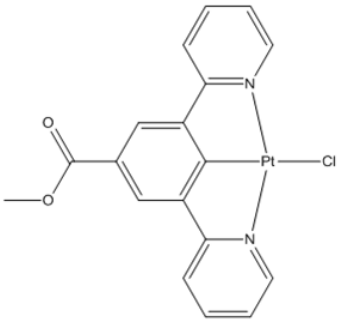

A literature procedure was used.[4]

To a stirred solution of Methyl-3,5-di(2-pyridyl)benzoate **(5)** (100 mg, 0.34 mmol) in acetonitrile (15 ml), a solution of $K_2[PtCl]_4$ (144 mg, 0.34 mmol) in water (5 ml) was added, and the resulting orange mixture was refluxed at 100°C for 3 days.

This was then allowed to cool, resulting in a vivid yellow precipitate, which was retained in a filter and washed with water (20ml), ethanol (20 ml), acetonitrile (20ml), and Et_2O (10 ml). The bright yellow solid was then dried.

Yield: 98mg, **55.4%.**

^{1}H NMR (500 MHz, $CDCl_3$) δ_H: 9.36 (d, $^3J_{H\text{-}H}$= 4.8 Hz, $^3J_{H\text{-}Pt}$= 41.1 Hz, 2H, *ortho-Py*), 8.12 (s, 2H, *pincer-Ph*), 8.01 (td, $^3J_{H\text{-}H}$= 7.8 Hz, $^4J_{H\text{-}H}$= 1.4 Hz, 2H, *para-Py*), 7.81 (d, $^3J_{H\text{-}H}$= 7.9 Hz, 2H, *meta-Py*), 7.36 (td, $^3J_{H\text{-}H}$= 5.7 Hz, $^4J_{H\text{-}H}$= 1.4 Hz, 2H, *meta-Py*), 3.97 (s, 3H, CO_2CH_3)

NMR analysis consistent with literature.

Crystallography: CIF file available in supporting information. Matches literature structure (AQEGOS)

7.2.10 Chloro[acetyl 3,5-di(2-pyridyl)phenyl]platinum (10) †

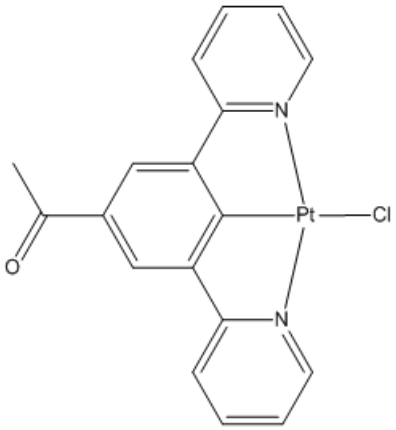

Procedure adapted from literature procedure.[4]

Cyclometallation performed as with **(9)**, substituting methyl 3,5-di(2-pyridyl)benzoate with acetyl 3,5-di(2-pyridyl)benzene **(6)**.

Yield: 85mg, 50%

^{1}H NMR (400 MHz, $CDCl_3$) δ_H: 9.38 (d, $^{3}J_{H\text{-}H}$= 4.5 Hz, $^{3}J_{H\text{-}Pt}$= 38.7 Hz, 2H, *ortho-Py*), 8.06 (s, 2H, *pincer-Ph*), 8.02 (t, $^{3}J_{H\text{-}H}$= 7.0 Hz, *para-Py*), 7.82 (d, $^{3}J_{H\text{-}H}$= 6.9 Hz, 2H, *meta-Py*), 7.35 (t, obscured by $CDCl_3$ signal, *meta-Py*), 2.67 (s, 3H, CO*CH$_3$*)

NMR analysis consistent with literature.

Crystallography: CIF file available in supporting information.

7.2.11 Chloro[ethyl 3,5-di(2-pyridyl)benzoato]platinum (11)* †

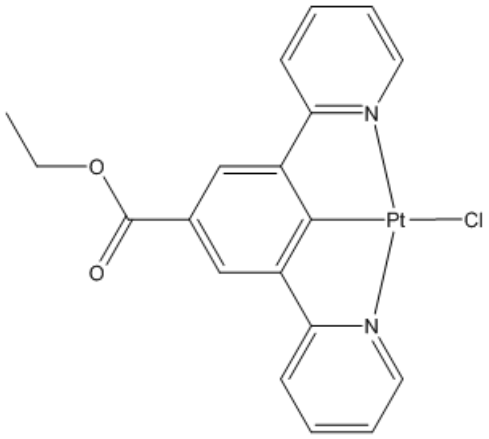

Procedure adapted from literature procedure.[4]

Cyclometallation performed as with **(9)**, substituting methyl 3,5-di(2-pyridyl)benzoate with ethyl 3,5-di(2-pyridyl)benzoate **(7)**.

Yield: 150mg, 85.5%

IR (cm^{-1}): ν(C=O) 1708

^{1}H NMR (500 MHz, $CDCl_3$) δ_H: 9.42 (d, $^3J_{H\text{-}H}$= 5.5 Hz, $^3J_{H\text{-}Pt}$= 42.4 Hz, 2H, *ortho-Py*), 8.20 (s, 2H, *pincer-Ph*), 8.04 (t, $^3J_{H\text{-}H}$= 7.6 Hz, 2H, *para-Py*), 7.86 (d, $^3J_{H\text{-}H}$= 8.1 Hz, 2H, *meta-Py*), 7.39 (t, $^3J_{H\text{-}H}$= 6.77 Hz, 2H, *meta-Py*), 4.46 (q, $^3J_{H\text{-}H}$ = 7.1 Hz, 2H, CO_2CH_2), 1.48 (t, $^3J_{H\text{-}H}$ = 7.1 Hz, 3H, $CO_2CH_2CH_3$)

Mass Spectrometry (positive loop injection): Chloride lost upon ionisation. Measured (MeOH) *m/z* – 498.0792, Calculated for $[C_{19}O_2N_2H_{15}Pt_1]^+$ – 498.078127. Correct isotope pattern.

Crystallography: CIF file available in supporting information.

7.2.12 Chloro[phenyl 3,5-di(2-pyridyl)benzoato]platinum (12)* †

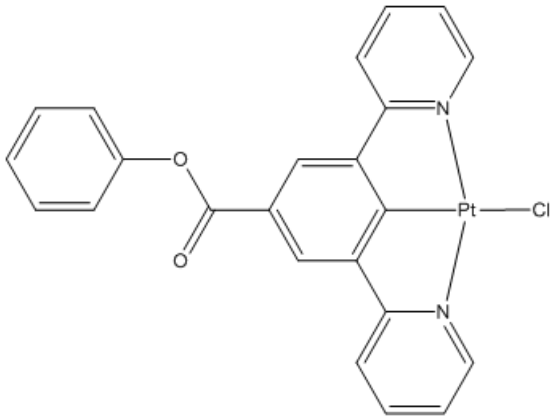

Procedure adapted from literature procedure.[4]

Cyclometallation performed as with **(9)**, substituting methyl 3,5-di(2-pyridyl)benzoate with phenyl 3,5-di(2-pyridyl)benzoate **(8)**.

Yield: 150mg, 85.5%

IR (cm^{-1}): ν(C=O) 1708

^{1}H NMR (500 MHz, $CDCl_3$) δ_H: 9.45 (d, $^3J_{H\text{-}H}$= 5.5 Hz, $^3J_{H\text{-}Pt}$= 41.9 Hz, 2H, *ortho-Py*), 8.34 (s, 2H, *pincer-Ph*), 8.06 (t, $^3J_{H\text{-}H}$= 7.6 Hz, 2H, *para-Py*), 7.89 (d, $^3J_{H\text{-}H}$= 8.1 Hz, 2H, *meta-Py*), 7.50 (m, 3H, *ortho+para-pendant Ph*), 7.42 (t, $^3J_{H\text{-}H}$= 7.2 Hz, 2H, *meta-Py*), 7.34 (t, $^3J_{H\text{-}H}$= 7.4 Hz, 2H, *meta-pendant Ph*)

Mass Spectrometry (positive loop injection): Chloride lost upon ionisation. Measured (MeOH) *m/z* – 546.0806, Calculated for $[C_{23}O_2N_2H_{15}Pt_1]^+$ – 546.078127. Correct isotope pattern.

Crystallography: CIF file available in supporting information.

7.2.13 Phenylethynyl[methyl 3,5-di(2-pyridyl)benzoato]platinum (13)*

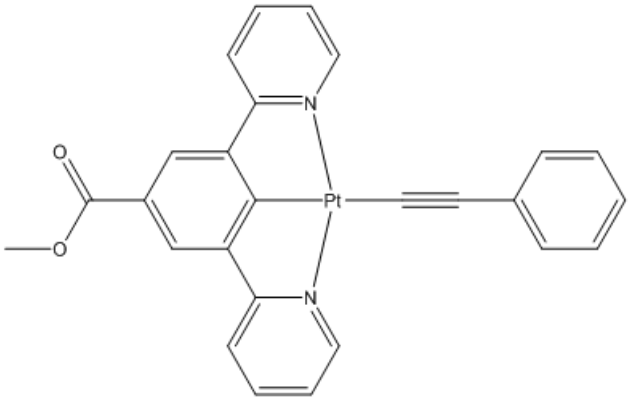

To a stirred solution of NaOH (7.5mg, 0.1875mmol) in degassed methanol (20ml), ethynylbenzene (0.021ml, 0.19mmol) was added and left to stir for 1h under inert atmosphere. Chloro[methyl 3,5-di(2-pyridyl)benzoato]platinum **(9)** (90mg, 0.173mmols) was then added, along with 5ml of DCM to aid dissolution, and the mixture was stirred for 3 days at 40°C. The resulting precipitate and solution were dried under reduced pressure, dissolved in DCM (20ml) and filtered through diatomaceous earth. The orange solution was then dried to form the pure product as a yellow/orange powder.

Yield: 72mg, 72%.

^{1}H NMR (500 MHz, CD_2Cl_2) δ_H: 9.51 (d, $^{3}J_{H\text{-}H}$= 5.6 Hz, $^{3}J_{H\text{-}Pt}$= 47.3 Hz, 2H, *ortho-Py*), 8.27 (s, 2H, *pincer-Ph*), 8.07 (t, $^{3}J_{H\text{-}H}$= 7.8 Hz, 2H, *para-Py*), 7.88 (d, $^{3}J_{H\text{-}H}$= 7.5 Hz, 2H, *meta-Py*), 7.55 (d, $^{3}J_{H\text{-}H}$= 8 Hz, 2H, *ortho-pendant Ph*), 7.33 (m, 4H, *meta-Py* + *meta-pendant Ph*), 7.23 (t, $^{3}J_{H\text{-}H}$= 7.4 Hz, 1H, *para-pendant Ph*), 3.98 (s, 3H, CO_2CH_3)

^{13}C {^{1}H} NMR (400 MHz, CD_2Cl_2) δ_C: 185.65, 169.20, 167.95, 155.96, 152.17, 143.75, 137.09, 131.97, 129.00, 128.59, 125.86, 125.59, 124.71, 120.54, 112.588, 52.56, 1.33

IR (cm-1): ν(C≡C) 2077, ν(C=O) 1696.

Mass Spectrometry (positive loop injection): Measured (MeCN) *m/z* – 608.0925, Calculated for $[C_{26}H_{18}N_2O_2Pt][Na]^+$ – 608.5. Correct isotope pattern.

Crystallography: CIF file available in supporting information.

7.2.14 1-naphthylethynyl[methyl 3,5-di(2-pyridyl)benzoato]platinum (14)*

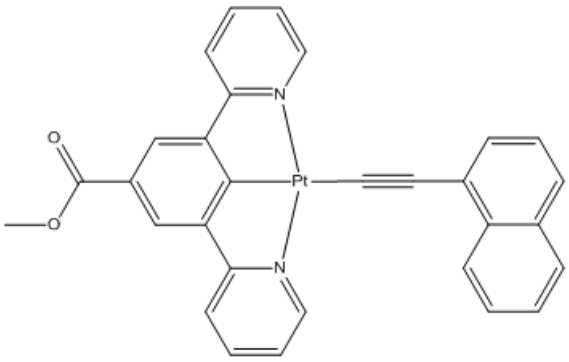

To a stirred solution of NaOH (14mg, 0.35mmol) in degassed methanol (20ml), 1-trimethylsilylethynylnaphthalene **(1)** (67mg, 0.3mmol) was added and left to stir for 1h under inert atmosphere. Chloro[methyl 3,5-di(2-pyridyl)benzoato]platinum **(9)** (150mg, 0.29mmols) was then added, along with 5ml of DCM to aid dissolution, and the mixture was stirred for 48hours at 40°C. The resulting yellow suspension was filtered, and filtered and the precipitate retained and washed with hexane (10ml). The yellow solid was then dissolved in dichloromethane, filtered through celite, and recrystallised by the careful layering of methanol antisolvent onto the solution and allowing slow mixing, producing orange crystals of pure product.

Yield: 99mg, 54%.

^{1}H NMR (500 MHz, CD_2Cl_2) δ_H: 9.57 (d, $^{3}J_{H\text{-}H}$= 5.5 Hz, $^{3}J_{H\text{-}Pt}$= 47.7 Hz, 2H, *ortho-Py*), 8.80 (d, $^{3}J_{H\text{-}H}$=8.2 Hz, 1H, *napththalene(2)*), 8.18 (s, 2H, *pincer-Ph*), 7.96 (t, $^{3}J_{H\text{-}H}$= 7.7 Hz, 2H, *para-Py*), 7.84 (d, $^{3}J_{H\text{-}H}$=7.9 Hz, 1H, *napthalene (4)*), 7.79 (m, 3H, *meta-Py + napthalene (5/8)*), 7.72 (d, $^{3}J_{H\text{-}H}$= 8.2 Hz, 1H, *napthalene (5/8)*), 7.53 (t, $^{3}J_{H\text{-}H}$= 6.8 Hz, 1H, *napthalene (6/7)*), 7.49 (t, $^{3}J_{H\text{-}H}$= 6.8 Hz, 1H, *napthalene (6/7)*), 7.44 (t, $^{3}J_{H\text{-}H}$= 7.4 Hz, 1H, *naphthalene (3)*), 7.24 (t, $^{3}J_{H\text{-}H}$= 6.2 Hz, 2H, *meta-Py*), 3.96 (s, 3H, CO_2CH_3)

^{13}C {^{1}H} NMR (400 MHz, CD_2Cl_2) δ_C: 185.45, 168.64, 167.57, 155.57, 152.14, 143.06, 141.76 138.81, 134.04, 133.45, 129.02, 128.02, 127.61, 126.00, 125.78, 125.73, 125.59, 125.06, 123.92, 119.82, 110.01, 52.14, 1.00

IR (cm-1): ν(C≡C) 2074, ν(C=O) 1697.

Mass Spectrometry (positive loop injection): Measured (MeOH) *m/z* – 658.1119, Calculated for $[C_{30}O_2N_2H_{20}Pt_1][Na]^+$ – 658.106751. Correct isotope pattern.

Crystallography: CIF file available in supporting information.

7.2.15 9-anthrylethynyl[methyl 3,5-di(2-pyridyl)benzoato]platinum (15)*

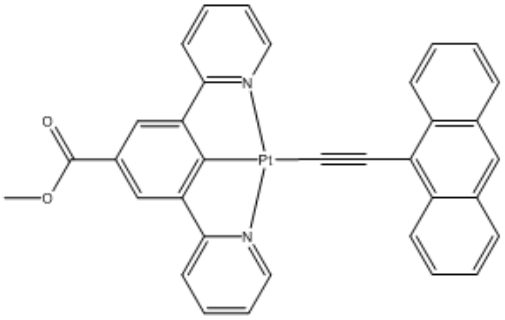

To a stirred solution of NaOH (14mg, 0.35mmol) in degassed methanol (20ml), 9-trimethylsilylethynylanthracene **(2)** (82mg, 0.3mmol) was added and left to stir for 1h under inert atmosphere. Chloro[methyl 3,5-di(2-pyridyl)benzoato]platinum **(9)** (150mg, 0.29mmols) was then added, along with 5ml of DCM to aid dissolution, and the mixture was stirred for 48hours at 40°C. The resulting orange/yellow suspension was filtered, the precipitate retained and washed with hexane (10ml). The orange/yellow solid was then recrystallised by dissolving in a minimum quantity of hot toluene, filtering through celite, and allowing it to crystalise in the freezer. Pure product was isolated as orange crystals.

Yield: 97mg, 49%.

^{1}H NMR (400 MHz, CD_2Cl_2) δ_H: 9.58 (d, $^{3}J_{H\text{-}H}$= 5.7 Hz, $^{3}J_{H\text{-}Pt}$= 47.3 Hz, 2H, *ortho-Py*), 8.92 (d, $^{3}J_{H\text{-}H}$= 8.4 Hz, 2H, *anthracene*), 8.28 (s, 1H, *anthracene*), 8.21 (s, 2H, *pincer-Ph*), 7.98 (m, 4H, *para-Py + anthracene*), 7.83 (d, $^{3}J_{H\text{-}H}$= 8.0 Hz, 2H, *meta-Py*), 7.49 (m, 4H, *anthracene*), 7.23 (t, $^{3}J_{H\text{-}H}$= 7.2 Hz, 2H, *meta-Py*), 3.91 (s, 3H, CO_2CH_3)

^{13}C {^{1}H} NMR (400 MHz, CD_2Cl_2) δ_C: 185.59, 169.24, 167.91, 156.02, 152.17, 143.78, 139.65, 132.24, 128.98, 128.78, 125.96, 125.92, 125.81, 125.60, 124.72, 124.03, 120.68, 108.36, 52.57

IR (cm-1): ν(C≡C) 2065, ν(C=O) 1706.

Mass Spectrometry (positive loop injection): Measured (MeOH) *m/z* – 708.1249, Calculated for $[C_{34}O_2N_2H_{22}Pt_1][Na]^+$ – 708.122672. Correct isotope pattern.

Crystallography: CIF file available in supporting information.

7.2.16 Cyano[methyl 3,5-di(2-pyridyl)benzoato]platinum (16)*

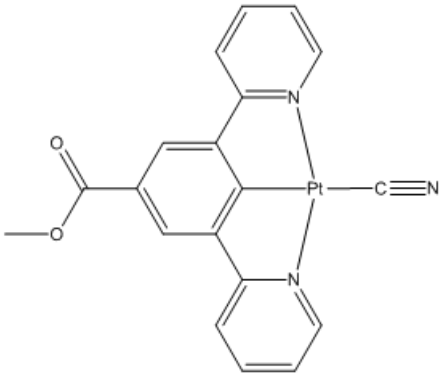

To a stirred suspension of freshly prepared AgCN (25.7mg, 0.192mmols) in 30ml of acetonitrile and dichloromethane (1:1), chloro[methyl 3,5-di(2-pyridyl)benzoato]platinum **(9)** (100mg, 0.192mmols) was added, and heated under reflux for 24 h at 85°C under a nitrogen atmosphere. The resulting orange/brown suspension was dried under reduced pressure, and then stirred with dichloromethane (30ml) until the sparingly soluble residues were dissolved. The yellow mixture was then filtered, and solvents removed *in vacuo*. The resulting bright red solid, was washed with an excess of diethyl ether, and recrystallised by dissolution in boiling methanol, filtering, and allowing to slowly cool.

Yield: 30mg, 30.6%.

IR (cm-1): ν(C≡N) 2118, ν(C=O) 1698

^{1}H NMR (500 MHz, CD_2Cl_2) δ_H: 9.13 (d, $^{3}J_{H\text{-}H}$= 5.2 Hz, $^{3}J_{H\text{-}Pt}$= 48.1 Hz, 2H, *ortho-Py*), 8.13 (s, 2H, *pincer-Ph*), 8.02 (t, $^{3}J_{H\text{-}H}$= 7.8 Hz, 2H, *para-Py*), 7.80 (d, $^{3}J_{H\text{-}H}$= 7.7 Hz, 2H, *meta-Py*), 7.28 (t, $^{3}J_{H\text{-}H}$= 6.5 Hz, 2H, *meta-Py*), 3.91 (s, 3H, CO_2CH_3)

^{13}C {^{1}H} NMR (500 MHz, CD_2Cl_2) δ_C: 156.17, 140.18, 125.46, 125.19, 120.70, 52.54

Low solubility did not allow detection of quaternary carbons.

Mass Spectrometry (negative loop injection): Proton lost upon ionisation. Measured (MeCN) *m/z* – 536.0977, Calculated for $[C_{19}O_2N_2H_{12}Pt_1][MeCN]^-$ – 536.081212. Correct isotope pattern.

Crystallography: CIF file available in supporting information.

6.2.17 Cyano[acetyl 3,5-di(2-pyridyl)phenyl]platinum (17)*

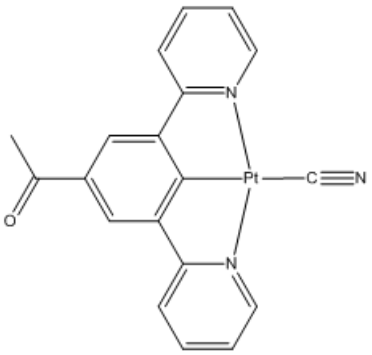

To a stirred suspension of freshly prepared AgCN (26.6mg, 0.199mmols) in 30ml of acetonitrile and dichloromethane (1:1), chloro[acetyl 3,5-di(2-pyridyl)phenyl]platinum **(10)** (100mg, 0.199mmols) was added, and heated under reflux for 24 h at 85°C under a nitrogen atmosphere. The resulting suspension was dried under reduced pressure, and then stirred with dichloromethane (30ml) until the residues were dissolved. The pale yellow mixture was then filtered, and solvents removed *in vacuo*. The resulting green solid, was washed with an excess of diethyl ether resulting in pure product.

Yield: 30mg, 30.6%.

^{1}H NMR (400 MHz, $CDCl_3$*) δ_H: 8.90 (d, $^{3}J_{H\text{-}H}$= 5.0 Hz, $^{3}J_{H\text{-}Pt}$= 46.3 Hz, 2H, *ortho-Py*), 7.95 (t, $^{3}J_{H\text{-}H}$= 8.0 Hz, 2H, *para-Py*), 7.88 (s, 2H, *pincer-Ph*), 7.71 (d, $^{3}J_{H\text{-}H}$= 7.7 Hz, 2H, *meta-Py*), 7.19 (t, $^{3}J_{H\text{-}H}$= 6.0 Hz, 2H, *meta-Py*), 2.56 (s, 3H, COCH_3)

^{13}C {^{1}H} NMR (400 MHz, $CDCl_3$*) δ_C: 201.47, 171.02, 159.00, 146.89, 143.38, 137.44, 128.39, 127.52, 123.88, 30.138

Low solubility did not allow detection of all quaternary carbons.

*a small quantity of MeOD was also added to aid solubility

IR (cm-1): ν(C≡N) 2114, ν(C=O) 1677

Mass Spectrometry (positive loop injection): Measured (MeOH) *m/z* – 517.0678, Calculated for $[C_{19}O_1N_3H_{13}Pt_1][Na]^+$ – 517.0678. Correct isotope pattern.

Crystallography: CIF file available in supporting information.

7.2.18 Cyano[acetyl 3,5-di(2-pyridyl)phenyl]platinum (18)*

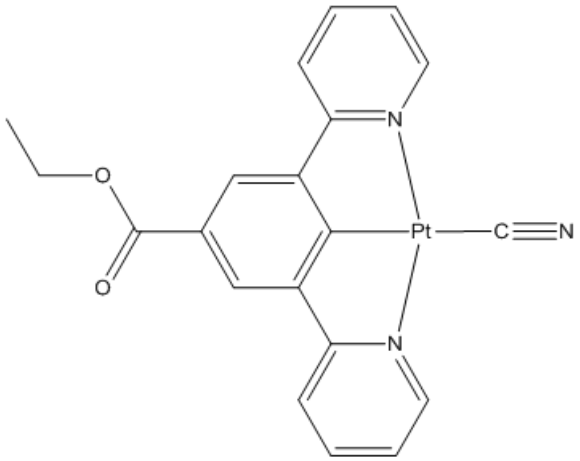

To a stirred suspension of freshly prepared AgCN (26.6mg, 0.199mmols) in 30ml of acetonitrile and dichloromethane (1:1), chloro[ethyl 3,5-di(2-pyridyl)benzoato]platinum **(11)** (100mg, 0.199mmols) was added, and heated under reflux for 24 h at 85°C under a nitrogen atmosphere. The resulting suspension was dried under reduced pressure, and then stirred with dichloromethane (30ml) until the residues were dissolved. The pale yellow mixture was then filtered, and solvents removed *in vacuo*. The resulting green solid, was washed with an excess of diethyl ether resulting in pure product.

Yield: 30mg, 30.6%.

^{1}H NMR (500 MHz, $CDCl_3$) δ_H: 9.28 (d, $^{3}J_{H\text{-}H}$= 5.8 Hz, $^{3}J_{H\text{-}Pt}$= 47.3 Hz, 2H, *ortho-Py*), 8.20 (s, 2H, *pincer-Ph*), 8.05 (t, $^{3}J_{H\text{-}H}$= 7.8 Hz, 2H, *para-Py*), 7.84 (d, $^{3}J_{H\text{-}H}$= 7.8 Hz, 2H, *meta-Py*), 4.46 (q, $^{3}J_{H\text{-}H}$ = 7.1 Hz, 2H, CO_2CH_2), 1.48 (t, $^{3}J_{H\text{-}H}$ = 7.1 Hz, 3H, $CO_2CH_2CH_3$)

^{13}C {^{1}H} NMR (400 MHz, $CDCl_3$) δ_C: 179.94, 167.72, 166.56, 155.73, 153.50, 143.22, 139.60, 136.91, 126.65, 125.01, 124.57, 120.27, 61.30, 14.52

IR (cm-1): ν(C≡N) 2111, ν(C=O) 1702

Mass Spectrometry (positive loop injection): Measured (MeOH) *m/z* – 547.0688, Calculated for $[C_{20}O_2N_3H_{15}Pt_1][Na]^+$ – 547.070599. Correct isotope pattern.

Crystallography: CIF file available in supporting information.

7.2.19 Cyano[acetyl 3,5-di(2-pyridyl)phenyl]platinum (19)*

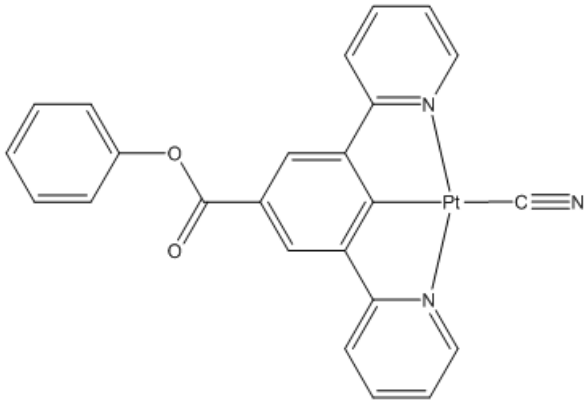

To a stirred suspension of freshly prepared AgCN (26.6mg, 0.199mmols) in 30ml of acetonitrile and dichloromethane (1:1), chloro[ethyl 3,5-di(2-pyridyl)benzoato]platinum **(12)** (100mg, 0.199mmols) was added, and heated under reflux for 24 h at 85°C under a nitrogen atmosphere. The resulting suspension was dried under reduced pressure, and then stirred with dichloromethane (30ml) until the residues were dissolved. The pale yellow mixture was then filtered, and solvents removed *in vacuo*. The resulting green solid, was washed with an excess of diethyl ether resulting in pure product.

Yield: 30mg, 30.6%.

^{1}H NMR (400 MHz, $CDCl_3$) δ_H: 9.32 (d, $^{3}J_{H\text{-}H}$= 5.3 Hz, $^{3}J_{H\text{-}Pt}$= 46.1 Hz, 2H, *ortho-Py*), 8.36 (s, 2H, *pincer-Ph*), 8.10 (td, $^{3}J_{H\text{-}H}$= 7.7 Hz, $^{4}J_{H\text{-}H}$= 1.5 Hz, 2H, *para-Py*), 7.90 (d, $^{3}J_{H\text{-}H}$= 7.7 Hz, 2H, *meta-Py*), 7.53 (t, $^{3}J_{H\text{-}H}$= 7.6 Hz, 2H, *meta-ester-Ph)* 7.37 (t, $^{3}J_{H\text{-}H}$= 7.3 Hz, 4H, *meta-Py* + *para-ester-Ph*), (*ortho-ester-Ph* obscured by $CDCl_3$)

^{13}C {^{1}H} NMR (500 MHz, $CDCl_3$*) δ_C: 180.43, 167.38, 165.405, 155.62, 150.78, 147.44, 143.48, 139.82, 136.125, 129.59, 126.10, 125.47, 124.90 121.61, 120.37

Low solubility did not allow detection of all quaternary carbons.

*a small quantity of MeOD was also added to aid solubility

IR (cm-1): ν(C≡N) 2116, ν(C=O) 1725

Mass Spectrometry (positive loop injection): Measured (MeOH) *m/z* – 595.0787, Calculated for $[C_{24}O_2N_3H_{15}Pt_1][Na]^+$ – 595.070634. Correct isotope pattern.

Crystallography: CIF file available in supporting information.

7.2.20 Phenylethynyl[acetyl 3,5-di(2-pyridyl)phenyl]platinum (20)*

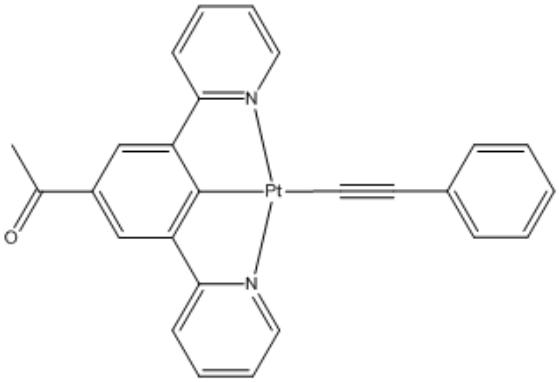

To a stirred solution of NaOH (7.5mg, 0.1875mmol) in degassed methanol (20ml), ethynylbenzene (0.021ml, 0.19mmol) was added and left to stir for 1h under inert atmosphere. Chloro[acetyl-3,5-di(2-pyridyl)phenyl]platinum **(10)** (90mg, 0.179mmols) was then added, along with 10ml of acetone to aid dissolution, and the mixture was stirred for 3 days at 40°C. The resulting precipitate and solution were dried under reduced pressure, dissolved in THF (30ml) and filtered through diatomaceous earth. The yellow/orange solution was then dried and washed with hexane leaving the pure product as a yellow powder.

Yield: 95mg, 93%.

^{1}H NMR (500 MHz, $CDCl_3$) δ_H: 9.55 (d, $^{3}J_{H\text{-}H}$= 5.5 Hz, $^{3}J_{H\text{-}Pt}$= 45.6 Hz, 2H, *ortho-Py*), 8.13 (s, 2H, *pincer-Ph*), 8.00 (t, $^{3}J_{H\text{-}H}$= 7.7 Hz, 2H, *para-Py*), 7.81 (d, $^{3}J_{H\text{-}H}$= 7.8 Hz, 2H, *ortho-pendant-Ph*), 7.58 (d, $^{3}J_{H\text{-}H}$= 7.1 Hz, 2H, *meta-Py*), 7.29 (m, *meta-pendant-Ph + meta-Py*), 7.20 (t, $^{3}J_{H\text{-}H}$= 7.3 Hz, 1H, *para-pendant Ph*), 2.67 (s, 3H, *CH_3*)

^{13}C {^{1}H} NMR (400 MHz, $CDCl_3$) δ_C: 168.59, 155.70, 143.18, 138.90, 131.66, 128.02, 125.54, 124.08, 119.73, 29.72, 26.75, 1.03

Low solubility did not allow detection of all quaternary carbons.

IR (cm-1): ν(C≡C) 2084, ν(C=O) 1658.

Mass Spectrometry (positive loop injection): Measured (MeOH) *m/z* – 592.1092, Calculated for $[C_{26}O_1N_2H_{18}Pt_1][Na]^+$ – 592.106687. Correct isotope pattern.

Crystallography: CIF file available in supporting information.

7.2.21 Platinum[methyl 3,5-di(2-pyridyl)benzoate]Ethynylferrocene (21)*

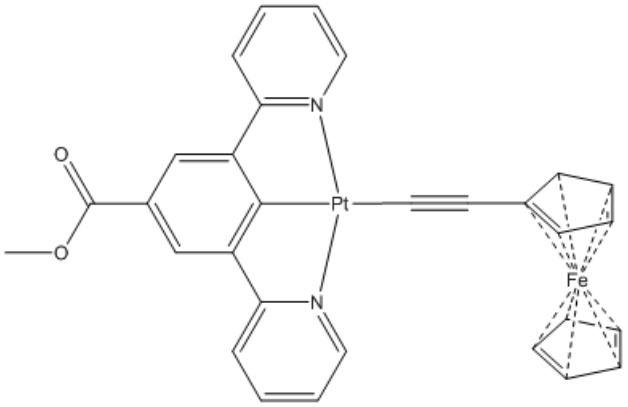

To a stirred solution of Ethynylferrocene (39mg, 0.19mmol) in degassed methanol (15ml), an excess of NaOH (10mg, 0.25mmol) was added, and left to react for 1 hour under argon at room temperature. Upon addition of a solution of Chloro[methyl3,5-di(2-pyridyl)benzoato]platinum **(9)** (90mg, 0.175mmol) in degassed dichloromethane (20ml) by cannula, a colour change to red was observed, and the resulting mixture was heated to 40°C and stirred for 48 hours.

Once cooled, the volatiles were removed, the solid residue re-dissolved in dichloromethane and filtered through Celite. The dichloromethane solution was then left to slowly evaporate, resulting in large, red, prismatic crystals of pure product.

Yield: 91mg, 78%.

^{1}H NMR (400 MHz, $CDCl_3$) δ_H: 9.61 (d, $^{3}J_{H\text{-}H}$= 5.6 Hz, $^{3}J_{H\text{-}Pt}$= 45.3 Hz, 2H, *ortho-Py*), 8.249 (s, 2H, *pincer-Ph*), 8.02 (t, $^{3}J_{H\text{-}H}$= 7.8 Hz, 2H, *Para-Py*), 7.83 (d, $^{3}J_{H\text{-}H}$= 7.8 Hz, 2H, *meta-Py*), 7.3 (t, $^{3}J_{H\text{-}H}$= 7.5 Hz, 2H, *Meta-Py*), 4.54 (t, $^{3}J_{H\text{-}H}$= 1.8 Hz, 2H, *ethynyl-Cp*), 4.29 (s, 5H, *Cp*), 4.17 (t, $^{3}J_{H\text{-}H}$= 1.8 Hz, 2H, *ethynyl-Cp*) 3.99 (s, 3H, COOCH_3)

^{13}C {^{1}H} NMR (400 MHz, $CDCl_3$) δ_C: 184.56, 163.17, 146.13, 145.05, 132.83, 120.36, 116.02, 107.17, 102.24, 100.95, 96.86, 85.75, 48.05, 46.6, 44.13, 30.12, 7.43.

IR (cm-1): ν(C≡C) 2088, ν(C=O) 1698.

Mass Spectrometry (positive loop injection): Ethynylferrocene unit lost upon ionisation. Measured (MeOH) *m/z* – 484.0668, Calculated for $[C_{18}O_2N_2H_{18}Pt_1]^+$ – 484.062477. Correct isotope pattern.

Crystallography: CIF file available in supporting information.

7.3 References

(1) Moggach, S. A.; Allan, D. R.; Parsons, S.; Warren, J. E. *J. Appl. Crystallogr.* **2008**, *41*, 249.
(2) Piermarini, G. J.; Block, S.; Barnett, J. D.; Forman, R. A. *Journal of Applied Physics* **1975**, *1975*, 2774.
(3) Sonogashira, K.; Tohda, Y.; Hagihara, N. *Tetrahedron Letters* **1975**, *16*, 4467.
(4) Williams, J. A. G., Beeby, A., Davies, E.S., Weinstein, J.A., Wilson, C. *Inorg. Chem.* **2003**, *42*, 8609.